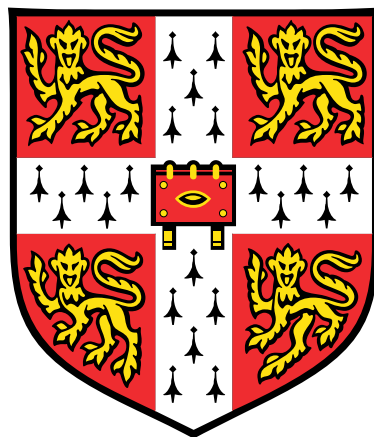


THE FORMATION OF CONTRAST IN SCANNING
HELIUM MICROSCOPY

SAM MORGAN LAMBRICK



Exploring a new imaging technique

This thesis is submitted for the degree of Doctor of Philosophy.

Hughes Hall

University of Cambridge

September 2021

Sam Morgan Lambrick: *The formation of contrast in Scanning Helium Microscopy*,
Exploring a new imaging technique, © September 2021

DECLARATION

This thesis is the result of my own work and includes nothing which is the outcome of work done in collaboration except as declared in the preface and specified in the text. It is not substantially the same as any work that has already been submitted before for any degree or other qualification except as declared in the preface and specified in the text. It does not exceed the prescribed word limit for the Faculty of Physics and Chemistry Degree Committee.

Sam M. Lambrick
Septemeber 2021

ABSTRACT

Over the last decade a new microscopy technique has emerged that uses neutral helium atoms as the probe particles. It has been termed scanning helium microscopy (SHeM), also known as neutral atom microscopy (NAM). SHeM produces helium atom micrographs by scanning the sample beneath a focused or collimated helium microprobe. As the technique is maturing, research efforts are moving on from the development of proof of concept instruments to the exploring of applications and optimising designs for the second generation of machine. In particular the mechanisms of contrast formation in SHeM are an active area of investigation.

The work presented in this thesis explores contrast formation in SHeM and how that knowledge might be used to interpret helium micrographs. Specifically a geometric model of contrast is developed which is implemented numerically in the form of both a ray-tracing framework and integral approaches. Work is also presented looking at design considerations for helium microscopes, informed heavily by simulations. A particular aspect of instrumentation, the ‘pinhole-plate’, is shown to allow the Cambridge A-SHeM (a first generation pinhole SHeM using a 90° total scattering angle) to operate in a modular manner with improved spatial resolution, improved angular resolution, or making changes in image perspective possible. Using the high spatial resolution mode the first helium micrographs with a large working distance and a beam width below $1\ \mu\text{m}$ are presented.

Measurements presented demonstrate that a ‘cosine-like’ diffuse model of scattering is the default atom surface scattering in SHeM for unprepared technological surfaces. Further measurements highlight the importance of multiple scattering as a key feature of topographic contrast in SHeM and how a proper understanding of multiple scattering is necessary for the interpretation of samples of technological interest. It is shown that multiple scattering is understood both quantitatively and qualitatively. Using a specialised arrangement of the Cambridge A-SHeM the first diffraction patterns measured from a microscopic spot size are presented. Diffraction contrast as an alternative to diffuse topographic contrast is then discussed. Finally a technique, coined heliometric stereo, that makes use of the observation of cosine-like scattering and multiple detection directions to perform 3D reconstructs is presented. The method is explored in detail using simulated data in order to demonstrate where it may most effectively be applied, and a proof of principle experimental reconstruction is performed on the A-SHeM.

The thesis finishes with a discussion of the overall conclusions that can be drawn from the current work, and the outlook for scanning helium microscopy in the near term.

PUBLICATIONS

Publications directly associated with this thesis:

S.M. Lambrick, M. Bergin, A.P. Jardine, D.J. Ward. ‘A Ray tracing method for predicting contrast in neutral atom beam imaging’. In: *Micron*, 2018.

M. Bergin, S.M. Lambrick, H. Sleath, D.J. Ward, J. Ellis, A.P. Jardine. ‘Observation of diffractive contrast in scanning helium microscopy’. In: *Scientific Reports*, 2019.

S.M. Lambrick, L. Vozdecký, M. Bergin, J. Haplin, D. MacLaren, P.C. Dastoor, A.P. Jardine, D.J. Ward. ‘Multiple scattering in helium atom microscopy’. In: *Applied Physics Letters*, 2020.

S.M. Lambrick, A. Salvador Palau, P.E. Hansen, G. Bracco, J.E. Ellis, A.P. Jardine, and B. Holst. ‘Helimetric stereo: true to size surface mapping with neutral helium atoms’. In: *Phys. Rev. A*, 2021.

Publications indirectly associated with this thesis:

M. Bergin, D.J. Ward, S.M. Lambrick N.A Jeinsen, J. Ellis, A.P. Jardine, W. Allison. ‘Low-energy electron ionization mass spectrometer for efficient detection of low mass species’. In: *Review of physical instruments*, 2021.

M. Bergin, T.A. Myles, A. Radic, C.J. Hatchwell, S.M. Lambrick, D.J. Ward, S.D. Eder, A. Fahy, M. Barr, P.C. Dastoor. ‘Complex optical elements for scanning helium microscopy through 3D printing’. In: *J. Phys. D: Appl. Phys.*, 2021.

Publications in preparation:

Work from chapter 5 is in preparation for a publication nominally titled ‘Helium atom imaging of technological samples’.

Work from chapter 7 is in preparation for a publication nominally titled ‘2D micro atom diffraction’.

ACKNOWLEDGMENTS

I would first like to acknowledge my supervisors, Prof. Andrew Jardine, for his continued support and advice throughout the course of my project, and Dr. David Ward for his supervision and continuous assistance for all my time in the Surface Physics group. In addition I'd like to make special mention of Dr. Matthew Bergin who was effectively my third supervisor during the first half of my PhD. I also cannot go on without expressing my gratitude for the many fascinating and useful discussions with both Prof. John Ellis and Dr. Bill Allison, as I'm sure so many others who have worked with atom scattering at Cambridge can recall.

Next I must extend my thanks to rest of the Surface Physics group including, Dr. Susanne Schulze, Dr. Nadav Avidor, Fulden Eatram, Jack Kelsall, Arjun Raghavan, Nick von Jeinsen, Alek Radić, and many others.

During my time at Cambridge I have had the pleasure of collaborating with members of the Centre for Organic Electronics at the University of Newcastle, both in research and in scientific outreach at the Royal Society Summer Exhibition, in particular Prof. Paul Dastoor and Tom Myles. My thanks must also extend to Dr. Donald Maclaren and Dr. John Halpin of the University of Glasgow, whom have manufactured countless pinholes as well as test samples. For the highly fruitful collaboration on 3D reconstructions I extend my gratitude to Dr. Adrià Salvador Palau and Prof. Bodil Holst.

For financial support, I thank The MathWorks, Inc. for their generous studentship.

The development of the Cambridge SHeM instruments could not have been achieved, and I could not have done the experiment I have, without the high quality workmanship of The Cavendish workshop. In particular I would like to thank Chris Burling for making so many iterations of difficult to manufacture pinhole-plates, and Kevin Mott for assistance in the student workshop. Additionally I would like to acknowledge the Cavendish electron microscopy suite for their helpfulness and assistance with all things SEM.

Finally I wish to thank all my friends and family for their support, including my parents, Cheryl Lambrick and David Lambrick, as well as Megan Carter who can't go without mention.

CONTENTS

1	INTRODUCTION: FORMING AN IMAGE WITH NEUTRAL PARTICLES	1
1.1	Scanning helium microscopy	1
1.1.1	Producing a helium beam	2
1.2	Image formation	4
1.3	Applications and contrast	4
1.4	The Cambridge A-SHeM	6
1.4.1	The 'standard' configuration	8
1.5	The Cambridge B-SHeM	9
1.6	Thesis overview	9
2	PREDICTING CONTRAST: A RAY TRACING FRAMEWORK	11
2.1	Principles of contrast in SHeM	11
2.2	Ray tracing	14
2.2.1	Simulation method	14
2.2.2	Implementation	18
2.3	Results of the simulation	19
2.3.1	Topographic test	19
2.3.2	Multiple scattering	21
2.3.3	Working distance contrast	21
2.3.4	Varying helium background signals	25
2.4	Application to designs	29
2.4.1	Alternative sample stub design	29
2.4.2	Considering alternative imaging conditions	29
2.4.3	Testing specific component design	34
2.5	Extension to diffractive and inelastic contrast	35
2.6	Study of the NAM	35
2.7	Summary	37
3	PREDICTING CONTRAST: INTEGRAL MODELS	38
3.1	Introduction	38
3.2	The signal for a circular aperture	39
3.2.1	Analytic form	41
3.2.2	Numerical region	42
3.2.3	Extension to elliptical apertures	43
3.3	Signal variation with aperture size	44
3.4	Signal variation with aperture shape	46
3.5	Defining the contrast to noise ratio	47
3.5.1	Difference to noise	47
3.5.2	RMS contrast to noise	47
3.5.3	Differential contrast to noise	48
3.6	Contrast to noise as a function of aperture size	48
3.6.1	Equivalent signal improvements	50

3.7	Contrast from surface deformation	51
3.7.1	The signal due to a deformed surface	51
3.7.2	Evaluating for a simple case	52
3.7.3	Visibility of deformation	53
3.7.4	The deformation due to the pressure of the helium beam	54
3.8	Conclusions	55
4	OPTICAL ELEMENTS (PINHOLE-PLATES)	57
4.1	'pinhole-plate' design	57
4.1.1	Anatomy of a pinhole-plate	57
4.1.2	New pinhole-plates	59
4.2	Design considerations	60
4.2.1	Working distance	60
4.2.2	Pinhole recess and membrane	62
4.2.3	Detector aperture	62
4.2.4	Source cone	64
4.2.5	Pumping around the sample	65
4.2.6	Pinhole choice for new pinhole-plates	66
4.3	Enabling normal incidence	67
4.4	Improving angular resolution	71
4.5	Improving spatial resolution	71
4.5.1	Constrained optimisation	72
4.5.2	Sub-micron beam width	73
4.5.3	The relation of beam width and resolution	75
4.5.4	Further improvements	76
4.6	Summary	77
5	DIFFUSELY SCATTERING SURFACES	79
5.1	Helium scattering distribution from technological surfaces	79
5.1.1	Potential scattering models	79
5.2	Using microspheres to measure scattering distributions	80
5.2.1	Qualitative comparison	81
5.2.2	Scattering distributions from spheres	83
5.3	Discussion	88
5.4	Modelling the scattering of atoms from rough surfaces	90
5.4.1	Random surfaces	90
5.4.2	'Billard ball' scattering	91
5.5	Summary	96
6	MULTIPLE SCATTERING	97
6.1	Diffuse illumination	98
6.2	Multiple scattering test sample	100
6.2.1	Modelling multiple scattering	101
6.3	Comparison of predictions and results	103
6.3.1	Distribution produced by the trench	108
6.4	'Real world' examples of deep features	110
6.5	Summary	111

7	DIFFRACTION CONTRAST	113
7.1	Atom diffraction from surfaces	113
7.1.1	Previous measurements	115
7.2	Improving instrumentation	115
7.2.1	Higher angular resolution	116
7.2.2	Rotator stage	117
7.3	SHeM diffraction measurements	118
7.3.1	Simulation of LiF diffraction	121
7.4	LiF diffraction scans	121
7.4.1	Sample tilt	125
7.5	'Light field' vs 'dark field' imaging	125
7.6	Summary	126
8	HELIOMETRIC STEREO: 3D RECONSTRUCTIONS FROM SHEM IMAGES	129
8.1	General Method: heliometric stereo	130
8.1.1	The photometric stereo technique	130
8.1.2	Simulated helium images	134
8.1.3	Heliometric reconstruction	135
8.2	Extensions and further considerations	137
8.2.1	Non-cosine and multiple scattering	137
8.2.2	Masked regions	139
8.2.3	Sample rotation	140
8.3	Detailed results	142
8.3.1	Rotation to give more detectors	142
8.3.2	Using a single detector	144
8.3.3	Non-normal incidence	144
8.3.4	The impact of aspect ratio on reconstruction	147
8.4	Discussion	149
8.4.1	Design recommendations	149
8.4.2	Limitations	150
8.5	Methods of implementation	151
8.5.1	A-SHeM	151
8.5.2	B-SHeM	152
8.6	Conclusion	155
9	SUMMARY AND OUTLOOK	157
A	THE CONDUCTANCE OF A CONE	160
A.1	Pinhole plates	160
B	CONSTRAINED OPTIMISATION FOR NON-NORMAL INCIDENCE	162
C	CONTRAST OF SUB-BEAM FEATURES	164
D	ALTERNATIVE SPHERE DERIVATION	165
D.1	Line scan	165
D.1.1	First case	166
D.1.2	Second case	167
D.2	Equivalence of the two derivations	168

E	RANDOM SURFACE GENERATION	169
F	INTEGRAL FOR TRENCH LOCALISATION	173
F.1	Three dimensional case	173
F.2	Two dimensional case	176
G	HELIOMETRIC STEREO SAMPLE	177
H	WORKING DISTANCE MEASUREMENT	178
H.1	Method	178
H.1.1	Calculation of average distance	178
H.1.2	Integration limits	180
H.2	The hardware	180
H.2.1	Chamber	181
H.2.2	Camera	182
H.3	Implementation	182
H.4	Calibration	184
H.4.1	Calibration measurement for metal on silicon	185
H.5	Accuracy of measurement	185
H.5.1	Pixel size limit	185
H.5.2	Identification error	186
H.5.3	$z = 0$ position	186
H.5.4	Location of pinhole	186
H.5.5	Selection of minimum working distance	186
	BIBLIOGRAPHY	188

INTRODUCTION: FORMING AN IMAGE WITH NEUTRAL PARTICLES

1.1 SCANNING HELIUM MICROSCOPY

Scanning helium microscopy (SHeM)[1–3] is a technique that uses a thermal energy helium atom beam to produce micrographs. The sample is rastered under a narrow beam of helium atoms with the scattered flux in a particular direction recorded, yielding a map of scattered intensity as a function of the position on the sample at which the beam was incident. The resulting map is plotted producing a helium atom image.

Helium atoms have a few unique advantages over alternative probes that can be used for microscopy. First, the wavelength of thermal-energy helium atoms is ~ 0.05 nm[4], making the theoretical Abbe diffraction limit on resolution very attractive. Second is the energy of the probe particles, whereas electrons used for SEM have energies in the range of 1 – 10 keV, as do ions used in Helium Ion Microscopy[5], and X-rays used in STXM have energies in the keV range, the helium atoms used in SHeM have energies ~ 60 meV. Even photons of visible light have energies ~ 2 eV, which is orders of magnitude larger than thermal helium atoms. Therefore SHeM is a completely non-destructive technique: the atoms are not energetic enough to cause changes to the sample under investigation. The low energy of the helium atoms also completely precludes penetration of the atoms into the sample surface[6], meaning that any information acquired using atoms is a result *only* of the structure of the surface. The same absolute surface sensitivity is not present with either light or electrons, as both can penetrate into the sample to some extent. High levels of surface sensitivity do exist with scanning probe instruments, such as atom force microscopy (AFM) and scanning tunnelling microscopy (STM), but, these techniques are limited to small scanning areas and require specialised tips in order to measure high aspect ratio features[7].

The advantages of helium atoms as a surface probe have been exploited extensively for measurement in reciprocal space without any spatial resolution. Many studies have been undertaken on atom diffraction, including early measurements that helped prove the wave nature of matter[8, 9]. Atom diffraction measurements allow the surface lattice of crystalline solids to be studied[6]. In addition to elastic diffraction measurements, inelastic scattering of helium atoms has been used to investigate surface phonons using time of flight measurements[10]. A type of helium atom scattering apparatus known as helium spin-echo[11] uses the nuclear spin state of helium-3 atoms

as a probe for surface diffusion on time and length scales that could not be investigated experimentally before the advent of the technique.

The first spatially resolved helium images were presented by Koch et al. in 2008[1] using a Fresnel zone plate to focus a beam of atoms, however these were taken in transmission mode. While transmission mode microscopy has proved an incredibly valuable tool with electrons (TEM & STEM) and with light, with atoms transmission mode images are of limited utility. The path of the atoms will be stopped by any solid material so helium transmission images can only produce stencils depicting the presence or absence of the imaged object. Reflection-mode images were first presented by Witham & Sanchez in Portland in 2011[2] using pinhole collimation; they termed the technique Neutral Atom Microscopy (NAM). This thesis uses the term ‘SHeM’ to refer to the technique in general and NAM specifically to the Portland implementation. In parallel to the work by Witham and Sanchez, a different design of pinhole scanning helium microscope was developed by a collaboration between the University of Cambridge and the University of Newcastle, Australia; the design was presented in 2014 by Barr et al.[3].

Since the introduction of the first generation of SHeM there have been numerous upgrades to both the Newcastle and Cambridge SHeM instruments. For example a version II of the Newcastle SHeM, with a reduced background signal, was presented in 2015 by Fahy et al.[12], while the Cambridge SHeM has been equipped with a custom high-sensitivity helium detector yielding orders of magnitude increase in signal[13, 14]. As of 2021 the first of a second generation of SHeM has been developed in Cambridge, with design elements informed by both experimental and theoretical studies in the intervening years – including work presented in this thesis. Recently a SHeM has also been built at the Tata Institute of Fundamental Research in Hyderabad by Bhardwaj et al.[15].

In addition to helium there have been neutral images taken with Argon and Krypton[14–16]. The use of alternative gases is an interesting direction for the technique, especially as, provided an appropriate detector is used, no changes need to be made to a SHeM in order for it to use a different neutral gas. In general focus has been on helium because of the low detector background for the mass to charge ratio of 4 enabling high signal to noise measurements.

1.1.1 *Producing a helium beam*

The key difficulty in SHeM, which caused the large gap between the first non-spatially resolved helium scattering experiments and the first SHeM micrographs, is the production of narrow beams of helium. An early review of the focusing elements was performed by MacLaren[17, 18], the discussion was brought up to 2018 by Bergin[14]. A short summary of potential focusing methods is given below with a focus on those used currently and likely to be used in the near future.

For metastable atoms (atoms in an electronically excited state that possess long lifetimes) or Helium-3 the magnetic moment of the atoms allows for magnetic focusing to be used, for example magnetic hexapoles have been used as lenses for both He-3[19] and metastable atoms[20]. However in addition to needing either rare and expensive helium-3 or excited atoms the achieved spot sizes are not yet comparable to those employed in the current generation of SHeM instruments. Imaging with metastable atoms would probe a quite different atom-surface interaction than using ground state atoms: the internal energy of atoms has a high probability of dissipating into the surface. Therefore while the approach is an interesting body of research it is a different class of technique to SHeM.

For ground state helium-4 atoms research has focused on three methods of focusing: atom mirrors, pinholes, and Fresnel zone plates. Extensive research effort has gone into developing mirrors capable of atom reflections[21–23]. While mirrors are in principle promising, the giant helium cross section to surface defects[6] has meant that effective mirrors for microscopy have thus far been elusive. Some of the best spot sizes reported are for a few 10 μm but with reflectivities of only a few percent.

The simplest method for producing a narrow beam of atoms is pinhole collimation. The ability of a pinhole to produce focused images has been known since antiquity with the principles described by Aristotle and Euclid, while Chinese philosopher Mozi is recorded to have produced the first camera-obscura using a pinhole in the 5th and 4th century BC[24]. Pinhole focusing was the first method to be used successfully to produce reflection-mode helium images. The key to the success of the pinhole is its simplicity, it simply consists of a hole created in a thin membrane. To date all helium microscopes capable of routine reflection-mode imaging have used pinhole focusing. However diffraction limits the achievable resolutions using simple collimation; the limit for the working distances similar to those used in practice is a few 100 nm. Using very small working distances as with near field optical-scanning microscopy[25] could push the resolution further.

An alternative to pinhole collimation is diffractive focusing with a Fresnel zone plate. Fresnel zone plates consist of a series of concentric open and closed rings with each open ring adding amplitudes in phase, to produce a focused spot. Helium atom zone plate focusing has been demonstrated for beam widths below 1 μm [26] and been used to produce transmission mode helium images[1]. Theoretical works show that zone plates will become competitive against pinholes at beam widths ~ 300 nm[27]. In addition the relatively benign scaling of signal with focus size of zone plates ($1/n^2$), compared to pinholes ($1/n^4$)[27], makes zone plates promising for the next generation of SHeM, especially as recent experiments are approaching the diffraction threshold for pinholes and moderate working distances. There are, however, downsides to zone plates: first there is an unfocused 0th order contribution, that has a higher flux than the focused 1st order contribution. In order to address the 0th order contribution zero order stops have been

developed that must be placed after the zone plate but before the sample[28]. Second, to achieve a beam width n the minimum feature size on a zone plate must be no greater¹ than n [27], therefore high resolution zone plates require precision manufacturing on the nanoscale. There are variations of a zone plate such as the atom sieve[29] which may simplify manufacture, but this occurs at the expense of beam intensity. Recently the development of focused helium ion beam milling[30] potentially allows small scale production of zone plates making iteration of designs of zone plates more feasible than wafer scale fabrication with lithography. Some recent work with zone plates (a similar principle could also be used with pinholes) has also demonstrated a mechanism for changing the resolution of a helium beam without the need to break the vacuum[31]. Such work can help to bypass the issue of having to choose between an instrument that images quickly with a poor spatial resolution or a high spatial resolution that requires long measurement times.

1.2 IMAGE FORMATION

In photography or traditional optical microscopy, an object is illuminated with a number of light sources. An image of the object is produced by the light rays scattered from the object passing through a series of lenses, and then being projected onto a light-sensitive detector/film with spatial resolution. In helium microscopy, and other scanning imaging techniques such as SEM, images are formed by illuminating the sample point by point with a focused or collimated beam and measuring the intensity collected by one or several detectors. By rastering the sample under the beam (equivalent to rastering the beam over the sample), an image viewed from the incident beam is generated through Helmholtz reciprocity; the same process that is used in scanning electron microscopes and in dual photography[32]. As a result of the reciprocity there is a reversal of the ‘roles’ of the source and detector in scanning based imaging (such as SHeM), as shown in figure 1.1, thus SHeM images appear to be ‘viewed from’ the focused beam direction and ‘illuminated’ from the detector. In principle, helium microscopy could also use the same imaging principle as photography. However, with present technology it is not possible to build a helium detector with spatial resolution, although design suggestions have been made with field ionisation detection [33, 34].

1.3 APPLICATIONS AND CONTRAST

Since the creation of the first SHeM instruments, focus has shifted onto the study of different samples and applications for the technique. Some of the first publications demonstrated that topographic features dominate micrographs for samples that had not undergone any surface preparation[3,

¹Feature sizes approximately the size of the beam width are required if chromatic aberrations and the source size are ignored, in practice smaller feature sizes are required.

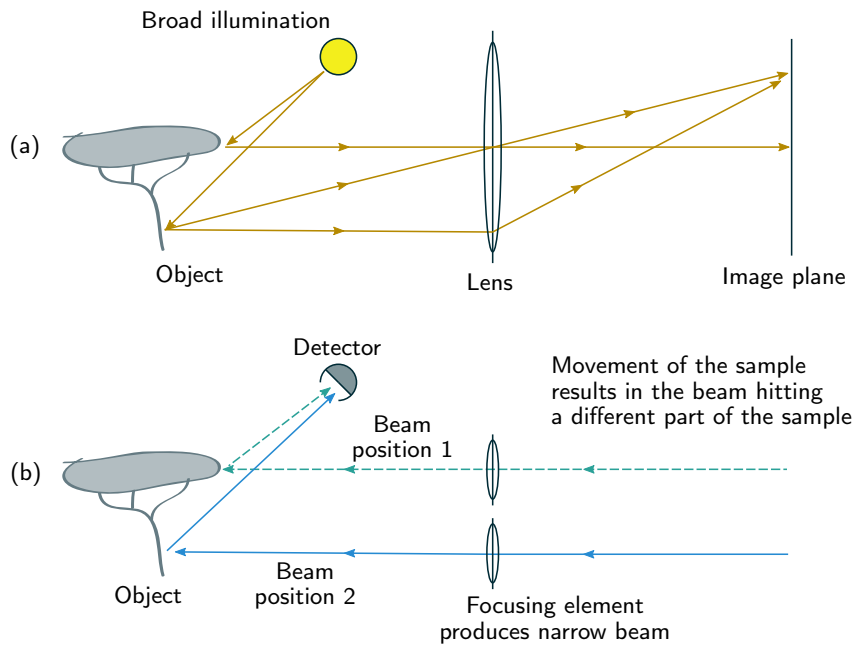


Figure 1.1: (a) The process of image formation using a lens and broad illumination and (b) the alternative method of producing images by scanning a focused probe follows from inverting the direction of the light rays to give an image appearing as if it were formed behind the focusing element. In (b) the two beam positions would not happen simultaneously. Understanding the projection allows the right coordinate system to be used for heliometric stereo.

[12, 16]. The dominant scattering model underlying topographic contrast was not initially clear, however further studies have started to indicate that an approximately diffuse cosine model is likely[35], consistent with the Knudsen model of randomisation. Some of the most recent results are presented in this thesis and provide quantitative evidence for the cosine model (chapter 5). An interesting development has been the use of the topographic imaging capabilities of SHeM to perform 3D stereo-photogrammetry measurements to aid the taxonomy of delicate specimens[36]. The study of topographic contrast has also led to the development of computational tools to assist in understanding contrast. The flexible framework developed by the author is presented in chapter 2, while models based on similar principles have also been used by Fahy[35] and Myles[37]. These tools have helped cement an understanding of the contrast formation process and focus experimental investigations.

Investigations have also yielded non-topographic contrast, in particular the material based contrast observed by Barr et al.[38] where thin films of metals deposited on a silicon substrate present different intensities when observed in SHeM. Other studies have demonstrated that contrast due to surface roughness also exists[14, 16]. While it cannot be proved conclusively

AFM measurements do suggest that the contrast observed from the thin films does not correlate with the roughness of the different metal surfaces[39].

One of the most studied processes of atom surface interaction is diffraction from the surface lattice. The first confirmed contrast observed in SHeM due to diffraction was presented by Bergin et al.[40] using Lithium Fluoride. However, the first configuration of SHeM proved ill-suited for measurements of diffraction patterns. Therefore efforts have been undertaken to improve the instrumentation to enable the measurements of atom diffraction patterns in SHeM, these are detailed in chapter 7.

While the evidence is starting to strongly point in the favour of the diffuse Knudsen model of scattering as the default in SHeM, the cause of the observed diffuse scattering remains an open question. It is also currently unknown how other helium scattering process will manifest in SHeM micrographs of non single crystal samples, for example the Debye-Waller[41] effect has been proposed as a source for the anomalous contrast observed by Barr et al.[38], but the models for clean single crystals are unlikely to be applicable without modification to the SHeM micrographs. In principle different surface Debye temperatures could result in different levels of specular scattering in SHeM, and thus produce contrast.

1.4 THE CAMBRIDGE A-SHEM

The majority of the experimental data presented in this thesis was collected using the Cambridge A-SHeM, therefore a detailed account of the instrument is given.

There are three principle components of the A-SHeM: the source, the sample chamber and the detector. The source produces the helium beam, the sample chamber houses the sample manipulator and defines the final optics of the instruments, finally the detector measures the flux of helium gas scattered off the sample.

A high pressure free-jet expansion, of the type described by Barr et al.[42], is used to produce the helium beam. Letting high pressure helium gas into a vacuum chamber creates a supersonic expansion[43], the centreline of the expansion is selected by a 100 μm diameter beam dynamics skimmer producing a monochromatic beam of helium atoms – the expansion and skimmer can be seen on the left of the schematic in figure 1.2. The skimmed beam then passes through a differential pumping chamber. Differential pumping prevents the leakage of helium from the source to the sample chamber or detector and the lower pressure of the chamber compared to the source chamber ensure there is no interference between the beam and background gas.

In 2019 an improved sample/differential pumping chamber, designed by DJ Ward, was installed. The new chamber significantly increased the pumping in the differential chamber as well as providing room for expanded sample manipulation and in situ sample preparation for future experiments.

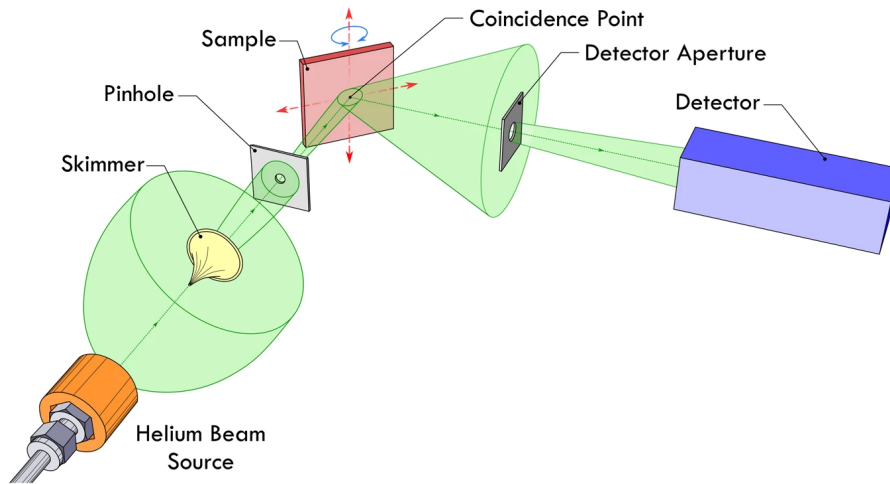


Figure 1.2: Schematic diagram of the SHeM technique, the diagram accurately represents the Cambridge A-SHeM and B-SHeM as well as the Newcastle SHeM. The helium beam is generated by collimating a free jet expansion of high pressure helium gas twice, first at a larger skimmer aperture and second at a microscopic pinhole. The sample is rastered beneath the beam in order to build up a helium reflectivity map that may be interpreted as an image. Diagram by Myles *et al.*[44].

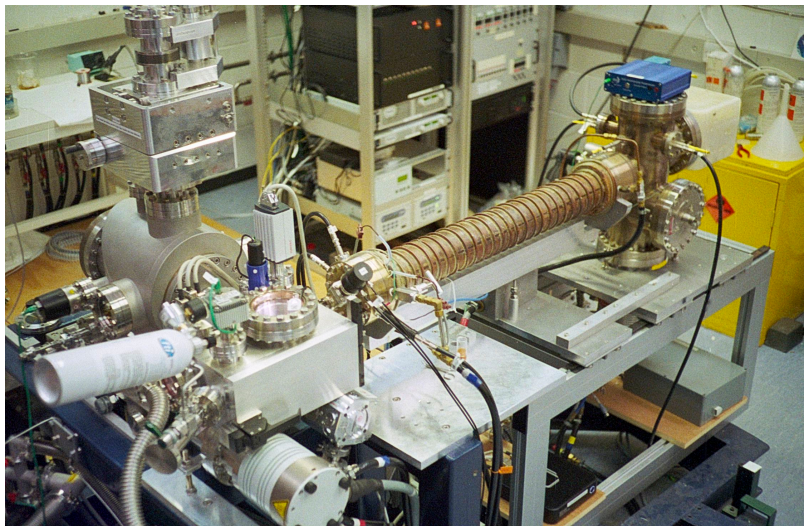


Figure 1.3: A photograph of the A-SHeM in 2019 with the new sample chamber installed. To the top left is the source chamber with the large rectangular nozzle manipulator above it. To the bottom left is the sample chamber with a hinged door. To the middle and right is the solenoid ionizing detector.

In addition a hinged door was added (rather than a bolted flange), making day-to-day operation of the machine simpler. A photograph of the A-SHeM, with the new sample chamber installed, is presented in figure 1.3.

The sample chamber provides space for installing the *pinhole-plate*, in addition to the sample and the nano-positioning stages used to raster the sample. In the walls of the sample chamber are two holes, one connects to the differential pumping chamber and allows the skimmer beam to be incident upon the pinhole, the second connects to a stagnation region that

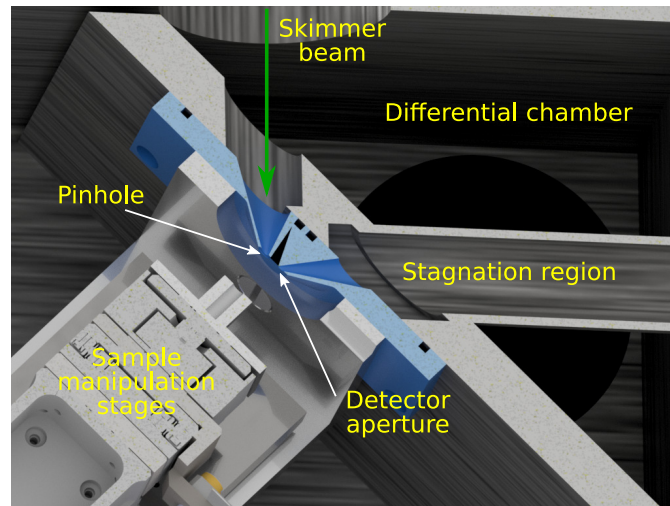


Figure 1.4: A render of the pinhole-plate (highlighted in blue) within the sample and differential chambers. The plate connects the differential chamber, which the skimmer beam passes through, to the sample chamber, and provides a path from detector aperture in the sample chamber to the stagnation region. The nanopositioning stages that manipulate the sample are mounted off an L-bracket that is attached to the pinhole-plate.

leads to the detector. Mounted over these holes, as shown in figure 1.4, is the pinhole-plate. The pinhole-plate mounts the collimating pinhole as well as providing a path from a detector aperture that is placed near the sample to the stagnation region. Thus the pinhole-plate can be considered the key optical element in the A-SHeM, and a detailed consideration of its design is given in chapter 4. The pinhole collimates the skimmer beam, which is a few millimetres wide, down to a suitable microprobe. Mounted from the pinhole-plate is an L-bracket upon which is mounted the xyz manipulator (and more recently an azimuthal rotator) that moves the sample beneath the beam. The details of the design of the sample manipulation and mount are given in chapter 2 of Bergin's thesis[14].

Connecting the pinhole-plate to the detector is a small tube in which the helium gas stagnates. The stagnation volume is connected at the other end to the custom ionizing detector. Electron bombardment is used within a confining solenoid to ionize helium atoms, the ions are then extracted and a magnetic sector is used to filter for mass to charge ratio of 4, finally the ion current enters a dynode channel electron multiplier system that amplifies the current to detectable levels. The current is measured either with a picoammeter or through a pulse counting arrangement. Details of the detector are given by Bergin et al.[13].

1.4.1 The 'standard' configuration

Throughout this thesis the terms 'standard' or 'original' A-SHeM configuration are referred to, especially in light of proposed or realised changes to the instrument. The standard configuration uses either the original pinhole-plate

in the original sample chamber, or a pinhole-plate with equivalent geometry and detection conditions in the new sample chamber – the latter is shown in figure 1.4. The standard configuration uses a 45° incidence angle with approximately 45° detection direction in plane with the incident beam, and a perpendicular working distance of approximately 2.1 mm. Unless stated otherwise the SHeM micrographs presented in this thesis were gathered in the standard configuration.

1.5 THE CAMBRIDGE B-SHEM

Recently constructed in Cambridge is a second generation SHeM coined the B-SHeM. The B-SHeM is intended to operate at slightly smaller working distances than the A-SHeM and, for the first time, includes the ability to have multiple detectors operating simultaneously. In addition the instrument includes a new more compact source with a computer controlled nozzle. While the B-SHeM has not been used to acquire any data presented here, a number of the features highlighted have informed the design of the instrument. For example the number of detectors for the B-SHeM was influenced by work on 3D reconstructions in chapter 8, and reducing the intended working distance was informed by the investigations in chapter 4.

1.6 THESIS OVERVIEW

The remainder of this thesis is arranged as follows. Chapter 2 introduces a purely geometric model for conceptualising and understanding contrast formation in SHeM, along with a computational ray tracing framework for predicting contrast according to that model. The framework is shown to be qualitatively successful at reproducing helium micrographs and is used to uncover specific features such as the effective depth of field in SHeM. The framework is also shown to be effective at considering alternative designs and imaging conditions beyond the standard configuration of the Cambridge A-SHeM. A further result is to highlight the significance of the underlying *scattering distribution* as the key to contrast and the major assumption in any model of contrast.

Chapter 3 builds upon the work in chapter 2 by using integral methods to predict contrast. These methods are used in specific studies of the effect of the detector aperture size on diffuse topographic contrast and in precluding the possibility of contrast due to sample deformation under the beam.

Chapter 4 takes some of the key conclusions from the first two chapters to inform the design of new pinhole-plates for the Cambridge A-SHeM. By having multiple pinhole-plates it is shown that a SHeM can operate in a modular manner, performing quite different experiments with a change in only one modest component. Three new configurations are presented: a normal incidence mode, a high angular resolution mode, and a high spatial

resolution mode. The final high resolution mode is shown to produce the first beam widths below $1\ \mu\text{m}$ for a large working distance helium microscope.

Chapter 5 presents a set of experiments that demonstrate quantitative agreement between the scattering distribution observed in SHeM with the Knudsen cosine model. Overall the conclusion is that the default scattering for unprepared/technological surfaces in helium microscopy is a *cosine like distribution*. It is shown in the second part of the chapter that roughness and a classical hard wall model for atom-surface scattering is insufficient to explain the observations.

Chapter 6 presents an in depth study of the novel contrast mechanism due to multiple scattering. As well as a discussion of the modest form of multiple scattering known as diffuse illumination, a study is performed on multiple scattering in deep features. It is shown that a quantitative understanding of multiple scattering is possible and that such an understanding is key to interpreting some SHeM micrographs.

Chapter 7 presents the first atom diffraction measurement taken from microscopic spot sizes. 2D atom diffraction maps are measured from a cleaved Lithium Fluoride crystal, and contrast from diffraction is discussed.

Chapter 8 builds upon the results from chapter 5 and uses the conclusion of cosine like scattering to develop a method for performing 3D reconstructions from a series of SHeM micrographs. The technique requires multiple detection direction, achievable with either multiple detectors or appropriate rotations of the sample, and produces a height map of the surface. The method is studied using simulated data and a proof of concept measurement from the A-SHeM is given.

Finally chapter 9 considers general conclusions from this thesis and the near-term outlook for the SHeM technique.

In this chapter a method and software framework for predicting the contrast in SHeM micrographs is presented. First the necessary parameters are considered, then an introduction of the method and implementation are provided. A series of example results of the simulation are then given to highlight the use cases and utility of the framework, with some qualitative comparisons to experimental data. Towards the end of the chapter, helium microscopes that operate with different imaging conditions to the Cambridge A-SHeM are explored with a case study of the Portland NAM (Neutral Atom Microscope).

A proof of principle simulation, specific to the A-SHeM, was initially developed for the authors Part III project (M.Sci), with the features of multiple scattering noted[46]. The framework presented here has undergone significant development, becoming a flexible method capable of incorporating different microscope geometries, different scattering distributions, and more complicated samples.

2.1 PRINCIPLES OF CONTRAST IN SHeM

The development of a tool capable of predicting contrast in the SHeM, and similar instruments, is vital to being able to interpret images and discover contrast mechanisms. While there are various approaches that could be employed, it is important to first identify the the key physical causes of contrast.

First the concept of ‘contrast’ needs to be given a meaningful definition. In this thesis a relatively general definition is used: contrast is changes in detected helium signal while varying the spatial position, or some other physical parameter, in a helium microscope. Thus a *contrast mechanism* is: some physical process that causes the detected helium signal to vary when a physical parameter is varied, primarily the spatial position of the sample. There are other specific quantitative definitions of contrast, such as the widely used Michaelson contrast, and where these are used it is stated explicitly. More on quantitative definitions of contrast can be found in §3.5.

Having defined contrast as changes in detected helium signal, the next step is to understand the factors that affect that signal. In general a helium microscope will have a detector that is connected to the scattering/sample chamber via an opening or tube. It is therefore reasonable to assume that – and simulations presented in §2.3.3 support the assumption – the detected

Work from this chapter has been published as ‘A ray tracing method for predicting contrast in neutral atom beam imaging’ by Lambrick et al. 2018[45].

signal is directly proportional to the flux of gas entering that opening, which is termed the *detector aperture*. To achieve spatial resolution in a scanning manner the helium must be incident on a small spot on the sample via a narrow beam. The beam parameters are not changed during the rastering motion, so a beam with identical properties is incident on each different part of the sample. Therefore contrast is controlled exclusively in the local sample environment, positioned between the incident helium microprobe and the detector aperture.

Within the local sample environment there are, for all microscopes produced or proposed for the near future, three lengthscales:

1. The *macroscopic*, ~ 1 mm, scale of the sample environment including the detector aperture and the distances between the sample, the detector and the beam focusing element.
2. The *micro*, $\sim 0.1 - 10$ μm , scale of the sample, principally the topography of the sample on the scale of the beam width.
3. The *nano*, ~ 1 nm, scale of the helium wavelength, λ_{He} , and atomic level surface.

The first two lengthscales can be considered purely geometrically as the lengthscale is $\gg \lambda_{\text{He}}$, while the third is on the lengthscale $\sim \lambda_{\text{He}}$, and therefore the wave nature of helium has to be considered. Each lengthscale will impact the helium flux into the detector in different ways:

1. The overall path of the helium atoms through the sample environment is affected by the positioning of the sample, the position and shape of the detector aperture, other physical parts of the microscope, and the pumping path away from the sample. In general contrast from different helium paths through the chamber having different probabilities is not desirable.
2. Sample topography will change the angle between the sample, the detector, and the incident beam, as well as potentially blocking the beam. Contrast from local sample topography is desirable and can be used to acquire information about the topography of the sample – this idea is explored in chapter 8.
3. The fundamental atom-surface interaction, which is affected by the nanoscale, will change the distribution of directions that the helium atoms follow when they leave the sample surface. Contrast from changes in the atom-surface interaction are desirable.

Complete modelling of the entire process in one go is, in practice, intractable, therefore it is chosen to separate the problem into an almost purely geometric one, and one of more fundamental surface science. A simplified, geometric description of the atom-surface interaction is needed to build a

geometric model as is proposed. For a particular surface and helium wavelength there will be a distribution function, termed the *scattering distribution*, which describes the relative probability of scattering in a particular direction from a particular incidence direction (for light the function is termed the bidirectional reflection distribution function[47]). As a geometric quantity, the scattering distribution can be combined straightforwardly with the macroscopic and microscopic geometries of the environment and sample.

Thus a geometric model of the contrast can be constructed with a scattering distribution(s) as one parameter, and the sample geometry and sample environment as other parameters. The basic concept of the model is shown in figure 2.1: a beam is defined, a sample topography is defined, a scattering distribution is provided, and then a detection geometry along with any other relevant sample environment geometry is specified.

The geometric problem presented in figure 2.1 can be approached in a number of different ways, the two considered in this thesis are: first a Monte-Carlo ray tracing approach that allows complex geometries and scattering distributions but is computationally expensive and acts like a ‘black box’; then in the next chapter an integral approach that is less flexible but is can be used on larger parameter spaces and more readily employed for optimisation.

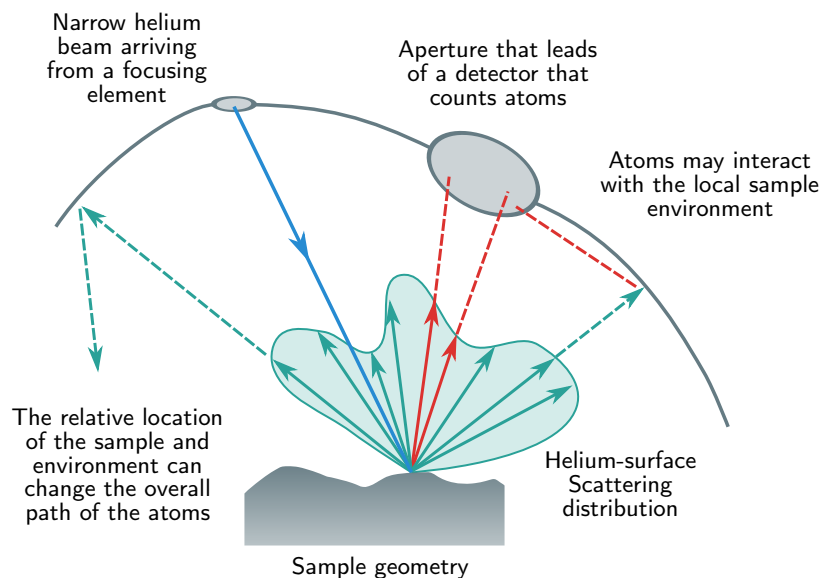


Figure 2.1: The basic concept of the geometric model of contrast in the scanning helium microscope, consisting of: a beam, a sample topography, scattering distributions, and detection geometry. The detected signal and hence the intensity of a pixel in an image is proportional to the number of atoms that fall into the detector aperture.

2.2 RAY TRACING

In light of the discussion above, a Monte-Carlo ray tracing framework, with the potential for adaptation and extension, was constructed[45, 46, 48]. The method creates simulated micrographs from a 3D model of the sample and sample environment. Ray tracing is used as the basis of the approach, treating helium atoms as classical ‘rays’ that travel in straight lines. In addition to being able to take into account the full sample environment and arbitrary scattering distributions, a key advantage of the method is its ability to model multiple scattering, an important feature of neutral beam microscopy. Ray tracing also allows the use of arbitrary sample geometries, allowing the modelling of complex samples that would be extremely difficult with more prescriptive analytic methods.

The simulation framework was developed from scratch, allowing maximal flexibility and control of the parameters, as well as allowing different modes of operation that enable different simplifications/assumptions to be implemented. In addition to the scattering distribution and sample environment geometries, the precise definition of the incoming helium beam can be specified.

2.2.1 Simulation method

Ray tracing is the implementation of ray optics which models the propagation of waves as lines, provided that changes in the medium that the waves travel through are on a much longer lengthscale than the wavelength of the waves. It has been used extensively in physics to model electromagnetic[49] and seismic wave [50], among others. As well as its use in science, ray tracing has been used extensively in the production of high quality photo-realistic computer graphics. Ray tracing calculations can, however, become complex in media where wave propagation is non-linear. As helium atoms in SHeM propagate through vacuum the paths are linear, so a large number of rays can be computed in relatively short amounts of time. As ray propagation is linear the rays can be described by a normalised direction, \mathbf{d} , and a position, \mathbf{e} , allowing the propagation of a ray to be parametrised with the equation

$$\mathbf{p}(t) = \mathbf{e} + t\mathbf{d} \quad (2.1)$$

which forms the basis of the numerical implementation.

The surfaces of solid objects can be represented for ray tracing using combinations of various analytic forms[51]. For the SHeM Ray Tracing Simulation it was chosen to model surfaces as triangulated meshes, which can represent arbitrary shapes. Such a mesh consists of a list of points in space and information on which points join together to form triangles. While triangulation can represent polyhedra of any complexity perfectly, one limitation is that it can only represent an approximation to curved surfaces. The inclusion

of a specific sample consisting of analytic spheres to avoid the problem of imperfect curvature demonstrates that alternatives can be included alongside the triangulated mesh.

An extension to the simple triangular mesh model is used where a material is associated with each triangle. The ‘material’ consists of information on which scattering model applies to that specific patch of surface and provides any parameters to that model which may vary between triangles with the same scattering model. Overall, therefore, the surface representation consists of

- V An $m \times 3$ matrix of vertex coordinates.
- F An $n \times 3$ matrix of specifying which vertices make up each triangle.
- N An $n \times 3$ matrix of normal vectors for each triangle.
- \vec{M} An n -vector of material compositions.
- P An $n \times q$ matrix of parameters for the scattering distributions.

The ray tracing method used generally follows that described in ‘The Fundamentals of Computer Graphics’ by Marschner [52]. In each ray propagation step the nearest intersection of the ray with a triangle is found. After the location of the intersection is found, the position of the ray is updated and its direction is replaced. As part of the procedure it is possible to store the number of times a particular ray has hit an object and the distance it has travelled.

Ultimately there are four possibilities for a traced ray, these are shown in figure 2.2. First, the ray may intersect another surface and the procedure is repeated, *i.e.* it may ‘continue’. Second, the ray may not hit any surface and pass beyond the simulation volume – it has ‘left’ the simulation and the ray is considered not to have been detected. Third, the ray may hit the detector surface, in which case its propagation is terminated and it is counted as ‘detected’. Finally, after a certain number of scattering events or a certain distance travelled, the ray may be artificially stopped which we describe as ‘discarded’. It is necessary to include the discarding of rays in the practical implementation to avoid the possibility of infinite loops. As such, the simulation acts to generate data on a single pixel at a time, and the number of detected, left, and discarded rays are collated.

Overall the simulation is performed for the rays with a fixed geometry. These individual fixed geometry simulations may be performed with changes to the geometry to model SHeM experiments. For example 2D images are constructed by rastering the sample, directly analogously to the operation of the experimental instrument, and using the number of detected rays for each position to form a simulated image. The framework, in principle, allows any combination of manipulations to be combined to constitute an overall simulation; practically implemented are 3D sample translations and sample rotations.

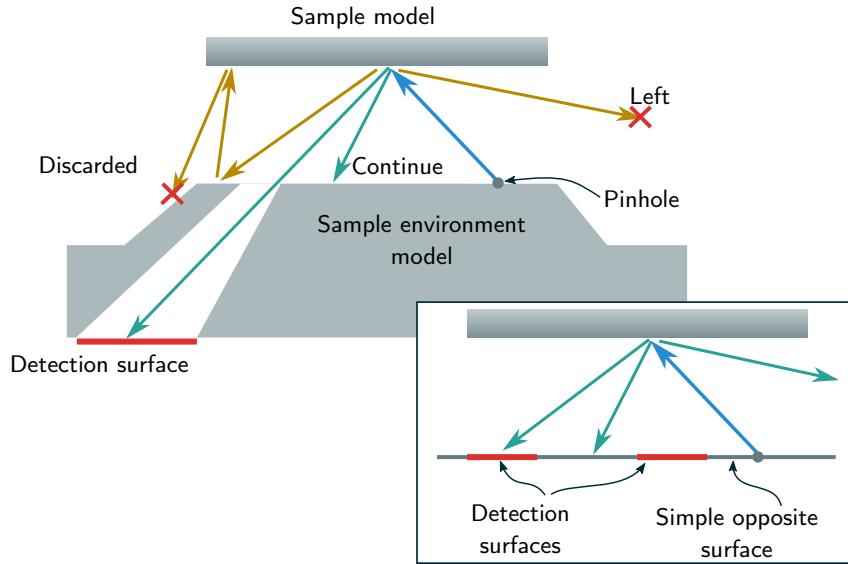


Figure 2.2: An outline of the components of the ray tracing simulation. A beam is generated at the pinhole and is incident on a 3D model of the sample, rays may then scatter around the simulation between the sample model and the sample environment – either a full 3D model as shown in the main figure or a simplified circular surface as shown in the inset – with three ultimate possibilities: the ray may leave the simulation volume, the ray may undergo more than the allowed number of scattering events and get discarded, or the ray may hit a detection surface. As shown in the inset there may be more than one detection surface.

The default scattering distribution chosen for the ray tracing simulation is the purely diffuse cosine scattering, known as Lambertian scattering[53] for light and Knudsen scattering[54] for atomic and molecular species. The model is chosen as it is simple and is representative of the disordered scattering from unprepared ‘rough’ surfaces that might be imaged in the SHeM. Chapter 5 quantitatively looks at the validity of the assumption of cosine scattering. Cosine scattering represents the case where the outgoing direction of a scattered species is independent of the incident direction: consider a infinitesimal surface element uniformly radiating, at a polar angle to the surface normal of θ . The solid angle subtended, from a point some distance away, by the surface element has been reduced to $\cos \theta$, thus the scattered flux for a uniformly scattering surface is also reduced by $\cos \theta$ —the geometry is displayed in two dimensions in figure 2.3. For modelling completely diffuse scattering in three dimensions, it is necessary to consider the solid angle of the element, $d\theta d\varphi$, of hemisphere being scattered into[55]. The intensity scattered into an infinitesimal solid angle, $d\Omega$, in a particular direction defined by the polar angle to the surface normal, θ , and the azimuthal angle, φ , is given by

$$I(\theta, \varphi) d\theta d\varphi = \frac{\cos \theta d\Omega}{\int_{2\pi} \cos \theta d\Omega'} \quad (2.2)$$

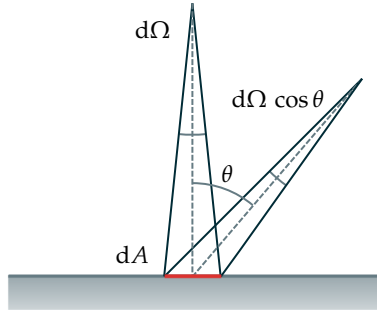


Figure 2.3: The cosine term in diffuse scattering arises from the reduced solid angle subtended by a surface element as the angle from the normal increases.

where the integral normalises the distribution over the outgoing half-space. Given that $d\Omega = \sin\theta d\theta d\varphi$, we can substitute and integrate to obtain the azimuthally integrated result,

$$I(\theta) = \frac{1}{\pi} \sin\theta \cos\theta. \quad (2.3)$$

The probability for the azimuthal angle follows the uniform distribution $P(\varphi) = \frac{1}{2\pi}$. Note that the result is a probability of directions with the polar angle θ across all azimuthal angles, φ . In a measurement along a single azimuth with a fixed solid angle detector the observed scattering intensity will follow only the cosine of the polar angle.

It is informative, at this point, to compare the cosine law for helium to the cosine law for light in light of the different approaches to image formation, both of which represent completely random scattering. SHeM, and similar scanning forms of imagining including SEM and dual photography[32], operate on the principle of Helmholtz reciprocity. Helmholtz reciprocity states that a light ray path (or equivalently the path of a helium atom) can have its direction reversed without any change to the physics, provided it does not pass through any non-linear media and that nothing else moves during the transit of the ray. Scanning microscopy uses the reversal of the light path, combined with a very specific incident direction (as opposed to a very specific detection direction in photography) to produce images that appear to be ‘viewed’ from the incidence direction. Similarly the detector in scanning microscopy appears as the source of illumination in images. Overall therefore there is a reversal of the ‘roles’ of the source and detector when moving from photograph/traditional optical microscopy and SHeM, as is illustrated in figure 2.4. The cosine law as derived from figure 2.3 applies equally to any randomly scattering species: $I d\Omega \propto \cos\theta d\Omega$. For SHeM there is nothing else to consider because each pixel has exactly equal illumination intensity, all pixels are formed from the same incidence beam, just with the beam incident on different parts of the sample. For photography, where the image is taken in one go, there is also the angle between the light source and the surface to consider. A particular surface element that will become one pixel in the final image will receive an intensity of illumination that is

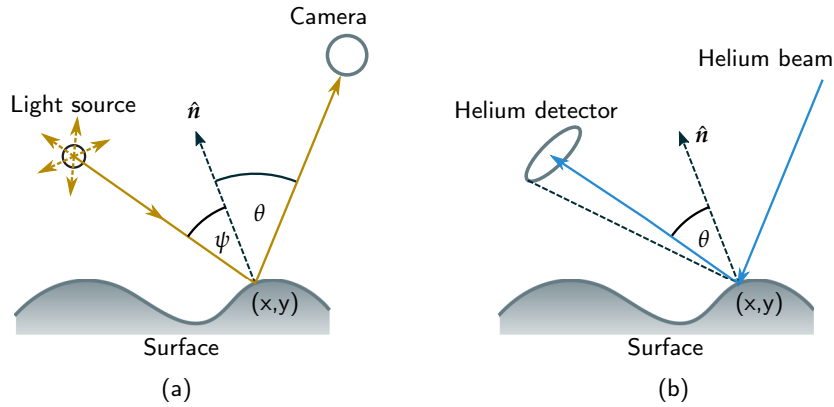


Figure 2.4: The equivalence between optical imaging, performed with a 2D detector/camera, and SHeM, imaging performed point by point by scanning, \hat{n} is the surface normal. (a) imaging with a ‘standard’ optical set-up. (b) imaging with a *scanning* helium microscope, due to the scanning method of imaging the effective ‘roles’ of the source and detector are reversed: thus SHeM micrographs appear to be viewed from the direction of the beam and appear to be illuminated by the detector.

proportional to the cosine of the angle between the illumination and the surface normal, $\propto \cos \psi$, using the definitions in figure 2.4, which can then be combined with the cosine factor derived from figure 2.3: $\propto \cos \psi \cos \theta$. Next the projection of the surface element into the camera needs to be considered, the actual size of a surface element for one pixel in the camera will depend on the angle between that element and the direction of the camera – for a surface that is at a larger angle to the camera a greater area of the surface covers the same area of the image. A larger area of surface implies a greater scattering area, meaning there is a greater intensity of light incident on the camera, hence there is a $1 / \cos \theta$ factor on the intensity. Therefore the overall intensity for light is $\cos \psi \cos \theta / \cos \theta = \cos \psi$, where the angle to the light source, ψ (figure 2.4 defines the angles), remains in the equation while the angle to the detector, θ , cancels. Hence the distinction between the Knudsen cosine law for helium which depends on the angle *to the detector* and the Lambertian cosine law for light which depends on the angle *to the light source*.

2.2.2 Implementation

The core ray tracing is performed using a C atom ray tracing library that has been built in order to optimise performance¹. As shown in figure 2.5 a MATLAB wrapper is used that prepares all the parameters and analyses data, MEX is used to call the core computation directly from within MATLAB. Sample and pinhole-plate geometries are imported into MATLAB as binary sterolithography files (.stl) or as text object files (.obj), which can be created by CAD software. AutoDesk Inventor and FreeCAD were used for

¹A persistent link to the up-to-date version of the code with a DOI can be found on Zenodo: doi.org/10.5281/zenodo.1228078.

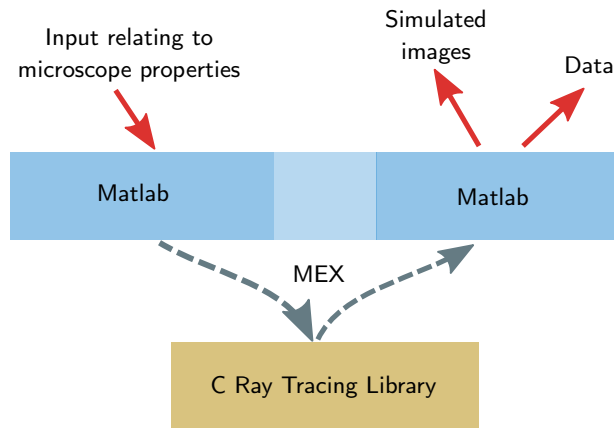


Figure 2.5: Schematic of the operation of the ray tracing code. A relatively general atom ray tracing library is written in C which is then called, using MEX, from MATLAB functions that set-up appropriate models. Finally the output of the ray tracing library is analysed and visualised using MATLAB.

all simulations presented in this thesis. The triangulation of surfaces is performed by the CAD package during the export to .stl/.obj files.

Rays can be generated either in C to optimise RAM performance or in MATLAB for greater flexibility. All geometry manipulation is performed in MATLAB making the compiled C code simpler. In effect each segment of the overall simulation with a fixed geometry (equivalent to a pixel in a SHeM image) forms an independent simulation performed in C. As each C simulation segment is independent, parallelization can be implemented trivially, considerably speeding up the computation and making the use of high performance computing practical.

2.3 RESULTS OF THE SIMULATION

2.3.1 Topographic test

Figure 2.6 shows a simulated and experimental micrograph of a TEM grid. It is clear that there is good qualitative agreement between the simulation and experiment; dark and light regions are reproduced in the same manner in the simulated image as in the experimental image. A triangulated mesh built to represent the sample is shown in figure 2.7, the surface is represented by a series of triangles that form a closed object.

One key topographic feature present in figure 2.6 and reproduced well by the simulation is masking. Masking is an established contrast feature in SHeM images[16, 35] that arises as a result of the line of sight between the sample and the detector being blocked by the sample itself, causing the detected signal to be small. Figure 2.8 illustrates the concept for a simple step. Note that masking is formed as a result of the scattered helium from a point on the sample being *blocked from entering the detector*, not as a result

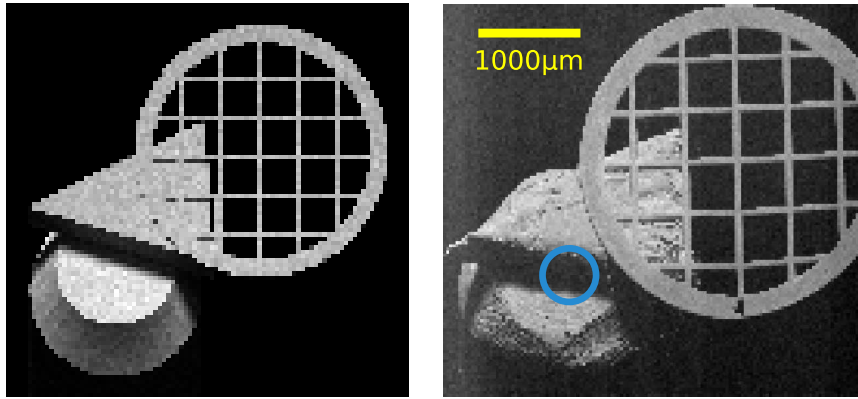


Figure 2.6: A simulated (left) and experimental (right) micrograph of a TEM grid attached to a sample stub with a triangular piece of carbon tape showing good qualitative agreement. An example of a mask is highlighted in the experimental image with the blue circle. In an optical image the highlighted feature would be interpreted as a shadow, but due to the 'reversal' of the roles of the detector and source in a scanning microscope it is properly interpreted as a mask in SHeM. Experimental data collected by M. Bergin.

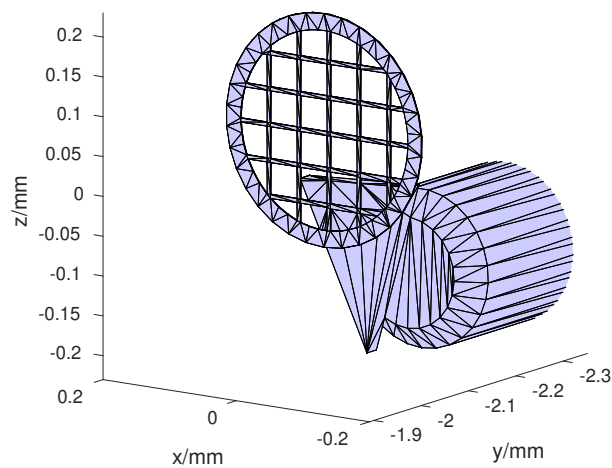


Figure 2.7: The triangulated mesh used to generate the simulated micrograph in figure 2.6. The model consists of a TEM grid mounted on a triangular piece of carbon tape on a sample mounting stub. The 3D model has not been extensively optimised to match the real sample exactly, but aims only to capture the major image features.

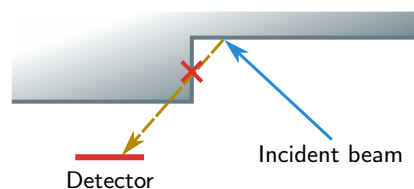


Figure 2.8: The contrast processes of masking, where the path from the sample to the detector is blocked.

of *lack of illumination* of the sample. Lack of illumination causes *shadowing*, a mechanism familiar from everyday life which manifests in optical images in the same way masking manifests in helium images. The reversal of the mechanism between standard optical images and helium images is a result of the scanning approach to imaging used with helium images produced by scanning *appear* to be illuminated from the detector and observed from the source. This ‘reversal’ of the roles of detector and source means that from a heuristic point of view masking may be considered similar to shadowing in everyday life, allowing an intuitive interpretation of SHeM images. It is, however, important to remember that the mechanism of shadowing does occur separately in the SHeM with different implications for images: regions of the sample that are not illuminated do not appear in the final images. The ‘reversal’ analogy with standard optical images can be used here too: shadowing in SHeM is equivalent to masking in photography, where path from the object to the camera is blocked by another object, and therefore the first object does not appear in the final image.

While masking does result in parts of the sample not being visible in the final image due them being rendered black, it can provide quantitative information on the topography, an idea explored in §6.3, and allows us to heuristically interpret images based on our experience with optical shadows. Therefore for topographic imaging some intermediate level of masking may be desirable, while too much would result in the loss of unacceptable levels information.

2.3.2 *Multiple scattering*

One of the key features of using ray tracing over alternative methods is the full inclusion of multiple scattering. As shown in figure 2.2 individual rays may scatter multiple times during the simulation, just as helium atoms may scatter an arbitrary number of times in the SHeM. Due to the negligible probability of absorption of He upon a scattering event, the proper modelling of multiple scattering is of significant importance in helium microscopy, unlike in SEM where it is less significant. Chapter 6 considers contrast due to multiple scattering and makes extensive use of the ray tracing framework.

2.3.3 *Working distance contrast*

The ray tracing simulation can be used to investigate particular contrast processes and exploit the mechanisms behind them. One example is a feature that has been termed ‘height contrast’[35] but might more properly be termed *working distance contrast* – the working distance is the distance from the pinhole focusing element to the plane of the sample. Samples that possess significant (at least ~ 0.5 mm for the standard configuration) 3D topography

may exhibit contrast that is a result of different distance between different parts of the sample and the detector aperture.

Working distance contrast arises from two primary causes: the solid angle subtended by the detector aperture, and the transmission probability of the ‘detector cone’ which connects the initial detector aperture entrance to a stagnation chamber in the SHeM. The detector cone can be seen in the main schematic in figure 2.2 where the detection surface is placed at the end of a conical tube.

The detected signal is dependent on the solid angle of the detector aperture: the larger the aperture appears, the greater the signal. Atoms scattered by the sample must pass through the cone to reach the helium detector. The response of the instrument is therefore dependent on the transmission of atoms through the cone, termed the *transmission probability*, which in the present context is a function of the working distance. Figure 2.9 demonstrates how these two factors vary with different working distances.

To investigate these effects the ray tracing simulation was used to perform what is termed a *z-scan*, the concept of which is depicted in figure 2.9: the sample is moved diagonally so that the beam is incident on the same spot on the sample but the overall beamline distance is increased and decreased. A flat sample was simulated moving backwards diagonally, as shown in figure

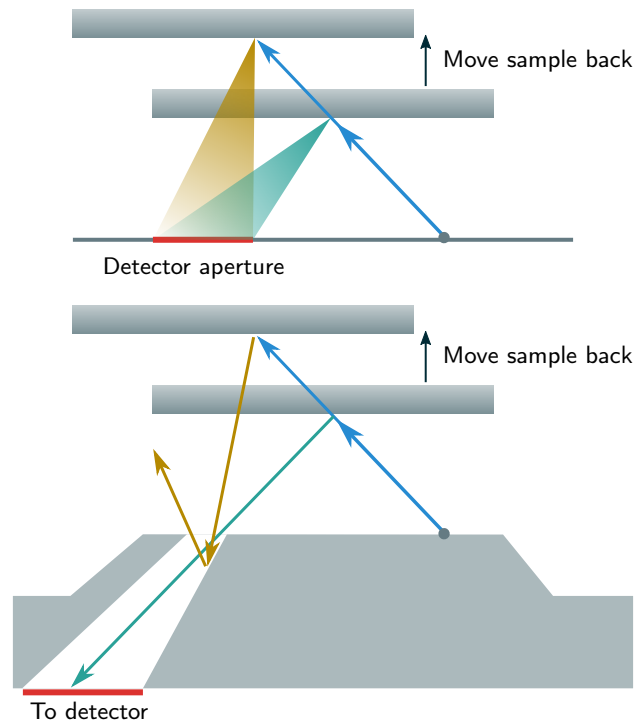


Figure 2.9: Diagrams demonstrating how the solid angle of the detector aperture (top) varies with the working distance used and how the transmission probability (bottom) may vary with the working distance. While here the effects are modelled by considering the sample being moved away from the pinhole, in practice the contrast can be observed in the topography of the sample.

2.9. To examine the effects of the cone transmission probability separately from the sample scattering distribution, a uniform scattering distribution was used—such a distribution dispenses with the cosine term included in a physical uniformly radiating surface. To sample a distribution where there is equal probability of scattering into any point on the hemisphere the intensity at a point $d\theta d\phi$ on the hemisphere is

$$I(\theta, \varphi) d\theta d\phi = \frac{d\Omega}{\int_{2\pi} d\Omega} \quad (2.4)$$

$$= \frac{1}{2\pi} \sin \theta d\theta d\phi \quad (2.5)$$

$$\implies I(\theta) = \frac{1}{2\pi} \sin \theta \quad (2.6)$$

where the integral normalises the distribution over the outgoing half-space. Sampling the scattered polar angle from equation 2.6 and the azimuthal angle from a uniform distribution will give the desired uniform scattering. As the solid angle of the detector entrance aperture changes with working distance, the simulation results were normalised by the solid angle to give a measure of the transmission probability separately.

Figure 2.10 plots the relative transmission probability and the relative solid angle as a function of the perpendicular distance between the sample and the pinhole/detector aperture plane, termed the ‘z’ distance. It is found that the transmission probability function is strongly peaked, indicating that there is a strong change in signal as the sample position is varied, which is not a result of the solid angle of the detector aperture changing. The solid angle of the detector aperture is also found to be peaked, but more

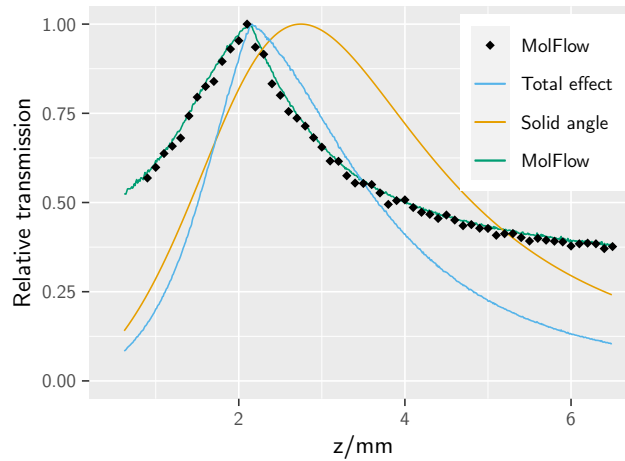


Figure 2.10: How the transmission probability of the detector cone varies with the distance from the pinhole (z). The transmission probability was calculated using the ray tracing simulation as well as using MolFlow[56, 57], the two can be seen to be in good agreement, in addition the solid angle of the detector aperture is shown. The total characteristic curve of the helium microscope set-up is the product of the solid angle and the transmission probability. MolFlow simulation performed by M. Bergin[14].

broadly and slightly displaced from the peak of the transmission probability. The results have several consequences. Firstly, it means the SHeM has an effective depth of field – of ≈ 2 mm related to the signal transmitted and the solid angle. Images can still be successfully taken outside of the range, but there is a substantial drop in signal that renders such images noisy. Secondly, the peaked shape of the response will result in contrast resulting from large scale sample height differences, which will be inverted depending on whether imaging is performed with the sample closer or further than the standard working position. If one were interested primarily in working distance contrast, arising from the effects of transmission probability and solid angle variations, it would be prudent to image on the steep slope just off the peak of the curve in figure 2.10. It should, however, be noted that other contrast mechanisms, such as those relating to the scattering distribution, as well as masking and multiple scattering effects, are manifest at all working distances. For microscopic samples, working distance contrast acts over distances larger than the usual sample heights, which tend to be over $10\mu\text{m}$. With signal to noise levels of ~ 30 , as are representative in high quality SHeM images, working distance contrast applies over distance of $\sim 50\mu\text{m}$ or larger which matches findings from Fahy et al.[35]. For those samples where working distance contrast is not expected to play a role, or where investigations are not interested in the transmission probability a simpler model of the geometry of the sample environment may be used. In the simpler model the pinhole-plate is modelled as a flat circle with the detection location at the aperture rather than at the end of the detection cone – the inset in figure 2.2 shows the simulation set-up for a simpler model.

After the detector cone there are further components through which atoms must pass before reaching the detector ionisation region itself. To examine whether the transmission through these additional components is affected by the direction or position of atoms entering the detector cone, a MolFlow+ [56, 57] simulation² was used to calculate the transmission probability of all components from the sample to the detector, also as a function of sample position. A uniform source of gas was used in the MolFlow simulation, moved backwards in the same manner as the sample in the SHeM simulation. The results, normalised by the solid angle of the entrance aperture, are shown as points in Fig. 2.10 and demonstrate a very high level of agreement with the ray-tracing framework. The agreement demonstrates that the relative transmission through the components beyond the detector cone are not affected by the distribution of atoms entering the cone—the additional components do give a reduced transmission independent of working distance that is found to be $\sim 45\%$. Overall, these results demonstrate that the geometry of detector apertures and detector cones can play a significant role in contrast in SHeM images, and that in the current setup of the Cambridge SHeM no further components need to be considered in simulations of contrast.

²MolFlow simulation performed by M. Bergin.

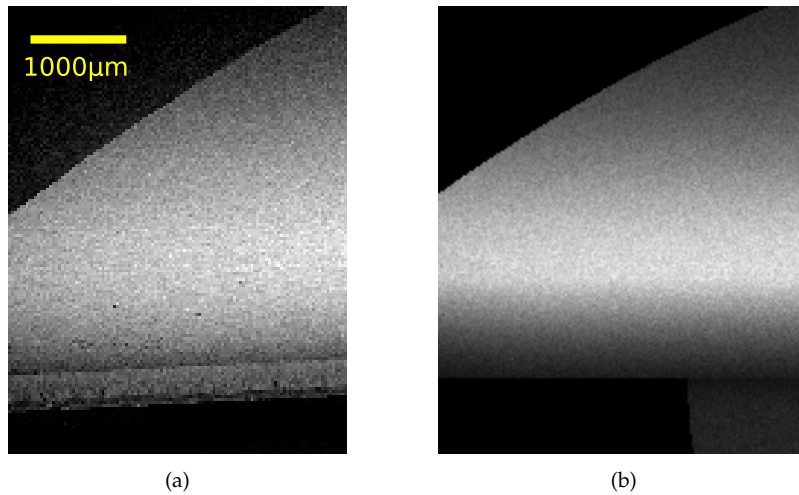


Figure 2.11: A helium micrograph (a) and simulated micrograph (b) of a sloped surface showing the working distance contrast that is a result of the solid angle of the detector aperture and the transmission probability of the detector cone varying with the distance of the sample-beam intersection from the pinhole. The sloped surface is at a continuous angle of 54° to the imaging plane. The inversion of the contrast is also seen, with a peak in signal about 40% of the way up the image. It should be noted that the experimental image has a lip at the top of the sloped region while the simulated image does not.

2.3.3.1 Images with working distance contrast

The previous section dealt with working distance contrast in an abstract way by considering a sample moving diagonally backwards away from the pinhole-plate. However working distance contrast can manifest itself in images where the topography is large enough. That contrast is not as it is shown in figure 2.10. The scattering distribution of the helium atoms from the sample surface will also play a role. The resultant contrast in a real helium image will be a combination of the transmission probability, solid angle, and the distribution.

Figure 2.11a shows helium micrographs of a SEM sample stub with a sloped surface – the angle of tilt of the sloped part of the stub³ is 90° . The micrograph clearly showing an increase and decrease in the detected signal as the sample surface moves from being close to the pinhole-plate to being far away. Figure 2.11b shows a simulated micrograph of similar sample with a sloped region.

2.3.4 Varying helium background signals

In SHeM there are slowly varying, with position in an image, background signals due to helium gas that reaches the detector from the sample chamber. These contributions are separate from the atoms that are scattered directly

³Part number AGG3162 “SEM Specimen Stubs, 12.7mm dia, 45/90° chamfer, 9.5mm pin” <https://www.agarscientific.com/sem/specimen-stubs-mounts/sem-specimen-stubs-g3162>.

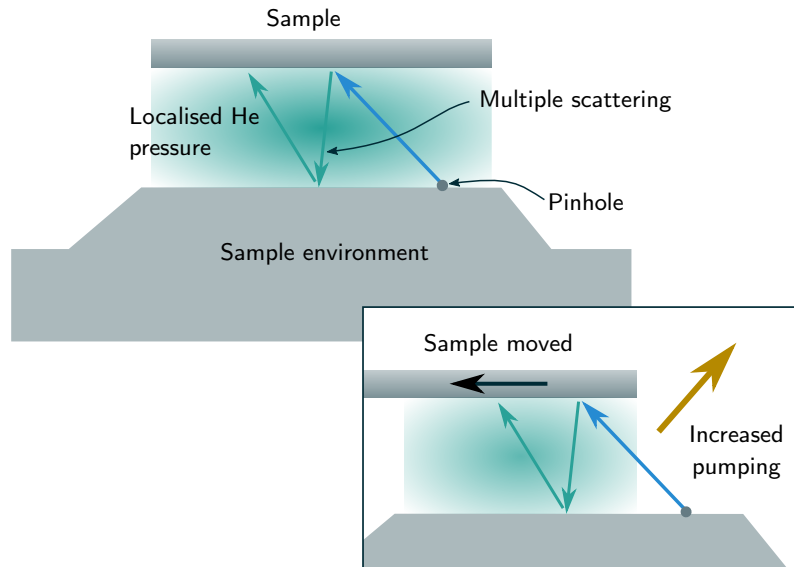


Figure 2.12: How multiple scattering between the sample and the sample environment causes a local pressure of helium in the sample vicinity leading to a background signal in the SHeM. The inset shows how when the sample is moved the pumping around the sample changes and thus how the background signal can vary across an image.

into the detector aperture from the collimated beam and degrade image quality.

2.3.4.1 Multiple scattering background

The proximity of the sample to the pinhole and detector mounting means that atoms that scatter off the sample but do not pass into the detector aperture can contribute to a local partial pressure of helium in the sample region. The production of the *multiple scattering background* is demonstrated in figure 2.12. Atoms from the local pressure⁴ can pass into the detector aperture and thus contribute to a background in images.

As the sample is rastered (over distances ~ 1 mm) under the beam the surface that faces the pinhole-plate changes, thus the local pressure can change in size, meaning that the multiple scattering background is slowly varying. Figure 2.12 demonstrates how when the edge of a sample is imaged the multiple scattering background is reduced, thus, in an image, the background will peak in the centre of a sample. A simulation showing the effect of multiple scattering across a large sample is shown in figure 2.13 (a). It should be noted that the lengthscale of variation is of the size of the sample region, ~ 1 mm. In experimental images the multiple scattering background is hard to distinguish due to the presence of the effusive beam background which is also slowly varying – the effuse background is the result of helium diffusing through the pinhole and is discussed in the next section.

⁴It should be noted that the magnitude of the partial pressure of He is significantly lower than the ambient pressure ($\sim 10^{-8}$ mbar), in the sample chamber, so the helium partial pressure has a negligible impact on the total pressure.

As the magnitude of the multiple scattering background is intrinsically linked to the magnitude of the direct beam signal – i.e. the desired signal – the methods for mitigating against it are limited. Only geometric changes that limit the accumulation of a local partial pressure near the sample by improving pumping can reduce the multiple scattering background signal relative to the direct beam signal; other changes such as changing source parameters or changing the size of the detection aperture will impact the direct beam intensity in similar proportions to the background signal.

2.3.4.2 Effuse background

As the beam created by the skimmer is significantly larger than the pinhole a flux of helium is constantly incident on the rear of the pinhole membrane, as demonstrated in figure 2.14. Immediately before the pinhole is a relatively narrow cone (the *source cone*) that inevitably constrains pumping which results in a local pressure behind the pinhole. Prior to the introduction of a new sample chamber the pumping in the differential chamber was also highly constrained, however, the new sample chamber has high pumping performance in the differential chamber meaning that the pumping from

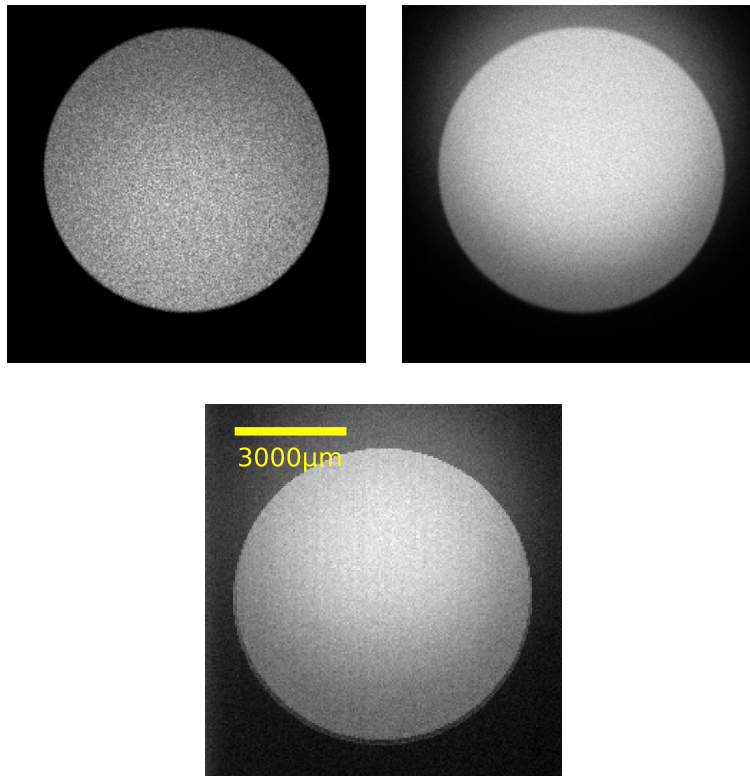


Figure 2.13: A SHeM micrograph (bottom) and a simulated SHeM micrographs (top) showing the multiple scattering and effuse backgrounds. On the top left is a simulation showing only the multiple scattering signal, while the top right includes an effusive beam that is comparable in magnitude to that seen in experimental data.. The slowly varying nature of these signals makes it important to reduce them as the varying effect can make quantitative inferences from images difficult.

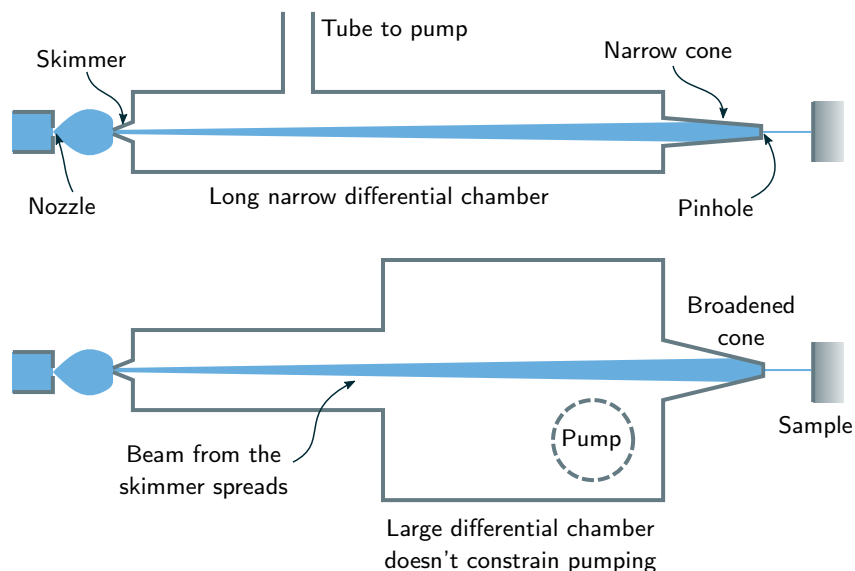


Figure 2.14: How gas from the skimmer accumulates behind the pinhole. The accumulated gas then effuses through the pinhole forming a secondary effuse beam that causes a helium background signal.

behind the pinhole membrane is constrained entirely by the cone. The second panel of figure 2.14 schematically demonstrates the difference between the old and new differential pumping stage.

As the mean free path of the helium atoms is significantly larger than the size of the pinhole and given that the pinhole membrane is significantly thinner (100 nm or 200 nm) than the pinhole diameter, then an effuse beam will be formed, which will follow the distribution of directions of the incident helium on the rear of the pinhole. Assuming that there is a constant pressure behind the pinhole then there is an equal chance of atoms incident on the pinhole from any direction, so the intensity will depend only on the projected area viewed from the incident atoms. Therefore the effuse distribution will follow a cosine distribution, centred on the perpendicular to the plane of the pinhole.

The effuse beam will act a broad source of illumination that is weakly peaked, therefore the detected signal from the effuse beam will be weakly dependent on the position of the sample and will manifest as a slowly varying background, similar to the multiple scattering background. One significant difference, however, is that the effuse background is present both when the direct beam is incident on the sample and when the beam misses the sample.

By implementing an alternative source distribution, ray tracing simulations were performed with an effusive beam. The simulation results are presented in figure 2.13 along with results for the multiple scattering background. The effuse beam background can be seen to continue beyond the edge of the sample stub causing significant brightening of the empty space around the circular sample. The effect seen in figure 2.13 occurs asymmetrically

due to a combination of the working distance used and the fact that the effuse beam is centred below the pinhole: when the sample is below the pinhole (corresponding to the top of the image) a greater flux of effuse gas is incident on the sample. Comparisons between ray tracing simulations and experiments suggest an effuse beam with an incident magnitude $\sim 3\times$ the incident magnitude of the direct beam.

2.4 APPLICATION TO DESIGNS

2.4.1 *Alternative sample stub design*

As has been discussed both the effusive beam §2.3.4.2 and localisation of gas between the sample and the pinhole-plate from multiple scattering §2.3.4.1 (from both the direct and effusive beam) lead to slowly varying backgrounds in images. To a first approximation both of these effects are linear with the area of the sample that faces the pinhole-plate. Thus a reduction in the macroscopic size of the sample would give a reduction in these backgrounds. The sample is mounted on a standard SEM stub, and as scan areas are, with rare exception, much smaller than the size of standard SEM stubs a reduction in the frontal facing area of these stubs would provide the desired reduction in macroscopic sample size.

To ensure that the frontal face of the stub is the only part of the sample that affects the detected signal it needs to be positioned a distance from the base of the stub, while maintaining compatibility with the SEM mounting system. As the range of motion of the nanopositioners is limited a stub of extended overall length puts limits on the lengths that are practical. A length of 10 mm was chosen as a practical compromise. Given that length it was found the smallest diameter practically usable and readily manufacturable was 2 mm. Figure 2.15 shows a photo of the stub design alongside a photo of type of standard SEM stub previously used.

Figure 2.16 compares z scans for a 2 mm stub and a 12 mm stub as used previously. It is clear that a considerable reduction in the effusive and multiple scattering backgrounds is predicted. The reduction predicted is a function of the z position of the sample but is roughly a factor of 15. Figure 2.17 shows SHeM images taken with the new sample stub and compares them to images taken with the old sample stub. The images demonstrate a significant improvement in the level of background signal.

2.4.2 *Considering alternative imaging conditions*

The ability to choose the parameters of the sample surrounding in the ray tracing simulation allows investigations of imaging conditions quite different to those employed in the SHeM. An investigation into potential imaging conditions may be helpful for informing discussion on the choice of



Figure 2.15: A photo of a standard SEM stub, (a), and a photo of the new SHeM stub, (b). The mounting pins on the back are the same size for both and thus either is compatible both with the SHeM or an SEM.

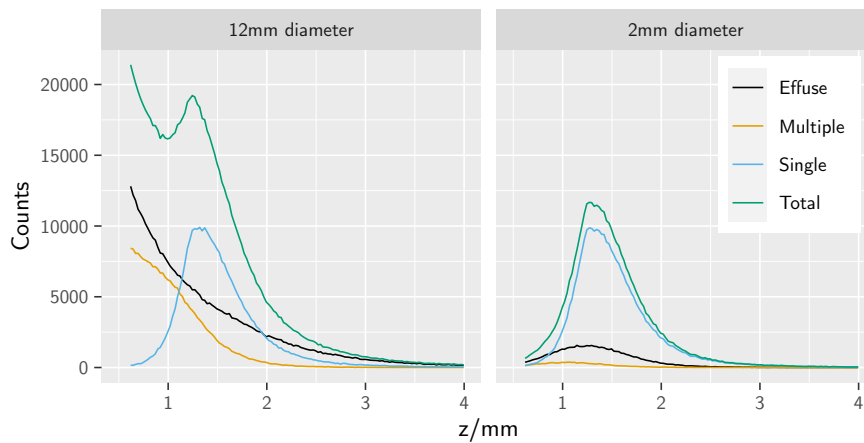


Figure 2.16: Simulated z scans with cosine scattering for the new SHeM sample stub (right) and a standard SEM stub (left). The single scattering curves are the same, within noise, in both graphs. For the case of the tradition SEM stub, 12 mm diameter, it can be seen that there are significantly greater effusive and multiple scattering contributions (black and yellow) than for the new SHeM stub. The simulations were performed with an effuse beam twice the magnitude of the direct beam.

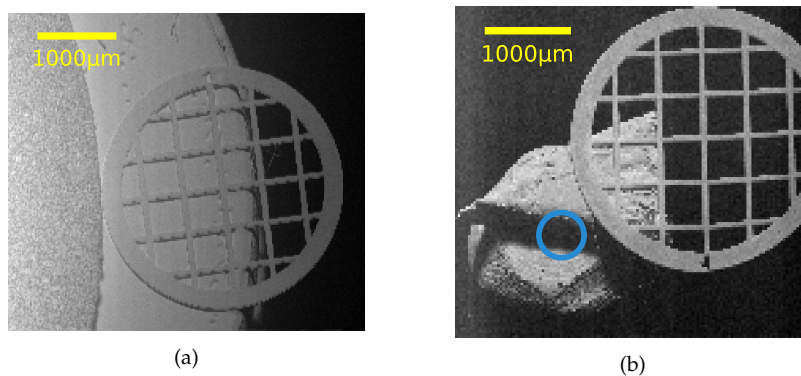


Figure 2.17: Two sets of SHeM images. (a) Image taken with sample mounted on the original, large sample stub. (b) Image of the sample mounted on a new small, sample stub (the stub end is smaller than the sample). The slowly varying background signals are clear in the images where there is a large overall sample/sample stub area whereas the varying nature of the background is not a significant feature of the images with a small sample/sample stub area. Data in subplot (b) was collected by M. Bergin.

future microscope designs. The investigation here is limited to a qualitative discussion of diffuse topographic contrast – all the simulations assume a cosine model of surface scattering.

Two significant parameters are the incidence angle and the detection direction(s). To assess the qualitative effects of the incidence angle and detection direction on contrast a test sample was constructed and simulated with a variety of incidence angles and detector directions with a few simple geometric shapes: an indented polygon, a pyramid and two spheres.

To examine the effect of the incidence angle two sets of four simulations were performed with increasing angles of incidence. The first set of simulations kept the detection direction fixed while the second kept the total scattering angle between the incidence beam and the detection direction fixed, all simulations use a detector aperture of the same angular size. The choice of the detection direction in the first set of simulations and the total scattering angle in the second were chosen to match the standard operating configuration of the Cambridge A-SHeM. The resulting images can be seen in figure 2.18 and 2.19. The incidence angles used were 0° , 20° , 45° , and 60° . The primary effect, seen in both sets of images, of the incidence angle is to change the perspective from which the sample is ‘viewed’. While normal incidence (0°) makes the sample appear as if it were viewed from directly above, progressively increasing the incidence angle has the effect of panning down to look at the sample from the side. As seen in figure 2.18 increasing the incidence angle has the benefit of making the topography of the sample more evident and lends a greater ‘3D’ feel to the images as a result of the vertical topography of the sample being more visible. Conversely the increasing incidence angle increases the length of the beam path from the pinhole to the sample causing greater beam spread and hence poorer resolution. Additionally increasing the incidence angle causes an increase in the amount of shadowing. Shadowing occurs where the beam does not reach a patch of the sample because there is an object in the way. As the beam does not reach certain regions of the sample, those regions do not appear in the images[35]. The shadowing effect will result in a poorer ‘view’ of horizontal topography in the plane of the sample; in the test sample, for 60° incidence flat regions of the sample are ‘hidden’ behind the pyramid and the sphere while very little of the base of the indented shape can be seen. By design no important information in the test sample is shadowed, but that would be unlikely to be the case with a real sample with significant topography. Overall a compromise between the extremes is likely to be preferable for general topographic imaging (if one is optimising for resolution the normal incidence choice should be made, as noted by both Bergin[27] and Salvador-Palau[58]). The final choice is subjective and will be affected by the practical construction of the instrument, however a suggestion is made that the range between 20° and 45° is a reasonable compromise. The Cambridge B-SHeM has been built with a default incidence angle of 30° .

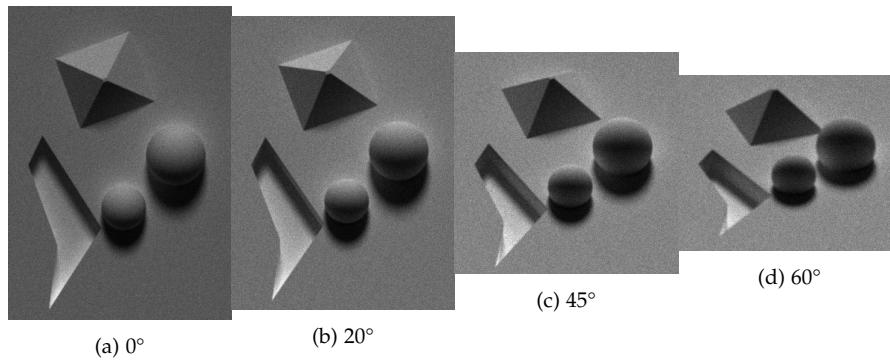


Figure 2.18: Simulated micrographs of a test sample with increasing angles of incidence (keeping the same detection condition). The 45° case is equivalent to the standard operation conditions of the Cambridge SHem.

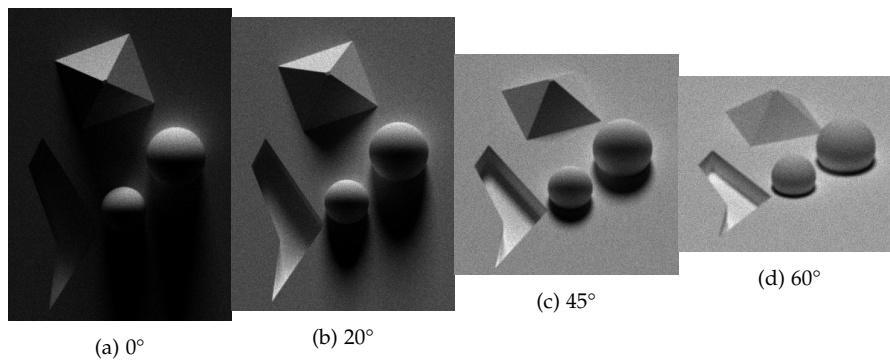


Figure 2.19: Simulated micrographs of a test sample with increasing angles of incidence with detection directions chosen to maintain a constant total scattering angle of 90°.

A further effect is seen with the increasing incidence angle: that the relative fraction of the image under mask increases – for example for 0° the spheres are largely light, whereas for 60° almost the entire spheres are dark. Where the beam is incident at a shallow angle and the detection is placed on the opposite side of the sample, there is a greater chance that the beam will be incident on a surface facing away from the detector and therefore that part of the sample will be masked. However, the effect is also dependent on the relative direction of the detector to the incidence direction. In figure 2.19 the total scattering angle is kept the same, here the low proportion of masking in the 20° case is increased while the high level of masking in the 60° case is decreased. The extreme detection angle in the 0° case results in large quantities of the image becoming masked and overall a high level of contrast. These imaging conditions are unlikely to be beneficial for many samples, although the high contrast may favour samples with very subtle topography. The results of both sets of simulations highlight that the positioning of the detector can be used in conjunction with the incidence angle to control the amount of masking that is apparent in images, however they also demonstrate that the level of masking does not have a simple relationship with either the incidence angle or the total scattering angle. The

greater difference in appearance of the images in figure 2.19 compared to the images in figure 2.18 suggests that while the incidence angle is significant for the image projection that is formed, the placement of the detector is more important for the overall contrast observed in an image, an observation that is consistent with the diffuse cosine model of scattering used in the simulations.

Figure 2.20 shows a simulation with five different detection directions for the same sample with 45° incidence. Four detectors are placed equidistant about the sample in four quadrants and a fifth is placed directly above the sample. A similar simulation is presented in figure 2.21 but with a normal incidence beam. The most apparent result is that the positioning of the detector changes the position that the masks appear in the images: the masks are produced opposite to the detector. For the 45° incidence case (figure 2.20) there is also a reduction in the overall masking when the detectors are moved to the side of the sample from being behind. Image 4 from figure 2.20 and image 3 from figure 2.21 demonstrate the interesting case of *backscattering detection* where the detection direction is approximately the same as the incidence direction. Here masking is virtually absent and the dominant contrast features are dark regions of the surface that are at right angles to the beam, and bright regions of multiple scattering. Implementing a backscattering detector will prove a technical challenge – an annulus around the pinhole may work – but it does have the potential for an alternative

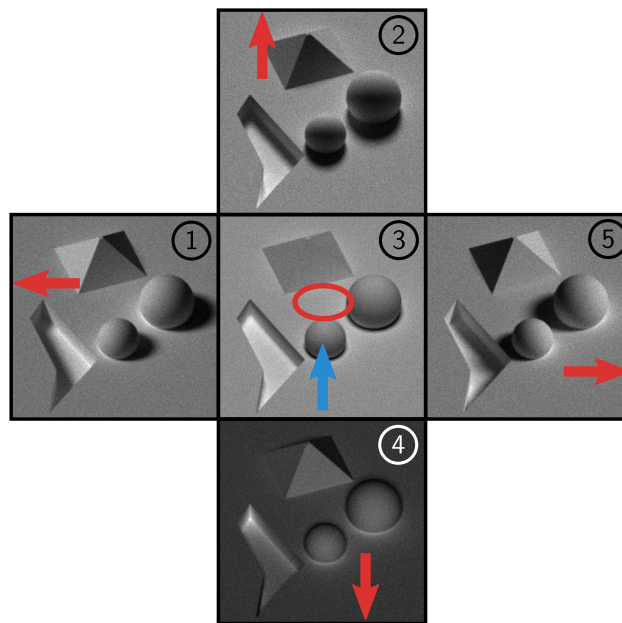


Figure 2.20: Images of the test sample taken with five different detection positions for both 45° incidence. Changing the position of the detector changes the location of the masks: the masks appear opposite to the placement of the detector. The red arrows show the direction of the detector, the ellipse represents directly above the sample, the blue arrow shows the incidence beam direction (the same for all images).

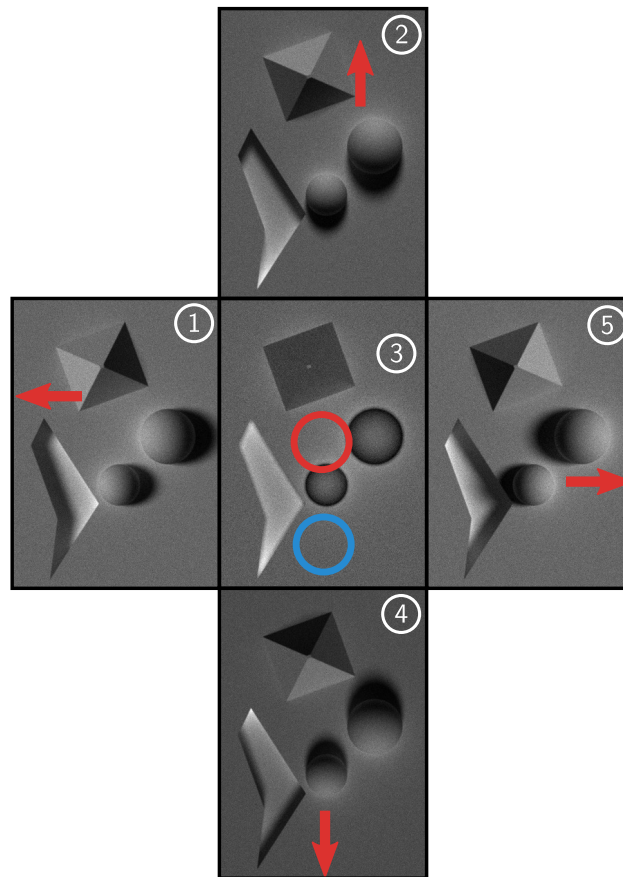


Figure 2.21: Images of the test sample taken with the same five different detection positions used in figure 2.20. The red arrows show the direction of the detector, the circle represents the beam incident from directly above (the same for all images).

imaging mode for a helium microscope that may be desirable for certain samples.

The Cambridge B-SHeM is being constructed with four detectors allowing multiple detection angles to be used at the same time, meaning that a choice of a single detection angle is not necessary. In addition both the A-SHeM and B-SHeM allow changing the pinhole-plate, which can change the detection angle, with the B-SHeM being particularly suited to this due to the multiple detector ports.

2.4.3 Testing specific component design

As CAD models of the sample surroundings can be directly imported into the ray tracing simulation, the framework can be used to assess the practicality and performance of specific component designs. Specifically the simulation can be used to help design pinhole-plates; §4.1 looks in depth at the design of pinhole-plates and how they define the optics of the SHeM.

2.5 EXTENSION TO DIFFRACTIVE AND INELASTIC CONTRAST

One major advantage of the ray tracing framework is that it allows arbitrary sample scattering distributions, therefore it can provide a useful tool to investigate alternative SHeM contrast mechanisms such as diffraction or potential inelastic contributions.

While in principle the framework always allowed the addition of new distributions, a streamlined process for adding new scattering distributions was implemented by D Serement[59]. After the refinement all that needs to be provided to include a new scattering distribution are: a C function that samples directions from the desired distribution, and an appropriate labelling of the distribution function so that it can be linked to a `.mtl` ‘material’ file that lists the compositions of a particular sample. Serement used the new flexibility to implement a model of the Debye-Waller effect, as well as a preliminary model of diffraction.

A further generalisation was made to better represent diffraction with the introduction of lattice parameters as an integral part of the surface representation, allowing arbitrary sample manipulations and separating the lattice representation from the peak intensities allowing investigations such as that presented in chapter 7 on Lithium Fluoride. The decoupling of the lattice parameters from the material specification allows different models of the diffraction peak intensities to be used with the same sample, including peak intensities calculated via simulation, see §7.3.1 for further details.

2.6 STUDY OF THE NAM

The NAM (Neutral Atom Microscope) is a different design of helium microscope developed in Portland USA[2, 16, 60]. The approach uses a pinhole to produce the microprobe in a similar manner to the SHeM, however, the NAM employs very short working distances, $\sim 10\ \mu\text{m} - 100\ \mu\text{m}$, along with a relatively small source to pinhole distance; the result is a higher intensity beam that broadens significantly with the distance from the pinhole. In addition, the detection region occupies a significant fraction of the outgoing hemisphere from the scattering point and is placed at a highly obtuse angle from the surface normal. Overall, therefore, the NAM presents quite a different imaging configuration to the Cambridge SHeM while still being based on the same fundamental principles. It therefore makes an interesting study with the ray tracing simulation.

Figure 2.22 highlights the key components of the NAM for the interest of performing a ray tracing simulation: the location of the pinhole, the beam direction, the sample position, and the detector placement.

In order to simulate the NAM, parameters of the instrument need to be specified. From a photo of the NAM provided by Witham[2] an estimate of the half cone angle of the detector entrance aperture is $15 - 20^\circ$, while the centre of the detector entrance aperture was estimated to be at an angle of

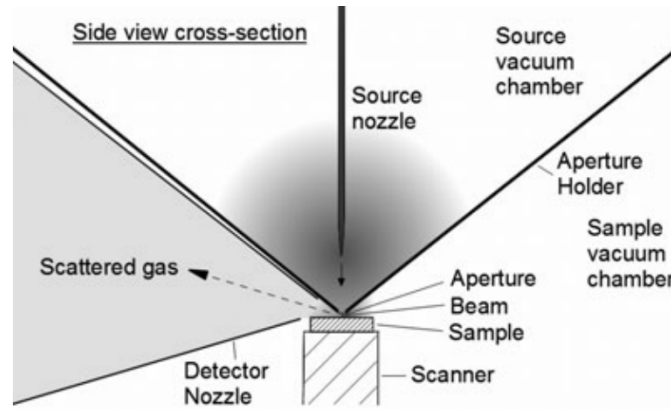


Figure 2.22: The basic design components of the NAM relevant for performing simulations. Note the large detector aperture entrance placed at a large angle from the surface normal and the normal incidence beam with a short source to pinhole distance that distinguish it from the SHeM. Diagram from Witham & Sanchez 2013[16].

70° from the surface normal. The ‘Current’ set of parameters from table II from Witham[2] were taken for the source. A working distance of 50 μm is specified, as is pinhole diameter of 1 μm .

The virtual source was modelled as a Gaussian with a width that will give the measured FWHM spot size of 1.5 μm [2] at the working distance of 50 μm . From Bergin[27] (ignoring diffraction) the beam standard deviation, ϕ is

$$\phi^2 = \frac{d^2}{12} + \sigma_s^2 f^2 \quad (2.7)$$

where f is the working distance, d the pinhole diameter, and σ_s the standard deviation of the source distribution incident on the pinhole. Thus $\sigma_s = 0.01$ rad.

A NAM micrograph and NAM simulation of a pollen grain is presented in figure 2.23 alongside a simulation of the same sample in the set-up of the SHeM. The basic features of the experimental image are reproduced with three significant differences being apparent between the NAM simulation and the SHeM simulation. First, due to the large acceptance angle of the detector and the extreme angle of detection, the masks in the NAM are very diffuse, with no clear boundary between masked and un-masked regions of the sample. Second is the image projection, using normal incidence as in the NAM the sample appears to be ‘viewed from above’ while in the SHeM the sample appears to be ‘viewed from the side’ highlighting the height of the pollen grain. Third is the beam spread, the more distant features, such as the background grid, are not in as sharp focus as features closer to the pinhole, the top of the pollen grain. The soft focus of more distant part of the sample is due to the significant size of the virtual source. In the SHeM simulation all parts of the sample are in a similar level of focus.

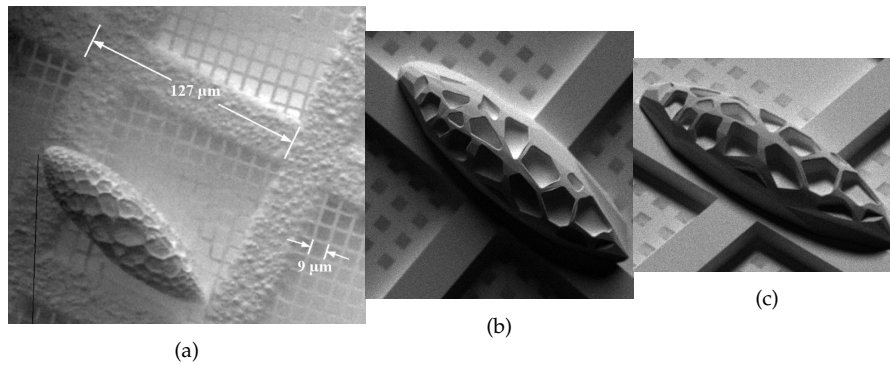


Figure 2.23: Two simulations of a pollen grain along with an image of a real pollen grain taken with the NAM. (a) An experimental NAM images from Witham 2011[2]. (b) the NAM setup with a small working distance and a broad virtual source, (c) with the standard SHeM set-up with 45° incidence and a small detector aperture. Panel (a) reprinted from [Witham & Sánchez 2011[2], with the permission of AIP Publishing.

2.7 SUMMARY

A general ray tracing framework for predicting contrast in scanning helium microscopy has been developed that has been shown to be capable of reproducing important image features such as masking and multiple scattering. The framework allows arbitrary scattering distribution models to be used. It can also be employed to investigate instrument effects, including the effuse background. Results from the simulation have highlighted that the ‘response curve’ of a SHeM causes an inversion of contrast and creates a practical depth of field. Further, the framework has been used to inform the design of new instrumentation of the Cambridge SHeM. Broader scoped investigations have provided insight into the impacts that the incidence angle and the detector positioning have on the appearance of SHeM images. The investigation demonstrated that changing the incidence angle and detection direction can create substantially different imaging modes than are currently used in the A-SHeM. Finally the flexibility of the method was demonstrated by performing simulations of an alternative helium microscope design – the NAM.

The next chapter considers specific cases where implementations of the geometric model of contrast using integrals can be useful.

3.1 INTRODUCTION

The ray tracing framework is adaptable and can be applied to complex problems, however when investigating specific problems more straightforward integral models can be highly informative.

In this chapter a model of the detected helium intensity for circular and elliptical detector apertures is developed. All the models presented in this chapter assume the cosine model of Knudsen scattering, which, empirical evidence shows, is a reasonable model for disordered surfaces in SHeM.

First, in §3.2 a model is developed that allows consideration of the effect of having a large detector aperture (one which occupies a significant solid angle) has on the contrast in SHeM micrographs. With the general cosine model of diffuse scattering, the detected signal varies depending on the cosine of the angle between the surface and the specific, infinitesimal, detection direction. An integral model is used to show that for large apertures occupying a circular region of solid angle, the same relation holds between the surface and the centre of the detection aperture.

The model developed in §3.2 is then extended to investigate the effect of changing the extent of the detection aperture. It is intuitive that larger detector apertures should give larger signals, but by integrating over larger regions of the scattering distribution, the signal is to some extent ‘averaged out’ and thus contrast might be reduced. By carefully defining quantities to measure the ratio between contrast and shot noise the results of section 3.6 show that there are indeed significant gains to be made with larger aperture than currently employed in the A-SHeM.

Results from the investigation into aperture size also highlight that for large apertures a new contrast mechanism becomes significant: contrast by partial masking, where the detector is partially masked over a range of surface orientations. The result is a signal that varies with the surface orientation in a qualitatively similar manner to diffuse cosine contrast and partially compensates for the averaging of the scattering distribution with larger apertures. Partial masking is evident experimentally in the images published by Witham & Sanchez[2, 16, 60] where a detector aperture larger than in Cambridge is employed.

By integrating apertures occupying elliptical regions of solid angle rather than circular the effect of the shape of the aperture on contrast can be investigated.

Integral models are also used to investigate the possibility of contrast due to *deformation of the sample under the beam*, given the hypothesis is that the

different elastic moduli of materials leads to different deformations of the surface under the pressure of the incident helium beam. The deformations then focus the scattered helium resulting in contrast between the materials – such as the contrast observed by Barr et. al[38]. The investigations imply that contrast due to deformation under the beam is not currently observable.

3.2 THE SIGNAL FOR A CIRCULAR APERTURE

The basic concept of the integral model is to have an element of surface some distance away from a detector aperture. That detector aperture is modelled as a circular (or in the extension in §3.2.3 elliptical) region of solid angle on the unit sphere. The detector aperture that is being modelled need not actually be a circle 1 unit away from the sample, for example the elliptical detector used in the standard configuration of the A-SHeM, by design, occupies a circular region of solid angle. The surface element radiates with a cosine distribution. Thus the detected signal is the integral of the radiating cosine distribution over the aperture.

Figure 3.1 demonstrates the geometry of the model. I , is a function of the angle between the surface normal and the centre of the detector aperture, ψ , and the half cone angle of the aperture, β . An integral is performed over the aperture modified by a cosine term, $\cos \chi$, where the angle χ is the angle between the surface normal and a single point on the aperture. The *signal* is thus

$$I \propto \int_{\text{aperture}} \cos \chi \, d\Omega. \quad (3.1)$$

Defining θ to be the angle to the axis from the integral point to the centre of the detector aperture and φ to be the azimuthal angle around the sample-aperture axis the integral becomes

$$I(\psi, \beta) \propto 2 \int_0^\pi d\varphi \int_0^\beta d\theta \sin \theta \cos \chi. \quad (3.2)$$

The cosine term, $\cos \chi$, may be written as the dot product between the unit normal to the surface and the normalised vector from the surface to the infinitesimal point on the aperture being summed. Defining φ to be relative to the x axis the unit normal is

$$\hat{\mathbf{n}} = \begin{pmatrix} \sin \psi \\ 0 \\ \cos \psi \end{pmatrix} \quad (3.3)$$

which is fixed as ψ is a constant. The normalised vector from the surface to a point on the aperture, $\hat{\mathbf{d}}$, can be found by considering a Cartesian coordinate system. The aperture lies on the unit sphere directly above the surface along the z axis by a distance $\cos \beta$. Referring to figure 3.2 points on the plane of the

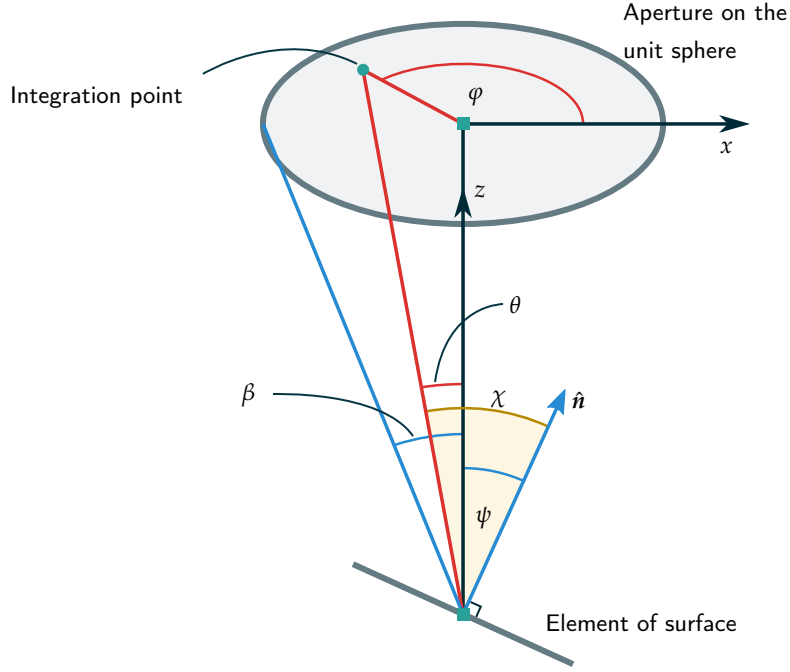


Figure 3.1: The geometric set up of the integral contrast model. A circular aperture is on a unit sphere with an element of surface at the centre of the sphere. The element of surface is at some angle ψ to the centre of the aperture and the extent of the aperture is defined by its half cone angle β . To calculate the signal intensity for a particular (ψ, β) the aperture is integrated over through the angles (θ, φ) . The integration variables and geometry are shown in red, and the variables of signal are shown in blue. The angle χ , in yellow, is between the normal to the surface element and the line from the surface element to the integration point, $\cos \chi$ weights the integral according to the cosine model of diffuse scattering.

aperture have positions given by the 2D polar coordinates of $(r = z \tan \theta, \varphi)$, thus the components of the vector are $x = z \tan \theta \cos \varphi$, $y = z \tan \theta \sin \varphi$. Thus the normalised vector to the infinitesimal point on the aperture is

$$\hat{\mathbf{d}} = \frac{\cos \beta}{\cos \beta \sqrt{(1 + \tan^2 \theta \cos^2 \varphi + \tan^2 \theta \sin^2 \varphi)}} \begin{pmatrix} \tan \theta \cos \varphi \\ \tan \theta \sin \varphi \\ \cos \beta \end{pmatrix} \quad (3.4)$$

$$= \cos \theta \begin{pmatrix} \tan \theta \cos \varphi \\ \tan \theta \sin \varphi \\ 1 \end{pmatrix}, \quad (3.5)$$

and the dot product is then

$$\cos \chi = \hat{\mathbf{n}} \cdot \hat{\mathbf{d}} = \cos \theta (\sin \psi \tan \theta \cos \varphi + \cos \psi), \quad (3.6)$$

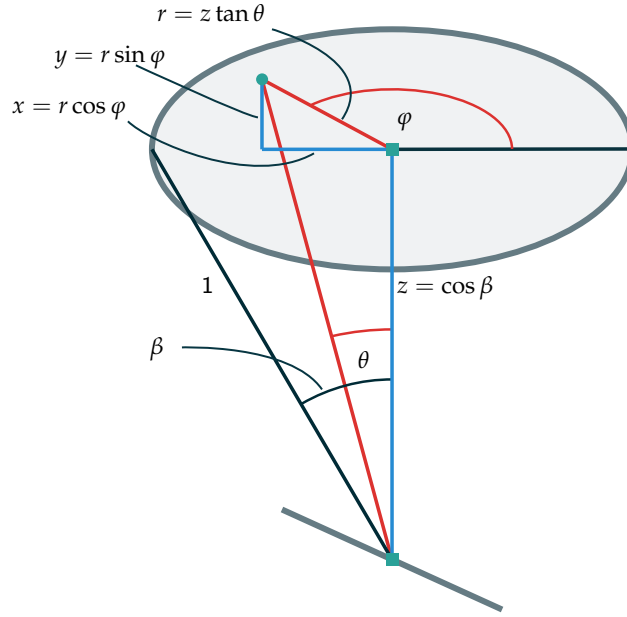


Figure 3.2: The geometry deriving the vector to the infinitesimal point on the aperture via a Cartesian system. The three components of the vector from the surface element to an integration point on the detector aperture are shown in blue, x and y in terms of the intermediate variable r . As in figure 3.1 the integration variables are shown in red. Due to the symmetry of the system in the y axis, the values of $-y$ and y are equivalent.

which allows the signal, from equation 3.2, to be written as

$$I(\psi, \beta) \propto 2 \int_0^\pi d\varphi \int_0^\beta d\theta \sin \theta \cos \theta (\sin \psi \tan \theta \cos \varphi + \cos \psi). \quad (3.7)$$

3.2.1 Analytic form

The integral in equation 3.7 can be evaluated analytically to give an explicit expression for the signal,

$$I \propto 2 \sin \psi \int_0^\pi \cos \varphi d\varphi \int_0^\beta \sin \theta \cos \theta \tan \theta d\theta \quad (3.8)$$

$$+ 2\pi \cos \psi \int_0^\beta \sin \theta \cos \theta d\theta$$

$$= 0 + 2\pi \cos \psi \int_0^\beta \frac{1}{2} \sin 2\theta d\theta \quad (3.9)$$

$$= \frac{1}{2} \pi \cos \psi (1 - \cos 2\beta). \quad (3.10)$$

Notably the final equation has the detected intensity *directly proportional to the cosine of the detection angle* just as in the initial Knudsen model of the scatter, thus where the detector aperture occupies a circular (or near circular) region of solid angle the simple cosine model needs no modification for real detector apertures with significant acceptance angles. The above holds, however, only

for a limited range of the (ψ, β) space – as the aperture becomes larger and the angle of the surface becomes larger part of the aperture falls ‘behind’ the surface, and thus would contribute nothing to the integral. Equation 3.10 may thus be applied when

$$\psi + \beta \leq \frac{\pi}{2}. \quad (3.11)$$

When equation 3.11 does not hold, a numerical approach is used.

An analytic form for the detected intensity as a function of surface angle is useful outside the investigation of the effect of detector aperture size. It allows the qualitative interpretation of images, and can be leveraged to extract quantitative 3D information from SHeM data, as is explored in chapter 8. In addition it can also be used to predict if certain features will be observable in the SHeM. An example use is given in section 3.7 where the contrast as a result of a sample deforming under the beam is considered.

3.2.2 Numerical region

Numerical 2D quadrature integration is used on an adapted version of equation 3.7. The infinitesimal element of aperture is behind the surface when $\chi > \frac{\pi}{2}$, which when we limit ourselves to $\chi \in [0, \pi]$ is equivalent to $\cos \chi < 0$. We have an expression for $\cos \chi$, thus we may set the value of $\cos \chi$ to be 0 when equation 3.6 evaluates to be negative. The signal

$$I(\psi, \beta) \propto 2 \int_0^\pi d\varphi \int_0^\beta d\theta \sin \theta f(\theta, \varphi), \quad (3.12)$$

$$f(\theta, \varphi) = \begin{cases} 0, & \chi \geq 0 \\ \cos \theta (\sin \psi \tan \theta \cos \varphi + \cos \psi), & \text{otherwise} \end{cases} \quad (3.13)$$

which is easy to represent programmatically using a conditional.

For the purposes of practical improvements it is illustrative to consider the signal level as a function of the radius of the detector aperture in a set-up equivalent to the standard A-SHeM configuration. Equation 3.10 becomes

$$I = \frac{1}{2} \pi \cos \psi \sin^2 2\beta \quad (3.14)$$

$$= \frac{1}{2} \pi \cos \psi \sin^2 \arctan R = \frac{1}{2} \pi \cos \psi \frac{R^2}{R^2 + 1} \quad (3.15)$$

where $R = r/d$ is the ratio of the radius of the detector aperture to the working distance 3 mm. Figure 3.3 plots the resulting signal change from the standard configuration (which is highlighted in yellow). A change in behaviour can be seen from quadratic at low radii to linear at large radii, as can also be seen in equation 3.15 by taking the limits $R \rightarrow 0$ and $R \rightarrow \infty$. That the relationship becomes closer to linear than quadratic once apertures become significantly larger than the present aperture, is worth noting.

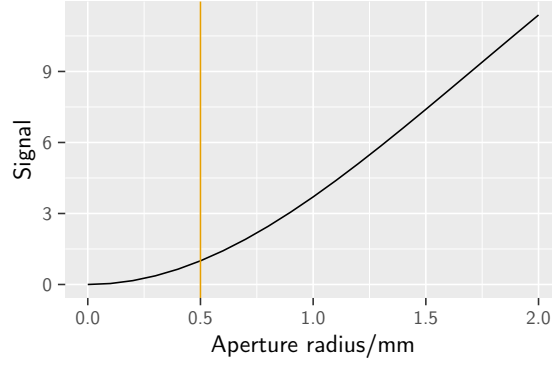


Figure 3.3: The detected signal as a function of the detector aperture radius. Assumes a 45° angle between the surface element and the detector aperture.

3.2.3 Extension to elliptical apertures

While detector apertures representing roughly circular regions of solid angle have been the most commonly used in existing helium microscopes an interesting question is if they are the optimal shape.

In order to investigate elliptical apertures, the equations for the solid angle subtended by an ellipse from Abbas[61] are used¹. The solid angle subtended by an ellipse is

$$\Omega(0,0,h) = \int_0^{2\pi} d\varphi \int_0^{\theta_1(\varphi)} d\theta \sin \theta \quad (3.16)$$

$$\theta_1(\varphi) = \arctan \frac{r_1(\varphi)}{h} \quad (3.17)$$

$$r_1(\varphi) = \frac{ab}{\sqrt{a^2 \sin^2 \varphi + b^2 \cos^2 \varphi}} \quad (3.18)$$

where a, b are the principle axes of the ellipse and h is the distance the ellipse is placed from the point on the sample. Translating into the variables used here: $a = \tan \beta_a$, $b = \tan \beta_b$, with β_a and β_b being the principle half cone angles of the ellipse. For the purposes of simplicity set $h = 1$. Then introducing the $\cos \chi$ term gives the integral

$$I \propto \int_0^{2\pi} d\varphi \int_0^{\theta_1(\varphi)} d\theta \sin \theta \cos \theta (\sin \psi \tan \theta \cos \varphi + \cos \psi) \quad (3.19)$$

$$\begin{aligned} &\propto \sin \psi \int_0^{2\pi} d\varphi \int_0^{\theta_1(\varphi)} d\theta \sin^2 \theta \cos \varphi \\ &\quad + \cos \psi \int_0^{2\pi} d\varphi \int_0^{\theta_1(\varphi)} d\theta \sin \theta \cos \theta \end{aligned} \quad (3.20)$$

$$\begin{aligned} &\propto \frac{1}{2} \sin \psi \int_0^{2\pi} d\varphi [\theta - \sin \theta \cos \theta]_0^{\theta_1(\varphi)} \cos \varphi \\ &\quad + \frac{1}{2} \cos \psi \int_0^{2\pi} d\varphi [-\cos^2 \theta]_0^{\theta_1(\varphi)} \end{aligned} \quad (3.21)$$

¹specifically section 2.1 and equations 2-5

$$\begin{aligned} &\propto \frac{1}{2} \sin \psi \int_0^{2\pi} d\varphi [\theta_1(\varphi) - \sin \theta_1(\varphi) \cos \theta_1(\varphi)] \cos \varphi \\ &\quad + \frac{1}{2} \cos \psi \int_0^{2\pi} d\varphi [1 - \cos^2 \theta_1(\varphi)] \end{aligned} \quad (3.22)$$

which must then be integrated numerically.

As with the circular aperture in equation 3.13 the integrand becomes 0 when $\chi \geq 90^\circ$. As there is a function in the integration limits here the most straightforward method is to perform a Monte-Carlo integration where the aperture is partially masked and use normal quadrature integration where it is fully visible.

3.3 SIGNAL VARIATION WITH APERTURE SIZE

Equations 3.13 and 3.11 may be used to plot the intensity of both the angle between the surface element and the detector, ψ , and the half cone angle of the detector aperture, β , using the results of §3.2. To specify a scale an approximation to the current signal is performed. The signal of the standard configuration is used to normalise the results, ($\psi = 45^\circ$ and $\beta = 5^\circ$). Thus $I(\psi = 45^\circ, \beta = 5^\circ) \equiv 1$.

The signal is plotted on a combined heatmap/contour plot in figure 3.4, alongside the signal to noise ratio, if shot noise is assumed. A vertical line demonstrates where the present machine would lie. The plots show that signal increases of ~ 100 , along with the corresponding SNR improvements of ~ 10 , are, in principle, possible by increasing the size of the detector aperture. However it is not the signal nor purely the signal to noise that we are interested in, it is the level of contrast in an image relative to the level of noise – the ‘contrast to noise’ is considered in §3.6.

In the plot of the signal there is a noticeable ‘kink’ in the contours that lie diagonally across the plot. The kink is located close to the condition where part of the aperture is behind the surface; mathematically it is where the analytic formula in equation 3.10 can no longer be applied and numerical integration must be performed with part of the integrand set to zero. In terms of contrast mechanisms it is where the surface is becoming partially *under mask* – figure 3.5 demonstrates the concept of partial masking. At the larger size of aperture we are getting contrast from *partial masking*, which is mechanistically distinct from contrast arising from the cosine distribution but will manifest in a similar manner in images.

The existence of partial masking extends changes in detected signal into regions that would be completely dark with a infinitesimal detector aperture: those with a surface angle $> 90^\circ$ in figure 3.4. Partial masking causes changes in signal over a range of surface angles equal to the full cone angle (twice the half cone angle) of the detector aperture. Thus for large detector apertures there is a significant new contrast mechanism beyond the slowly varying cosine function: *contrast by partial masking*.

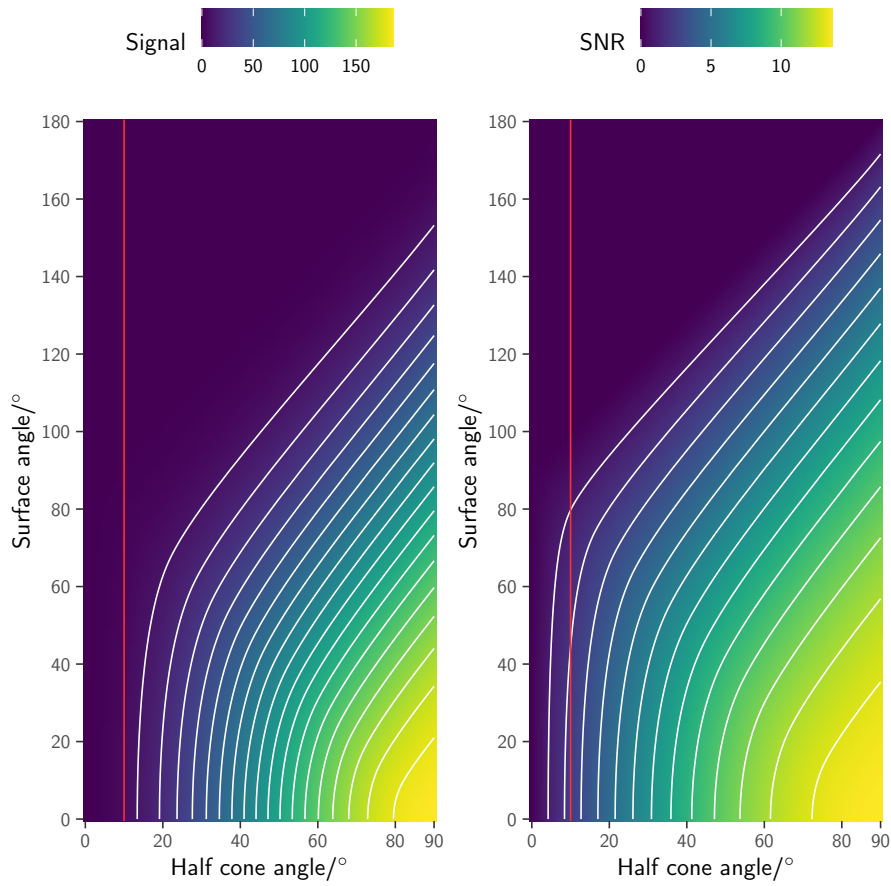


Figure 3.4: The signal and the signal to noise ratio as a function of the half cone angles and the angle of the surface. Both are normalised such that the signal from a flat region of sample in the present microscope corresponds to 1. The vertical red line is the aperture of the present microscope. For the signal plot the contours are separated by 10 while for the SNR plot the contours are separated by 1.

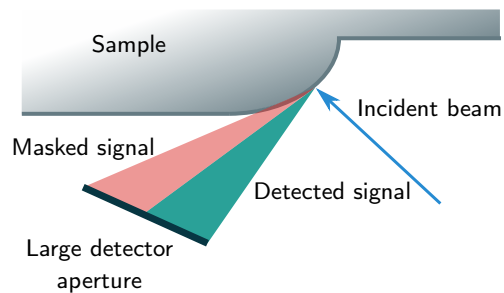


Figure 3.5: The process of partial masking. From the point where the beam intersects the sample there is line of sight to only part of the detector, thus the detected signal is reduced. As the beam moves over a curved surface different proportions of the detector will be visible causing contrast in the resulting micrographs.

3.4 SIGNAL VARIATION WITH APERTURE SHAPE

To investigate the impact of the shape of the aperture, a series of different aspect ratio of elliptical detectors were considered. The aspect ratio of the ellipse here is defined to be the ratio of the half cone angles of the two principle axes of the ellipse: $AR = \beta_a / \beta_b$. Both the case of major axis of the ellipse being in plane with the sample surface tilt ψ and with the major axis perpendicular to the surface tilt were considered. In order to keep the test consistent, the solid angle of the ellipse needs to be kept constant while the shape of the aperture is varied. The formula from Conway[62] is used to calculate the solid angle of an ellipse.

Figure 3.6 displays the detected signal as a function of angle between the surface normal and the detector aperture, ψ , for different aspect ratios of detector, and for both orientations of the ellipse. All calculations were performed with a detector of solid angle the same as the standard A-SHeM configuration. For the case of ‘wide’ apertures, figure 3.6 (a), that have the major axis of the ellipse perpendicular to the plane of tilt ψ the detected signal is not significantly affected until more extreme aspect ratios are reached. For the case of ‘long’ apertures, figure 3.6 (b), where the major axis is in plane with the sample tilt there is an extension of signal beyond $\psi = 90^\circ$ due to partial masking. The extension of signal then causes an extension of contrast because contrast is changes in signal, which here is effectively the gradient of the curve.

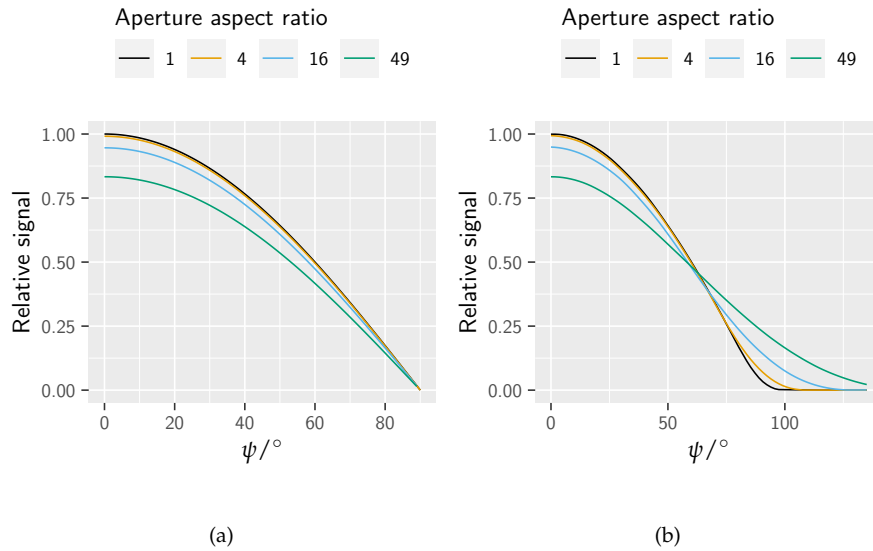


Figure 3.6: The detected signal as a function of the sample tilt for a series of different aspect ratios for (a) ‘wide’ apertures and (b) ‘long’ apertures. Where the surface tilt is perpendicular to the major axis of the aperture then significant changes are only seen at extreme aspect ratios. However where the major axis is in plane with the angle of surface tilt then contrast is extended to greater tilt angles via partial masking. Plot (a) does not take into account partial masking.

Two conclusions may be drawn from figure 3.6. First, in terms of optimising contrast/signal, slight variations from circular apertures is neither beneficial nor detrimental. Second, the contrast mechanism of partial masking can be enhanced by changing the shape of the detector aperture without increasing the overall size of the aperture, although the effect will be asymmetric.

3.5 DEFINING THE CONTRAST TO NOISE RATIO

Michelson contrast is a widely used definition of contrast[63]:

$$C_M = \frac{I_{\max} - I_{\min}}{I_{\max} + I_{\min}}, \quad (3.23)$$

which considers the contrast between a maximum and minimum intensity. The primary purpose of the Michelson contrast is to quantify the visibility of interference fringes, or similar patterns that have roughly equivalent dark and light areas, hence the alternative name for the quantity being the *visibility*. However as SHeM images are computationally plotted with a choice of the 'black' and 'white' values it is not an appropriate measure of contrast in SHeM images.

3.5.1 *Difference to noise*

In practice when a SHeM image is computationally plotted it is the ratio between the difference in signal between two pixels and the noise on those signals, here it is assumed that shot noise is the dominant form of noise. The background weighting that is in the denominator of the Michelson definition is to emphasize how *visible* features are, however in SHeM images the background value is ignored when a greyscale for the image is chosen. Thus the *difference to noise ratio* is

$$DNR = \frac{|I_2 - I_1|}{\sqrt{(I_2 + I_1)/2}} \quad (3.24)$$

which weights by the shot noise in an image.

3.5.2 *RMS contrast to noise*

The difference to noise measure is relevant for two specific pixels, or groups of pixels in an image. Where an entire image with different levels of signal is to be considered a different measure is needed.

The *root mean square contrast*[64] is the standard deviation of the pixel intensities across an image. For the purposes of investigating the effect of the aperture size on the contrast the definition is changed slightly: instead of using an example image the definition is applied to a curve over all the possible angles between the sample and detector, ψ , is used as representative

of the possible surface facets in a sample. Specifically the RMS contrast is defined as the standard deviation across all the values of ψ for a specific value of the detector half cone angle, β , as above it is then scaled with the shot noise of that signal. Thus the *RMS contrast to noise* is

$$CNR_{\sigma} = \frac{\sigma}{\sqrt{\mu}} = \frac{1}{\sqrt{\mu}} \sqrt{\frac{1}{N} \sum_{i=1}^N (I_i - \mu)^2} \quad (3.25)$$

where $\{I_i\}$ are the signals across the range of ψ and μ is the mean.

3.5.3 Differential contrast to noise

The RMS contrast to noise considers the spread of the signals across all the available surface angles. In practice in the SHeM we are not usually interested in the deviation in signal for two wildly different angles to the detector but in how the signal varies continuously as the angle to the surface changes: we often wish to know if a region of sample has curvature, rather than if two regions of sample are angled a large distance from each other. Thus we are interested in infinitesimal contrast with small changes in the surface angle. Proposed therefore is the *differential contrast to noise* where the contrast is given by the average of the absolute value of the derivative of the signal curve over the range of surface angles that are of interest. The definition is

$$CNR_{\partial} = \left\langle \left| \frac{dI}{d\psi} \right| \right\rangle \frac{1}{\sqrt{\langle I \rangle}}. \quad (3.26)$$

An additional advantage of the differential contrast to noise is that it weights every infinitesimal change in ψ equally, whereas the RMS contrast to noise will be dominated by large deviations away from the mean intensity.

3.6 CONTRAST TO NOISE AS A FUNCTION OF APERTURE SIZE

Having defined useful measures of the contrast to noise ratio and with a full data set of the detected intensity as a function of (ψ, β) , the contrast to noise can be plotted to help find the optimal detector aperture size.

Figure 3.7 plots the difference of the signal and the difference to noise of the signal as a function of the detector aperture half cone angle, β , for three pairs of ψ were chosen to represent moderate and large changes in the surface orientation: $(0^\circ, 45^\circ)$, $(0^\circ, 90^\circ)$, and $(45^\circ, 90^\circ)$. Figure 3.8 plots both the RMS contrast to noise and the differential contrast to noise as a function of β .

As expected the contrast to noise by all three measures increases with the half cone angle, then at larger angles (significantly larger than any used at present) the contrast to noise peaks and falls off again. As can be seen in the

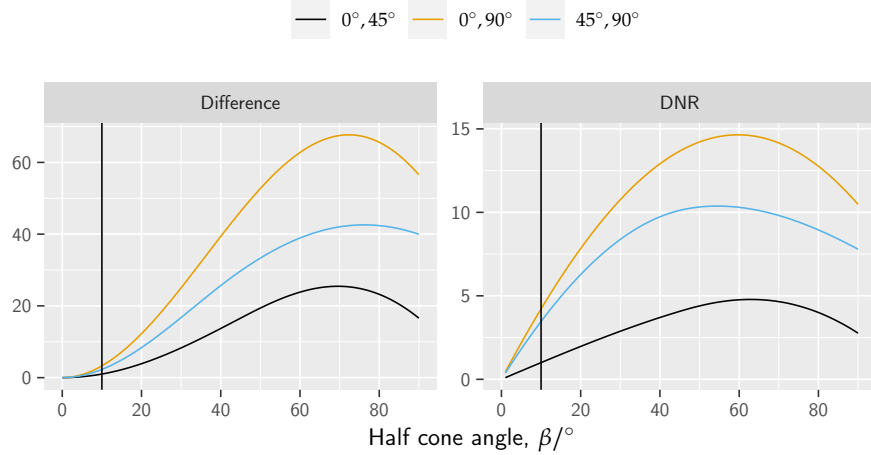


Figure 3.7: The difference and difference to noise ratio for three different intervals of ψ (the angle of the surface normal to the detector). The vertical line is $\beta = 10^\circ$ where the difference and the DNR of the $0^\circ, 45^\circ$ difference is set to 1.

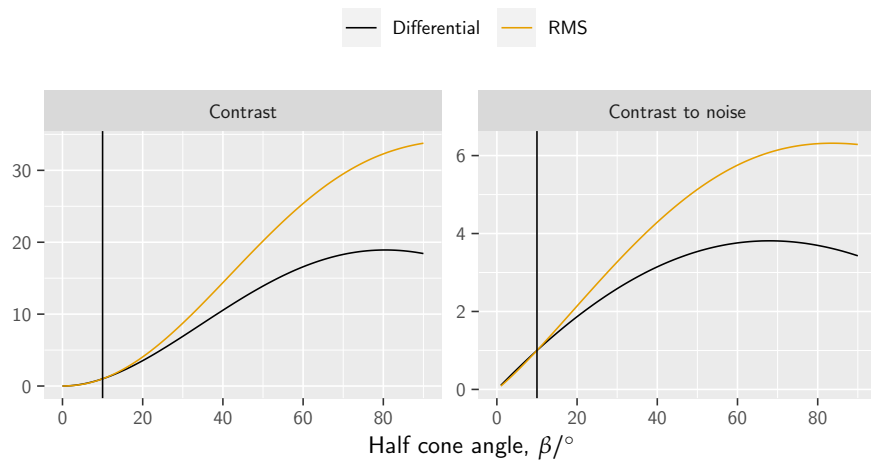


Figure 3.8: The RMS contrast to noise ratio as a function of β , the half cone angle of the detector aperture. The plot is normalised such that an aperture of $\beta = 10^\circ$ has a value of 1, which is displayed with the vertical line.

plot of the difference the peak in contrast to noise is shifted slightly compared to that of pure contrast. The maxima for each measure all occur in a similar range of very large aperture, apertures that are likely impractical to construct. The three methods can be said to be consistent with each other in their trends, however the exact location of the maxima will depend on exactly how one defined the criteria for it. Overall it is clear that significant improvement can be made to the contrast in SHeM images from the arrangement used as standard in the A-SHeM by using larger detector apertures.

3.6.1 Equivalent signal improvements

It is useful to know what the equivalent increase in signal would be without any change to the detection geometry – via either more efficient detectors or more intense sources.

If the detector aperture is to be kept the same as it is then an increase of signal by a factor of n would yield a contrast to noise improvement. Taking the RMS contrast to noise then a signal increase would cause

$$CNR_{\sigma} = \frac{1}{\sqrt{\mu}} \sigma \rightarrow \frac{1}{\sqrt{n\mu}} n\sigma = \sqrt{n}CNR_{\sigma} \tag{3.27}$$

and the contrast to noise improvement is \sqrt{n} . Set $CNR_{\sigma}(\beta = 10^{\circ}) = 1$, the standard A-SHeM configuration, thus the equivalent signal increase can be plotted as a function of aperture size by squaring change in CNR_{σ} from 3.8. The same argument follows for the differential contrast to noise.

Figure 3.9 plots the equivalent signal improvements required to achieve the same RMS contrast to noise and differential contrast to noise improvements as increases in the half cone angle of the detector aperture. In principle it shows that an equivalent to increasing the signal by a factor of ~ 40 if the RMS measure is used, or ~ 15 if the differential measure is used, can be achieved by only increasing the detector aperture size. The optimum half cone angle of the detector using either measure is, however infeasibly large. Practically it would be reasonable to conclude that an equivalent increase in signal of between ~ 12 and ~ 23 can be achieved (depending on which measure of contrast is used) through enlarging the detector aperture to $\beta = 45^{\circ}$, since covering roughly half a hemisphere is the largest a collection aperture could reasonably achieve.

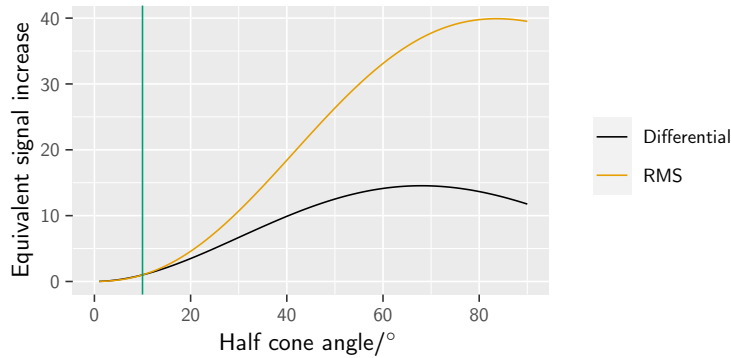


Figure 3.9: The equivalent signal change to the improvement in RMS and differential contrast to noise plotted as a function of a change in the half cone angle of the detector aperture. The vertical line is 5° which is set to a signal change of 1.

3.7 CONTRAST FROM SURFACE DEFORMATION

In this section the potential for contrast due to deformation of the sample is explored by developing the appropriate algebra. At the end of the section the developed expressions are used to demonstrate that in SHeM contrast due to deformation by the incidence helium beam is not possible with current technology.

3.7.1 *The signal due to a deformed surface*

The derivation considers a helium beam incident on a surface that has been deformed from a flat surface into one following the function $z = f(\mathbf{r})$.

The optical geometry is kept constant and equivalent to the standard A-SHeM configuration: incidence and detection angle of 45° and a detector aperture of 10° half cone angle. Let a helium beam profile on the surface plane be $B(\mathbf{r})$, and let the unit normal to the surface be $\hat{\mathbf{n}}(\mathbf{r})$, where \mathbf{r} is the position on the sample plane. Assume that the deflection is small and thus ignore spatial deflections of the surface and only consider the change in orientation of each element of surface. The incidence and detection directions are denoted $\hat{\mathbf{i}}$ and $\hat{\mathbf{d}}$ respectively. The unit normal is the gradient of the surface defined by $f(\mathbf{r}) = 0$, where

$$f(\mathbf{r}) = g(x, y) - z, \quad (3.28)$$

thus $\mathbf{n}(\mathbf{r}) = -\nabla f(\mathbf{r})$ is the unnormalised normal to the surface. For a particular surface orientation the detected intensity is given by equation 3.10, the whole range of the beam and the deformation needs to be integrated over to give the total intensity from the deformation. The term $\cos \psi$ in equation 3.10 may be written as $\hat{\mathbf{n}}(\mathbf{r}) \cdot \hat{\mathbf{d}}$. The changing incident direction across the deformation needs to be taken into account: the relative intensity on $dx dy$ will be proportional to $-\hat{\mathbf{n}}(\mathbf{r}) \cdot \hat{\mathbf{i}}$, which is projecting the normal of the surface into the incident direction of the beam. Therefore the general integral for the intensity resulting from the surface deforming under the beam can be written as

$$I_D[f] = \frac{1}{2}\pi(1 - \cos 2\beta) \iint_{\mathbb{R}^2} -B(\mathbf{r}) [\hat{\mathbf{n}}(\mathbf{r}) \cdot \hat{\mathbf{d}}] [\hat{\mathbf{n}}(\mathbf{r}) \cdot \hat{\mathbf{i}}] d\mathbf{r} \quad (3.29)$$

where I_D is a functional on the deformation given a fixed beam profile. The beam profile is normalised such that $\int B(x, y) dx dy = 1$. Introducing the gradient of f :

$$I_D[f] = \frac{1}{2}\pi(1 - \cos 2\beta) \times \iint_{\mathbb{R}^2} -B(x, y) [\nabla f(\mathbf{r}) \cdot \hat{\mathbf{d}}] [\nabla f(\mathbf{r}) \cdot \hat{\mathbf{i}}] \frac{1}{|\nabla f(\mathbf{r})|^2} d\mathbf{r} \quad (3.30)$$

which is the general form for the detected intensity from a surface deformed into the curve defined by f . The model assumes that there is no region of the deformation under shadow or under mask, i.e. the entire surface can 'see' both the incident beam and the detector aperture.

Both the incidence direction and detection direction are at 45° to the surface: $\hat{\mathbf{i}} = (1/\sqrt{2}, 0, -1/\sqrt{2})$ and $\hat{\mathbf{d}} = (1/\sqrt{2}, 0, 1/\sqrt{2})$, therefore

$$I_D[f] = \frac{1}{4}\pi(1 - \cos 2\beta) \iint_{\mathbb{R}^2} -B(x, y) \left(\frac{\partial f}{\partial x} + \frac{\partial f}{\partial z} \right) \left(\frac{\partial f}{\partial x} - \frac{\partial f}{\partial z} \right) \frac{1}{|\nabla f(\mathbf{r})|^2} dx dy \quad (3.31)$$

$$= \frac{1}{4}\pi(1 - \cos 2\beta) \iint_{\mathbb{R}^2} -B(x, y) \left(\frac{\partial f^2}{\partial x} - \frac{\partial f^2}{\partial z} \right) \frac{1}{\partial_x f^2 + \partial_y f^2 + \partial_z f^2} dx dy \quad (3.32)$$

$$= \frac{1}{4}\pi(1 - \cos 2\beta) \iint_{\mathbb{R}^2} -B(x, y) \left(\frac{\partial f^2}{\partial x} - 1 \right) \frac{1}{\partial_x f^2 + \partial_y f^2 + 1} dx dy \quad (3.33)$$

and the integrand is independent of z . Consider a flat surface with $\partial_x f, \partial_y f = 0$ then the resulting intensity is $\frac{1}{4}\pi(1 - \cos 2\beta)$, as would be expected from the way we set up the integral in equation 3.29.

3.7.2 Evaluating for a simple case

For the purposes of simplicity assume the beam is uniform and incident only on a circular region of surface $r < R$ and that the deformation in that region is parabolic with $g(x, y) = \alpha(x^2 + y^2)$. Then, dropping the constant prefactors,

$$I_D = \iint_{r < R} (1 - 4\alpha^2 x^2) \frac{1}{4\alpha^2 x^2 + 4\alpha^2 y^2 + 1} dx dy \quad (3.34)$$

then converting from Cartesian to plane polar coordinates:

$$I_D = \int_0^{2\pi} d\theta \int_0^R dr r \frac{1 - 4\alpha^2 r^2 \cos^2 \theta}{1 + 4\alpha^2 r^2} \quad (3.35)$$

$$= 2\pi \int_0^R \frac{r}{1 + 4\alpha^2 r^2} dr - \pi \int_0^R \frac{4\alpha^2 r^3}{1 + 4\alpha^2 r^2} dr \quad (3.36)$$

$$= 2\pi \left[\frac{\ln(4\alpha r^2 + 1)}{8\alpha} \right]_0^R - \pi \left[\frac{r^2}{2} - \frac{\ln(4\alpha r^2 + 1)}{8\alpha} \right]_0^R \quad (3.37)$$

$$= \pi \frac{\ln(4\alpha R^2 + 1)}{4\alpha} - \frac{\pi R^2}{2} + \pi \frac{\ln(4\alpha R^2 + 1)}{8\alpha} \quad (3.38)$$

$$= \frac{3\pi \ln(4\alpha R^2 + 1)}{8\alpha} - \frac{\pi R^2}{2}. \quad (3.39)$$

Define the aspect ratio as $A \equiv \alpha R^2/2R = \alpha R/2$, without loss of generality we can then set $R = 1$ and we get $\alpha = 2A$, thus

$$I_D(A) = \frac{3\pi}{16A} \ln(8A + 1) - \frac{\pi}{2}. \quad (3.40)$$

For $A = 0$ the intensity is $I_D(0) = \pi$ (can be seen from equation 3.40), therefore the equation above is normalised to have the flat surface being an intensity of 1 by removing the factor of π .

3.7.3 Visibility of deformation

Let the signal to noise ratio be s , for the change to be visible that change needs to be larger than the noise. The baseline of signal is set at 1, so $s = 1/n$ where n is the noise. Therefore the signal to noise required to see the change in intensity as a result of deformation is

$$s(A) = \frac{1}{n(A)} = \frac{1}{\frac{3}{2} - \frac{3}{16A} \ln(8A + 1)}. \quad (3.41)$$

In practice there is also a background signal, label it by the relative size of the background compared to the flat surface signal b . In the presence of background $s(A)$ gives the relative size of the change we wish to see compared to the direct beam helium signal. The ratio of the change to the overall signal is

$$\frac{\frac{3}{2} - \frac{3}{16A} \ln(8A + 1)}{1 + b} \quad (3.42)$$

which needs to be smaller than the noise to be visible. If N is the count rate for the signal and background on the flat surface then the contrast to noise ratio is

$$CNR(A, N, b) = \frac{N \left[\frac{3}{2} - \frac{3}{16A} \ln(8A + 1) \right]}{\sqrt{N + bN}} \quad (3.43)$$

set $CNR = 1$ then the count rate required to see the change is

$$N(A, b) = \frac{1 + b}{\left[\frac{3}{2} - \frac{3}{16A} \ln(8A + 1) \right]^2}. \quad (3.44)$$

And the signal to noise ratio is \sqrt{N} . The total current background is ~ 1 times the size of the direct beam helium signal we want. Applying the above formula then for an aspect ratio of 1 in 1000 a SNR of 240 is needed on the flat sample, which corresponds to a count rate (assuming one data point per second) of 56000. For 1 in 100 the required signal to noise and respective count rate are 25 and 620 respectively. Count rates in the SHeM are of the order kilohertz, hence the ratio of 1 to 100 is likely to be observable but that

of 1 to 1000 is not. In practice this means a deformation of the order 10 nm is needed for it to be observable in the SHeM.

3.7.4 The deformation due to the pressure of the helium beam

Following results published by Barr et al.[38], that demonstrated contrast that varies depending on the material composition of the surface, there has been speculation about the underlying mechanism of contrast. One hypothesis on contrast formation from different materials is that due to different stiffnesses of material, they deform a different amount under the helium beam to create concave structures and that the different aspect ratios of the concave regions could 'focus' the helium atoms, leading to contrast.

The sample in the SHeM is under high vacuum, therefore the only significant pressure on the sample is due to the incident helium beam. Therefore it is reasonable to explore the deformation of the sample due to that beam pressure.

From Johnson & Johnson (pg. 57)[65] the vertical displacement caused by a uniform circular pressure on a surface is

$$\bar{u}_z = \frac{2(1-\nu^2)Pa}{E} \quad (3.45)$$

where a is the radius of the circle, E is the Young's modulus, and ν is Poisson's ratio.

For a single helium atom incident on the surface at 45° and with a outgoing direction with $P(\theta) \propto \cos \theta$ then the average impedance is

$$\langle \Delta p \rangle = mv_z^{\text{initial}} - mv_z^{\text{final}} \quad (3.46)$$

$$= mv \cos 45^\circ - mv \int_0^{\pi/2} d\theta \cos \theta (2 \cos \theta \sin \theta) \quad (3.47)$$

$$= mv \left(\frac{1}{\sqrt{2}} + \frac{2}{3} \right). \quad (3.48)$$

Thus the average pressure on the surface will be

$$P = \frac{\langle \Delta p \rangle \dot{N}}{A} = \frac{\dot{N}}{A} mv \left(\frac{1}{\sqrt{2}} + \frac{2}{3} \right) \quad (3.49)$$

where $A \sim 1 \mu\text{m}^2$ is the beam area and \dot{N} is the flux of atoms per unit time. The speed of the helium atoms is

$$\frac{1}{2}mv^2 = \frac{5}{2}k_B T \implies v = \sqrt{\frac{5k_B T}{m}} = 1.76 \times 10^3 \text{ms}^{-1} \quad (3.50)$$

Assuming a parallel beam then

$$\dot{N} = I_0 \frac{A}{\lambda^2} \quad (3.51)$$

where I_0 is the intensity of the beam in atoms per second per steradian and $l \approx 23$ cm is the distance from the source to the sample. Assuming no interference the beam intensity is[66]

$$I_0 = 0.36 P_0 d_{\text{noz}} (mk_B T_0)^{-\frac{1}{2}} \approx 5 \times 10^{21} \text{s}^{-1} \text{sr}^{-1} \quad (3.52)$$

where $P_0 \approx 75 \times 10^3$ Torr is the beam pressure, $T_0 = 300$ K is the beam temperature, and $d_{\text{noz}} \approx 1 \times 10^{-3}$ cm is the nozzle diameter. Then $\dot{N} \sim 10^{10} \text{s}^{-1}$.

The helium pressure at the surface of the sample is then $P \sim 0.2$ Pa.

Calculating the deformation for the Young's modulus² (take $\nu = 0$) of Chromium, Nickel, Gold, Platinum, and Silicon[67] (the surfaces imaged by Barr et al.) yields deformations on the lengthscale $\sim 10^{-18}$ m. The calculated deformation is many orders of magnitude smaller than what is predicted to be visible: an aspect ratio of between 1 in 100 and 1 in 1000 on a spot size of ~ 1 μm would give a minimum visible depression of $\sim 10^{-8} - 10^{-9}$ m. Even some of the lowest values of the Young's modulus, $E \sim 0.01$ GPa for Rubber[67], give depressions $\sim 10^{-14}$ m, far too small to be detectable.

Overall it is safe to conclude that where diffuse contrast dominates and with sources of comparable, or even significantly increased, intensity to present contrast due to the deformation of the beam will not be observable.

3.8 CONCLUSIONS

This chapter utilised integral implementation of the geometric contrast model presented at the start of chapter 2 in order to investigate specific questions about contrast in SHeM. Expressions were derived for the diffuse signal as a function of the size of the detector aperture, and the evaluation of those expression combined with definitions of the contrast to noise yielded a number of conclusions.

First, introduced in §3.3, is *contrast by partial masking*. Partial masking is where only part of the detector aperture is within line of sight of the element of sample surface, and that the visible proportion of the detector aperture can vary across the sample with the angle of the surface to the aperture. Where the detector aperture is relatively small, compared to a hemisphere, then partial masking results in the edges of masks being smudged out – which is neither particularly useful nor harmful and is the case in images published thus far both in Cambridge and Newcastle. When the detector aperture is large then partial masking behaves in a manner not dissimilar to that of diffuse contrast: the detected signal is dependent on the angle between the surface normal and the detector aperture with the highest signal when the angle is 0° .

²Values of E : Chromium = 248 GPa, Nickel = 170 GPa, Gold = 74 GPa, Platinum = 147 GPa, Chromium = 130 – 185 GPa.

Calculations of contrast investigating the size of detector apertures suggest that there are significant potential gains, equivalent to an order of magnitude of signal, to be made by increasing the size of detector apertures from those used in the A-SHeM. The results suggest that from a theoretical perspective the optimal size of detector aperture has a half cone angle $> 60^\circ$, and thus a full cone angle of $> 120^\circ$, therefore the limit on detector size is almost certainly going to be due to other considerations. In terms of contrast/signal, for diffuse scattering, the larger the aperture can be made, the better. In addition to the practicality of manufacture the ratio of pumping from behind the detector aperture to the ionisation region needs to be considered. It was noted in §2.3.3 that roughly 40% of the signal in the standard A-SHeM configuration is lost due to atoms escaping back out to the detector aperture. Pumping into the detector is discussed in chapter 4 where specific designs of pinhole-plate are considered.

It was noted that modest deviations away from a circular detector into an elliptical detector did not have any significant affect on the overall level of signal/contrast. Thus there is no need to strictly adhere to circular apertures for the purposes of signal/contrast – an advantage remains in the analytic relation between surface angle and signal derived in §3.2.1. The ability to enhance partial masking without the need for larger apertures is, however, something that could be considered in the future.

The consideration of the deformation of the sample under the beam strongly indicates that such deformation cannot currently contribute to contrast in SHeM, and can be ruled out as a mechanism for the contrast observed by Barr et. al[38].

Results from this chapter are taken forward in the next chapter where the designs of pinhole-plates are considered. In particular the relation between contrast and the detector aperture size is used to help optimise the designs.

In the Cambridge A-SHeM, one of the key components, as introduced in §1.4, is the *pinhole-plate* that mounts the pinhole membrane and defines the detector aperture. It can be considered the ‘core’ optical element of the microscope. Input on one side of the pinhole-plate is the beam produced by the skimmer (from the differential pumping chamber) and on the other is the stagnation volume leading to the detector. Both of these are connected via holes in the sample chamber wall. Within the constraints that the incoming beam hits the pinhole to form a collimated beam, that O-rings seal the back of the plate, and that the design allows for the mounting of the nano-positioning stages, the design can be very flexible. Without changing any other components of the A-SHeM, the spatial resolution, angular resolution, incidence angle, and the detection angle can all be modified by changing the pinhole-plate used. Thus, having multiple pinhole-plates allows the A-SHeM to operate in a modular manner.

While the discussion in this chapter focuses specifically on the practical design of components for the A-SHeM, many of the considerations discussed are of relevance to any existing, or proposed, helium microscope. The discussion starts with a detailed introduction to the pinhole-plate and highlights important factors that need to be considered in their design. In particular the methods for increasing the desired signal and reducing background signal are explored. Next, a set of calculations are presented that assist in the choice of pinhole size for a particular pinhole-plate design. Finally, three new designs for particular modes of operation that allow new experiments are presented: a plate that adapts the microscope to normal incidence, one that allows measurements with an improved angular resolution, and one that improves the spatial resolution. Measurements presented demonstrate beam widths of 750 – 1000 nm and a series of concrete steps are proposed in order to achieved widths of ≈ 500 nm. The normal incidence and angular resolution designs are critical pieces of instrumentation needed for the experiments presented in chapters 7 and 8.

4.1 ‘PINHOLE-PLATE’ DESIGN

4.1.1 *Anatomy of a pinhole-plate*

In order to facilitate an in depth discussion of the design of pinhole-plates for the A-SHeM, it is necessary to highlight some of the key components of the design. Figure 4.1 presents a technical drawing of the original A-SHeM pinhole-plate with key features identified, as listed below.

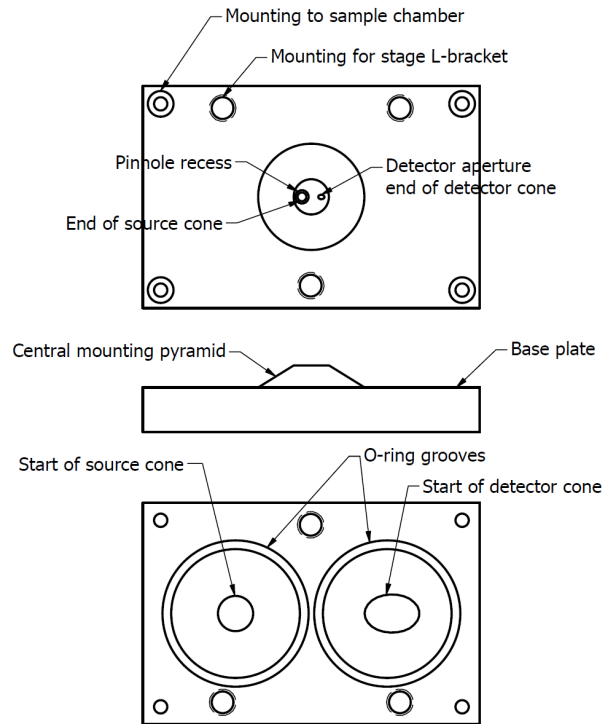


Figure 4.1: Key design features of the pinhole-plates for the Cambridge A-SHeM. Used as a model is the original pinhole-plate. The rear side of the pinhole-plate has fixed locations for the O-ring grooves and 4 outer mounting holes while the front side is constrained to have the 3 inner mounting holes and to keep a clear line of sight for the beam to hit the pinhole.

Source cone	A cone from the differential pumping that brings the skimmed beam to the back of the pinhole.
Pinhole recess	A recess at the end of the source cone for mounting the pinhole membrane.
Detector cone	An aperture leading to a cone that connects to the start of the detector stagnation region.
Base plate	The structural base of the pinhole-plate that mounts to the chamber wall.
Central pyramid	A central mounting pyramid that sticks out the base plate with the detector aperture and the pinhole recess in it. The location of these on the front of the cone determine the working distance and normal detection angle of the microscope.
O-ring grooves	Grooves to seal the source and detector cones using viton O-rings.
L-bracket mount	Tapped mounting for the L-bracket which holds the nano-positioning stages.

Mounting holes Mounting holes to allow the plate to be attached to the sample chamber.

The final three components are the same for all pinhole-plates designed for the Cambridge A-SHeM, while the others may vary. The O-rings are present to prevent leakage of helium gas from the differential pumping chamber to the sample or detector stagnation chambers. To test the sealing of the O-rings the end of the source cone was glued completely shut with vacuum leak sealant and the signal in the detector monitored with the beam on and off, no detectable leak was found. The four screw at the corners of the plate are used to screw it onto the chamber wall.

Of the components of the design that are fixed, of particular note are the mountings for the stage L-bracket, these are the three holes arranged around the central pyramid in figure 4.1. A large L-bracket is directly mounted from the pinhole-plate and the nano-positioning sample stage assembly is then mounted on the L-bracket. As a result the location of the sample, and the axes of motion of the sample, are defined relative top the front face of the pinhole-plate rather than being fixed to the overall chamber. The mounting of the sample and stage assembly from the pinhole-plate is relevant to adaptation to the design that allow for normal incidence in §4.3.

4.1.2 *New pinhole-plates*

Four new pinhole-plates have been designed to enable new modes of operation. The intentions are to be able to operate the A-SHeM in a normal incidence configuration, to improve angular resolution, and to improve spatial resolution. Success with the first design to improve spatial resolution has led to the 4th design which aims to improve the resolution beyond that presented here. In addition there are 2 'original' plates, one for the old A-SHeM sample chamber, and one for the new sample chamber. A list of all six plates discussed is given below

Original plate	The original plate, shown in figure 4.1, with a 10 mm thick base plate, a 2.1 mm perpendicular working distance, and narrow source and detector cones. Populated with a 1.2 μm pinhole.
New chamber	A pinhole-plate using the same basic dimensions as the original but designed for the new sample chamber, therefore having a 5 mm thick base plate, as do all plates designed for the new chamber. Populated with a 2 μm diameter pinhole this plate provides a baseline of 'good signal'. The same detector aperture/cone is used as the original plate, but a larger source cone is used, as it is for all the following designs.

- Normal incidence A enlarged plate that allows the sample manipulator to be mounted perpendicular to the beam. Accepts a 3 mm disc aperture, has a significantly reduced footprint of the central mounting turret, and uses a relatively larger working distance of 3 – 5 mm. Populated with a 5 μm pinhole.
- Angular resolution A pinhole-plate that reduces the solid angle of the detector aperture in order to improve the angular resolution. Has the pinhole and the detector aperture mounted on separate turrets to improve pumping. Accepts a 3 mm disc aperture. Populated with a 10 μm pinhole.
- 1mm WD A pinhole-plate that reduces the perpendicular working distance to 1 mm while maintaining the same detector aperture diameter. Accepts a 3 mm disc aperture and retains the circular shape of the central mounting turret. This represents approximately the smallest achievable working distance with a 3 mm disc pinhole membrane.
- 0.6mm WD Given the success of the 1 mm working distance plate, a plate that reduces the perpendicular working distance to 0.6 mm, as result the detector aperture is rotated 90° meaning it does not occupy a circular region of solid angle. It also has the sides of the mounting turret removed to improve pumping. Approximately the smallest achievable working distance with the 1 mm square aperture membranes.

4.2 DESIGN CONSIDERATIONS

4.2.1 Working distance

The working distance is the distance between the focusing element and the sample. As the pinhole is mounted into the front face of the pinhole-plate, which is normally at 45° to the beam axis, a distinction is made between the *beamline working distance* and the *perpendicular working distance*, also known as the *z distance*. The beamline working distance is the distance along the axis of the beam between the pinhole and the sample. The perpendicular working distance is the distance, along the axis normal to the sample, between the front face of the pinhole-plate, onto which the pinhole is mounted, and the sample.

The working distance will have a direct impact on the geometric spread of the beam, and thus the resolution[27, 68]. Larger working distances allow the beam to broaden to a greater degree due to the finite size of the virtual source. Therefore it is clear that in order to optimise resolution small working distances should be employed.

Although decreasing the working distance is optimal for improving the spatial resolution there are other factors to be considered. One practical limitation is that in order to operate at small working distance, the distance itself needs to be measured to a high accuracy in order to avoid collisions between the pinhole membrane and the sample – a method for more accurately measuring the working distance is given in §4.2.1.1. Similarly very small working distance will limit the ‘height’ of sample that can be imaged, else large protruding parts of the sample could collide with the pinhole. In addition small working distances will restrict pumping in the vicinity of the sample and make the mitigation of the multiple scattering and effuse backgrounds more difficult.

Overall working distances in the range of a few 100s μm are proposed. These will allow a decent depth of field as well as allowing samples with significant topography to be imaged straightforwardly. The reduction from the values used previously will allow improvements in the spatial resolution. Where the highest spatial resolution is not critical, working distances of a few millimetres may still make designs easier to implement.

4.2.1.1 *Measurements of the working distance*

One of the factors limiting the use of small working distances with the SHeM is the ability to measure the working distance accurately. Therefore a new process for measuring the working distance accuracy has been implemented. To that end the new A-SHeM sample chamber includes a CF16 port with a optically flat viewing window installed that is in plane with and placed directly above the sample-beam intersection. A compact USB microscope is set-up to take photos through the window.

The camera system is used to take a series of photographs of the sample at different z positions. The series of photographs is then used to plot a graph of the nano-stage encoded z coordinate against the separation between the sample and pinhole in the photos. The axis intercept of a linear fit then gives the datum for $z = 0$ which then allows any working distance to be known from the encoded z coordinate.

Accuracies between of 30 – 50 μm can be achieved for measurements of the perpendicular working distances with the new measurement process, thus allowing the use of significantly smaller working distances than could be achieved previously with manual inspection. Working distance of multiple 100 μm can be considered reasonable after the implementation of the new method.

Appendix H contains further details of the measurement process as a reference of for future users.

4.2.2 *Pinhole recess and membrane*

Any pinhole-plate must mount the pinhole. In the SHeM the pinhole is FIB milled into a thin silicon nitride membrane which is held in a scaffold. The scaffold is then glued into a small recess in the pinhole-plate. Two types of membrane are used; the standard 3 mm discs used in TEM, and smaller 1 mm square membranes that are snapped from a large array. The 3 mm discs have proven more reliable to mount in a pinhole-plate than the smaller and so are generally preferable for cases where smaller membrane sizes are not critical. However, large membranes constrain the placement of the detector aperture by occupying a significant fraction of the hemisphere around the sample. When larger working distances are used, $\gtrsim 1$ mm, the space occupied is not a significant impediment, but when small working distances are used placement of the detector aperture becomes difficult. Therefore to achieve perpendicular working distances much below ~ 1 mm the smaller membranes have to be used.

The purpose of the recess itself is to allow easy placement of the pinhole. Where working distances are critical, having a recess can inadvertently increase the working distance by having the pinhole recessed into the plate, this effect is seen in the results in §4.5. Therefore where minimising working distance it may be preferable to forego the recess, despite increased difficulty in placement of the membrane.

4.2.3 *Detector aperture*

One of the key conclusions of chapter 3 was that there are potential gains for contrast and signal from using very large detector apertures, and that the limit on the detector aperture size will be practical rather than reaching a theoretical limit. Another conclusion was that the exact shape of the detector aperture is not critical. However, if the aperture occupies a circular region of solid angle, it will maintain the cosine dependence of the signal, which may be desired in some circumstances.

In practice the primary limitation, for the A-SHeM, on the size of the aperture has been found to be the ‘backscattering’ of atoms out of the detector cone/stagnation region. Atoms that enter the detector may follow one of two paths: they may continue into the ionization region of the detector, or they may scatter out of the aperture back into the sample chamber. Increasing the size of the aperture will increase the probability of latter. §2.3.3 investigated the effect as a function of the z position of the sample and found that $\sim 50\%$ of the signal is lost with the original pinhole-plate.

The proportion of gas that makes it to the detector will depend on the back pumping from this region and the pumping speed to the detector. The pumping speed from the stagnation region to the detector was calculated to be 0.4 ls^{-1} [13]. The ratio of back pumping to forward pumping to the

detector will provide the amount of signal reduction as a result of scattering out of the detector cone.

Assuming gas stagnates a short distance behind the detector aperture the conductance back into the sample chamber may be approximated as the conductance of an orifice[69]:

$$C_O = 11.6FA \quad (4.1)$$

where A is the area of the orifice and F is a factor depending on the gas used, 3.5 for helium. Then the proportion of signal that will end up being detected is

$$p \sim \frac{0.4}{0.4 + C_O}. \quad (4.2)$$

The effect of the pumping can be combined with the effective signal increase due to an enlarged detector aperture considered in §3.6.1 to investigate if there is scope for improved signal with an enlarged aperture.

Significantly the formula for the conductances, and hence the impact on the detected signal, are function of the *area* of the detector aperture while the detected signal is a function of the *solid angle* of the detector aperture. Therefore an advantageous route to increasing the solid angle becomes moving the detector aperture closer to the sample, which does not require an increase in the area of the aperture. Figure 4.2 plots the effective signal increase, accounting for backscattering out of the aperture for two perpendicular working distances, the 2.1 mm of the original pinhole-plate and a 1 mm pinhole-plate (the calculation uses the RMS contrast to noise ratio). It can be seen that there is scope for up a $\times 2.5$ equivalent increase with the larger working distance while with the reduced working distance increases approaching an order of magnitude are possible.

The results in figure 4.2 clearly indicate that there can be a significant benefit from increasing the detector aperture size in the A-SHeM, but that it can only be realised with smaller working distances. The increased signal can be combined with the reduced beam spread with smaller working distances to improve the spatial resolution of the A-SHeM, a realisation of which is presented in §4.5

While the placement of the detector aperture does not directly affect the signal level it can have a significant impact on the nature of the contrast. Generally the placement will affect the form that the contrast takes (§2.4.2 considered this in some detail) and which features to emphasise, e.g. it can emphasise masking or reduce it, with the precise choice depending on what the operator wishes to be emphasised. If the plate is intended for general purpose imaging, a compromise between any extreme choice would be advisable.

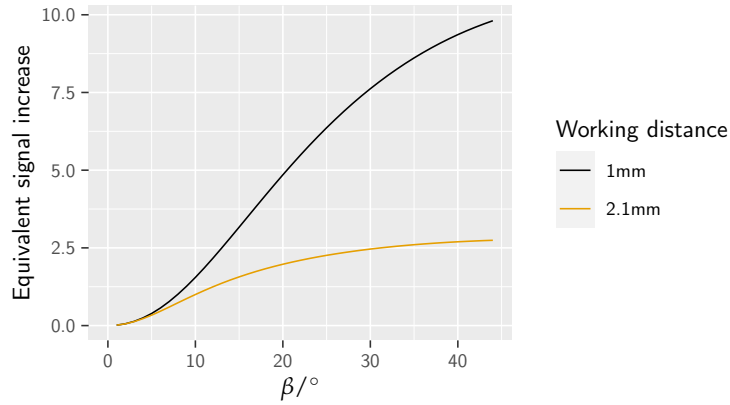


Figure 4.2: Once the backscattering out of the detector aperture is considered the equivalent signal increase from increasing the size of the detector will achieve at most a $\times 2.5$ increase with the use of a 2.1 mm working distance. Reducing the working distance to 1 mm, however, allows the gains of larger detector apertures to be realised. The RMS contrast to noise was used for the calculation.

4.2.4 Source cone

The source cone connects the pinhole to the differential chamber and allows the skimmed beam to be incident on the pinhole. In addition, to allow the beam to pass, the cone must also allow the gas deposited by the beam behind the pinhole to be pumped away. Therefore it is advantageous to make the source cone as large as possible. The original pinhole-plate had a relatively long thin cone (21 mm long with a wide end opening of radius 8 mm). When a new sample chamber was installed in the SHeM, a new pinhole-plate with equivalent detection conditions but a shortened and broadened source cone (14 mm long with a wide end opening of radius 15 mm) was manufactured for the new chamber. The broadened cone improves the pumping immediately behind the pinhole by a factor of ≈ 7 , calculated according to semi-empirical formulae developed by Mercier[70] (details can be found in appendix A). The new sample chamber also improves pumping in the differential chamber that the source cone attaches to. In the new chamber the pumping speed behind the pinhole is constrained mostly by the cone rather than the path through the chamber or the turbopump.

Two micrographs taken of a simple flat circular sample with both the old and the new pinhole-plates and sample chambers are presented in figure 4.3. A clear reduction in the effuse background signal can be seen. A comparison between the images and simulated data sets gives a reduction in the magnitude of the effuse beam contribution of 6 ± 1 , which is consistent with the change in conduction of the source cone. After the improvement it is estimated that the flux of the effuse beam is 50% the magnitude of the direct beam. A similar improvement in image quality was observed in the Newcastle SHeM with an enlarged source cone[12].

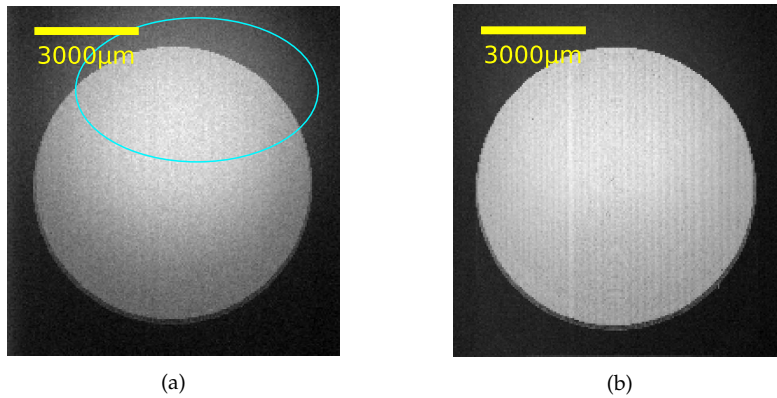


Figure 4.3: Micrographs taken, (a), with the old pinhole-plate in the old sample chamber, and, (b), with the a new pinhole-plate with an enlarged source cone in the new sample chamber. On the left a significant effuse beam is present – seen as the large smudge, highlighted in cyan – while on the right there is very little evidence of an effuse beam, although there is still evidence of the multiple scattering background. Comparisons with simulation suggest that the new configuration results in a reduction in intensity of the effuse beam of $2 - 3\times$.

While a significant reduction in the effuse background has been achieved there still remains some background signal that could impact quantitative interpretation of data. In addition there are designs of pinhole-plates that do not allow such generous cones, in particular the normal incidence design presented in §4.3 requires a much longer cone. Therefore if the effuse background is found to cause issues with future experiments an alternative approach will be needed. For both the A-SHeM and B-SHeM there is a port on the differential chamber to allow the placement of an aperture or slit in the beam and thus reduce the amount of helium incident on the back of the pinhole. For the results presented in this thesis further suppression of the effuse background was not considered necessary.

4.2.5 Pumping around the sample

Both the effuse beam and multiply scattered helium atoms result in a localised helium partial pressure near the sample that then diffuses into the detector. Improving the pumping around the sample is a clear way of reducing the intensity of these background signals. Improving the pumping by changing the sample mounting was shown to be effective in §2.4.1, however, this only consists of half of the space around the sample, and in some cases may not be practical: some samples are large and it may be unacceptable to break them up into smaller pieces. Therefore carefully designing of the front of the pinhole-plate becomes critical.

By removing material from the central mounting turret the pumping around the sample can be improved without putting restrictions on the sample size. Some of the approaches taken are presented in figure 4.4, designs C-E demonstrate improved pumping. Use of the normal incidence

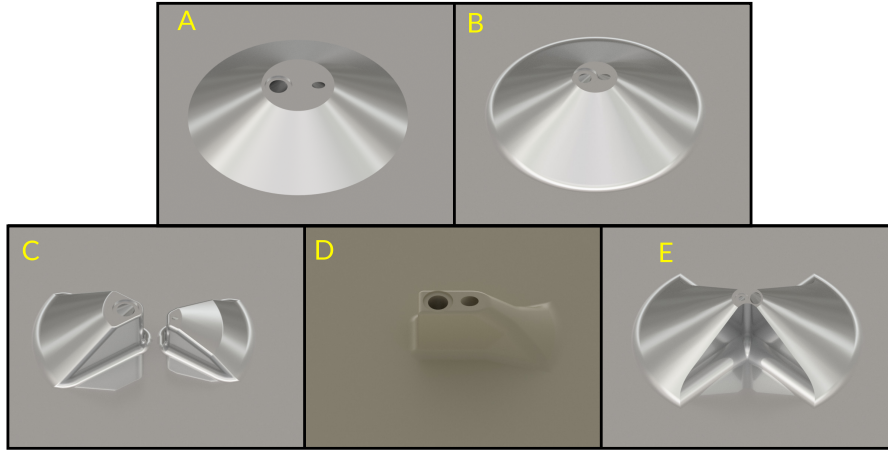


Figure 4.4: Renders of the central mounting turret of various designs of pinhole-plate for the A-SHeM. A is the original plate for both the old and new sample chamber, which has a large frontal facing area, B is a 1 mm working distance plate, used in §4.5, which also has a large frontal facing area. Designs C-E represent ways the frontal facing area of the pinhole-plate can be reduced by removing material. C is the high angular resolution plate, used in chapter 7, which can have the detector mounted on a separate turret as it is moved further away from the sample. D is the normal incidence plate, which can have a very small turret because the source cone goes directly down. R is a 0.6 mm plate proposed for future resolution improvements and represents an improvement from design B.

plate (model C) and the angular resolution plate (model D) have not presented issues with the slowly varying background signals that were present with the original configuration. A quantitative like-for-like comparison performed in Newcastle demonstrated a quantitative improvement through increased pumping around the pinhole-plate that was in agreement with predictions made by the ray tracing simulation[71].

4.2.6 Pinhole choice for new pinhole-plates

Various new pinhole-plates have been designed and one important consideration is the size of pinhole to be used with the new plates. Pinholes need to be chosen that are large enough to provide sufficient signal, while pinholes that are too large will cause an unacceptable degradation in the lateral resolution.

With cosine scattering it was shown, in §3.2.1, that the signal level with an aperture of half cone angle β and at an angle ψ to the surface normal is

$$I(\psi, \beta) = \frac{1}{2} \pi \cos \psi (1 - \cos 2\beta). \quad (4.3)$$

As the value of ψ will vary across the sample and will not change as a result of the detector location it is only the dependence on β that is of interest here, therefore it is appropriate to use

$$I(\beta) \propto 1 - \cos 2\beta \quad (4.4)$$

with

$$\beta = \arctan \frac{d_a}{2x} \quad (4.5)$$

where d_a is the aperture diameter and x is the distance from the sample to the aperture. Therefore the predicted signal level is

$$I \propto 1 - \cos 2 \arctan \frac{d_a}{2x}. \quad (4.6)$$

In addition to the change from the size of the detector aperture the pumping of the detector cone needs to be considered as it was in §4.2.3. Here two models of the pumping of the aperture are used: that of an orifice and that of a cone. The two models are considered to cover the possible range of conductances depending on far down the detector cone atoms initially pass (the formula of Mercier[70] are used – appendix A). It is assumed that the signal change that will occur due to the pumping, p , lie between the two extreme approximations,

$$\frac{0.4}{0.4 + C_{\text{cone}}} < p < \frac{0.4}{0.4 + C_O}. \quad (4.7)$$

The product of equations 4.6 and 4.7 will give the total signal change as a result of a new pinhole-plate set-up. Four pinhole-plates that require apertures are considered. The standard pinhole-plate used with the new sample chamber, populated with a 2 μm pinhole, is used as a baseline of signal – an arrangement that produces high quality SHeM images. The predicted signal level is plotted, for the four new designs, in figure 4.5 allowing a choice of an appropriate pinhole diameter to be made for each pinhole-plate. For the reduced working distance models the signal level is also considered for an increased source to pinhole distance (which reduces the angular source size) which is necessary for achieving resolutions significantly below those presented here – see §4.5.4 for details.

4.3 ENABLING NORMAL INCIDENCE

In SHeM the incidence angle has a significant effect of the micrographs that are produced, primarily through the image projection as discussed in §2.4.2. The standard configuration uses a 45° incidence angle providing a projection that appears to be viewed from an significant angle. However there are circumstances where an ‘top down’ image projection is more desirable. For example, the top down projection makes measurements of feature sizes in the plane of the sample simpler and is potentially more intuitive; a particular need for normal incidence arises in the application of 3D reconstructions that are discussed in chapter 8. Given the needs and advantages of normal incidence a pinhole-plate was designed and built to enable the A-SHeM to operate in a normal incidence mode.

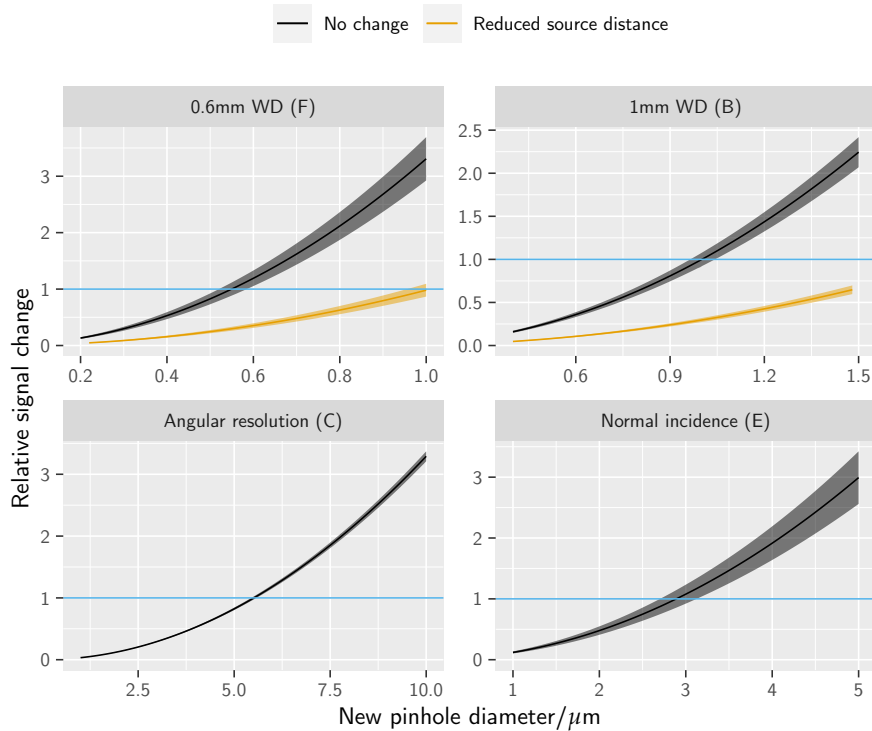


Figure 4.5: Changes in signal with different pinhole sizes for four new pinhole-plate designs. The ribbons represent the range of signals based on the two different methods for calculating the conductance of the detector cone. The signal level is normalised by that used by the previous ‘standard’ configuration. These plots can be used to choose pinhole sizes that will provide a suitable level of signal to noise for these pinhole-plates. For the two reduced working distance designs the signal level with the original source distance of 22 cm and an increased distance of 30 cm are shown.

There are, as demonstrated in figure 4.6, two key restrictions that the larger assembly of the A-SHeM imposes on the design of a pinhole-plate. First the collimated helium beam (highlighted in blue in the diagram), produced by the skimmer, is fixed. In order to produce an image, the beam needs to be incident on a pinhole, therefore the pinhole-plate needs to provide for a line of sight for the beam to hit the pinhole. Second the scattered helium atoms collected by the detector aperture must pass into the stagnation region to become detected (highlighted in red in the diagram). A third additional restriction is that the sample positioning stages must be mounted from the pinhole-plate and there must be sufficient space for them (alternative mounting from the chamber rather than pinhole-plate would be possible but is less desirable).

Given the relative freedom in design it is not difficult to conceive of a pinhole-plate that rotates the stage assembly by 45° to enable the sample to be at 90° to the beam. A visualisation of the concept is presented in the left panel of figure 4.6.

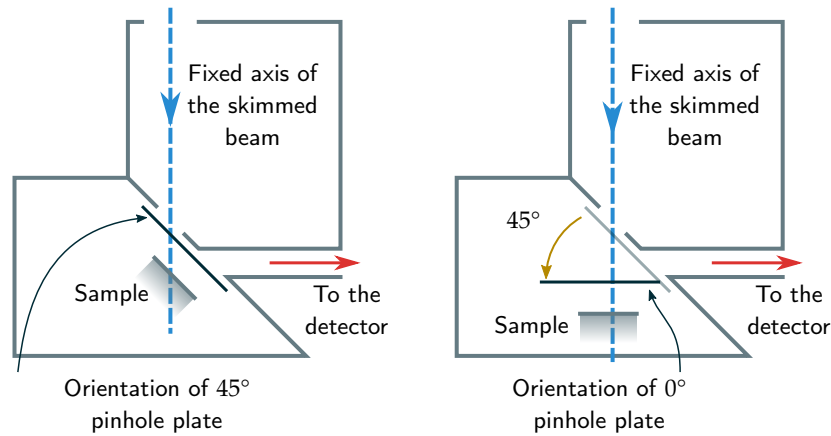


Figure 4.6: The fixed components of the A-SHeM: the skimmed beam and the tube to the detector. Provided the beam is incident on a pinhole and there is some route from the detector aperture to the stagnation region then any pinhole-plate will function. Therefore, by rotating the pinhole-plate orientation, and the sample that is mounted from the pinhole-plate, by 45° a normal incidence configuration can be achieved.

Figure 4.7 presents a photograph of the normal incidence pinhole-plate alongside a render of the plate within the sample stage assembly with the beam axis highlighted. Overall the normal incidence pinhole-plate presents a more complex part to be manufactured than the 45° plates presented here. Therefore high resolution plastic 3D printing was used over CNC machining. The pinhole-plate was vacuum baked (to prevent outgassing) and installed by A Radić[72].

The plate designed and shown in figure 4.7 uses a relatively modest detection direction – 38° from the surface normal – and detector aperture size due to its intended application for 3D reconstruction (see §8.4.1 for design recommendations for 3D reconstruction). In order to keep the detection angle modest it was necessary to keep the working distance large, $\sim 3 - 5$ mm, which puts a restriction on the achievable spatial resolution. It is important to note that these restrictions on the detector aperture were imposed due to the specific use case of the pinhole-plate and not fundamental limitation of normal incidence. In principle normal incidence would be well suited to improving resolution as the beam line working distance is $\sqrt{2}$ smaller than it would be for a 45° pinhole-plate with the same perpendicular working distance. A technical hurdle to be overcome however would be the measurement of that working distance, which cannot be measured using the camera set-up presented in §4.2.1.1 as the sample is not aligned with the chamber window.

To test the operation of the normal incidence plate, a sample containing a TEM grid and glass microspheres was imaged. A test image is presented in figure 4.8 alongside a similar image taken in a 45° configuration. The change in perspective between the images is clear, with the 45° case giving the impression of being viewed from the side while the normal incidence case appears to be viewed from above. The appearance of the images compares

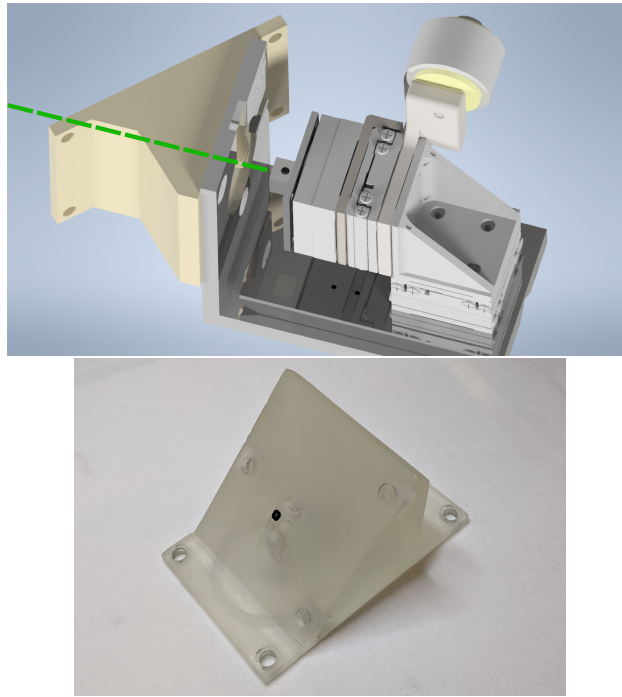


Figure 4.7: Top – render of the normal incidence plate within the sample stage assembly with the beam axis highlighted in green. Bottom – photograph of the 3D printed normal incidence pinhole-plate populated with a 5 μm pinhole aperture.

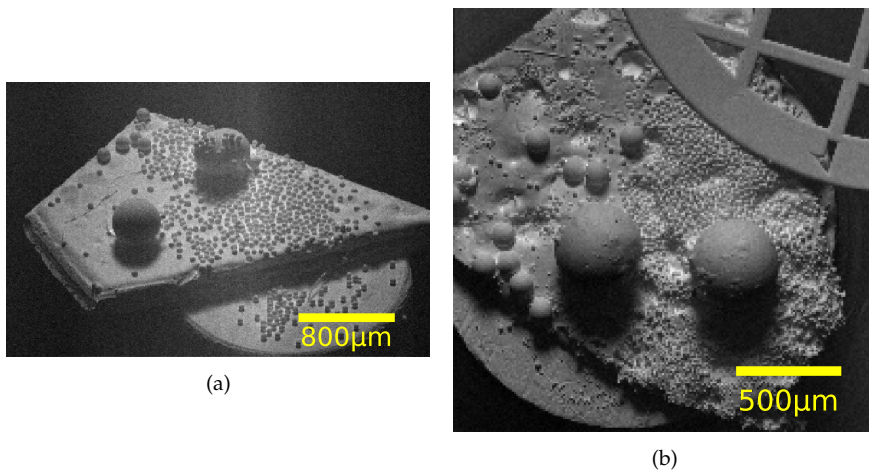


Figure 4.8: SHeM images of a selection of microspheres, (a) with a 45° incidence pinhole-plate, and (b) with the normal incidence pinhole-plate. The change of effective viewing angle is evident, with a clear perception that the sample is being observed from an angle in the 45° case while in the normal incidence case the sample seems to be observed from directly above. The data in (b) was collected by N. von Jeinsen & A. Radić.

favourably to the simulations of changing incidence angle presented in section 2.4.2.

4.4 IMPROVING ANGULAR RESOLUTION

In §4.2.6 it was highlighted that the average signal in SHeM is a function of the pinhole size and the detector aperture size. As a result a trade-off arises where only one or other of the pinhole diameter or the detector aperture acceptance angle can be made small while maintaining an acceptable level of signal. Thus configurations that are intended to achieve a high spatial resolution will have a poor angular resolution – how specific the angles of detection are – and configurations intended to achieve a high angular resolution will have a poor spatial resolution; traditional HAS apparatus may be considered one extreme of the spectrum. The previous standard configuration was a compromise that optimised neither, however as the exploration of the SHeM technique broadens more specialised ‘high angular resolution’ modes of operation are required. In particular, diffraction measurements presented in chapter 7 require an angular resolution that can resolve individual diffraction peaks.

Achieving improved angular resolution relies upon the detector aperture occupying a smaller region of solid angle. Reducing the solid angle may be approached in two ways: the aperture may be made smaller, or the aperture may be placed further away from the sample. For the pinhole-plate designed to perform measurements of diffraction from Lithium Fluoride the latter approach was used in addition to the former due to the difficulty of cleanly machining holes much smaller than 1 mm diameter. A cross sectional diagram of the high angular resolution pinhole-plate is given in figure 7.5 where the spot-profile diffraction measurements of Lithium Fluoride are discussed.

4.5 IMPROVING SPATIAL RESOLUTION

One of the aims of new pinhole-plate designs is to improve the spatial resolution of the SHeM without the need for significant changes to the overall machine. Reducing the working distance is the primary avenue for achieving higher resolution as it reduces the beam spread from geometric optics. As discussed in the previous section there is a trade off between spatial and angular resolution, in order to maintain signal levels the angular resolution must become poorer by using a larger detector aperture. Using smaller working distances allows detector apertures that cover larger regions of solid angle without a significant increase in the in the area (in mm^2) which prevents the pumping out of the detector cone becoming a problem.

Here the primary measure of resolution used is the *beam width* as a well defined physical property due to the term ‘resolution’ being somewhat ambiguous. The use of beam width is consistent with Bergin[27], Palau[58, 68], and Witham[60]. In general the beam FWHM (full width at half maximum) is used assuming a Gaussian shape.

4.5.1 Constrained optimisation

Two theoretical models have been developed for the prediction and optimisation of SHeM optics by Palau[58, 68] and Bergin[27], with Bergin showing that the methods are in agreement. Here the constrained optimisation using Lagrange multipliers of Bergin is used.

For the case of a pinhole, the beam width is determined to be a combination of the geometric pattern of the pinhole, the geometric spread due to finite source size, and Airy disc diffraction. Approximating each term as a Gaussian allows adding of the contributions in quadrature. The approach gives the formula for the beam standard deviation, for a normal incidence microscope, as

$$\phi = \sqrt{\underbrace{\left(\frac{d}{2\sqrt{3}}\right)^2}_{\text{geometric pattern}} + \underbrace{\left(\frac{\beta f}{\sqrt{3}}\right)^2}_{\text{geometric spread}} + \underbrace{\left(\frac{0.42\lambda f}{d}\right)^2}_{\text{Airy diffraction}}}. \quad (4.8)$$

The Cambridge SHeM generally operates in a 45° incidence mode, therefore the terms need to be modified for the ‘horizontal’ beam width¹:

$$\phi = \sqrt{\left(\frac{d}{2\sqrt{3}}\right)^2 + \left(\sqrt{2}\frac{\beta f}{\sqrt{3}}\right)^2 + \left(\sqrt{2}\frac{0.42\lambda f}{d/\sqrt{2}}\right)^2} \quad (4.9)$$

where λ is the helium wavelength, f is the working distance, d is the pinhole diameter, and β is the angular source size. Three factors of $\sqrt{2}$, shown in bold in equation 4.9, are introduced: one in the geometric spread term as the virtual source is 45° to the direction of scanning; and two in the diffraction term, one due to the scanning direction being 45° to the beam propagation direction, and a second due to the pinhole aperture being effectively $\sqrt{2}$ smaller as it is at 45° to the beam. Introduced factors of $\sqrt{2}$ cancel in the geometric pattern term. The angular source size can either be predicted or values can be taken from previous measurements. Predictions can be performed either assuming the virtual source is much larger than the skimmer diameter or from previous measurements of the angular source size. Where the source is assumed to be larger than the skimmer then the skimmer determines the angular source size as $\beta = r_{\text{skimmer}}/x$, with x being the skimmer-pinhole distance, measured to be $21.5 \pm 1\text{cm}$, and $r_{\text{skimmer}} = 50\ \mu\text{m}$. Previous measurements have recorded a $\sim 100\ \mu\text{m}$ angular source FWHM for beam pressures $\geq 60\ \text{bar}$ [14]. For a given working distance and desired

¹The beam width will be different in the ‘horizontal’ and ‘vertical’ scanning directions for non-normal incidence.

resolution the optimal configuration, that which provides the highest level of signal, consists of

$$d_0 = \sqrt{6}\sigma \quad (4.10)$$

$$\beta_0 = \frac{\sqrt{3}}{\sqrt{2}f} \left(\frac{\sigma^2}{2} - \frac{(0.84\lambda f)^2}{6\sigma^2} \right)^{\frac{1}{2}} \quad (4.11)$$

for the case of 45° incidence. A derivation of the constrained optimisation for non-normal incidence is given in appendix B.

4.5.2 Sub-micron beam width

A major step for the SHeM technique is to achieve resolutions smaller than a micrometer, which would make the resolving power comparable to the best optical techniques. Sub-micron imaging was achieved in the NAM[2, 60] using very small working distances, however the depth of field advantage that the SHeM possesses was lost. Separately, focusing of a helium beam below 1 micron has been demonstrated with Fresnel zone plates[26] at larger working distances, but zone plates have not yet been used to produce reflection-mode images. Here, the first beam widths of less than 1 μm with a large depth of field (defined to be multiple 100s μm) are presented, with a proposal for measurements with beam widths < 500 nm given. In order to reduce beam width a 1 mm perpendicular working distance pinhole-plate was tested with a 500 nm pinhole.

Beam widths are measured by moving a sharp edge beneath the beam using a very small step size. An error function, with an offset for the background signal b ,

$$I(x) = a \operatorname{erf}(x/\sigma) + b, \quad (4.12)$$

is fitted to the resulting intensity profile giving the beam standard deviation, σ . Assuming a Gaussian beam the full width at half maximum (FWHM) of the beam is $2\sqrt{2 \ln 2} \sigma$. The measured beam widths are presented in figure 4.9 alongside predictions based on assuming the skimmer diameter to be the virtual source and based on the previously measured virtual source size[14].

In the practical range of working distances the effective beam width is between 750 nm and 1250 nm representing an improvement of at least a factor of 2 on the previously used arrangements. While at smaller working distances reliable measures of sub-micrometre beam widths were taken.

Notable in figure 4.9 is the deviation between the predicted beam widths and both the current beam width measurements and the predictions based on previous source size measurements. It is reasonable, therefore, to conclude that the angular source size is larger than the simple model of treating the skimmer as the virtual source predicts.

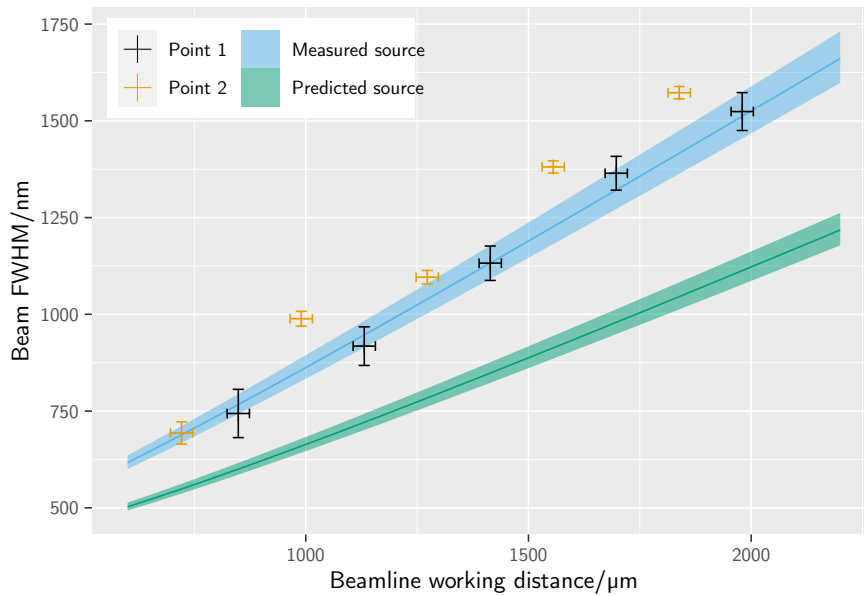


Figure 4.9: Measured beam FWHM, from two different points on the sample, in the horizontal scanning direction with the a 500 nm pinhole and a 1 mm z distance pinhole-plate. Working distances are quoted as true beamline working distances. The two predictions use both a theoretical angular source size and a measured one, the confidence intervals are from the error on the distance between the skimmer and the pinhole. A compensatory additional 100 μm z distance was added to the model to allow for the pinhole being recessed into the front of the plate.

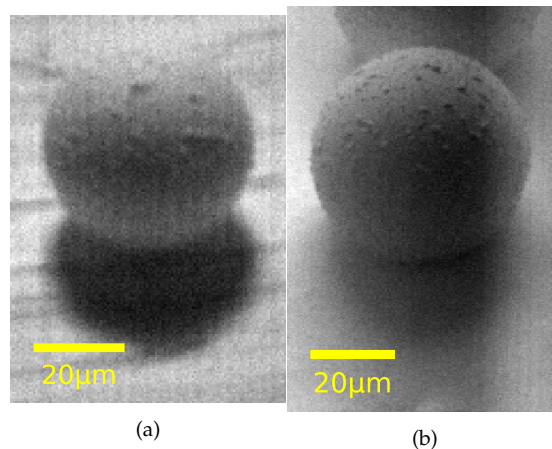


Figure 4.10: SHeM images of a small (nominally 50 μm) glass microsphere. (a) with the original SHeM pinholeplate, and (b) with the new high resolution pinhole-plate. The image in (b) is noticeably sharper than that in (a) demonstrating the practical improvements to imaging made by the new pinhole-plate.

Figure 4.10 presents two SHeM images, the first in the original configuration with a pinhole-plate with a 2.1 mm perpendicular working distance, and the second with the new high resolution pinhole-plate. The images demon-

strate that the improvement in resolution measured in figure 4.9 results in a significant practical improvement to micrographs taken in the A-SHeM.

If the intention was to aim for $\sim 1 \mu\text{m}$ resolution (sub-micron) at a perpendicular working distance of 1 mm, as was achieved in figure 4.9 then it is found that the optimum configuration would involve a 1040 nm pinhole with a source size that would correspond to a source to pinhole distance $\approx 5 \text{ cm}$ larger than is currently employed. Therefore it can be concluded that the current measurements are limited by the source size rather than the pinhole size. The results in figure 4.9 demonstrate what is achievable without any changes to the larger microscope. Any further improvements will require careful considerations of the source size.

4.5.3 The relation of beam width and resolution

The term ‘beam width’ is used as an unambiguous measure of the length scale at which the SHeM can resolve features, however it is not necessarily a measure of the ‘resolution’ which can be different to the beam width depending on the definition or resolution used.

The Rayleigh Criterion[73] states that the resolution is the distance from the centre of the Airy disc to the first minima of the diffraction pattern. Approximating an Airy disc as a Gaussian the standard deviation is $0.42\lambda f/d$, with the criterion being a distance of $1.22\lambda f/d$, 2.9 times larger than the standard deviation. The FWHM is 2.36 times larger than the standard deviation, thus the *Rayleigh resolution* is 23% larger than the FWHM.

Witham & Sanchez used a 12%-88% interval on a step edge to define their resolution, which is equivalent to measuring the FWHM. They achieved 350 nm FWHM at very small working distances of 10 – 30 μm [60].

4.5.3.1 Minimum resolvable feature

The size of the minimum resolvable feature is related to the width of the helium beam but is not necessarily equal to it. It is, therefore, informative to briefly consider the relationship between the beam width and resolvable feature size. As an example linear features are considered in principle and experimentally.

Consider a thin strip of dark on light, such as the mask cast by a step edge, that is smaller than the beam width by a factor n . Define the minimum resolvable feature to be the point where the contrast is twice the level of the noise. With I_f the ‘dark’ intensity of the feature and I_s the ‘light’ intensity of the surroundings then (assuming a circular beam) the observed intensity, I_o , is:

$$I_o = F(n) I_f + [1 - F(n)] I_s \quad (4.13)$$

$$F(n) = \frac{2}{\pi} \left(\frac{1}{n} \sqrt{1 - \frac{1}{n^2}} + \arcsin \frac{1}{n} \right) \quad (4.14)$$

with $F(n)$ being the fraction of the area of the feature under the beam, and n being the feature size over the beam diameter. Derivation of these formulae can be found in appendix C.

To 'resolve' a feature requires the difference in intensity to be $2\times$ the FWHM noise level (the noise level from the line scans used to generate figure 4.9 were used). Inverting equations 4.13 and 4.14 gives the width of a resolvable feature that is 37% the width of a circular beam, or equivalently 54% the FWHM of the beam. Thus features approximately half the beam width can be resolved.

An example of the ability to resolve features smaller than the beamwidth is given in figure 4.11 where step edges of 300 nm (that create masks 600 nm width) are observable with a relatively broad beam width of $\sim 2\ \mu\text{m}$.

4.5.4 Further improvements

The results in §4.5 give an improved lateral resolution in the A-SHeM, however they also demonstrate that those measurements of resolution were primarily limited by the virtual source size. Therefore any further improve-

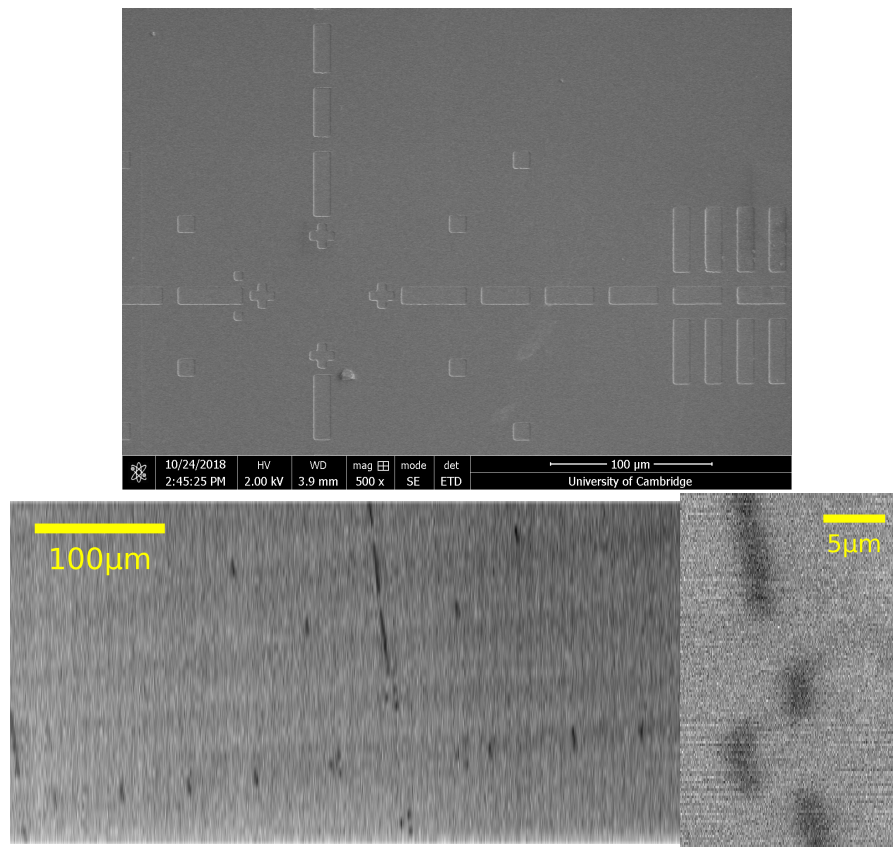


Figure 4.11: Top – an SEM micrograph of the sample showing the topography of the sample. Bottom – SHeM micrographs of shallow depressions in a surface, the height of the steps are 300 nm which case masks of width 600 nm, and therefore the features being resolved are less than half the width of the beam (beam FWHM used $\sim 2\ \mu\text{m}$).

ments in lateral resolution would require a reduced virtual source size. A practical way of reducing the source size is to move the source further away from the sample, however this occurs at the expense of signal – the intensity follows an inverse square law with the source-sample distance. In addition, given the success of the 1 mm plate and the new camera set-up, the working distance could be reduced further. In order to realise these proposed changes a pinhole-plate with a 0.6 mm working distance has been designed.

A 0.6 mm perpendicular working distance gives a 0.85 mm beam line working distance. Aiming for a beam FWHM of ~ 500 nm gives optimal values for the pinhole diameter of 520 nm and for the optimal source size an increase from the current source distance of ≈ 18 cm. From figure 4.5 it can be seen that there would be a loss of signal by a factor of ~ 4 compared to the previous arrangement with a ‘good’ signal level, which is comparable to the signal level seen for the sub-micro resolution measurements presented in §4.5 and therefore is a realistic aim. Work by N von Jeinsen has implemented a 0.6 mm working distance plate of the design proposed and shown that with appropriate changes to the source distance beam-widths of ≈ 500 nm can be achieved[74]. Corresponding to a minimum observable feature size of ~ 250 nm.

4.6 SUMMARY

Presented in this chapter was a modular use of the ‘pinhole-plate’, the defining optical component of a SHeM. Various design considerations of the component have been considered, such as the pumping around the sample and how the relative contribution of the effuse beam can be controlled. In addition the impact of the detector aperture size on the signal level was considered in detail allowing informed choices of the size of pinhole to be used in different SHeM configurations.

The flexibility of the modular approach was demonstrated by creating pinhole-plates suited to three new imaging modes for the SHeM without changes to the rest of the instrument. First a normal incidence configuration was designed and demonstrated effective. Second a high angular resolution configuration was presented, enabling the results on diffraction presented in chapter 7. Finally the spatial resolution of the A-SHeM was improved with changes to the pinhole-plate only: beam widths $< 1 \mu\text{m}$ were measured. The results from the improvement in spatial resolution indicate an arrangement that is dominated by the virtual source size and therefore proposals for future increases in resolution were made in line with a more optimal configuration.

Overall the importance of the relatively modest component of the SHeM that defines the geometry around the sample has been heavily underlined. Any future helium microscope must consider the design of the pinhole-plate or equivalent component carefully.

Plate name	Purpose	Detector half cone angle	Perpendicular WD	Populated pinhole
Original plate	General purpose imaging without specialisation	10°	2.1 mm	2 µm diameter disc membrane
Normal incidence	To operate the SHeM with normal incidence allowing 3D reconstructions. Has a detection angle of 38° at the design working distance.	10°	3 mm	5 µm diameter disc membrane
Angular resolution	To improve angular resolution sufficiently to resolve diffraction peaks.	3°	2 mm	10 µm diameter disc membrane
1 mm WD	To enable improvements in spatial resolution, with beam widths below 1 µm.	19°	1 mm	500 nm diameter disc membrane
0.6 mm WD	To enable, in combination with an increased source distances, improvements in spatial resolution, with beam widths below 500 nm.	35°	0.6 mm	470 nm diameter square membrane

Table 4.1: Some key parameters of the pinhole-plates designed in this chapter, including the original style pinhole-plate for the new sample chamber is included.

A significant question for the field of helium microscopy is to find out what the most common mechanism of contrast is. Following on from the discussions in chapter 2 the question required to be answered to explain contrast is ‘what is the default scattering distribution in the SHeM?’ Surface studies using helium atom scattering (HAS) have shown that many different scattering mechanisms processes are possible, for example atom diffraction[6], pure specular reflections[21], rainbow effects[75], as well as various inelastic processes[10, 76]. A significant difference between the majority of these studies and the majority of samples imaged in the SHeM is the level of sample preparation and the condition of the surfaces. HAS has generally been applied to pristine single crystal samples that have been cleaned *in situ*, whereas in SHeM, images are typically taken of unprepared surfaces that are unlikely to be ordered on any meaningful scale. Such surfaces are referred to as *technological surfaces*. Thus understanding how helium atoms scatter from technological surfaces is a key question in the emerging field of helium microscopy.

In this chapter a series of measurements are presented of the scattering distribution obtained directly in the SHeM, with a cosine model shown to be close to the experimental data; in addition a brief discussion of the key contrast features from ‘diffuse topographic contrast’ is given. Observation of the same features of diffuse contrast from a number of different studies, combined with the quantitative data presented, enables the conclusion that a ‘cosine-like’ distribution should be expected by default in SHeM. At the end of the chapter a brief discussion is made on the scattering of atoms from rough surfaces, that provides an initial attempt to gain understanding of the causes of the diffuse distribution observed.

5.1 HELIUM SCATTERING DISTRIBUTION FROM TECHNOLOGICAL SURFACES

5.1.1 *Potential scattering models*

For disordered surfaces there are three primary models for the scattering of an incident beam of atoms:

1. True diffuse scattering with a cosine distribution centred on the surface normal, where there is no correlation between incoming and outgoing directions. Known from gas atoms as Knudsen’s law[54] and as Lambert’s law for light[53].

2. A broad specular scattering, with atoms being scattered in many directions but with a bias for the specular direction. Such scattering may be expected for a mirror surface that is somewhat disordered.
3. Diffuse scattering with a significant backscattered component, which can occur where the surface roughness is very large.

A study of the scattering of atomic beams from macroscopically rough surface by O’Keefe & Palmer[77] presents evidence for all three models. However the macroscopic roughness used in their experiments would be resolved as topography in SHeM, as investigated by Bergin[14]. Therefore investigations have been undertaken using the SHeM to ascertain which model is the dominant scattering mechanism. There are a some advantages to performing the measurements directly in SHeM. First HAS instruments are, in general, not designed to do the (relatively) low resolution measurements over a large range of detection conditions that are required. Second there may be a difference in the level of order between the $\sim 1 \mu\text{m}^2$ spot size of the SHeM and the $\sim 1 \text{mm}^2$ spot size of modern atom scattering apparatus. Third the different levels of vacuum may also affect the results; HAS is generally performed under good UHV while SHeM operates in un-backed HV – the greater number of contaminants in HV, in particular water, may change the level of order of measured surfaces. Conversely the SHeM is not designed to perform scans through detection angle so the choice of angles to measure at is not as free, data interpretation requires extra steps, and the angular resolution is poorer.

5.2 USING MICROSPHERES TO MEASURE SCATTERING DISTRIBUTIONS

As the SHeM is not set up to perform scans of detection direction an alternative approach is taken to acquire scattering distribution information: 2D images of microspheres provide information on lots of different incidence and detection conditions. The basic concept is presented in figure 5.1 where a helium beam is scanned across a sphere causing the incidence and detection angles to change. The microspheres have an advantage over the alternative approach, scanning the detection angles using z scans as introduced in §2.3.3, as the transmission probability of the detector cone does not change and there is no variation in the various background helium signals across the data set.

A set of standard glass microspheres were imaged¹ in three diameters, 50 μm , 100 μm , 400 μm , both with and without a thin, sputtered, gold plating. The 50 μm and 100 μm diameter spheres are small enough that changes in detection probability across them can be ignored. However 400 μm spheres are large enough to have meaningful changes of detection probability across

¹The spheres were Monodisperse Standards from Whitehouse Scientific, MS0009, MS0026, MS0049, MS0114, & MS0406, www.whitehousescientific.com/category/monodisperse-standards?c341c912_page=2.

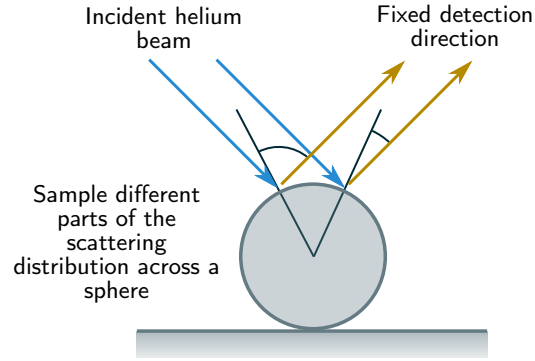


Figure 5.1: As the helium beam moves across a sphere the detection and incident angles changes allowing us to gather data on the scattering distribution of the surface of the sample. The concept extends to the whole 3D surface of the sphere.

them and are therefore useful only for comparisons via ray-tracing simulations.

5.2.1 Qualitative comparison

Figure 5.2 presents SHeM images alongside equivalent ray tracing simulations of 400 μm microspheres for two working distances and two different surfaces: the sample was imaged twice, the second time coated with a thin coating of gold. Ray tracing simulations were performed for both a pure cosine model and a broad specular distribution.

The broad specular model uses a Gaussian centred on the specular condition combined with a cosine term to account for the surface area projection. The probability of scattering in a direction \mathbf{d} with an angle θ to the specular condition and an angle ψ to the surface normal is,

$$P_{3D}(\mathbf{d}) \propto \cos[\psi(\mathbf{d})] \sin[\theta(\mathbf{d})] \exp\left[\frac{-\theta^2(\mathbf{d})}{2\sigma^2}\right] \quad (5.1)$$

$$\theta(\mathbf{d}) = \arccos(\mathbf{d} \cdot \mathbf{d}_S) \quad (5.2)$$

$$\psi(\mathbf{d}) = \arccos(\mathbf{d} \cdot \hat{\mathbf{n}}) \quad (5.3)$$

where \mathbf{d}_S is the vector in the specular direction. The distribution has a single parameter σ , which in the limit of narrow distributions will be the standard deviation of the distribution. For the simulation 50% of the signal was set to be diffuse and 50% to be broad specular with a parameter value of $\sigma = 30^\circ$ was used, which corresponds to a standard deviation of 24° for the resulting distribution – the distributions used in the simulation are represented in 2D in figure 5.3. A mix of ‘specular’ and ‘diffuse’ scattering was considered to represent a mix of ordered and random scattering, the width of the specular was chosen as approximately the broadest it can be while maintaining a clear specular peak. Broader distributions could be used but would no longer have

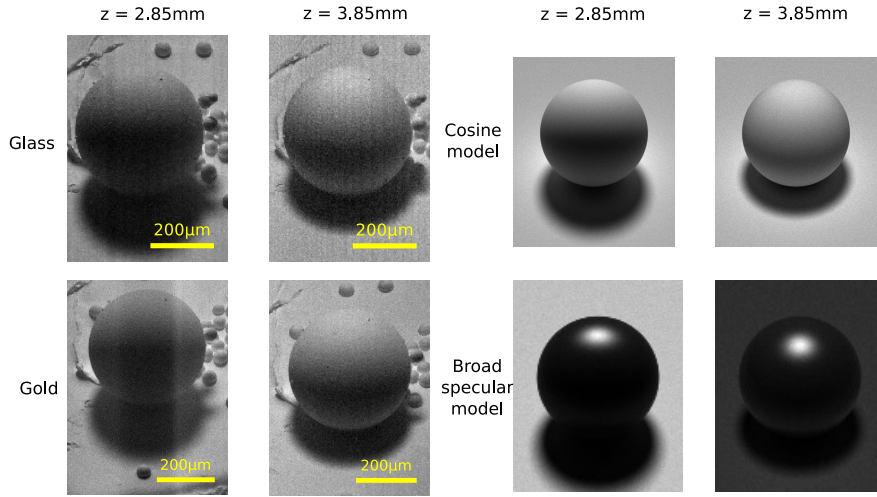


Figure 5.2: SHeM images of $400\ \mu\text{m}$ spheres and comparisons with equivalent ray tracing simulations with both cosine scattering and a broad specular scattering model. Good qualitative agreement is seen between the experimental data and the simulation, with both displaying slowly varying contrast across the surface of the sphere as well as strong contrast arising from masking. The strongest contrast in the case of the broad specular scattering is not masking, but instead is the specular highlight (which includes the flat surface for the $z = 2.85\ \text{mm}$ case).

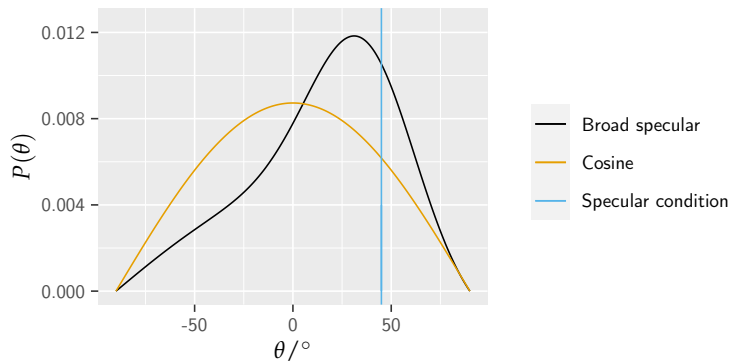


Figure 5.3: A 2D representation of the scattering distributions used in the ray tracing simulations presented in figure 5.2.

a well defined peak, and might more accurately be termed ‘diffuse scattering with a forwards bias’.

Good qualitative agreement can be seen between the cosine simulations and the experimental data, as well as between the two sets of experiments, despite the surfaces being composed of very different materials: the intensity peaks are in the same place and the gradients in intensity all follow the same trends. Notably the slowly varying intensity across the surface of the sphere that is weakly peaked towards the detection direction – upwards in the figure – with some of the strongest contrast arising due to masking of the detector. In addition the experimental images are very different in appearance to the simulated images assuming a broad specular distribution, where strong

peaks in intensity are seen at the specular condition. Masking being a strong contrast mechanism is evidence for a slowly varying scattering distribution, if there were strong peaks in the distribution then contrast from different surface orientations would dominate.

The agreement seen in figure 5.2 is strong evidence for a slowly varying scattering distribution that is peaked closer to the surface normal than specular. However, it only demonstrates qualitative alignment with results that assume the Knudsen cosine model. In order to quantitatively test the agreement with that specific model the scattering angles across the sphere must be extracted.

5.2.2 Scattering distributions from spheres

5.2.2.1 Derivation of angular relationship

In order to make quantitative use of data on spheres the relationship between the coordinates, X, Y , in an image need to be converted into the incidence angle Θ and the detection polar and azimuthal angles θ, ϕ . A vector approach is taken in the native coordinate system of the image projection, x, y , which has the z axis parallel to the incidence beam. The derivation of the relationships assumes that the sphere is small and therefore changes to the detection conditions across the sphere are negligible.

The Cartesian coordinate system used is shown in figure 5.4, relative to the spherical sample and the basic instrument geometry, with the z axis parallel to the beam making the (x, y) coordinates equivalent up to a linear transformation to the scan coordinates (X, Y) . In this coordinate system, assuming spheres of negligible size, there is a constant vector to the detector, $\hat{\mathbf{d}}$, what must then be derived is the local normal vector of the sphere $\hat{\mathbf{n}}(x, y)$. The combination of the two vectors can fill in parts of the scattering distribution: in the simplest case the polar angle is

$$\theta(x, y) = \arccos \left[\hat{\mathbf{d}} \cdot \hat{\mathbf{n}}(x, y) \right], \quad (5.4)$$

which will allow comparison to the cosine distribution for completely random scattering.

Consider a sphere of radius r , with its centre on the origin, as shown in 5.4. At a distance R from the centre of the sphere, on the positive z hemisphere, the unit normal will have a component in z of magnitude $\sin \left(\arccos \frac{R}{r} \right)$ and a component in the (x, y) plane radially away from the centre of the sphere of R/r . Then

$$\hat{\mathbf{n}} = \begin{pmatrix} x/r \\ y/r \\ \sqrt{1 - \frac{x^2 + y^2}{r^2}} \end{pmatrix}. \quad (5.5)$$

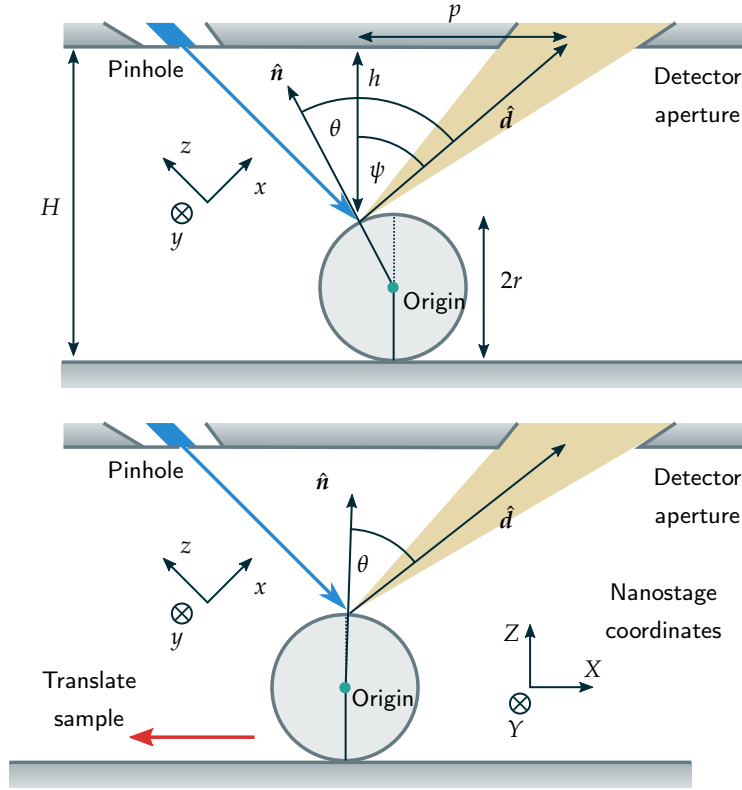


Figure 5.4: Co-ordinate system and vectors used in the derivation of the relation between image positions and incidence and detection angles. \hat{d} is the vector from the sphere to the detector, and \hat{n} is the unit normal to the sphere at the beam-sphere intersection point. The coordinate system is defined to have the z axis parallel to the beam and the origin at the centre of the sphere. The distance from the scattering point to the pinhole plate h does vary across the sphere but can be neglected for small enough spheres.

Next the vector from the sphere to the detector needs to be acquired. Using the variables from figure 5.4:

$$\hat{d} = \begin{pmatrix} \cos\left(\frac{\pi}{4} - \arctan\left(\frac{p}{h}\right)\right) \\ 0 \\ \sin\left(\frac{\pi}{4} - \arctan\left(\frac{p}{h}\right)\right) \end{pmatrix}. \quad (5.6)$$

The (x, y) coordinate system used here has the same y axis as the nanostages. The x axis is not the x direction of the stages, but a linear scaling can be applied to the stage positions X , to find the image coordinate x . Note that $\arctan\left(\frac{p}{h}\right) = \psi$. A full description of the scattering distribution is a function of the incident angle to the surface, which can be calculated using the local surface normal above and the incident beam direction,

$$\hat{e} = (0, 0, -1), \quad (5.7)$$

thus the incidence polar angle, Θ is

$$\Theta(x, y) = \arccos \left(-\sqrt{1 - \frac{x^2 + y^2}{r^2}} \right). \quad (5.8)$$

Assume that the surface is isotropic so it is possible to ignore the incident azimuthal angle, Φ . The outgoing polar angle is

$$\theta(x, y) = \arccos \left[\frac{x}{r} \cos \left(\frac{\pi}{4} - \psi \right) + \sqrt{1 - \frac{x^2 + y^2}{r^2}} \sin \left(\frac{\pi}{4} - \psi \right) \right] \quad (5.9)$$

which leaves the outgoing azimuthal angle, ϕ , which is the angle between the specular direction and the detector direction. The specular direction is

$$\hat{s} = \hat{e} - 2(\hat{e} \cdot \hat{n})\hat{n} \quad (5.10)$$

and the azimuthal angle is the angle between the \hat{d} and \hat{s} vectors in the plane normal to \hat{n} . Projection onto the plane can be performed by subtracting the component of the vector that is parallel to the normal vector. Using bar to denote the projected vectors:

$$\bar{u} = u - \frac{u \cdot \hat{n}}{\|\hat{n}\|^2} \hat{n}, \quad (5.11)$$

which must then be normalised, gives the azimuthal angle as

$$\cos[\phi(x, y)] = \bar{s} \cdot \bar{d} \quad (5.12)$$

$$= \frac{1}{\|\bar{s}\| \|\bar{d}\|} [\hat{s} - (\hat{s} \cdot \hat{n})\hat{n}] \cdot [\hat{d} - (\hat{d} \cdot \hat{n})\hat{n}] \quad (5.13)$$

$$= \frac{1}{\|\bar{s}\| \|\bar{d}\|} [\hat{s} \cdot \hat{d} - (\hat{d} \cdot \hat{n})(\hat{s} \cdot \hat{n})]. \quad (5.14)$$

Thus the scattering distribution information can be derived from a SHeM image of a sphere. The general scattering distribution extractable is a function of three variables: $I(\Theta, \theta, \phi)$ and it should be noted that only a small part of the total space will be sampled. It can be directly compared to potential models of scattering without the need for ray tracing simulations.

A helium micrograph of a sphere has been isolated in figure 5.5 and the corresponding detection angles labelled to demonstrate the process of extracting the scattering distribution.

5.2.2.2 Results

Figure 5.6 plots the extracted scattering distribution information as a function of the polar detection angle for a 100 μm glass sphere imaged at two different working distances, both with and without a gold coating. The results clearly demonstrate the broad nature of the underlying scattering distribution with atoms being sent into trajectories at all possible outgoing polar angles. Therefore, it is safe to conclude that *diffuse* scattering is occurring. In the plots there

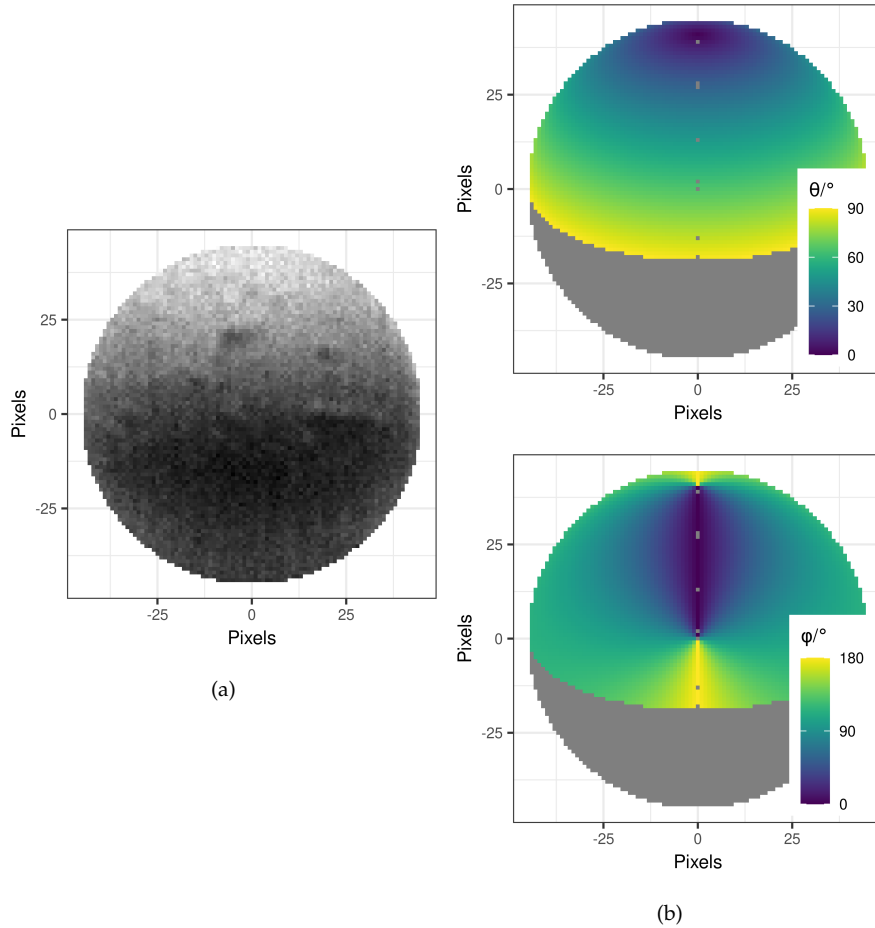


Figure 5.5: The angles of detection across a microsphere image. (a) shows a SHeM image of a sphere plotted as a function of the pixels (x, y) . (b) shows a heatmap of both the polar, θ , and azimuthal, ϕ , detection angles. The ϕ plot demonstrates that there is scattering into many different azimuths, including both forwards, backwards, and out of plane scattering. The grey regions do not have direct line of sight to the detector and so are excluded from the analysis.

is also strong evidence that the distribution is peaked near to the surface normal. Overall the data strongly indicates an *cosine-like* distribution with diffuse scattering in all directions and a greater intensity scattered normal to the surface.

The data as presented in figure 5.6 however, does not consider one of the major models of scattering from rough surfaces: that of backscattering.

5.2.2.3 Considering backscattering

An opposing model to the cosine distribution is one where a significant number of atoms are scattered back in the incidence direction due to a very rough surface. The plots presented in figure 5.6, cannot be used to consider that model because they use only the polar detection angle, which by definition only extends from 0 to $\pi/2$. As the three dimensional parameter space is not fully sampled using the current method it is not feasible to compare to the

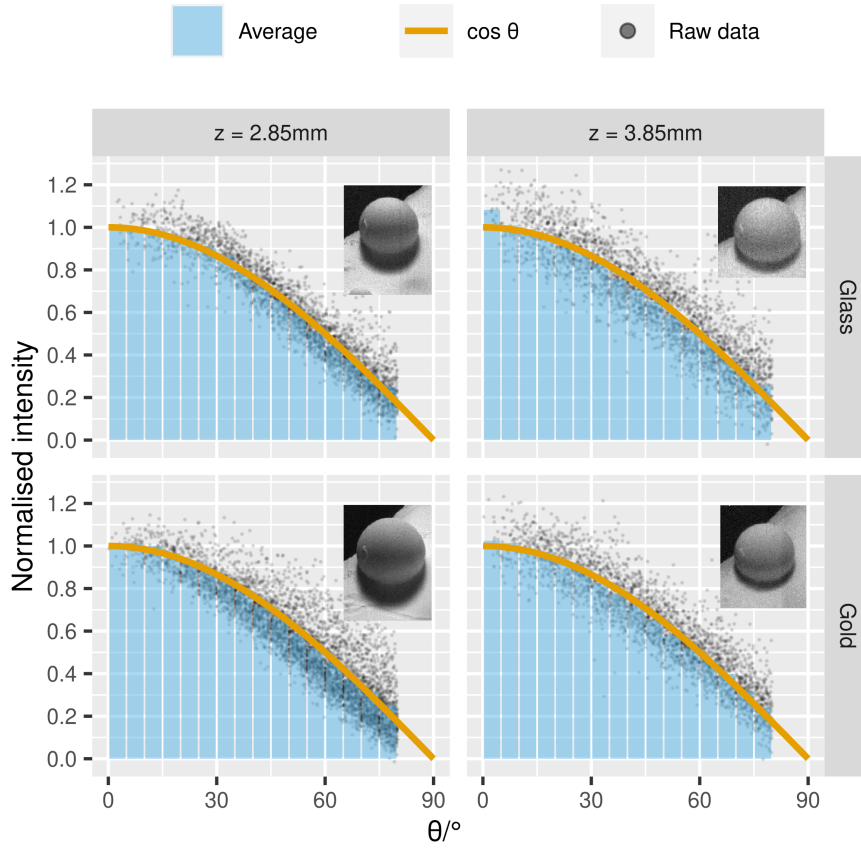


Figure 5.6: Extracted scattering distributions from the 100 μm sphere, both with and without gold plating. The data is normalised by fitting a cosine curve to the averaged data. It is clear that the atoms are scattered in a broad diffuse distribution with a stronger tendency for scattering close to the surface normal.

proposed model in the full parameter space. However, an approach can be taken where the outgoing azimuthal angle is used to distinguish between ‘forwards’ and ‘backwards’ scattering, effectively condensing θ, ϕ detection space into $-\pi/2 < \psi < \pi/2$ for a particular incidence condition. The new angle ψ is defined thus,

$$\psi = \begin{cases} \theta, & |\phi| < \pi/2 \\ -\theta, & |\phi| > \pi/2 \end{cases} \quad (5.15)$$

where the outgoing azimuthal angle, ϕ , is defined in the range $-\pi < \phi \leq \pi$. In figure 5.5 the range of $|\phi|$ is plotted across an image of a sphere, it can be seen there that there are significant regions of the image where $\phi > \pi/2$, implying backscattering. Figure 5.7 presents a diagram demonstrating how scattering of certain points on the sphere leads to a measurement of backscattering. Thus more information than simply the polar angle can be extracted and compared to the cosine model, which, given it is independent

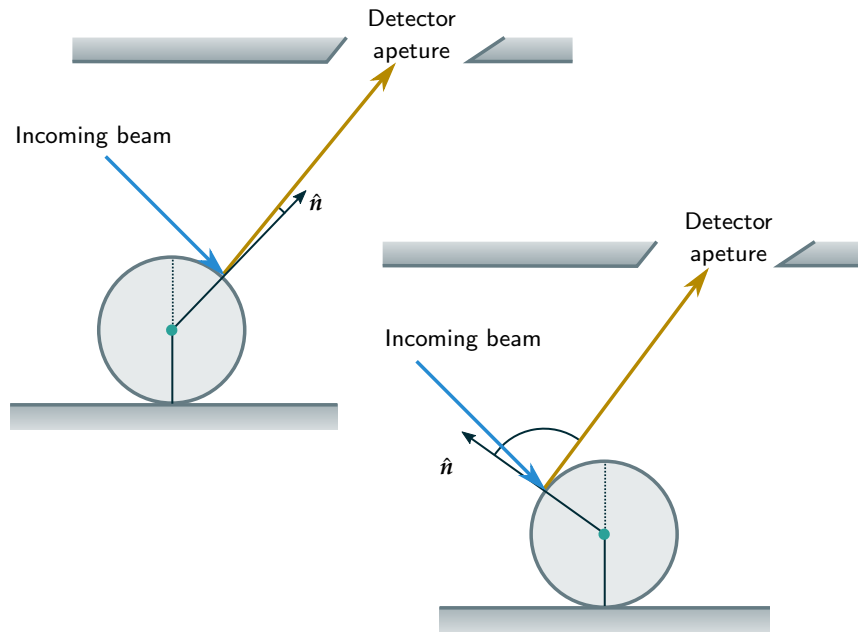


Figure 5.7: A diagram demonstrating how scattering of certain regions of a sphere leads to a measurement of backscattering – the definition of backscattering is that the atoms are scattered into the same half of the hemisphere as they were incident upon (or $|\phi| > \pi/2$). The two examples here demonstrate the effect along the centre line of the sphere, less extreme values of ψ are achieved through out of plane scattering.

of incident angle, does not distinguish between forwards and backwards scattering. It must, however, be remembered, when considering the plots that include negative ψ , that they are condensing a significant amount of out of plane scattering onto a single dimension.

Figure 5.8 presents the extracted scattering distribution information with the backscattering filter applied. Overall the agreement is still good compared to the cosine model with the peak in the distribution being close to the surface normal. None of the data sets present evidence of strong backscattering, meaning that the cosine-like diffuse scattering model holds. There is, however, for the gold sphere case for $z = 2.85$ mm evidence of slightly more backwards scattering than forwards scattering. Due to the level of noise in the data there is not much that can be concluded from this observation, but the effect is seen to be weak and does not significantly shift the peak in the resulting distribution. Overall the results are still reasonably consistent with the cosine model.

5.3 DISCUSSION

Two different materials were used to acquire the data used to come to the conclusion of a cosine-like distribution, which makes a significantly stronger case for general technological surfaces than a single data set, but could not be termed conclusive. However, the same slowly varying contrast that is

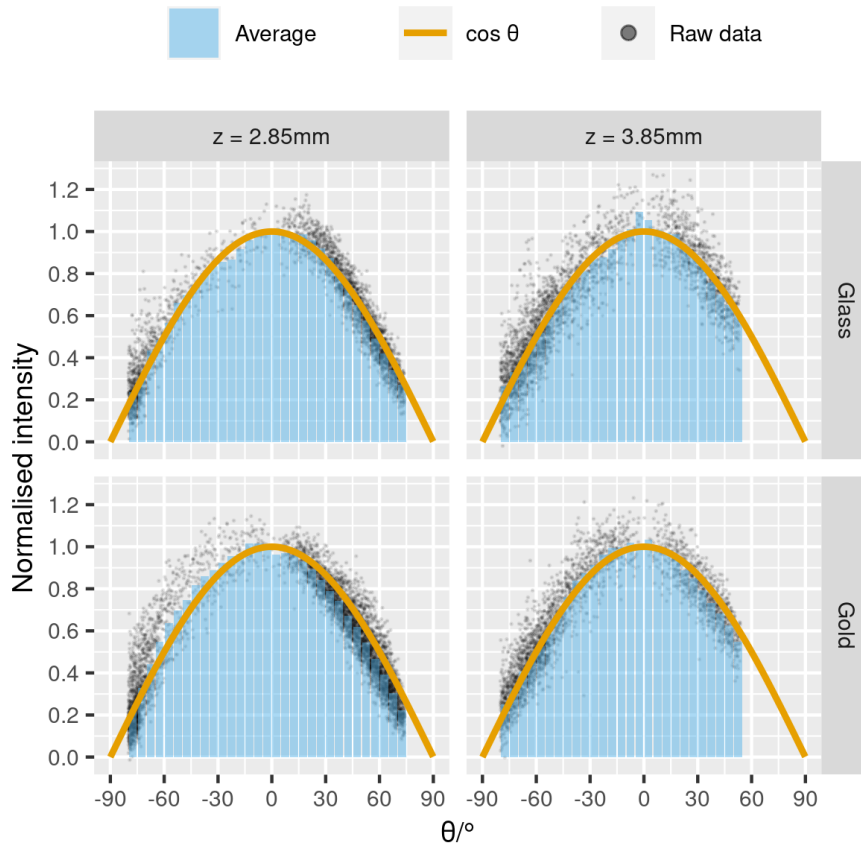


Figure 5.8: Extracted scattering distributions from a $100\ \mu\text{m}$ sphere, both with and without gold plating. The data is normalised by fitting a cosine curve to the averaged data. It is clear that the atoms are scattered in a broad diffuse distribution with a stronger tendency for scattering close to the surface normal. Generally there is agreement with the simple cosine model, with a small indication of backscattering in the $z=2.85\text{mm}$ Gold case, however that does not detract from the overall claim of ‘cosine-like’ scattering.

observed in the images of the microspheres is also observed qualitatively in many other samples. If the same basic contrast features are seen with other samples as are seen for the sample that are known to scatter diffusely, then it can safely be assumed that a *similar* scattering distribution is occurring. These ‘similar’ distributions are labelled ‘cosine-like’ because they possess the two key features of being very broad and have a bias closer to the surface normal than the specular condition, but as the analysis is qualitative not quantitative it remains unknown if they are precisely ‘cosine’ shaped.

Topographic contrast as a mix of high contrast masking and weaker slowly varying contrast is observed as the most common type of image produced in the SHeM. In addition to the glass and gold microspheres these features are observed in SHeM micrographs presented in this thesis for the TEM grid and sample stub in figure 2.6; the example of HOPG graphite in figure 2.17; the AlvetexTM scaffold and the collagen scaffold presented in figures 6.10 and 6.11; and finally the aluminium potassium sulphate crystal in figure 8.16. As

well as the data presented here other specimens imaged in the Cambridge A-SHeM have demonstrated qualitatively similar contrast, for example: eroded diamond, small samples of wood, fabrics, coral specimens, and the fly's eye measured by Bergin[14]. Further many items from the literature also present the main feature of diffuse topographic contrast: butterfly wings measured by Fahy et al.[35], honey bee wings by Barr et al.[38], a sugar crystal and the eye of a honey bee by Fahy et al.[35], Port Jackson shark skin studied by Myles et al.[44], and the pollen grains measured by Witham[60].

In addition there is quantitative agreement between ray tracing simulations (that assume cosine scattering) of multiple scattering and experimental data – chapter 6[78] – and qualitative agreement with other data[45].

The extent of qualitative observations of diffuse contrast in SHeM combined with the quantitative results presented here allow the tentative conclusion that diffuse cosine-like contrast is the dominant scattering mechanism for unprepared technological surfaces. Having a default model for scattering in SHeM is incredibly useful for image interpretation, and leads to the development of full 3D reconstruction method for SHeM images that is presented in chapter 8.

5.4 MODELLING THE SCATTERING OF ATOMS FROM ROUGH SURFACES

Given the observations of a cosine-like distribution in SHeM the natural next step is to understand why such a distribution is observed. What is presented here is not intended to be a full investigation that will reach a definitive conclusion, but simply the first step in the investigation. The approach taken is to start from the simplest possible model, gain whatever information can be gained from that model, then propose a slightly more realistic model. For the purposes of simplicity the present discussion is limited to two dimensions.

5.4.1 *Random surfaces*

A randomly rough surface is one that presents no periodicity. Such surfaces are commonly characterised by a height distribution function (HDF) that gives the probability distribution of heights across the surfaces, and an autocovariance function (ACF), which describes the self-correlation of the surface across lateral distance[79]. Here Gaussian HDF and an exponential ACF are used. Details of a method for surface generation developed by B Carr[80] are given in appendix E. The vertical lengthscale given by the HDF is the RMS height. The lateral lengthscale defined by the ACF is the correlation length, which is the distance at which points on the surface are uncorrelated. The RMS height and the correlation length are used to define the roughness for the remainder of this chapter.

5.4.2 'Billiard ball' scattering

The simplest model of scattering atoms off rough surfaces is a 'billiard ball' model that uses a hard wall interaction. As the implementation of such a model is relatively straightforward, a brief investigation of the behaviour of atoms scattering off rough surfaces is given.

Without the presence of any potential field the atoms trajectories will only ever follow straight lines in space, thus only the direction and not kinetic energy of the atoms need to be considered and an adaptation of the ray-tracing framework introduced in chapter 2 can be used.

Because the energy of the helium atoms is ignored then there is only one relevant parameter: the ratio between the correlation length and the RMS height. Therefore for the billiard ball model the roughness is quantified by the ratio,

$$R_{\text{roughness}} = \frac{RMS}{L_{\text{corr}}}, \quad (5.16)$$

with larger values corresponding to a rougher surface.

5.4.2.1 Implementation

An adapted version of the ray-tracing framework was written to work in 2D, using line elements instead of triangles, as the basis of simulation and without any of the code to raster the surface and build up images: the interest lies with the distribution of the final directions of rays with the sample fixed in a single position.

The surface generated consists of a series of points (x_i, y_i) . In 2D space, in order to trace rays scattering off the surface, the surface points are considered connected by straight lines to create line segments, each consisting of two vertices (v_1, v_2) and a direction normal to the line segment (n). First the gradient is acquired and the y -intercept of the line segment obtained,

$$m = \frac{v_{2x} - v_{1x}}{v_{2y} - v_{1y}} \quad (5.17)$$

$$c = v_{1y} - mv_1 \quad (5.18)$$

which gives the equation of the line for segment. The rays are stored as a position and a direction, e, d respectively, and the line of a ray is parametrised by t . To find the value of t that intersects the line segment of surface,

$$t = \frac{e_y - md_x - c}{md_x - d_y}. \quad (5.19)$$

The above equation will give the intersection of the ray with an infinite line, as each line segment has finite length it must be checked if the intersection point is within the extent of the line segment. Check if the x component of the intersection position, $p = e + td$, is between the x positions of the two

vertices, if it is not then the intersection is not valid – the intersection is also disregarded if the value of t comes out negative.

The intersection points between the ray and all the line segments in the surface are considered and the shortest travel distance is chosen to progress the ray position to. Once the new position is known the direction can be reflected:

$$\mathbf{d}_{\text{new}} = \mathbf{d} - 2(\mathbf{n} \cdot \mathbf{d})\mathbf{n}. \quad (5.20)$$

The method was validated by comparing results from the simulation to a simple analytic model for low roughness values, as follows. For each surface element the scattered direction will follow equation 5.20. These outgoing directions are weighted by the projection of the incoming beam onto the surface element,

$$W = \mathbf{d} \cdot \mathbf{t}, \quad (5.21)$$

where \mathbf{t} is the tangent vector to the surface element. The method does not consider masking or multiple scattering, and does not preclude scattering into the surface, however, for low values of roughness these effects are negligible. For ratios $R \leq 0.1$ the models were in good agreement, thus validating the simulation method.

5.4.2.2 Results

Some sample results are given in figure 5.9 for a series of different roughness parameters. The bottom panel of the figure gives histograms of the resulting scattering distribution far from the sample, and the top panel of the figure gives a series of example surface profiles for the roughness values used, to allow an intuitive understanding of the roughness. The results do show that even using the most simple model of scattering can reproduce a cosine-like distribution. However the results also show that cosine-like scattering is only reproduced at very large roughness values with even more extreme values diverging from cosine-like scattering into backscattering. Overall the changes in the resulting distributions can be summarised as changing from specular, to broad specular, to cosine-like, to backscattering with increasing roughness.

While interesting, the results of figure 5.9 cannot be considered to explain the observations in the first half of this chapter: the roughness values needed for cosine like scattering are both extreme and specific. Therefore more physically realistic models are going to be needed.

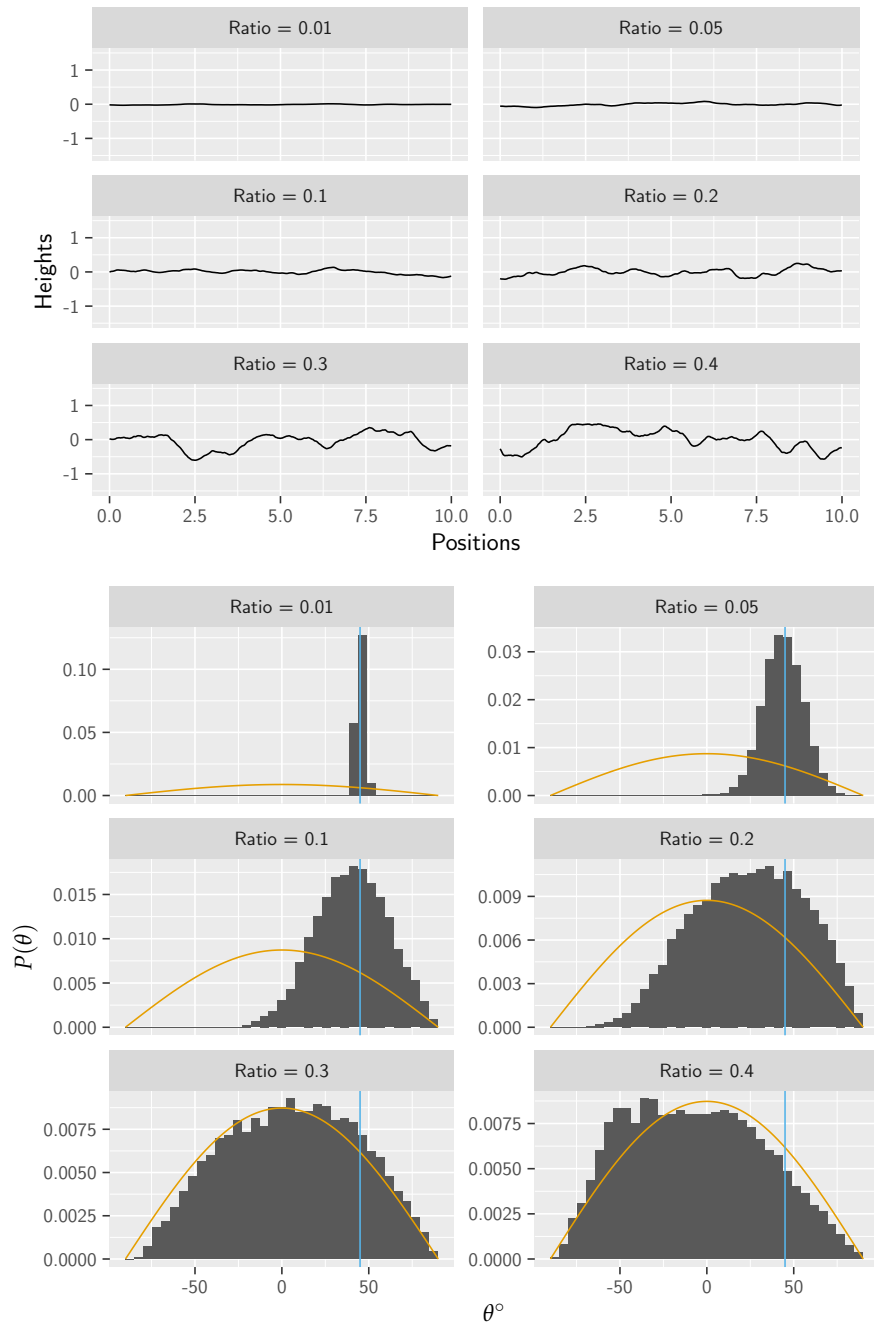


Figure 5.9: The outgoing distribution of directions as a result of billiard ball scattering from different roughness's of surface. The roughnesses are quantified by the ratio of the RMS to the correlation length. The results show that a cosine-like distribution can be recovered, but only for very rough surfaces, and if the surface is made too rough then backscattering occurs. The example profiles given at the top are plotted with equal lengths on the x and y axes allowing a intuitive understanding of the meaning of the roughness parameter.

5.4.2.3 *Non-specular intrinsic scattering*

As the model for the scattering of atoms from a rough surface is based on the ray tracing framework alternative, ‘intrinsic’ scattering models can easily be implemented in place of the specular model used to obtain the results shown in figure 5.9. For example, the effect that the roughness has on the observed distribution when the individual surface elements scatter diffusely would be useful for discussions of roughness contrast. Figure 5.10 presents resultant distributions for increasing values of roughness for an intrinsic cosine distribution. It can be seen that low roughness values do not cause a deviation from a cosine-like distribution, that moderate values cause an increase in backscattering, and extreme values results in a dual peaked distribution with significant backscattering.

That moderate values of roughness do not cause significant deviation from the cosine model is consistent with the general observations of diffuse scattering from many different samples. In addition knowing that the model is reasonably robust to small changes allows the model to be applied more broadly and with more confidence in the qualitative and quantitative interpretation of images.

5.4.2.4 *Potential further simulations*

With the simplest ray-tracing model not reproducing the observed ubiquity of cosine-like scattering the next ‘most simple’ models are considered. One approach would be to maintain the hard wall potential but treat the helium atoms beam as a scalar wave. Studies of the scattering of a scalar wave from rough surfaces have been performed in the literature, some with EM waves in mind[81], while others specifically consider atom beams[82]. These simulations produced similar qualitative results to the much more simplistic model presented above: specular scattering gives way to broad specular scattering as the roughness increases. Then for specific high values of roughness cosine-like scattering can be reproduced, but with even rougher surfaces backscattering starts to occur. Overall the wave scattering studies performed thus far also fail to fully explain the observations.

An alternative approach that is more physical is to include a soft potential for the helium-surface interaction. The simplest model with a soft potential would be a classical particle trajectory simulation that uses something similar to a Morse potential for the interaction. Coding a 2D particle trajectory simulation would not pose much difficulty, however the increased number of relevant parameters would require a more involved investigation than presented in §5.4.

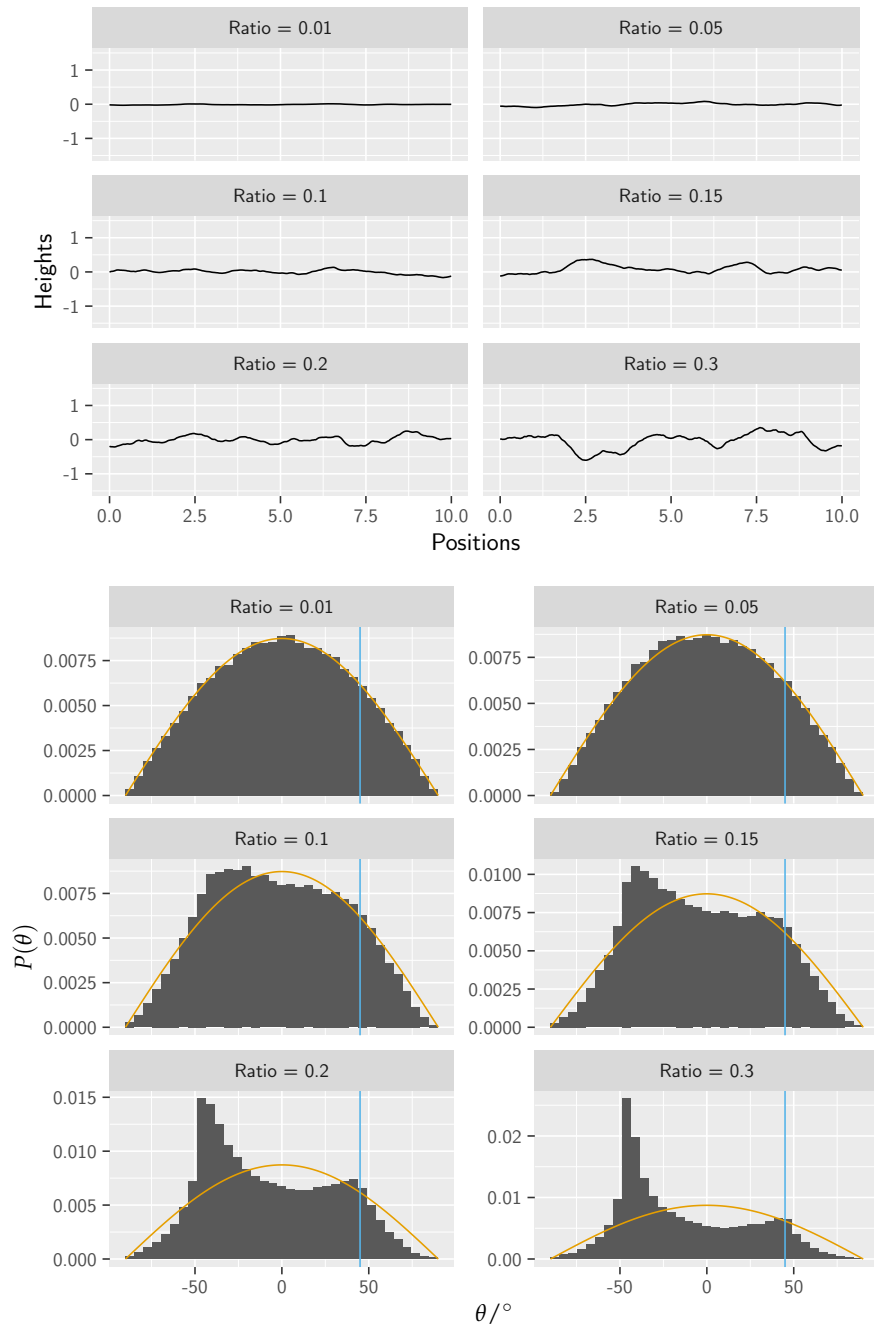


Figure 5.10: Resulting outgoing directions of rays scattered from rough surfaces with an intrinsic cosine model of scattering. The cosine distribution maintains for small values of roughness, while larger values of roughnesses result in backscattering. At extreme roughness's a dual peaked distribution emerges with a smaller peak in the specular direction.

Beyond classical models with a soft potential are those that consider the quantum nature of the atom surface interaction. For example close coupled simulations with MultiScat[83] could be attempted, or full wavepacket simulations. These, however, would require significantly more effort.

5.5 SUMMARY

The quantitative results here indicate an approximately cosine scattering distribution for two quite different surfaces: glass and sputtered gold. Knowing the scattering distribution for these samples allows an understanding of the contrast features in SHeM micrographs where diffuse scattering is occurring. Identification of these contrast features as dominant for a large variety of samples studied in SHeM over the last few years, allows the conclusion that diffuse cosine-like scattering should be expected by default in SHeM for unprepared technological surfaces.

While the evidence points in the direction of cosine-like scattering a major question does remain: why is a cosine-like model observed? It was shown that a simple model of a rough surface and a hard wall interaction are incapable of recreating the observations. As cosine scattering implies outgoing directions independent of the incoming directions some process must occur to cause a 'loss of memory' of the incident directions, for example processes related to the *chattering* (chaotic scattering) observed by Borondo et al. and Guantes et al.[84, 85]. An alternative explanation could be that there is a high degree of thermalisation occurring, however, elastic scattering has long been observed to be dominant in HAS from single crystals. Crucially the relevant difference between the surfaces of the samples measured in HAS and the surfaces of samples imaged in the SHeM is not yet clear. Investigations of atoms scattering from rough surfaces could continue by performing more realistic simulations. The next 'most simple' model could consider the classical scattering of atoms from a soft potential, such as a Morse potential, enabling the inclusion of effects such as chattering and the giant cross section of defects.

MULTIPLE SCATTERING

A particularly important feature of SHeM is that, since there is essentially zero possibility of sample penetration by, or adsorption of, the probe particles, incident helium atoms can undergo multiple scattering events and still be detected. Given atoms travel along straight line paths, there is a limited probability of them reaching the detector entrance aperture after a single scattering event ($\sim 0.5\%$ in the standard A-SHeM configuration). However, by scattering from the sample multiple times, atoms can reach the detector indirectly, and thus multiple scattering makes a further contribution to topographic contrast.

While multiple scattering effects are present with both light and electrons[87] the more significant consideration is usually scattering events occurring within media[88, 89], e.g. diffraction occurring twice or more in the sample in transmission electron microscopy. The case of multiple scattering with helium is purely a surface phenomenon. While there are similar effects with light on the macro scale, such as diffuse illumination around corners and specular reflections in mirrors, similar effects tend not to be seen in optical microscopy or with secondary electron SEM imaging¹. As the surface multiple scattering process in SHeM shares some characteristics with light on the macro-scale multiple scattering can, when present in modest amounts, call upon our everyday experience to help with the intuitive interpretation of SHeM images.

Multiple scattering leads to patches of the image exhibiting moderately increased signal levels, a process often termed diffuse illumination in analogy to the phenomenon with light. The phenomenon has been previously noted by Witham & Sanchez 2014[16] and discussed by Fahy et.al 2018[35]. An interesting case arises however where there are features in which the helium atoms could get 'trapped' and cause a significant amount of multiple scattering. Such an example is considered here: features deeper than they are wide. In order to investigate the impact of multiple scattering in these cases a test sample consisting of trenches of varying depth was constructed. The resulting helium micrographs were compared to ray tracing simulations and an analytic integral model. It is found that multiple scattering can completely change the appearance of images and a proper understanding of it is necessary to interpret SHeM images, particularly for porous samples possessing deep features.

Work from this chapter has been published as 'Multiple scattering in scanning helium microscope' by Lambrick et al. 2020[78]

¹The mode which produces images most analogous to SHeM

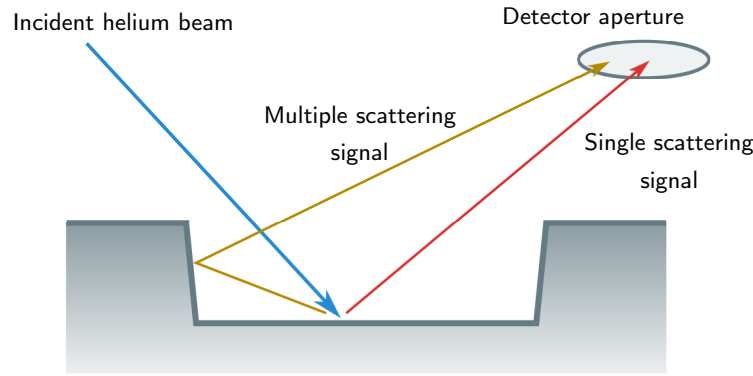


Figure 6.1: An illustration showing how multiple scattering can contribute to the detected signal using the example of a shallow trench. The detected signal inside the trench is elevated compared to the co-planar surroundings of the trench due to the scattering of helium off the sides of the trench.

The ‘multiple scattering contrast’ discussed here is related to the phenomenon of the ‘multiple scattering background’ discussed in §2.3.4.1 in that the helium atoms are scattered multiple times before being detected. However, unlike the undesired background signal from multiple scattering that occurs from scattering between the sample and instrument geometry, multiple scattering contrast arises from scattering locally near the beam-sample intersection. As a result multiple scattering contrast can encode topographic information and is not necessarily undesirable.

6.1 DIFFUSE ILLUMINATION

The main impact of multiple scattering is to brighten regions of the image: as shown in figure 6.1 atoms scatter off the initial point of incidence on the sample, hit another part of the sample then get detected. The phenomena has been termed *diffuse illumination* in the literature[16, 35, 45] based on the diffuse scattering of atoms at the initial scattering point illuminated other surfaces. The term *multiple scattering* describes the general phenomenon with diffuse illumination being a specific process where scattering from a single object onto its surroundings causes a local, relatively modest, increase in signal.

Contrast from multiple scattering appears in almost all SHeM images to a greater or lesser degree. An example showing a few readily identifiable multiple scattering contrast features is presented in figure 6.2 (a): a series of small glass microspheres. Figure 6.2 (b) compares the experimental data to a representative ray tracing simulation of a similar sample separated into the single and multiple scattering components. Diffuse illumination caused by scattering off the spheres onto the surrounding flat surface (highlighted region A) increases the intensity of regions at the base of the sphere which would otherwise be completely dark. Diffuse illumination caused by scattering off the flat surface onto the spheres (highlighted region B) slightly

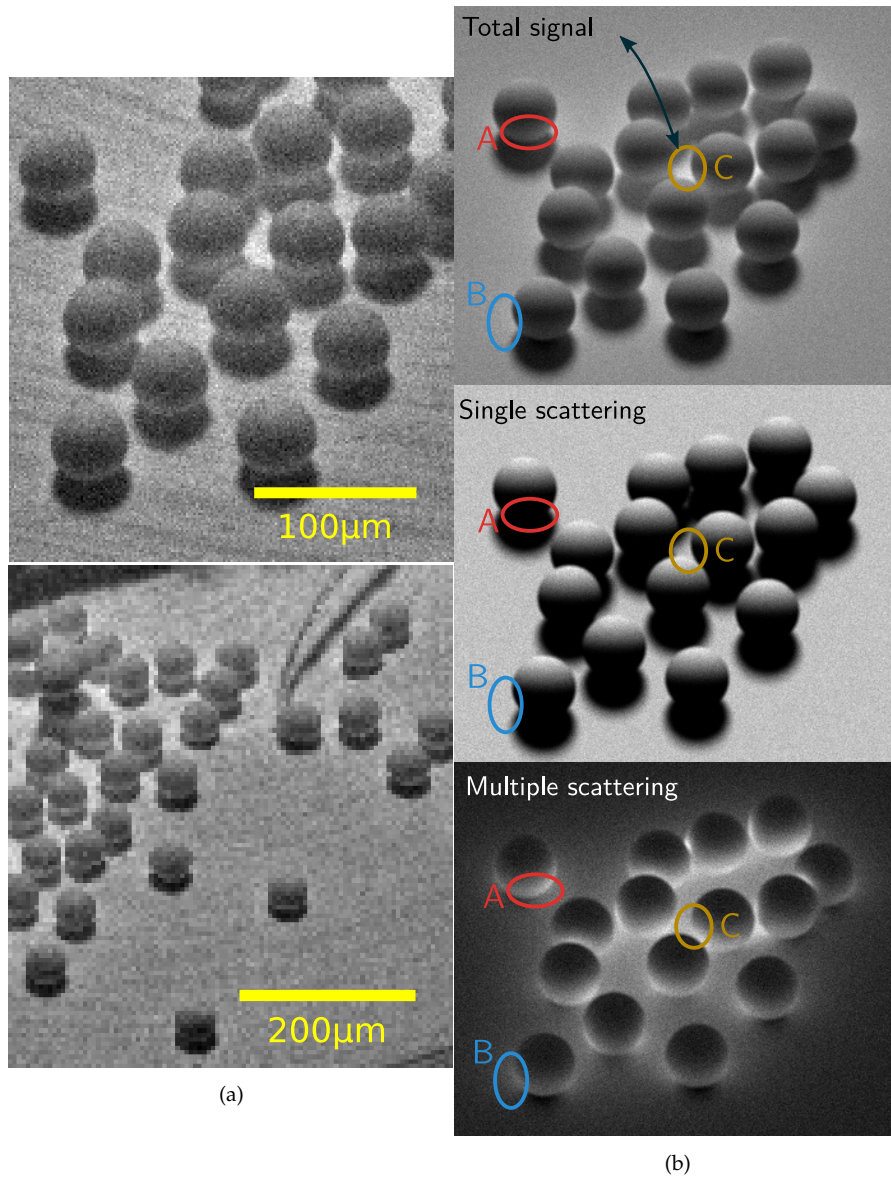


Figure 6.2: (a) SHeM micrographs of small glass microspheres that demonstrate diffuse illumination to either side of the sphere and, more strongly, in between them when they are close together. (b) simulated micrographs of small spheres with the multiple scattering component separated highlighting where the multiple scattering component is a key contrast feature in the image. Highlighted are three locations where multiple scattering has an impact on the contrast, A and B are where atoms from the sphere or surface scatter onto (diffusely illuminate) the surface or sphere respectively and increase the signal. Feature C highlights where multiple surfaces are close together result in a significant increase in signal compared to other flat regions of the sample.

increases the intensity of flat regions either side of the spheres. In addition to these modest features, where the spheres are close together the confined spaces created a significant increase in the brightness of the images (highlighted region C) as atoms can scatter off multiple surfaces, channelling

them towards the detector. The final case hints at a more significant form of multiple scattering contrast discussed in the next section.

6.2 MULTIPLE SCATTERING TEST SAMPLE

To investigate multiple scattering contrast in detail, a test sample consisting of a series of trenches of increasing depth was constructed. Trenches were chosen as they provided the required surface facets orientated in different directions to create significant multiple scattering and can also be considered an alias for topographic features indented into a surface that may be found in many samples. Varying the depth of the trenches allows the relative significance of multiple scattering to contrast formation to be investigated as a function of the aspect ratio of the feature.

The test sample was manufactured by FIB milling, to create the sample out of a silicon wafer. J.E. Halpin of the School of Physics & Astronomy, University of Glasgow, manufactured the test sample. It consisting of a series of trenches of increasing depth but consistent footprint – an SEM micrograph is presented in figure 6.3.

The trenches can roughly be split into two categories: *deep* and *shallow*, which demonstrate different contrast. The category of shallow is where the depth is smaller than the width, or alternatively those with an aspect ratio $\lesssim 1$, whereas deep refers to those whose depth is greater than their width. The distinction between deep and shallow is significant because, given the 45° angle of incidence of the beam, where the aspect ratio is greater than 1

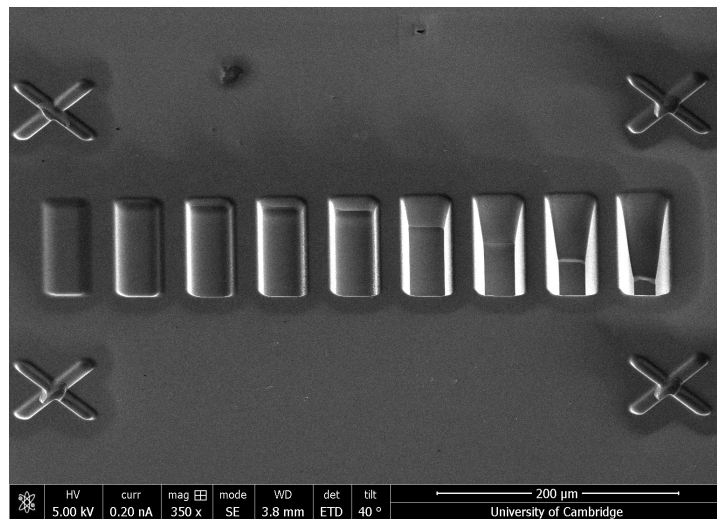


Figure 6.3: An SEM secondary electron micrograph of the FIB milled test sample consisting of a series of trenches of different depths between $7.6\ \mu\text{m}$ and $104\ \mu\text{m}$ in depth, each with the same footprint. The measured depths of the trenches are, from left to right: $3.7\ \mu\text{m}$, $7.6\ \mu\text{m}$, $11.1\ \mu\text{m}$, $14.8\ \mu\text{m}$, and $18.7\ \mu\text{m}$. Note the curved edges and sloped sides of the trenches. As viewed here the helium beam in the SHeM is incident from the left and the detector is to the right.

the beam will never hit the bottom of the trench. Thus, the whole interior of the trench will be masked, meaning any observed contrast will be due only to multiple scattering. The shallow trenches represent a controlled example of the diffuse illumination, similar to the effects seen in figure 6.2.

6.2.1 Modelling multiple scattering

6.2.1.1 Analytic model

To further examine multiple scattering contrast in the case of deep trenches, an analytic model was developed to predict the detected intensity across a trench. As illustrated in figure 6.4, when atoms enter deep trenches, only a fraction of the singly scattered atoms leave the trench without scattering again. The helium atoms that remain in the trench form a localized gas which undergoes multiple scattering events, thus fully randomizing their trajectories. The multiply scattered atoms eventually emerge from the trench diffusely, with a broad distribution of directions, a proportion of which reaches the detector. The total multiple scattered intensity that emerges from inside a trench is dependent on the proportion of atoms that remain localized after the first scattering event. Assuming a cosine model to be representative of diffuse scattering from these ‘unprepared’ surfaces, the proportion of helium atoms that escape on first scattering can be calculated. From Figure 6.4, if the beam is incident at a distance, d , into an infinitely deep and long trench with width, w , then the localized proportion as a function of the ratio d/w is,

$$P\left(\frac{d}{w}\right) = \underbrace{\frac{1}{2} \int_0^{\arctan \frac{d}{w}} \cos \theta \, d\theta}_{\text{Top half of distribution}} + \underbrace{\frac{1}{2} \int_0^{\frac{\pi}{2}} \cos \theta \, d\theta}_{\substack{\text{Bottom half of distribution} \\ \text{all stays in trench}}} \quad (6.1)$$

$$= \frac{1}{2} \sin\left(\arctan \frac{d}{w}\right) + \frac{1}{2} = \frac{1}{2} \left(1 + \frac{d}{\sqrt{d^2 + w^2}}\right). \quad (6.2)$$

The above 2D result is shown to be mathematically equivalent to the full 3D integral in appendix F. In the SHeM, samples are scanned under the beam, so with lateral movement the beam falls a different distance into each trench, thus the variable d in equation 6.2 may be directly replaced with the lateral position across the trench, x ,

$$P(x) = \frac{1}{2} \left(1 + \frac{x}{\sqrt{x^2 + w^2}}\right). \quad (6.3)$$

Equation 6.3 gives the proportion of the incident beam that is localized. If the scattering distribution from the surface and the distribution emanating from the trench are exactly the same then the detected signal will be equal to the proportion localized. If the atoms in the trench had been completely randomised then a cosine distribution of directions may be expected. However,

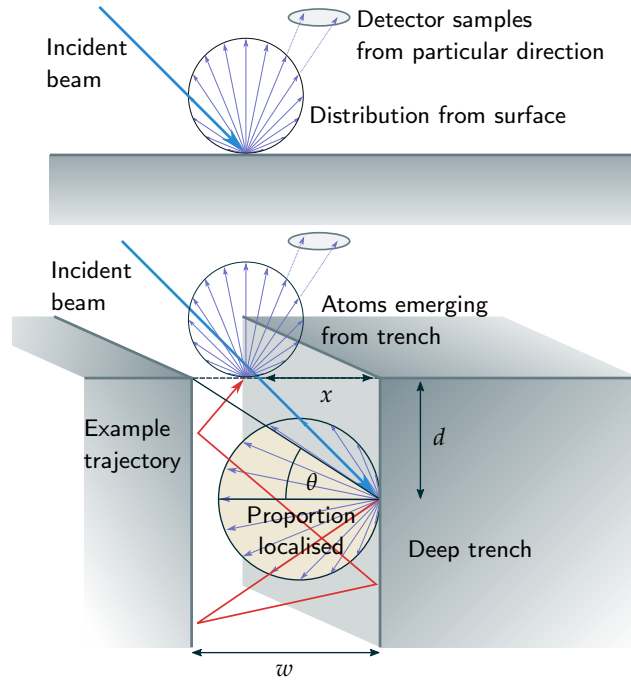


Figure 6.4: (Top) Unprepared surfaces typically scatter with a diffuse distribution. The distant detector samples part of that distribution in a particular direction. (Bottom) Atoms falling a long distance, d , into a deep trench of width, w , become localized, losing memory of their original trajectory. When they escape the trench they leave with a diffuse distribution that is again sampled in a particular direction by the detector. As the same part of the distribution is sampled, the trench gives the same signal as the flat surface, scaled by the fraction localized and any difference in the distribution produced by the localisation. x is the horizontal position in an image.

given many of the atoms will escape with only one or two further scattering events full randomisation is unlikely, therefore it is probable a distribution deviating from the surface scattering distribution will be produced. A similar phenomenon is seen with gases in long narrow tubes: atoms backscattering out of the entrance to a long tube follow a very broad distribution of directions[90] (the comparison with tubes is considered further in §6.3.1). However in the case of tubes atoms may exit at the other end so the distribution produced will be different to the current case where all atoms must leave the same way they entered. The case of a different distribution being produced by the localized gas emerging from the trench must be considered in the model. The detector in the SHeM, as indicated by the ellipses in figure 6.4, samples a fixed proportion of the scattering distribution. The detected intensity as a function of x can therefore be written

$$I(x) = m(\xi) P(x), \quad (6.4)$$

where $m(\xi)$ gives the probability of detection of the localized gas distribution relative to the surface scattering distribution for some source and detector geometry denoted ξ . In the case of the test sample ξ is constant across any

one image and in general is fixed for a single image feature – in SHeM the sample is rastered while the beam and detector remain fixed. In the A-SHeM ξ can be varied by changing the detection angle via a change in the perpendicular working distance z .

6.2.1.2 Ray tracing

Monte Carlo ray tracing simulations, as described in chapter 2, may also be used to predict the multiple scattering – and single scattering – contrast for the test sample given a 3D model of the sample, as it was used for the qualitative comparison in figure 6.2. Simulations were performed for both a deep and a shallow trench.

To accurately model the sample a curvature was given to the corners of the edges of the trenches and the sides were sloped in a manner consistent with SEM micrographs taken – figure 6.3. A cosine surface scattering distribution was used for the simulations and a full model of the detection geometry was used in order to provide quantitatively comparable results.

6.3 COMPARISON OF PREDICTIONS AND RESULTS

The test sample was imaged and simulated for a series of different detection angles. Figure 6.5 shows the SHeM images along with a sketch of the corresponding surface profile. The helium images clearly shows distinction between the shallow trenches on the right hand side of the image, exhibiting dark masked regions that widen with depth, and deep trenches on the left hand side of the image, showing very similar, almost uniform, contrast without distinct dark regions. The transition from shallow to deep trenches occurs at a depth/width ratio of about 1 (between trenches E and F), although in the case of $z = 1.5$ mm the transition starts to occur at smaller aspect ratios with trench E fully masked. In the A-SHeM the transition will never occur for an aspect ratio > 1 as the beam will never be incident on the base of the trench. The deep trenches appear significantly brighter than the dark regions in the shallow trenches. Looking closely, the intensity inside the deep trenches increases from left to right, and on the inside right even exceeds the intensity of the flat substrate for some of the detection angles.

The observed contrast in the shallow trenches arises as there is a region of the base of the trench that is masked from the detector by the trailing edge of the trench – see those trenches on the right hand side of figure 6.5. Masking manifests as the dark region that extends from left to right across the trench, and increases with trench depth. Where the trenches become deeper than they are wide they become completely masked. However, at this point their appearance also changes, indicating that multiple scattering of helium has become the dominant mechanism of contrast as there can be no effect from direct scattering. For general features the transition would be expected to occur where complete masking of the interior occurs, which will

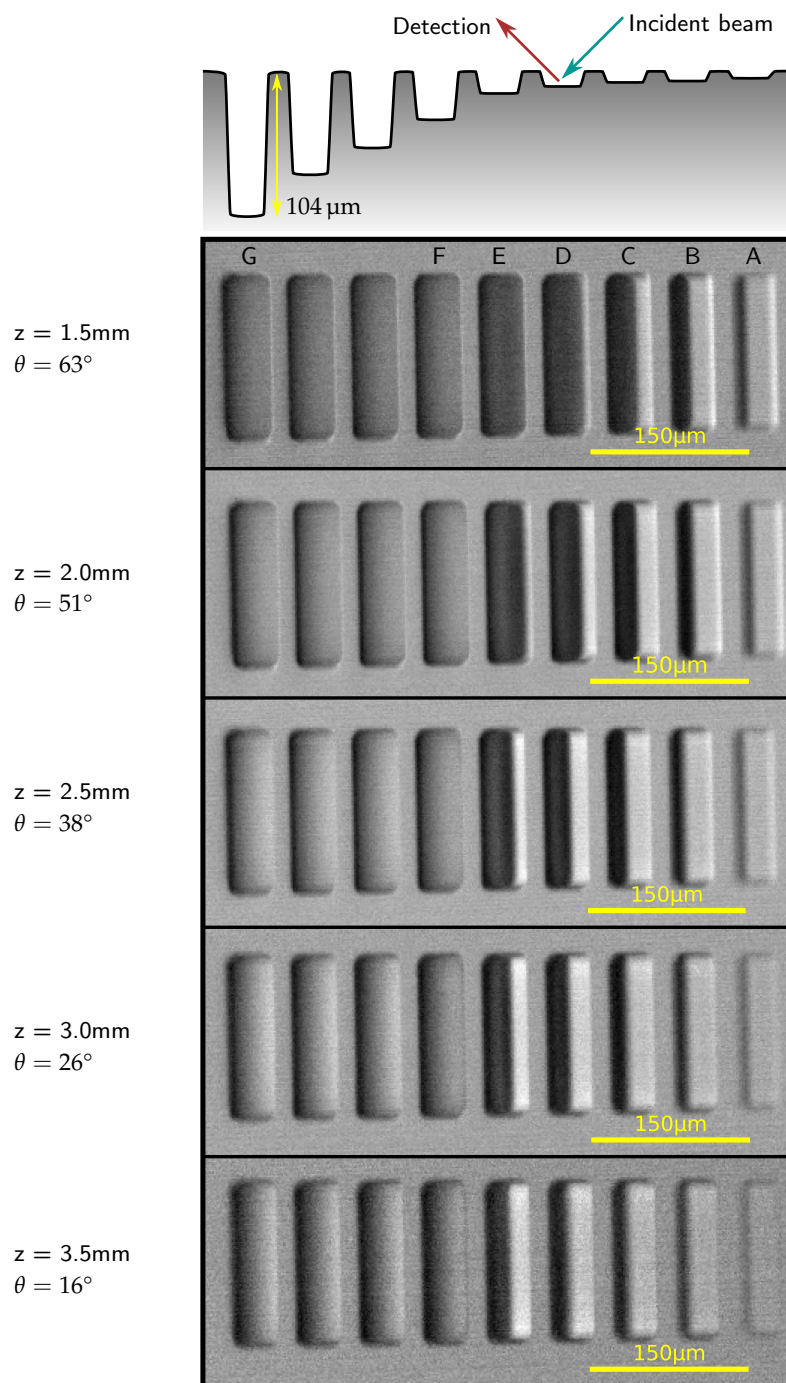


Figure 6.5: SHeM micrographs of the test sample at a series of different z positions – and hence detection directions, θ° . The helium beam is incident from the right as shown, while the detector is located to the left. As a result of re-deposition during ion beam milling the sides of the trenches are not vertical and edges of the trenches are rounded. Note that as the z distance is increased that the masks become smaller relative to the width of the trench. For $z = 1.5\text{mm}$ the mask in trench E becomes large enough that the entire trench is masked.

vary depending on the detection geometry used. For example for $z = 1.5$ mm trench E is fully masked while trench D is almost fully masked and for $z = 2.0$ mm trench E is almost fully masked. The case of trench E is interesting as even though it is fully masked, as the even deeper trenches are, it appears relatively dark because the shallowness of the trench does not allow for the localisation of helium within the trench. For the larger values of z a similar phenomenon is seen where trench F is slightly darker than the deepest trenches.

As with shadows observed with light, the sizes of masks are dependent on the sizes of the features casting them, thus the images of the shallow trenches offers the potential for gaining quantitative topographic information from an interaction independent contrast mechanism. In the set up used here there is only a single incident condition, which does not allow for a complete reconstruction, but given the knowledge that the sample consists of trenches with steep sides an estimation of the depth can be obtained from the masked SHeM images. These depth measurements compare well with the trench depths measured using an optical profiling microscope, given in table 6.1. As can be seen by comparing figures 6.5 and 6.3, well defined masking is a feature of SHeM but not of SEM. The presence of such a simple contrast feature in SHeM, that makes no assumption on the interaction with the between the atoms and the surface, is what allows the measurements, such as those in table 6.1, to be made for a single image. If quantitative topographic measurements such as these were to be made in SEM multiple images would be needed in order to perform triangulation in the manner of stereophotogrammetry.

Trench	SHeM/ μm	Optical profiler/ μm
A	4.5 ± 1.4	3.7 ± 0.1
B	7.8 ± 1.0	7.6 ± 0.2
C	11.1 ± 0.9	11.1 ± 0.2
D	14.6 ± 1.0	14.8 ± 0.3
E	18.3 ± 1.2	18.7 ± 0.4

Table 6.1: Measured depth of the trenches from the series of SHeM images, found by measuring the sizes of masks in the images, and from an optical profiling microscope. Note that the uncertainty in SHeM mostly arises from the size of pixels used and is similar to the resolution of the instrument. The values agree to within error. Optical profiler measurements performed by Dr. Z. Chang of CN Technical Services Ltd.

Figure 6.6 presents a detailed comparison between the contrast predictions and the experimental data for the case of $z = 2.5$ mm. The top panel shows a comparison through images of the experimental data with both the analytical model – see §6.2.1.1 and equation 6.4 – and the simulated ray tracing model with and without multiple scattering. In the case of the analytic model it was found that a value of $m = 1.3$ was in good agreement with the experimental data and, moreover, since the value of m is greater than 1 it

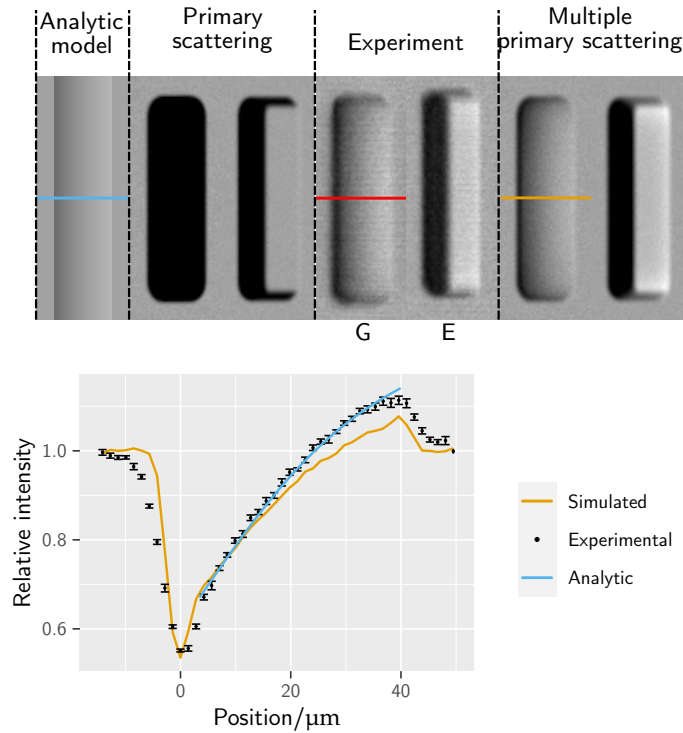


Figure 6.6: Comparison between the experimental and simulated images of a deep and shallow trenches with depth/width ratios of 3.5 and 0.3 respectively. Primary and multiple scattering contributions are shown separately, once multiple scattering is included the simulation matches the experimental data closely, with only a slight discrepancy at the edges of the trench where the exact curvature is unknown. It can also be noted that the primary scattering image of the deep trench is symmetric while the multiple scattering image is not, thus the multiple scattering contrast is adding information about the orientation of the trench, with respect to the scattering geometry, that is not present with only primary scattering. (Bottom) Line scans extracted from experimental and simulated data along with the analytic model from equation 6.4. The analytic model with a value of $m = 1.3$ predicts the direction and form of the intensity change and matches the experimental data well.

implies the distribution of multiply scattered atoms is biased toward towards the detector. In figure 6.6, the simulated ray tracing images for the shallow trench (right hand panels) show that although the dominant masking feature is reproduced by primary scattering, including multiple scattering improves the agreement by increasing the intensity on the right hand side of the trench.

In contrast to the shallow trench images, the helium signal observed experimentally for deep trenches (left hand in each pair of images in figure 6.6), is only seen in the simulated images that include multiple scattering (on the top right of figure 6.6), with primary scattered rays producing a fully masked dark image. Moreover, not only is the brightness of the deep trenches increased, with respect to masked regions of the shallow trenches, but also the intensity across the deep trenches varies. Given that the whole interior of the trench is masked from the detector, the observed variation can only come from multiple scattering. A quantitative comparison of the intensity

variation across the deep trenches is given in the lower panel of figure 6.6, which plots line scans across the experimental, analytic, and simulated deep trench helium images. There is very good quantitative agreement between the experimental and MC multiple scattering simulations, confirming that the observed deep trench helium contrast does indeed originate from multiple scattering of the incident helium atoms. There is also good quantitative agreement between the experimental and analytical line scan data with the fitted value of m . Both models exhibit the same shape across the inside of the trench, but break down near the edges where the topography is more complicated.

Comparisons of the intensity profiles for all the different detection conditions for the deepest trench (trench G, aspect ratio 3.5) are given in figure 6.7. Quantitative agreement between the ray tracing predictions and the experimental data is seen for four out of the five plots, with the qualitative features being reproduced in the fifth case. Good agreement with the shape

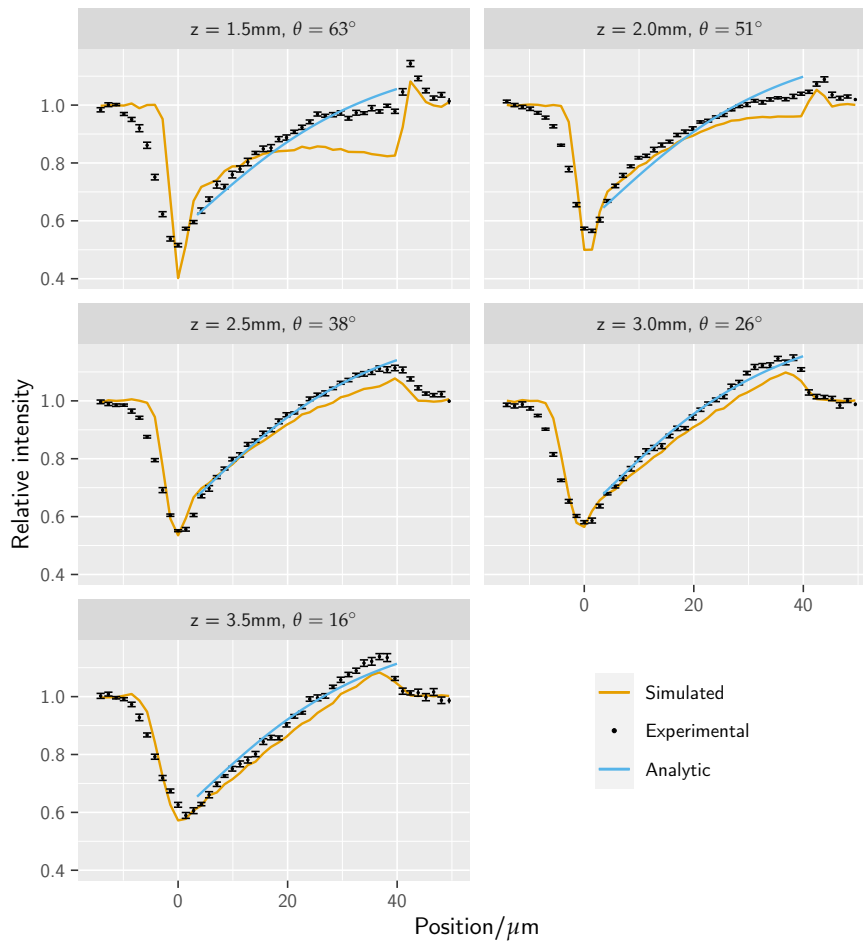


Figure 6.7: Line scans across the deepest trench (trench G, aspect ratio 3.5) for a number of different detection directions. The fitted values of m were (to 2 s.f.) 1.24, 1.29, 1.34, 1.36, 1.31, indicating that the distribution of multiply scattered rays emerging from the trench is peaked roughly in the vicinity .

of the analytic curve is found in all cases, with slightly different values of m being fitted. Larger values of m imply a greater helium signal being directed towards the detector, thus it can rather crudely be estimated that a peak in the distribution produced by multiply scattered atoms emerging from the trench is likely be found between 38° and 26° detection angles. The discrepancy observed in the case of $z = 1.5$ mm largely appears to be a result of an underestimation in the multiple scattering signal from within the trench by the ray tracing simulation. A potential explanation is that where the detection angle is large only atoms scattered from a small region near the top of the trench can reach the detector, as shown in figure 6.8, whereas where the detection angle is smaller more of the atoms will come from deeper in the trench and therefore the resulting signal will be less dependent on the exact profile of edge. As the exact profile of the edge, including the overall slope of the sides of the trench, is not known² it is reasonable, given the good agreement in the other cases, that the real sample has a somewhat different edge shape to the simulated one.

6.3.1 Distribution produced by the trench

The ray tracing simulation may be used to predict the distribution of atoms leaving a deep trench: the direction and position of the rays being simulated may be captured at the end of their trajectory and the resulting distribution of directions plotted. Rays were incident into a trench of aspect ratio 3.5 and the final directions recorded with those scattering roughly in plane (to within 6°) plotted as a histogram in the top panel of figure 6.9. It can be seen that the distribution deviates noticeably, albeit modestly, from the cosine model with a slight peak towards forward scattering. As all the fitted values of m were greater than one then there is always more scattering towards the detector than for a cosine model. The bias for forwards scattering is also seen in the simulation, although as a slightly weaker effect, especially at the larger detection angles.

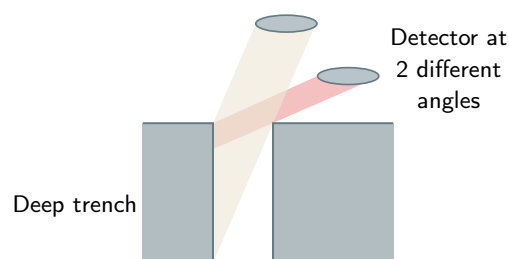


Figure 6.8: Where the detection angle is large atoms in the trench can only reach the detector after scattering from the top edge, while where the detection angle is smaller more of the atoms being detected will come from deep inside the trench, where the exact profile is less important.

²Interpretation from both SHeM and SEM images is qualitative and the optical profilometer did not produce reliable results for steep sided features.

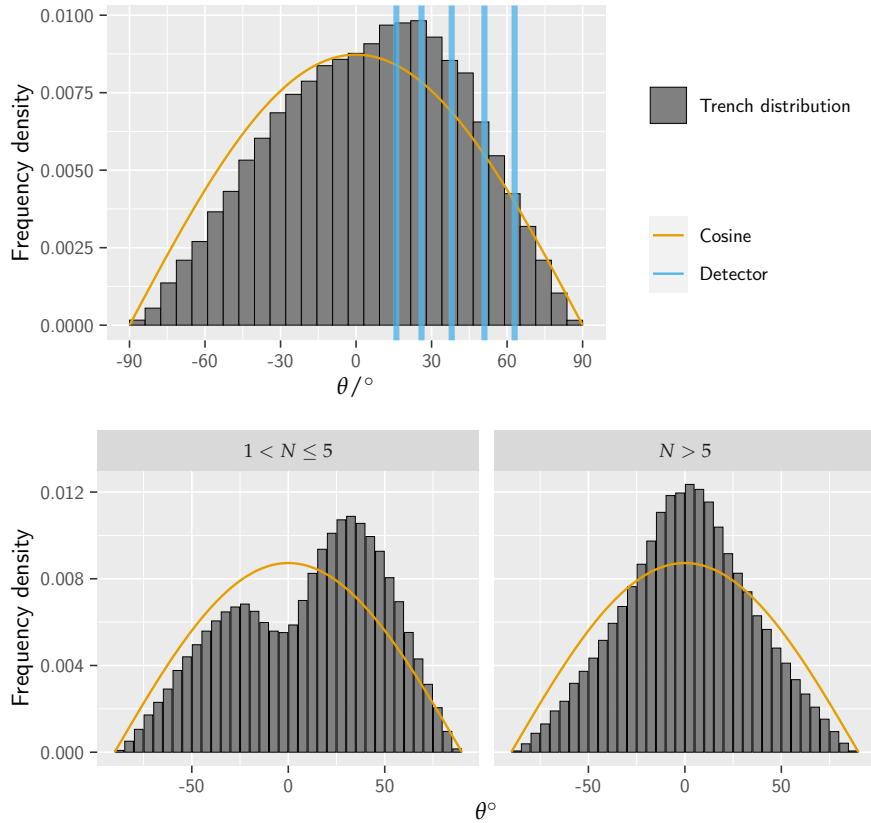


Figure 6.9: Top – In-plane (multiple scattering) distribution of directions emerging from the trench in the ray-tracing simulation. The distribution is very broad covering all angles but deviates noticeably from the cosine model. The blue vertical lines highlight the detection angles used to gather the images in figure 6.5. Bottom – The multiple scattering signal split into a relatively small number of scattering events ≤ 5 and a large number of scattering events > 5 . Here two different effects are seen, for low numbers of scattering effects a two peaked distribution is seen while for large number of scattering events, a normally centred distribution with a sharper peak than a cosine is seen.

With the ray tracing simulation the resulting distribution can be split into two cases: a relatively small number of scattering events where there will be an effect due to the incident direction and a large number of scattering events where the incident direction will have been forgotten. The two contributions are plotted in the bottom panel of figure 6.9. It can be seen that for relatively small numbers of scattering events scattering away from the normal is more likely with a dual peaked distribution predicted, while for large numbers of scattering events a distribution peaked at the normal is produced. The distribution for large numbers of scattering events is more strongly peaked than a cosine distribution and thus is similar to the distributions seen to be produced by gasses passing through tubes, the two peak distribution however has analogy to the distributions produced by backscattering out of tubes through the entrance aperture[90]. The trenches therefore appear to

exhibit a combination of the two effects seen with narrow tubes, resulting in the weakly peaked distribution seen in the top panel of figure 6.9.

6.4 'REAL WORLD' EXAMPLES OF DEEP FEATURES

An understanding of multiple scattering effects, and how they manifest in contrast, is of particular importance for SHeM imaging of a wide range of surfaces and interfaces of technological interest. As a case study example, porous scaffolds are used extensively in the biomedical sciences for growing tissue samples. These scaffolds are constructed out of delicate insulating materials and, as such, have proved challenging to image in electron microscopy without degradation, a conductive coating, or significant levels of charging[91]. The non-destructive nature of the neutral SHeM incident atom beam enables the imaging of tissue scaffolds in their native state, allowing tissue growth on exactly the same scaffold as has been imaged.

A disc of Alvetex™, with nominal pore diameter of 42 μm, was imaged in the SHeM. Alvetex is a cross-linked form of porous polystyrene, manufactured using a method known as emulsion templating involving the formation of a polyHIPE (high internal phase emulsion). The material is used as a scaffold for a broad number of applications in 3D cell culture and tissue modeling—notably the formation of skin[92, 93]. The pores in the scaffold are akin to the high aspect ratio trenches discussed earlier; helium gas enters the pores and has no direct line of sight to the detector, but localization in the pores results in multiple scattering and hence an enhanced probability of reaching the detector. A difference with the model trenches is the very high depth of the pores in Alvetex™, regardless of the angle of the incident beam to them; behind the surface pores is a complex structure of large voids and further pores. Therefore there is no significant change in the proportion of the incident beam localized across the pores, the beam always strikes surfaces a long way into the structure and not near the surface. As there is no change in localization across the pores the intensity across them is expected to be roughly constant. Figure 6.10 shows a helium image taken of the Alvetex™ scaffold. The structure can be seen as either light, when pointing towards the detector, or dark, when pointing away from the detector. The voids in the pores appear grey rather than dark (regions A and B) as expected from our localization model, highlighting the importance of a detailed understanding of multiple scattering.

A similar scaffolding structure made of collagen presented in figure 6.11 also has a deep porous structure that render mid-grey in helium images. Here there are small strands between layers of the structure that appear as either bright or dark compared to the deep porous voids depending on if the surface of the strands faces towards or away from the detector. Where the strand faces the detector the strand appears bright, while where it faces away from the detector the surface is under mask and appears dark.

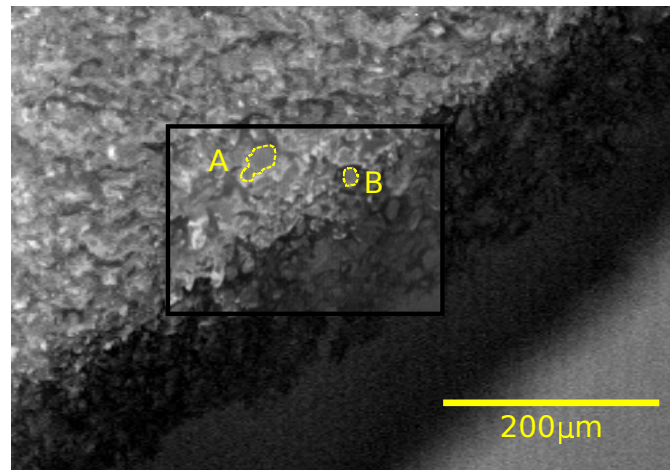


Figure 6.10: Helium images of the edge of the Alvetex™ scaffold. The insert is at a higher pixel density. The regions A and B denote two scaffold pore regions, one on the flat region of the sample and the second along the edge of the sample, which demonstrate a mid-level of signal compared to the bright and dark scaffold material.

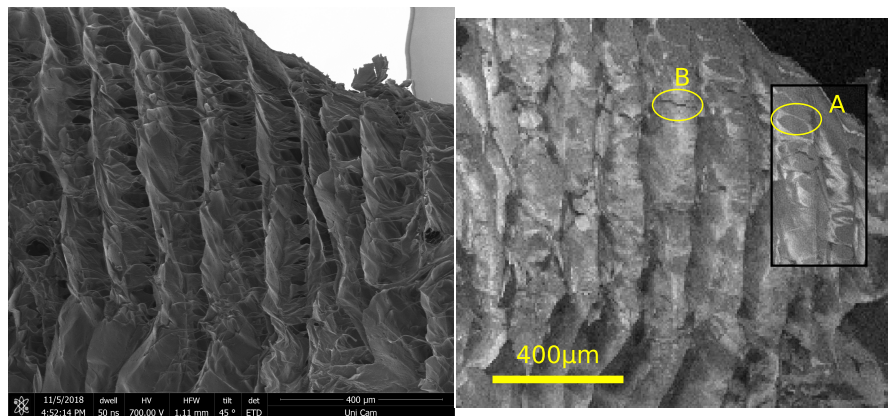


Figure 6.11: An SEM and a SHeM image of a collagen scaffolding structure. Similar deep features are found here that appear mid grey in the helium image. Strands between the layers of collagen can appear lighter or darker than the voids in between depending on if the surface of those strands is masked or not. Region A highlights a bright strand while region B highlights a dark strand.

6.5 SUMMARY

The previous section demonstrated that multiple scattering is an important topographical contrast mechanism in the SHeM and can contribute significantly to images. It is driven by the fact that the ultra-low energy helium atoms scatter exclusively from the surface topography with negligible probability of adsorption or penetration. We have shown that multiple scattering contrast can be understood both qualitatively and quantitatively using analytical modeling and Monte-Carlo ray tracing. These studies show that for shallow features primary scattering dominates, producing topographic contrast that is controlled by surface masks, which can be used to estimate

the depths of the surface features. In contrast, for deep features multiple scattering dominates, producing enhanced contrast within the trench or void. The transition between shallow and deep features occurs at a depth/width ratio of approximately 1, which is defined by the 45° scattering geometry.

With the development of a thorough comprehension of multiple scattering, in addition to the studies in the previous chapter on diffuse scattering, it can reasonably be said that topographic contrast in SHeM is well understood, and that the interpretation of topographic images has been placed on a firm foundation. The next chapter moves on from topographic contrast to consider a topographic process: atom diffraction.

Atom diffraction has been extensively studied with helium atom scattering (HAS)[6, 8, 94, 95] and presents the possibility of a new contrast mechanism in SHeM – one that could provide the crystallographic information that can be done in HAS but with the addition of spatial resolution. A proof of principle measurement demonstrating that atom diffraction can cause contrast in SHeM was published by Bergin, Lambrick et al.[40]. The primary drawback of these proof of concept measurements was the lack of instrumentation designed with the measurement of diffraction in mind: in particular there was no ability to rotate the sample and angular resolution was too poor to isolate diffraction peaks.

Presented in this chapter is a process for performing 2D diffraction measurements in SHeM that combines scans through the detection angle and the azimuthal orientation of the crystal. The process is demonstrated with measurements using lithium fluoride (LiF) as a test specimen, and the lattice parameter of LiF is successfully measured using only SHeM data. In order to perform these measurements a series of improvements to instrumentation were made, crucially an increase in the angular resolution and the introduction of an azimuthal rotator. The observed diffraction patterns are in agreement with the known lattice parameter of LiF and align well with simulated data.

7.1 ATOM DIFFRACTION FROM SURFACES

As a matter wave, atom beams may undergo diffraction. The quintessential example of matter wave diffraction is the double slit experiment which was first demonstrated for electrons[96], then later for neutral atoms[97], and even larger particles such as C^{60} [98]. When scattering off a crystalline surface, the atom wave may diffract off the corrugated surface potential produced by the lattice[6], where plane waves scattered off the corrugation interfere to give patterns similar to those in the Bragg diffraction of X-Rays. Figure 7.1 illustrates a plane wave that scatters off a corrugated surface, and how constructive interference leads to a diffraction peak occurring for a specific scattering condition.

Let the incident wavevector be split into the in-plane and out-of-plane components: $k_i = (K_i, k_{iz})$, and similarly for the outgoing wavevector. The

Work discussed in §7.1.1 has been published as ‘Observation of diffractive contrast in scanning helium microscopy’ by M. Bergin & S.M. Lambrick et al., 2020[40]. The data presented was acquired in collaboration with M. Bergin.

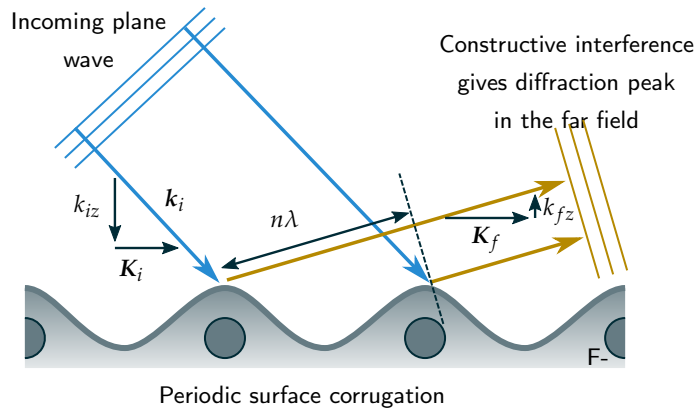


Figure 7.1: Plane wave elements reflected off the corrugated surface interfere to produce peaks and troughs in intensity in the far field giving the atom-surface diffraction pattern.

diffraction condition, following the method used by Bledsoe & Fisher[99], is then,

$$\mathbf{K}_f = \mathbf{K}_i + p\mathbf{G}_1 + q\mathbf{G}_2; \quad p, q \in \mathbb{Z} \quad (7.1)$$

where the surface reciprocal lattice vectors are $\mathbf{G}_1, \mathbf{G}_2$. Taking the surface to be in the xy plane the z component will simply be $k_{iz} = -k_{fz}$. The result when observed is a pattern of peaks evenly spaced in K space. In the far field the outgoing directions from the sample that correspond to the peaks in K space will form the diffraction peaks observed in scattering experiments.

At present, there are no practical 2D atom detectors. Therefore measurements of diffraction patterns in HAS involve changing detection condition or changing both the detection and incident condition simultaneously with a fixed overall scattering geometry. Changing the detection condition independently may be achieved by moving a detector arm such as in the TEAMS¹ apparatus in Laboratorio de Superficies de la Universidad Autónoma de Madrid[100]. For a fixed overall scattering geometry tilting/rotating the sample can be used to simultaneously change the detection and incidence conditions, as in the MiniScat apparatus in Cambridge[101]. Using sample and detector manipulation 1D, or, occasionally, 2D[102] scans of diffraction peak intensity maps can be built up. The spot profiles presented later in this chapter make use of both sample manipulation and detection condition changes in unison.

While a variety of surfaces have been shown to produce helium diffraction patterns[103–105] most require some method of in situ sample cleaning due to adsorbed and absorbed surface contaminants. However there are some surfaces that are diffractive without sophisticated cleaning, lithium fluoride (LiF) is one of these, requiring only a freshly air-cleaved surface. In addition, as LiF has been extensively studied in HAS, there are measured He-LiF

¹Thermal energy atomic and molecular scattering

potentials[106, 107] that can be used in simulations. The high corrugation of the LiF surface – it being a highly ionic compound – also results in significant diffraction peak intensity relative to specular[108], compared to less corrugated low index metallic surfaces that present a strong specular but weak diffraction[109]. LiF therefore presents an ideal test sample for the first diffraction spot profile measurements using SHeM.

7.1.1 Previous measurements

A preliminary study of LiF (lithium fluoride) diffraction in SHeM showed strong evidence of diffraction[14, 40]. Data was obtained by scanning the detection angle via z scans – z scans were introduced in §2.3.3 and involve moving the sample diagonally backwards so that the same point on the sample remains under the beam. However the instrumentation used did not allow the proper separation of individual diffraction peaks due to the large acceptance angle of the detector. In addition it was not possible to perform azimuthal rotations of the crystal limiting acquired data to a single polar angle scan with no precise choice of the crystallographic arrangement of the sample.

During the measurements three z scans were taken from points on the sample with differing levels of apparent distortion in the images: one on a region of sample that appeared flat, another on a lightly distorted region of sample, and a third on a highly distorted region of sample. Figure 7.2 plots the z scans as a function of average detection angle. The case of the flat sample shows multiple peaks that cannot be explained by a slowly varying scattering distribution. The heavily distorted region shows a pattern that is broadly as expected from a diffuse scattering and the lightly distorted region lies somewhere in between.

Although the results, displayed in figure 7.2, strongly indicate the presence of atom diffraction, and provide the first observation of atom diffraction with microscopic lateral resolution, it would be a stretch to describe them as measurements of the underlying diffraction pattern. Therefore new instrumentation has been added to the SHeM in order to perform scans of diffraction scans with enough angular resolution to separate diffraction peaks, and with variable crystal orientation.

7.2 IMPROVING INSTRUMENTATION

In order to obtain 2D diffraction patterns in SHeM 3 key instrumental improvements were needed: improved angular resolution, azimuthal rotation of the sample, and improved measurements of the working distance. The third point is required because the ‘ z position’ of the scattering point determines the polar angle of detection. Figure 7.3 shows the relation between z and θ for the arrangement used for the data collection in this chapter. The introduction

of the aperture, however, due to the difficulty of cleanly machining smaller holes an alternative approach was taken: move the detector aperture further away from the sample.

To compensate for the reduced signal from the smaller solid angle detector aperture a larger, 10 μm pinhole was used which was predicted to give $> 3\times$ the signal level of a previously used arrangement known to produce good quality images. An increase in signal was desired to ensure that there would be good resolution of the measured diffraction peaks. See §4.2.6 and figure 4.5 for details on how the signal level changes with the new pinhole plate.

7.2.2 Rotator stage

Azimuthal rotations of the sample are required for two reasons: first, in order to align the scattering plane with principle crystallographic directions. Second, to allow multiple scans through detection angle θ to be performed at different azimuthal crystal orientations. A high accuracy rotation stage needs to be installed in the A-SHeM in addition to the xyz motion already present

The stages used for sample movement in the SHeM are Attocube EC30 series piezoelectric stages. Three ECS3030/NUM² stages are used for the xyz motion, which are mounted via a kinematic magnetic system to an L-bracket that is attached to the pinhole plate, figure 7.4 (a). Attocube manufacture the ECR3030/NUM³ rotator stage which is compatible with the xyz system. The best placement of the rotator is in-front of the other stages as then the scan patterns of the *xy* stages do not need to be modified. However because the *y* axis has to act against gravity weight compensation springs are required in order to put the rotator on the front of the stages. The Attocube ECS Lift 3030 system⁴ is used together with an appropriate constant force spring to provide the weight compensation. Figure 7.4 (b) demonstrates the stage assembly after the installation of the rotator and the ECC Lift device. Further details about the assembly of the stages can be found in chapter 3 of M. Bergin's thesis[14].

With the installation of the ECR rotator in total four positioners are used with the SHeM, requiring two ECC controllers. The use of two controllers required the re-development of the control software. The revised software was implemented in 2 levels rather than a single level as the previous software was: a low level C/MEX code that could interface directly with the Attocube provided library and recognises the two controllers by a programmed index, and a higher level layer of interface code written in MATLAB that can be easily used when writing measurement scripts. Using C code to interface with the Attocube library also has the benefit of avoiding calling the ECC

²<https://www.attocube.com/en/products/nanopositioners/ambient-vacuum-nanopositioners/ecsx3030ststnumuhv>

³<https://www.attocube.com/en/products/nanopositioners/ambient-vacuum-nanopositioners/ecr3030ststuhv>

⁴<https://www.attocube.com/application/files/3615/5057/5069/ecs-lift-specs-download.pdf>

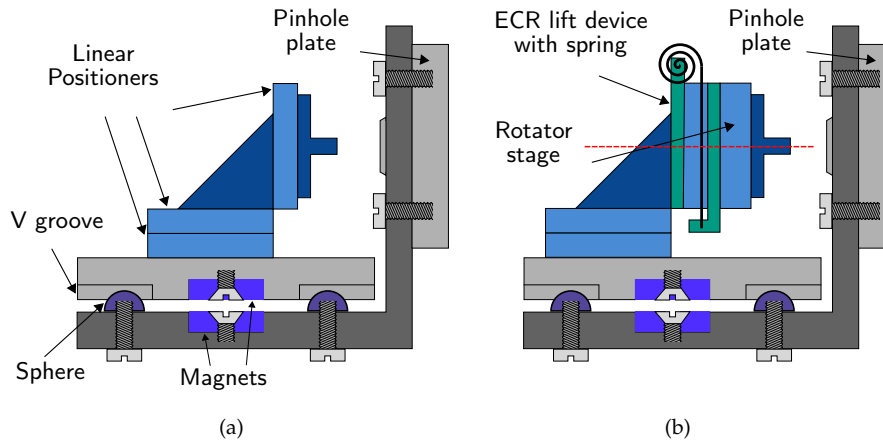


Figure 7.4: Schematic diagram of the sample mount prior to (a), and after (b), the installation of the rotator stage. The 3 linear stages are mounted in an xyz configuration on top of a metal plate that is magnetically attached to the L-bracket via a kinematic mount, in turn the L-bracket is attached with screws to the pinhole plate. The ECR lift device (in green) provides weight compensation to the y stage in the form of a fixed force spring allowing the rotator to be placed immediately behind the sample. The rotator rotates the sample continuously around the z axis, displayed as a red dashed line. Figure modified from an original by M. Bergin[14].

shared libraries directly from MATLAB which has been found to be somewhat unstable.

In order to perform spot profile measurements at different azimuthal angles points on the sample need to be tracked while changing both the z and rotator position. To that end a point tracking algorithm was implemented by N. A. von Jeinsen & A. Radić. Tracking in z is a matter of a simple offset in x. Tracking with rotation angle requires a series of images being taken of a easily identifiable feature in order to calculate the coordinate of the centre of rotation. A circle is fitted to the observed xy locations of the feature, with the centre of the circle giving the centre of rotation. Tracking of rotations also allows the following of features for imaging that is relevant for 3D reconstruction discussed in §8.5.

A series of large scale SHeM images of the LiF crystal were taken at significantly different z and rotator positions that allowed the confirmation of tracking. It was found that the tracked points deviated by no more than 30 μm .

7.3 SHEM DIFFRACTION MEASUREMENTS

The SHeM measurements proposed scan through two parameters to build up a 2D diffraction pattern. First, the detection angle, θ_f , is scanned through via changing the working distance in a z scan. The second axis scanned through is the azimuthal orientation of the crystal, which is labelled α . Other than a shift in the origin to align with a principle crystallographic direction α is equal to the encoded position of the rotator stage.

Varying both z and α gives a raw data set $I(z, \alpha)$, translatable into a data set $I(\theta, \alpha)$. It is important to note that the angle α is not equivalent to an azimuthal detection angle as all scattering events occur in plane. Figure 7.5 diagrammatically demonstrates the concept of the measurement with data being at different z and α values with scattering from the same point on the sample.

From figure 7.3 the polar detection angle from the scattering point is

$$\theta_f = \arctan \frac{2b - (z + a)}{z + a}. \quad (7.2)$$

For the pinhole plate used in the current measurements, $a = 1.5$ mm and $b = 3.5$ mm.

The raw data may be plotted as a function of z, α as a polar heat map directly, which will be able to represent all the data, but will not conform to an easy to identify diffraction pattern or peak spacing. Individual lines along either z or α may be plotted as a function of angle simply on a scatter plot.

Alternatively the in plane momentum change ΔK may be plotted instead of the z distance or detection angle, producing a plot of $I(\Delta k, \alpha)$.

To present something closer to a traditional diffraction measurement of a periodic lattice a plot in K -space is used. The Δk will be the same in the lab frame, for a specific detection angle θ_f , regardless of the value of α , therefore the wavevectors used to plot are defined in a reference frame aligned with the reciprocal lattice that rotates along with the crystal, with the specular

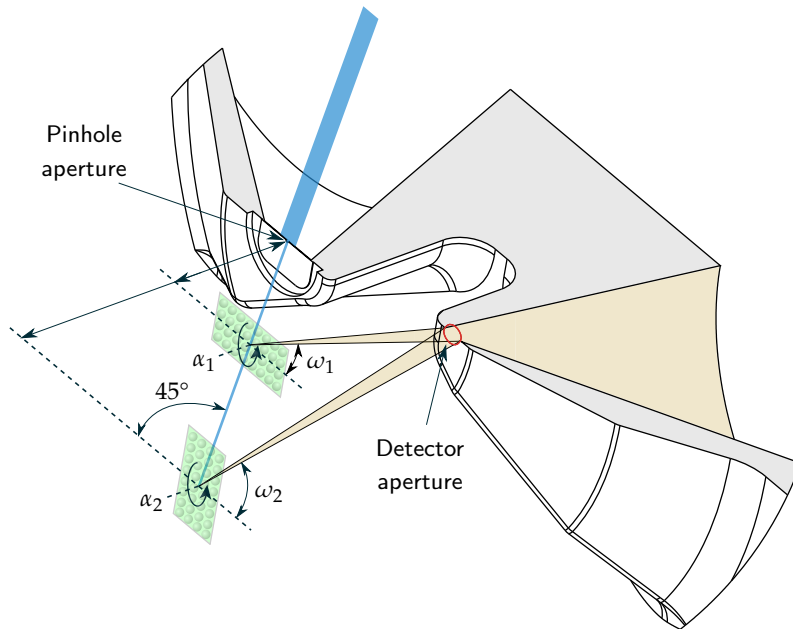


Figure 7.5: The practical sample movements involved in acquiring a 2D pseudo-diffraction pattern in the SHeM. The polar detection angle, $\theta_f = \frac{\pi}{2} - \omega$ is changed by changing the working distance used in a z scan, then the sample is rotated beneath the beam to scan scattering along different crystallographic directions.

condition chosen to be the origin. The plot will then be the detected helium intensity as a function of xy components of the outgoing wavevector relative to the lattice. For these plots only the data with z values greater than the specular condition are used.

In practice the outgoing wavevector relative to specular needs to be calculated from the polar detection angle θ_f and the azimuthal orientation of the crystal α . Define $\alpha = 0$ to be along one of the two principle crystallographic directions. Defining a coordinate system that rotates with the lattice in figure 7.6 gives the outgoing 'pseudo' wavevector as

$$\mathbf{k}_f^{\text{pseudo}} = \begin{pmatrix} K \sin \theta_f \cos \alpha \\ K \sin \theta_f \sin \alpha \\ K \cos \theta_f \end{pmatrix}. \quad (7.3)$$

Then subtract the specular condition to get the final wavevector relative to the lattice which can be used to plot the diffraction pattern.

$$\mathbf{k}_f^{\text{pseudo}} = \mathbf{k}_f - \begin{pmatrix} K \sin \frac{\pi}{4} \cos \alpha \\ K \sin \frac{\pi}{4} \sin \alpha \\ K \cos \frac{\pi}{4} \end{pmatrix} \quad (7.4)$$

$$= \begin{pmatrix} K(\sin \theta_f - \frac{1}{\sqrt{2}}) \cos \alpha \\ K(\sin \theta_f - \frac{1}{\sqrt{2}}) \sin \alpha \\ K \cos \theta_f \end{pmatrix}. \quad (7.5)$$

With $\mathbf{k}_f^{\text{pseudo}}$ defined a plot can be made of $I(k_x^{\text{ps}}, k_y^{\text{ps}})$ that will display a representation of the reciprocal lattice.

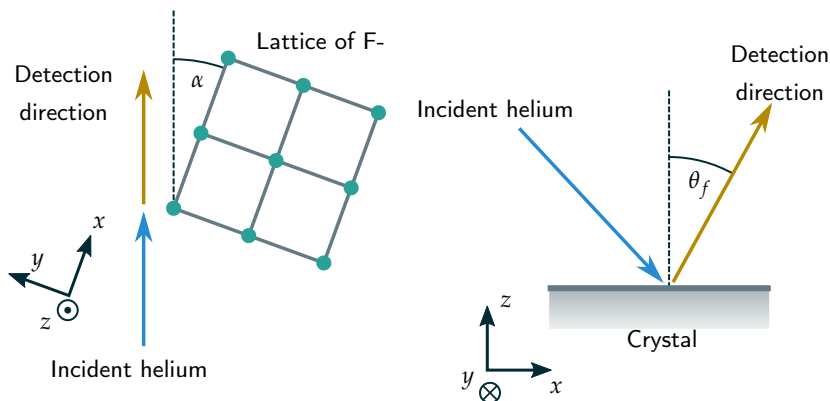


Figure 7.6: When the sample is rotated the lattice of the crystal shifts, define a coordinate system that rotates with the crystal allowing a 2D diffraction scan to be plotted as a function of the change in the surface k -vector relative to specular.

7.3.1 Simulation of LiF diffraction

To aid with the interpretation of the data, and to ensure the measurement process is fully understood simulated diffraction patterns have been undertaken. First the diffraction pattern of LiF needs to be known and provided as an input to the ray tracing framework. With the appropriate detection geometry ray tracing simulations can then generate SHeM diffraction scans.

While predicting the locations of helium diffraction peaks is as simple as applying the modified form of Bragg's law presented in figure 7.1 and equation 7.1, the relative intensity of those peaks presents more of a challenge. Multiscat[83] is a numerical code that calculates diffraction peak intensities from a provided atom-surface potential using close-coupled methods to solve the Schrodinger equation. Potentials for the He-LiF potential have been developed by Celli et al.[107] from diffraction measurements and by Riley et al.[106] using He-3 Spin Echo. The Celli potential is used here as it was developed for He-4 and there is some evidence of differences in diffraction for He-3 & He-4[110]. The MultiScat simulations used to generate the simulated diffraction scans presented here were performed by Boyao Liu[] and linking to previous ray tracing discussion in chapter 2.

MultiScat provides the relative diffraction peak intensities for each p, q peak in K space. In order to utilise them in ray tracing the spatial locations of diffraction peaks need to be calculated and arbitrary peak intensities need to be provided as simulation parameters. Functionality to scatter using a diffraction pattern was implemented by D Serement[59], however their model did not allow importing of diffraction peak intensities or general spatial manipulations of the sample. Arbitrary intensities along with arbitrary sample rotation – both required to model the SHeM spot profile measurements – required the implementation of a new mode of scattering with a large number of parameters (the peak intensities) and the introduction of surface lattice vectors in the main simulation coordinate system as an intrinsic component of the surface representation.

7.4 LIF DIFFRACTION SCANS

A small, ~ 2 mm square crystal of LiF was cleaved in air and as quickly as was feasible was mounted on a sample stub and placed in the SHeM sample chamber. Figure 7.7 shows a helium micrograph of the LiF crystal with the locations that were used for spot profile diffraction labelled. The majority of the small crystal was observed to be roughly flat with some distortion near the edges, all spot profiles were taken on the flat looking region of the sample. In order to confirm the functionality of the new point tracking algorithm a series of images were taken at significantly different z and α values, it was found that tracking worked to within $\sim 30 \mu\text{m}$, a few times larger than the beam width, but given the flat and uniform nature of the

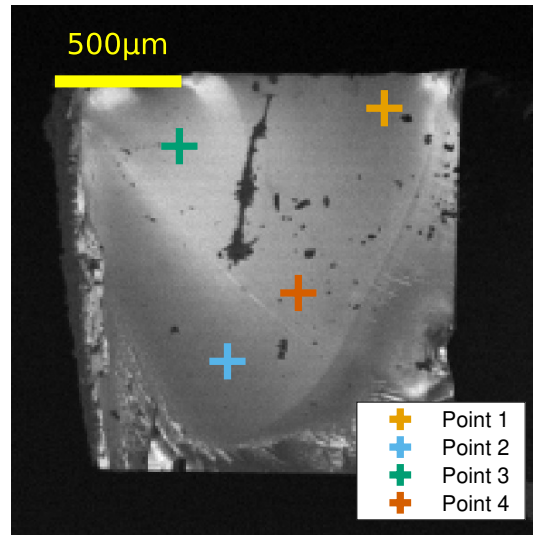


Figure 7.7: Locations on the cleaved LiF crystal of the spot profile pseudo-diffraction scans.

regions of sample chosen to acquire data from, this level of accuracy was considered sufficient.

Partial diffraction scans from the 4 points on the sample are displayed in figure 7.8, demonstrating that the same diffraction process is occurring across the whole flat region of the sample as expected. After conversion to k space linear interpolation has been applied to the data in order to create a uniform grid; the same approach is used in all 2D plots in k space presented in this chapter. The cubic structure of the lattice is clear from the square pattern of peaks that is observed, and the $(\bar{1}, \bar{1})$ peak is clearly the most intense, while the peaks that result from a k displacement from only one or other of the reciprocal lattice vectors (those that are along the horizontal and vertical in the figure) are clearly of lower intensity. These intensity differences are reproduced in the simulated data in figure 7.10.

A full 360° diffraction scan from point 3 on the crystal is presented in figure 7.9. The symmetry of the pattern can be observed and the relative intensities of the peaks discussed in the previous paragraph are again clear. Figure 7.10 plot the results of ray tracing simulations of scattering from a perfectly flat LiF crystal. While the peak pattern and intensities of the experimental data does match the simulated data well, a noticeable discrepancy is observable in the absence of a 'specular ring' in (a). As the location of the specular peak is independent of the crystal orientation it should appear at the same z for all values of α , however, only hints of specular are seen at certain values of α with nothing being observed at other values. While the specular peak for LiF has been observed to have notably lower intensity than some diffraction peaks for various incident conditions[108], for the SNR of the present data it would still be expected to be visible. However the simulated data that presents a clear specular assumes a perfectly flat sample well aligned with the scattering geometry. Tilt in the surface of the crystal relative to the scattering

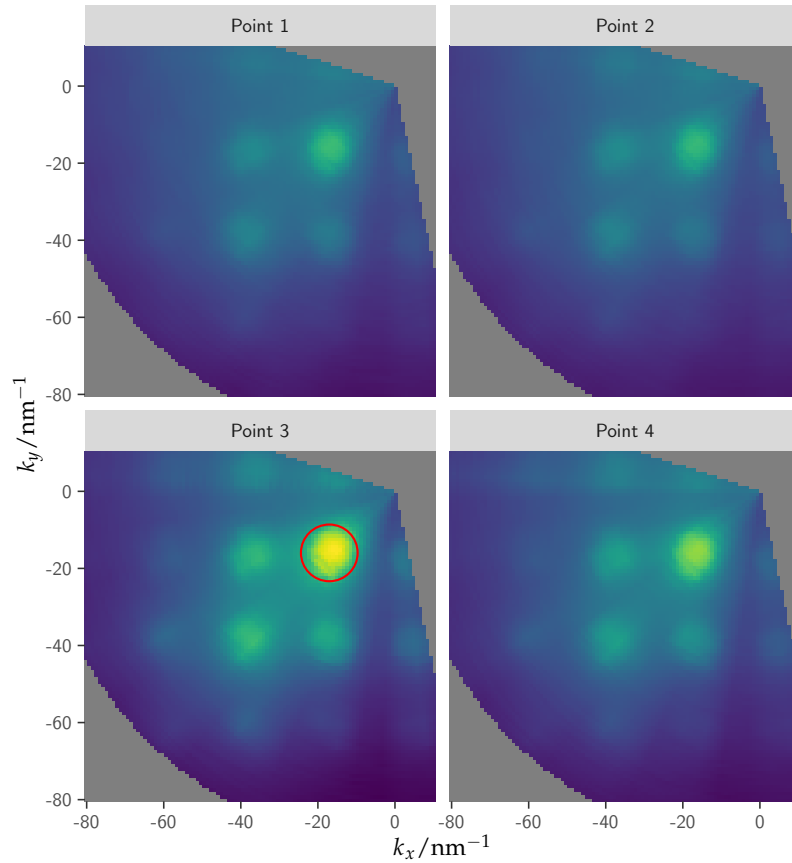


Figure 7.8: Pseudo-diffraction patterns from the 4 locations on the LiF crystal labelled in figure 7.7, all are from the flattest region of the crystal. That the same diffraction process is occurring across the sample is clear from these plots, and the cubic structure of the F- lattice can be identified from the square pattern observed. In addition a difference in intensity between the 'diagonal' diffraction peaks, those being displaced by both reciprocal lattice vectors, and the 'horizontal'/'vertical' peaks, those only being displaced by one *or* other of the reciprocal lattice vectors, occurs. The $(\bar{1}, \bar{1})$ is highlighted with a red circle.

geometry can lead to the absence of specular at certain orientations – §7.4.1 below examines the tilt of the current sample in detail.

By identifying the locations of peak intensity on the k-space plot of the He-LiF diffraction pattern the lattice spacing may be measured from the experimental data via

$$a = \frac{2\pi}{k} \sqrt{2} \quad (7.6)$$

where the $\sqrt{2}$ is necessary as the surface lattice constant is smaller than the bulk lattice constant. After identification of the diffraction peaks the average spacing between them was calculated giving

$$a = 401 \pm 6 \text{ pm}, \quad (7.7)$$

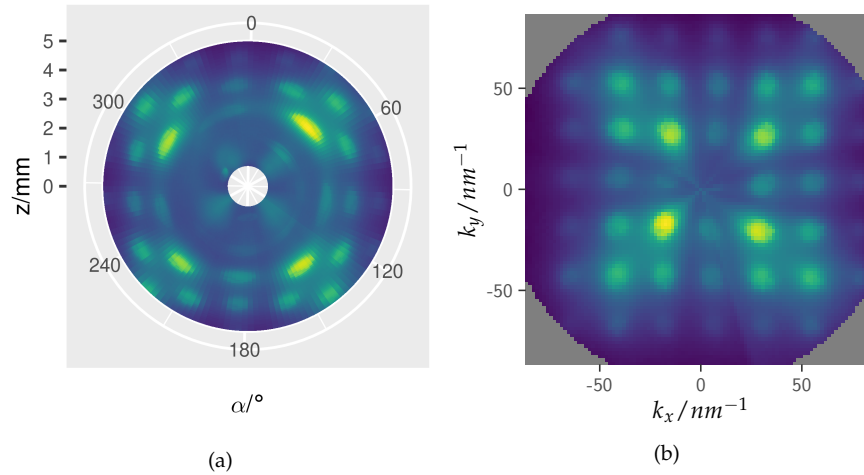


Figure 7.9: Taken from point 3 in figure 7.7 a full 360° spot profile at higher resolution as both (a) a raw polar plot and (b) a pseudo-diffraction pattern. By identifying the centre of diffraction peaks in (b) the lattice spacing was estimated to be 401 ± 3 pm, which is within error of literature values. Notably absent in (a) is the clear ring of specular that is seen in the simulated data in figure 7.10 which is attributed to sample tilt.

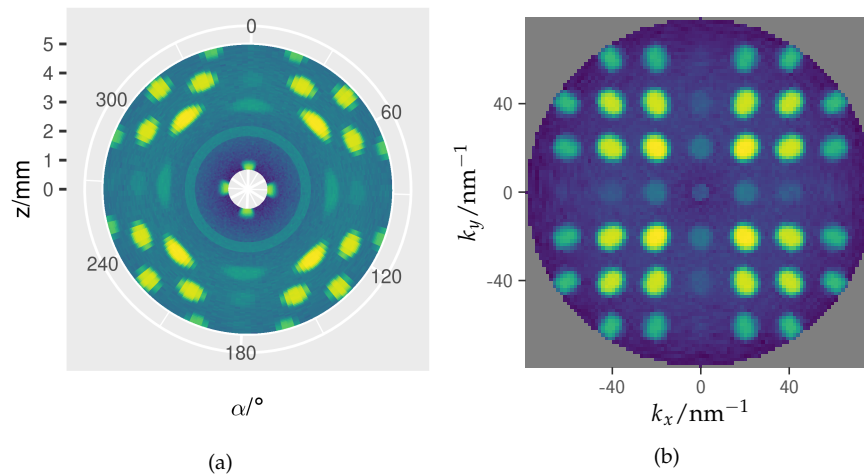


Figure 7.10: Spot diffraction plots of a simulated LiF sample. The peak intensities were calculated by MultiScat and ray tracing was used to calculate the detected signal. (a) shows the intensity as a plot of the raw z, α coordinates, note the obvious circle of specular that occurs regardless of the crystal orientation. (b) uses the coordinates $I(k_x^{\text{ps}}, k_y^{\text{ps}})$ which are wavevector components relative to the specular condition. The data taken at low z had to be cutoff in the wavevector plot, however as can be seen in the z, α plot only small amounts of information are present in the current set-up. In (b), and all k-plots, the data has been linearly interpolated onto a square grid in k space.

which is within experimental error of the literature value of 401.8 pm[111], and the value found by Estermann and Stern[8] of 402.3pm (as with the SHeM measurement they measured the F- reciprocal lattice). Despite the relative broadness of the diffraction peaks and the size of the acceptance angle of the detector aperture, a value for a of reasonable accuracy can be

gained due to the range of the k -space that can be probed through spot profiling in the SHeM.

7.4.1 Sample tilt

Evident in figure 7.9 and from in situ optical inspection of the sample is that the surface of the LiF crystal is not completely flat with respect to the scattering geometry of the SHeM. Photos taken with the in situ camera (that used to measure the working distance, §4.2.1.1) of the sample suggested a tilt of the range⁵ $\sim 2^\circ - 8^\circ$. While further ex situ investigations could inform on the overall tilt of the sample relative to the stub it was mounted on, they will not account for the exact *local* orientation of the crystal at the scattering point, or any slight misalignment in mounting the stub to the fixed SHeM stages. Therefore a local tilt of the sample is estimated from the diffraction pattern observed.

Using the same identified peak centres as was used for the estimation of the lattice spacing the offset of the k_x^{ps} and k_y^{ps} diffraction pattern in 7.9 (b) was estimated to be $\Delta k_x = 6.8 \text{ nm}^{-1}$ and $\Delta k_y = 3.8 \text{ nm}^{-1}$. It was estimated from these offsets that the local sample tilts are $3.8^\circ \pm 0.5^\circ$ in x and $2.1^\circ \pm 0.5^\circ$ in y . The approximation assumes that any mis-orientation of the sample itself are significantly greater than any misalignment of the sample positioning stages.

Figure 7.11 gives the results of the simulation with the introduction of the sample tilt. The offset of the diffraction pattern is reproduced in the simulation, as is the fragmented specular peak that only appear at certain values of α rather than the specular ring that appears in the ideal case (figure 7.10). The general shift of peaks is also seen in the (α, z) plot at larger values of z .

7.5 'LIGHT FIELD' VS 'DARK FIELD' IMAGING

With ordered scattering, in the form of atom diffraction, being demonstrated in SHeM, the possibility of different imaging modes arises. By changing the orientation of the sample and the detection angle imaging can be performed where detection is near a diffraction peak, near specular, or not near any intensity peak. Choosing to image where the average sample surface will be orientated such that the average scattering condition is near a diffraction peak, will enhance contrast from regions that slightly deviate from either the crystal arrangement or present slightly different topography. Alternatively imaging where the average scattering condition is away from a peak in intensity will result in more muted contrast and an image that will emphasise significant topography over subtle changes, overall contrast in the second case will be closer to the diffuse topographic contrast considered in chapter 5. These

⁵The camera is not set up in such a way to attempt accurate measurements of orientations.

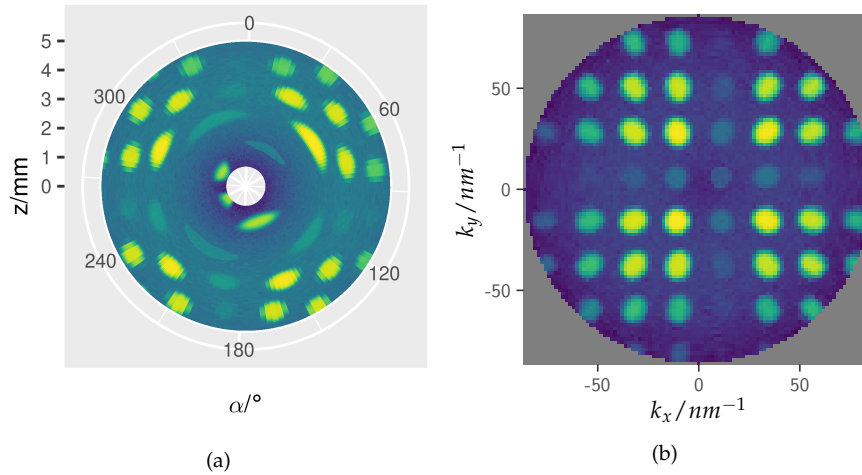


Figure 7.11: Ray tracing simulations of a diffractive LiF surface with an introduced sample tilt. The offset in k space and the fragmentation of the specular observed in the experimental data are both reproduced in these simulations.

two imaging modes are analogous to dark field and light field imaging in electron microscopy. For samples displaying a significant specular a third mode arises by placing the detection condition near the average specular condition: one that is highly sensitive to small changes in topography but not to crystallographic changes.

Two modes of imaging are presented in figure 7.12. (a) with the average detection condition near a diffraction peak, and (b) with the average detection condition away from any diffraction peak. Figure 7.12 (a) shows enhanced contrast, with small deviations away from the flat surface easily visible, while (b) shows more muted contrast, with only significant deviations away from the flat surface having an intensity noticeably bright or dark.

7.6 SUMMARY

Improved angular resolution and sample rotation were introduced to the SHeM allowing 2D diffraction scans to be performed with sufficient angular resolution to distinguish individual diffraction peaks. A small, cleaved, lithium fluoride crystal was used to gather the first microscopic atom diffraction patterns and to investigate different imaging modes that the SHeM can operate in. Measured diffraction patterns were consistent with the literature values of the LiF lattice spacing and the cubic structure of the F^- lattice which helium atoms are sensitive to. Despite the reactively poor angular resolution compared to traditional atom scattering apparatus, the lattice spacing measurement was of reasonable accuracy due to the large domain of k -space accessible to the SHeM. Displacement of the diffraction pattern was shown to be a result of sample tilt and was consistent with simulated data. The potential of data normalisation to inform on the underlying diffraction

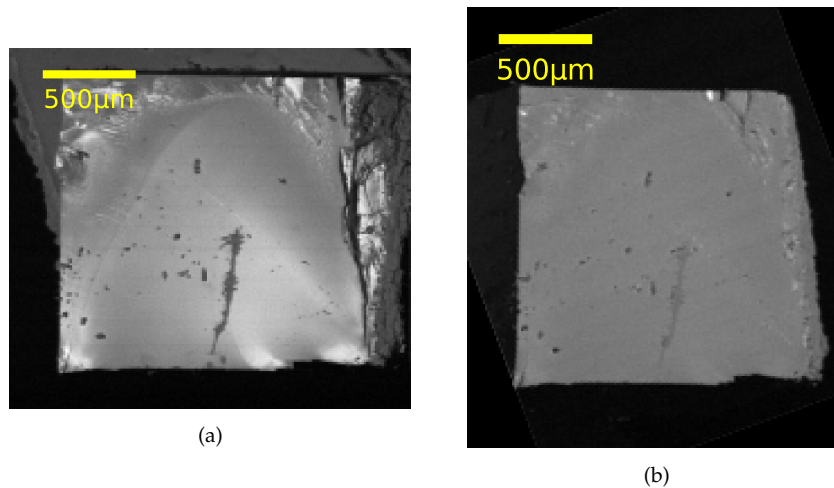


Figure 7.12: SHem images of LiF taken with, (a) the average detection condition near a strong diffraction peak and, (b) taken with the average detection condition away from any diffraction. The enhancements in contrast are clear in the 'diffractive' image. Image (b) has been rotated into the same orientation as image (a).

pattern was demonstrated, and is likely to be of key importance with future investigations.

A couple of shortcomings of the current measurements may wish to be addressed for future experiments, these are summarised below. First is the range of motion that enables the detection angle to be changed, the current set-up is not capable of measurements with detection angles much greater than 45° . An alternative pinhole-plate that moves the pinhole further away from the sample would allow a greater range of detection angles. Second is the point tracking method. The method currently employed was sufficient for the large pinhole used, $10\ \mu\text{m}$, especially with the highly uniform single crystal imaged. However more accurate tracking will be needed as the resolution is pushed down and with poly-crystalline samples. Third is the level of alignment of the crystal surface with the sample stages and detection geometry, for the current sample it was estimated that there was misalignment of $\sim 5^\circ$, which led to difficulty in measuring the specular peak. For future measurements methods for improving the alignment will be desirable. Finally LiF is one of a relatively small number of surfaces that present helium diffraction patterns without in-vacuo preparation. Future measurements on samples such as graphene or metallic sample will likely require at the least the ability to temporarily heat the sample. A small heater could be incorporated into a sample stub without needing to re-design the overall sample environment.

With SHem now capable of differentiating between diffraction peaks new imagining modes roughly analogous to dark field and light field imagining in TEM arise. In addition measuring the diffraction pattern itself from microscopic spots furthers the analogy with electron microscopy, in particular EBSD (electron backscattered diffraction) in SEM and diffraction mode in

TEM/STEM. Combining the novel modes of SHeM operation presented here with the established topographic imaging mode that utilise diffuse scattering completes the analogy between electron microscopy and helium microscopy: the basic modes in electron microscopy all have a roughly equivalent mode in SHeM

This chapter has demonstrated the ability of the SHeM, with suitable adaptations, to perform crystallographic measurements of diffraction patterns, and discusses different modes of imaging arising from contrast due to diffraction. As diffraction makes direct use of the unique thermal energy helium probe it is hoped that it will be the start of a fruitful area of study in the near and more distant future. The next chapter returns to topographic contrast and makes use of the observations in chapter 5 to propose a technique for measuring the 3D topography of samples using only SHeM micrographs.

HELIOMETRIC STEREO: 3D RECONSTRUCTIONS FROM SHeM IMAGES

One of the key conclusions of chapter 5 was that a diffuse scattering distribution centred on the surface normal is a good approximation to scattering in SHeM images of unprepared surfaces. These observations are consistent with Knudsen's cosine law which predicts a scattered intensity that varies only with the outgoing polar angle[54],

$$I \propto \cos \theta. \quad (8.1)$$

Knudsen scattering then implies that the detected signal for a particular pixel in the SHeM, I , is dependent primarily on the angle between the surface normal and the detector aperture. Given the relatively simple relation between surface orientation and signal that the cosine model presents, it becomes pertinent to investigate inverting the equation to infer topographic information from SHeM images. Clearly multiple images are needed due to the number of degrees of freedom present, and as the detection angle defines the intensity, multiple detection conditions are needed.

Lambert's cosine law for light has led to the development of a technique called *photometric stereo* where the light intensities in a series of images illuminated from different angles are used to produce 3D reconstructions of the object being imaged[113, 114]. With appropriate modifications, a very similar technique may be applied to SHeM images.

In this chapter, the method of *heliometric stereo* is introduced that uses the cosine-like scattering of atoms from technological surfaces to perform full 3D reconstructions of surface topography, with the point-by-point illumination of the sample in SHeM allowing for a straightforward implementation of the reconstruction process. The conditions that need to be met are considered, as are the similarities and differences between the helium case and the light case. The quality of the reconstruction for two test samples is investigated using ray tracing simulations, demonstrating a good level of reconstruction for modest topographies up to an aspect ratio of ~ 1 .

The development of the heliometric stereo technique that is discussed in this chapter was performed in collaboration with Adrià Salvador Palau of the Department of Physics and Technology in the University of Bergen. In addition to general discussions on the topic the specific contributions of Palau were to develop the first iteration of the heliometric stereo software used to perform

Work from this chapter has been published as 'True to size surface mapping with neutral helium atoms' by SM Lambrick, & A Salvador Palau et al. PRA 2021[112].

reconstructions (extensions to use experimental data, and general ease of used improvements, were implemented by the author), the development of the thresholding method to deal with masking, and naming the technique: ‘heliometric stereo’. The formalisation and adaptation of photometric stereo to helium microscopy was done jointly with roughly equal contributions. With the exception of figure 8.6, demonstrating the thresholding method, all final figures and results presented here were generated and prepared by the author. The author also performed all ray tracing simulations presented.

8.1 GENERAL METHOD: HELIOMETRIC STEREO

8.1.1 *The photometric stereo technique*

Photometric stereo relies on the assumption that a point on the surface of the sample will scatter light with a given angular distribution, known as a bidirectional reflection distribution function (BRDF), which gives the scattered intensity as a function of the incoming and outgoing angles [115]. If the camera position is fixed, the intensities recorded by the camera will depend only on the local surface orientation and the scattering distribution; and for the same material and surface condition, all points on the sample can be assumed to have the same scattering distribution.

If the bidirectional scattering distribution function is known, a series of images obtained by illuminating the sample from different directions can be used as intensity maps to infer the local surface orientation, and thus the local surface gradient. These gradients may then be integrated over the surface to give a 3D height map of the sample.

8.1.1.1 *Obtaining surface normals*

Photometric stereo techniques generally assume Lambertian scattering[53], a type of scattering that corresponds to a surface which is a perfect diffuse light scatterer [113]. Lambertian scattering is also referred to as cosine scattering, as the light intensity values recorded at pixel (x', y') in the camera image is

$$I_{(x',y')} = \rho \cos \theta = \rho \hat{\mathbf{n}} \cdot \hat{\mathbf{d}}, \quad (8.2)$$

as illustrated in in figure 8.1 (a) for scattering from position (x, y) on the surface. Here (x, y) is used to refer to a spatial position in a coordinate system of interest (could be arbitrary, but usually that of the sample with the z axis parallel to the overall sample normal) while (x', y') refers to a position in the image. Here, θ is the angle between the surface normal and the incident light source, $\hat{\mathbf{n}}$ is the unit normal to the surface, $\hat{\mathbf{d}}$ is a unit vector from the surface to the light source, and ρ is the albedo or reflectance factor for that point on the surface. For light the outgoing angle, χ , does not appear

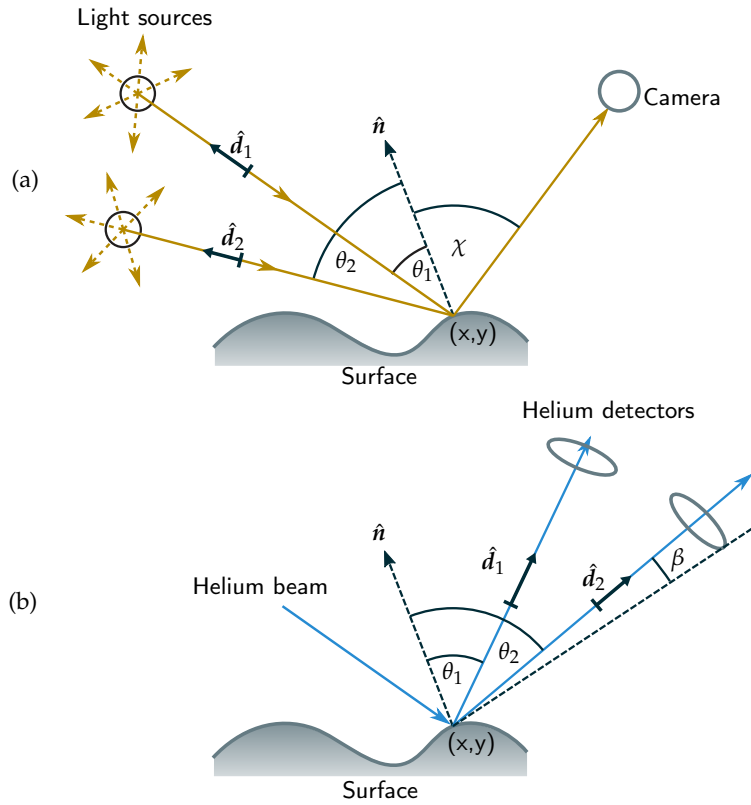


Figure 8.1: Correspondence between photometric stereo, (a), and heliometric stereo, (b). \hat{n} is the local unit normal to the surface, \hat{d}_i are the directions to the light sources or detectors. In the case of photography multiple light sources are used to generate images with different \hat{d} vectors, in the case of helium microscopy multiple detectors are used with a single focused illumination to give different \hat{d} by the reciprocity of focused beam imaging.

in the intensity equation as the $\cos \chi$ dependence in the scattering is exactly compensated by the $(\cos \chi)^{-1}$ dependence from the projection of the surface area into the camera. Instead, the cosine term arises from the projection of the light source onto a surface at angle θ ; the area of surface that the light hits is proportional to $(1/\cos \theta)^{-1}$.

Where there are multiple light sources the set of intensity equations can be combined into a single matrix equation,

$$\vec{I}_{(x',y')} = \rho D \hat{n}, \quad (8.3)$$

in which \vec{I} is a m -dimensional vector of pixel intensities corresponding to m images taken from those different light sources. D is a $m \times 3$ matrix containing the normalized vectors connecting the light sources and the point (x', y') for each image. As there are three degrees of freedom in the system there have to be at least three non co-planar vectors in D for a unique solution to exist, corresponding to three distinct light sources. The surface normals, \hat{n} ,

and reflectances, ρ , can be obtained from equation 8.3 by solving the system of linear equations for each pixel in the image,

$$\rho_{(x',y')} = |\mathbf{D}^{-1}\vec{I}_{(x',y')}|, \quad (8.4)$$

$$\hat{\mathbf{n}}_{(x',y')} = \frac{1}{\rho}\mathbf{D}^{-1}\vec{I}_{(x',y')}. \quad (8.5)$$

If the height of the surface can be described by a function of the lateral position, *i.e.* $z = f(x, y)$, then

$$\hat{\mathbf{n}}(x, y) = \nabla F(x, y, z) = \nabla[z - f(x, y)]. \quad (8.6)$$

Thus once the surface normals are found, the gradient field given by equation 8.6 may be integrated to obtain an equation $z = f(x, y)$ of the surface profile, *i.e.* a topographic map of the sample.

8.1.1.2 Surface reconstruction from normals

The gradient field in equation 8.6, can be integrated using established methods from the field of surface reconstruction. Here Harker and O'Leary's MATLAB toolbox is used[116]. For a more detailed explanation and mathematical proofs their work should be referred to [117, 118] as only a brief outline is given below.

A least squares approach is used to find the matrix of heights Z that upon derivation with respect to x and y gives the least distance from the measured gradient field, given by the normals $\hat{\mathbf{n}}$. The discrete derivatives of Z can be written as $L_x Z$ and $Z L_y^T$. The matrices \hat{Z}_x and \hat{Z}_y represent the *measured* gradient field given by $\hat{Z}_x = n_x/n_z$, $\hat{Z}_y = n_y/n_z$. Thus, the least squares minimization corresponds to minimizing ϵ :

$$\epsilon = \|\hat{Z}_x - Z L_x^T\|_F^2 + \|\hat{Z}_y - L_y Z\|_F^2, \quad (8.7)$$

where $\|\dots\|_F$ represents the appropriate norm. Expanding and differentiating to minimize ϵ yields an equation with a unique solution [117].

8.1.1.3 Image projection

A complication of the photometric stereo technique is the way a physical object is projected onto an imaging plane so that pixel indices can be related to physical coordinates. In a camera (without the use of a telecentric lens) a perspective projection is formed, meaning that displacements on the image do not correspond directly to physical distances: the physical distance between two pixels changes across the image depending on the distance to the object and the focal length of the lens used. Helium microscopes, however, are pixel-by-pixel imaging instruments that necessarily produce images in an orthographic projection: the image is formed through the two-dimensional rastering of the sample by fixed distances between pixels. Thus there is

a fixed correspondence between pixel locations in an image and physical locations on the sample.

In either photography or helium microscopy the sample is mapped onto a plane with a projection. In a photograph the object is projected through the lens onto the camera sensor, the axis of projection is then normal to the camera. The projection axis corresponds to the z axis in equations 8.2-8.6. Translating to helium microscopy the z axis in the heliometric stereo method is parallel to the beam and the points x', y' used in the method are defined by the direction of the beam, and not necessarily in the plane of the motion of the microscope's nanopositioning stages. The implications of the projection have to be considered carefully when sample rotations are used to acquire extra 3D information on the sample (see §8.2).

8.1.1.4 Applying photometric stereo to helium microscopy

As discussed in chapter 5, Knudsen's cosine law is a good approximation for the scattering of helium atoms from unprepared surfaces in SHeM. Therefore the photometric stereo method can be translated relatively straightforwardly. Assuming cosine scattering of helium atoms from the sample surface, the scattered intensity into an element of solid angle $d\Omega$ is

$$dI_{(x',y')} \propto \cos \theta d\Omega, \quad (8.8)$$

where θ is the angle between the detector and the surface normal at the point (x, y) . The intensity reaching a particular detector is then

$$I_{(x',y')} \propto \int_{\Omega_D} \cos \theta d\Omega, \quad (8.9)$$

where Ω_D is the solid angle of the detector entrance aperture. In certain existing helium microscopes the detector apertures occupy a significant fraction of solid angle, covering a wide range of detection angles [2] so the extent of the solid angle needs to be considered. For an aperture occupying a suitable small region of solid angle the integral could be approximated by $\Omega_D \cos \theta$, however that is not generally the case for the current generation of helium microscope¹. For an aperture occupying a small circular region of the solid angle hemisphere ($< 5\%$ of the total hemisphere), with half-cone angle β and angle from the surface to the centre of the aperture of θ , it can be shown that the signal becomes (see §3.2.1)

$$I_{(x',y')} \propto \frac{1}{2} \pi \cos \theta (1 - \cos 2\beta), \quad (8.10)$$

¹An exception may be the high-angular-resolution modifications made for the measurements in Chapter 7, however that was at the expense of lateral resolution.

which also has a cosine dependency with θ . Thus, where detector apertures are very small or occupy circular regions of equal solid angle then the intensity detected in a helium microscope can be written as

$$I_{(x',y')} \propto \cos \theta = \rho \hat{\mathbf{n}} \cdot \hat{\mathbf{d}}, \quad (8.11)$$

which is the equivalent to equation 8.2. The application of the basic photometric stereo method in helium microscopes follows with $\hat{\mathbf{d}}$ defined as the unit vector from the point (x, y) to the detector aperture.

If, due to the practical considerations of design, the solid angles of the detector apertures are not all equal, or if the detectors do not have the same efficiency, the modification of equation 8.3 is

$$\vec{I}_{(x',y')} = \rho \hat{\Omega} D \hat{\mathbf{n}}, \quad (8.12)$$

where $\hat{\Omega}$ is a constant diagonal matrix containing the solid angles and detection probability of the various detectors and D and ρ have the same meaning as in equation 8.3. In practice the values in $\hat{\Omega}$ can be attained via a calibration of the detectors prior to the acquisition of the data.

8.1.2 Simulated helium images

Simulated helium micrographs were generated, using the ray tracing method introduced in chapter 2, to test the heliometric stereo method.

To demonstrate what can be achieved with present technology the simulations use a set-up that has dimensions similar to the recently constructed B-SHeM in Cambridge, with key feature of multiple detectors present and with the option for either normal incidence or 30° incidence. The simulated beam-source and detector geometry are comparable to the existing A-SHeM in Cambridge[3], although a larger source distance has been used. As shown in figure 8.2, the set up assumes a helium beam diverging from a circular virtual source, corresponding to the skimmer in a supersonic helium source. The helium microprobe is then formed by collimation using a pinhole of 2 μm diameter [119]. The ‘virtual source’ is assumed to be a uniformly emitting disc of radius 50 μm at a distance 50 cm behind the pinhole (*i.e.* rays are emitted from all elements of the surface and at all angles with the same probability). The large distance between the virtual source and pinhole, compared to the distance between pinhole and sample (1 mm), means that the beam has only a small divergence. Thus the spot size of the beam is approximately 2 μm , with a depth of field of several millimetres.

To obtain simulated images, four detectors were placed at 90° from each other and at 35° from the sample normal, with a normal incidence beam ($z = z'$), as shown in figure 8.2. Given these source and detection geometries, only the number of rays to use and the sample itself need to be provided to complete the simulation set up. The number of simulated rays were chosen

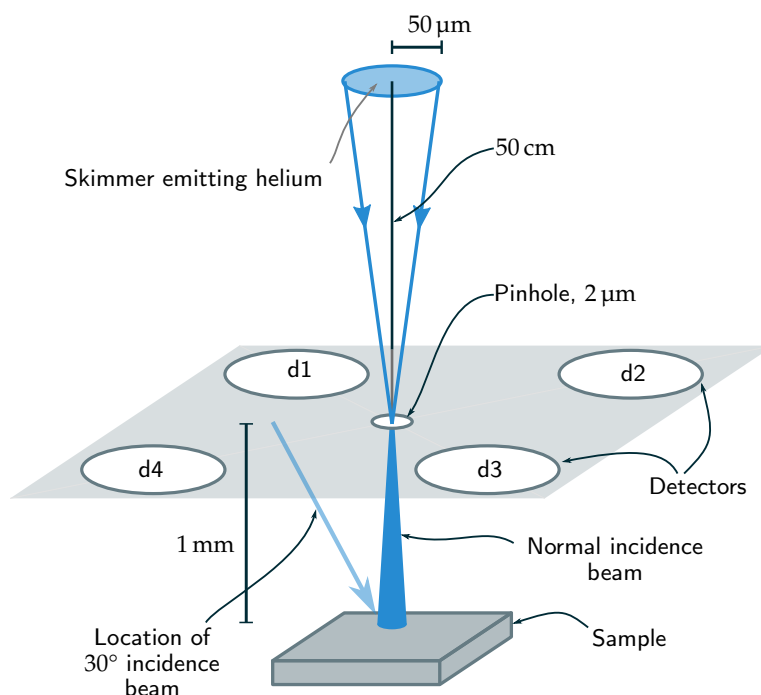


Figure 8.2: The simulation set up that was used to generate the images of the test sample and the model of the source used. Four detectors were placed on a plane equidistant around the sample with an angle of 35° to the sample normal. The beam rays are generated in the virtual pinhole with a divergent distribution assuming a circular uniform virtual source shown at the top of the figure (skimmer), for the non-normal incidence simulations the beam source was moved but the detectors were kept in the same locations.

to provide a realistic level of signal to noise (SNR) to recent experiments. The data from figure 1 in Lambrick et. al [78] – also panel 3 of figure 6.5 – was used as a representative experimental SHeM image. The darkest pixel in the image was assumed to be representative of the background signal and was subtracted, then the standard deviation and mean intensity from pixels on a flat region of the sample were taken to be the noise and the signal level respectively, giving an SNR of ~ 30 . All simulated images used below have equal or lower signal to noise ratios than that experimentally measured value.

8.1.3 Heliometric reconstruction

In order to test the heliometric stereo technique, a test sample containing a series of technologically inspired geometric structures was simulated: an octagonal pyramid with a depressed top, a rectangular pyramid, a cap of a sphere, a series of increasingly deep pyramidal depressions and a three-dimensional triangle. The feature sizes are all in the 5-100 micron range and have low aspect ratios ($\sim 0.1 - 0.4$), with detailed dimensions given in figure G.1 of appendix G. These geometries were chosen for different

reasons: The increasingly deep pyramidal depressions test the quality of reconstruction with depth. The octagonal pyramid with a depressed top tests how the reconstruction handles complicated geometries with a further depression. The rectangular pyramid has different slopes and is aimed to test the reconstruction precision with angle. The spherical cap is intended to test for the reconstruction of smooth geometries and continuously changing surface gradients. Finally, the three-dimensional triangle has vertical surfaces and tests reconstruction of geometries with abruptly varying heights. Due to their regular forms, these samples resemble artificial structures and it is notable that the sharp edges would make it very difficult to image them true to size using secondary electron emission based techniques.

Figure 8.3 illustrates the stages of producing synthetic helium images from the known sample surface and using them to reconstruct the surface: 1. the original sample surface is input to the ray tracing simulations; 2. four images are generated from the four detectors, it can be seen that the lightest areas in the images point towards the respective detector while the dark areas point away. 3. the four images are then used to calculate the surface normals, by solving equation 8.5, which represent the gradient field of the surface. 4. finally, the gradient field is integrated to find a reconstructed surface. It can be seen that there is a good qualitative match between the original surface and the reconstructed surface in the first and fourth panels. The quantitative accuracy of the reconstruction is discussed below.

8.1.3.1 Accuracy of reconstruction

Figure 8.4 shows a normalised percentage error plot of the basic reconstruction shown in figure 8.3. The error has been normalised by the height of the tallest feature on the surface: the large pyramid structure on the bottom left. The overall RMS error was 2.4%, however there are sections of significantly larger error within the plot. It should be noted that the 2.4% RMS error will be a combination of an intrinsic error to the method and errors resulting from the noisy initial data (simulated images). Noise in the images will result in noise in the gradient field, which will relate in a non-trivial way to errors in the reconstruction. The impact of SNR is discussed further in the next section. Three line profiles comparing the original and the reconstructed surfaces are given in figure 8.5 to allow a more intuitive understanding of the errors. Noticeable discrepancies are the sharp edges on the central pyramid and the deepest of the trenches on the top left side of figure 8.3. Therefore it may be concluded that the reconstruction works well with two identified caveats, the first being surfaces that are parallel to the beam (vertical in the case of normal incidence) and hence do not get illuminated; and second multiple scattering: the deepest trench causes a significant amount of multiple scattering, which results in a loss of the well defined relationship between signal and surface orientation.

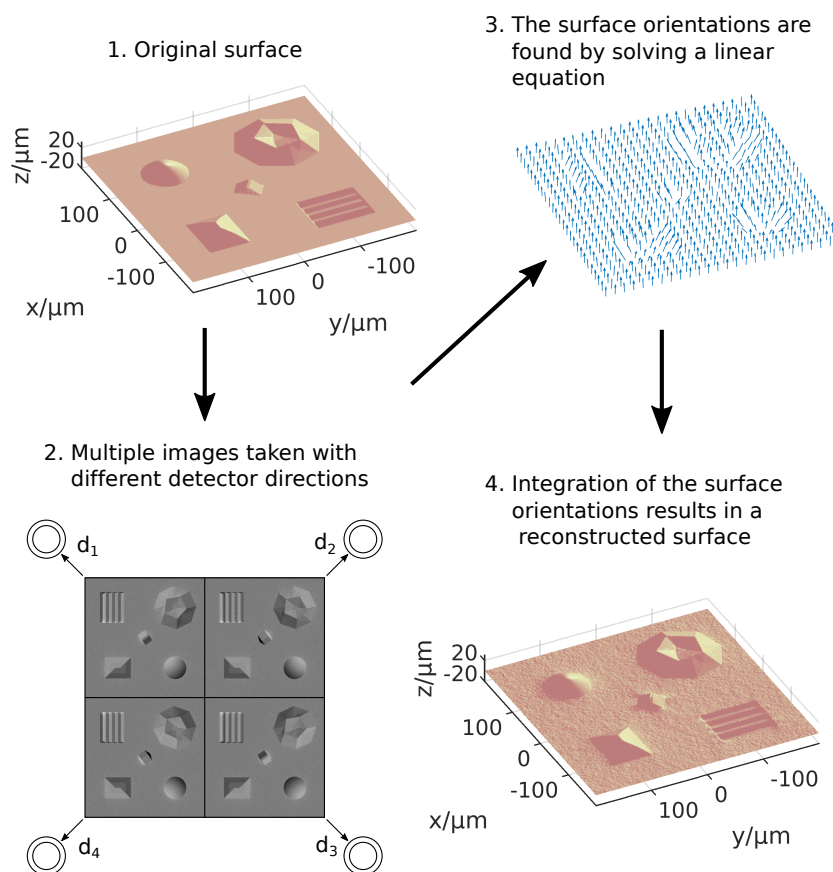


Figure 8.3: Overview of the basic heliometric stereo method. 1. The original sample. 2. The sample is imaged using multiple detectors placed in different directions to yield a series of helium images, in the example shown here, the set up shown in figure 8.2 was used to generate the simulated helium images. 3. Those helium images are used as the terms \vec{I} in equation 8.5 to acquire the surface normals. 4. Finally, as the normals to a surface are the gradient of that surface they may be integrated to give a reconstructed surface. The accuracy of the reconstruction presented here is discussed in §8.1.3.1.

8.2 EXTENSIONS AND FURTHER CONSIDERATIONS

8.2.1 *Non-cosine and multiple scattering*

As discussed in chapter 5 cosine scattering is a good first approximation for the scattering of helium atoms from technological samples. However, this type of scattering does not always fully explain experimental data. For example, the existence of non-topographic forms of contrast where the scattering distribution is not fixed across the sample necessarily require some deviation from cosine scattering – e.g. diffraction, Chapter 7 and potential chemical effects[38]. Heliometric stereo can be extended to more general forms of scattering by emulating pre-existing photometric stereo methodologies, for example by using a parametrised scattering distribution

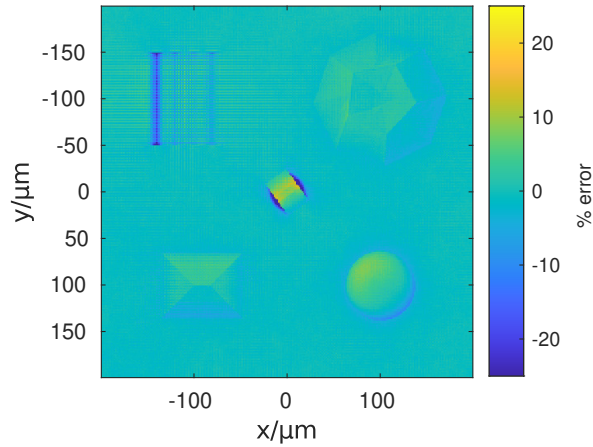


Figure 8.4: The percentage error between the reconstructed surface using the 4 detector geometry shown in figure 8.2 and the original surface (surface plots of both are shown in figure 8.3). The error has been normalised by the height of the tallest of the large pyramid structure on the bottom left of the sample. The RMS percentage error was 2.4% overall.

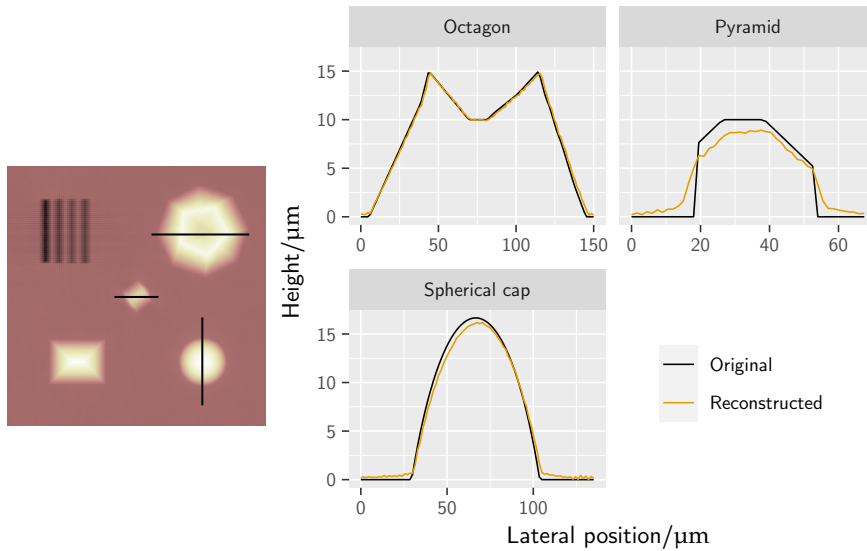


Figure 8.5: Three lines profiles extracted from the reconstructions presented in the figure 8.3. The locations of the line profiles are shown on the image of the original surface on the left. The high quality of the reconstruction in the case of the octagonal and spherical cap features is evident and the limitations near sharp edges can be seen in the case of the pyramidal feature.

that is fitted to the data (see, for example, [120–124]). In the current work, the albedo or reflectance factor is assumed to be sufficient.

An additional contrast feature of helium atom microscopy is the multiple scattering discussed in detail in chapter 6. Multiple scattering can cause regions in images to appear brighter, in particular where there is significant topography in the form of deep or tall features (high aspect ratios). In the present work it is assumed that over-constraining the problem combined with the albedo factor can largely negate the issue of multiple scattering for samples with modest topography. The implications of multiple scattering are considered further in section 8.3.4.

8.2.2 Masked regions

A significant contrast feature of helium microscopy is the presence of masking [16, 35, 45] – discussed in §2.3.1 – where the direct line of sight between the beam-sample intersection and the detector is blocked by another part of the sample rendering parts of the image dark.

While 3D information is coded in the size and shape of the masks, directly including masked areas in the reconstruction of the normals leads to substantial error. Where the images contain significant masking the simplest approach is to exclude the masked regions. However care must be taken not to under-constrain parts of the reconstruction. If only a small fraction of the image is masked ($\sim 1 - 5\%$ of an image) it is possible that they need not be excluded—the low intensity recorded in the masks would render the normal to be perpendicular to the detection direction, not a bad approximation where the regions concerned are small.

In the current work, masking is addressed using an automatic threshold method: masked regions of an image are excluded from the reconstruction by choosing an intensity level below which pixels are discarded. For a particular set of images the maximum value that the threshold value can take while still allowing a successful reconstruction is obtained by imposing that for every point in the image the following system of equations has at least three independent linear equations:

$$W\vec{I}_{(x',y')} = W\rho\hat{\Omega}D\hat{n} \quad (8.13)$$

where W is a diagonal matrix of 1's and 0's. The masking threshold is chosen as a scalar smaller than the threshold value that visually captures the masking contributions, which can be seen in the intensity histogram of the images as peaks in small intensity values, as is demonstrated in figure 8.6.

An alternative to the threshold approach, a weighting strategy is possible in order to handle masked regions, or regions with low signal to noise ratio. For example, one can weight regions with lower intensities less so that when a value of $I_{(x',y')}$ is fed into the linear least squares minimisation algorithm used to solve eq. (8.12), that value contributes less [125]. A straightforward way to achieve a weighting would be to make the weighting of pixels to monotonically increase with the intensity. Note that in Poisson statistics the

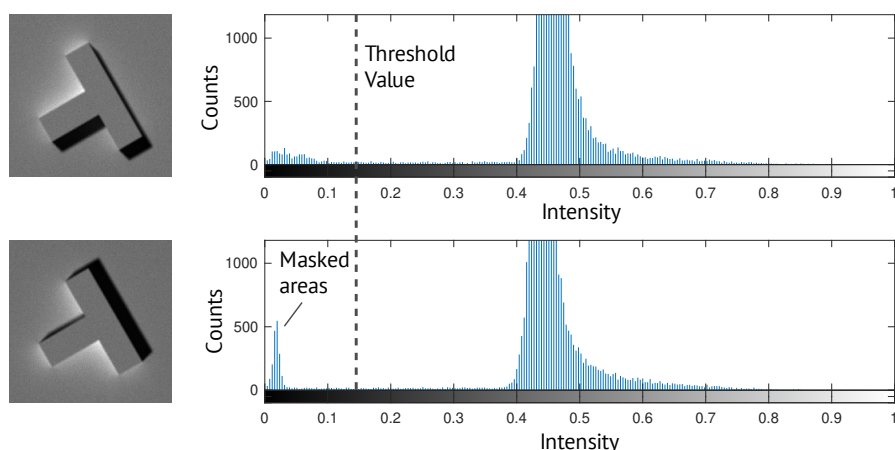


Figure 8.6: Using a threshold to cut out the masking in an image before use in heliometric stereo. On a histogram of intensity a cutoff value is chosen with any pixels having intensity below the cutoff not included in calculation of the surface normals. Figure created by A Salvador Palau.

standard deviation of the count rate is inversely proportional to its square root (higher intensities mean that the quality of the signal is better [126]).

8.2.3 Sample rotation

It is possible to obtain more independent observations of each point and improve the quality of the reconstruction by azimuthally rotating the sample. The same ‘trick’ can also be used to allow helium microscopes that do not possess enough physical detectors to perform heliometric stereo. Two different types of rotation are identified. First rotations performed about the beam axis, which allows a straight-forward mathematical implementation of equation 8.12 as the image plane, and hence coordinate system are the same throughout all images. Secondly there are other rotations, *not about the beam axis*. For rotation that are not about the beam axis the correspondence between points on rotated images becomes more complex, although there can be benefits of doing so.

8.2.3.1 Rotation about the beam axis

As helium microscopy produces images in an orthographic projection, rotating the sample about the beam axis mathematically corresponds to an inverse rotation of the detector position. By rotating the new images I so that each (x', y') coordinate in the image corresponds to the (x, y) coordinates of the rest of the images, the new data can be incorporated as an additional detector. Additionally, the corresponding vector \vec{d} has to be rotated in the opposite direction to the sample by the same angle.

Aligning two images of the same sample at different rotation angles can be done through image recognition software, or through a rotation of the

scanning pattern. Image recognition software sometimes requires human input, which can lead to error in the reconstruction. Alternatively, rotating the scanning pattern with the sample so that each pixel of the image always corresponds to the same position on the sample produces images aligned down to the accuracy and calibration of the positioning stages. The latter method is chosen here for the simulated data as there are no issues with the accuracy of the ‘virtual positioning stages’.

Applying rotations about the beam axis allows for i) the implementation of heliometric stereo with a single detector, and ii) a convenient method to obtain more data and reduce reconstruction error.

8.2.3.2 Rotation about other axes

For rotation about an axis other than the beam axis, the beam hits different regions of the sample at different angles, so that there is no complete bijective correspondence between the points of two images (see figure 8.7). On one hand, this makes it difficult to use sample rotation to obtain more independent data points for equation 8.5. On the other hand, rotations about axes other than the beam axis allows to image parts of the sample that otherwise would never intersect the incident beam as a result of shadowing.

The fact that shadowing prevents the beam from intersecting all sample points in every rotated image is not an impediment to recovering the 3D surface of a sample from a set of images taken at different rotation angles. To do so, several different sample surface reconstructions can be combined into a single surface after the application of heliometric stereo. Such an approach contrasts with rotating the sample about the beam axis, in which equation 8.8 is over-determined.

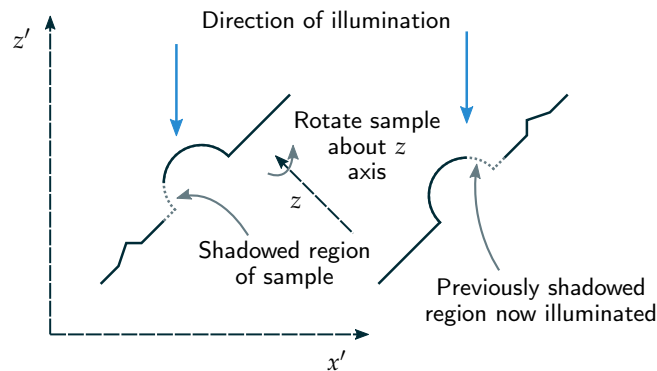


Figure 8.7: Sketch of the lack of bijective correspondence between helium microscope images in the case of rotation not about the beam axis. Regions of the sample that are shadowed can be imaged if we rotate about an axis other than the beam axis. The primed coordinates are the heliometric stereo coordinates with the z' axis parallel to the beam while the unprimed coordinates are those of the sample with z parallel to the overall sample normal.

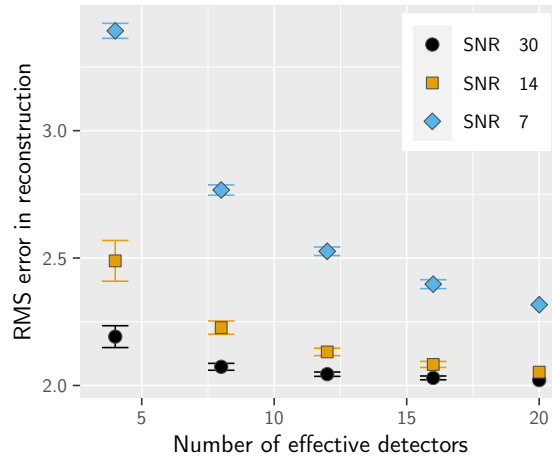


Figure 8.8: Plot of the reconstruction accuracy as a function of the number of effective detectors. It can be noted that improvements in SNR ratio have a similar impact as increasing the number of detectors by an equivalent amount: SNR improvement by a factor of 2 (and thus measuring time by ~ 4) has a similar impact as increasing the number of detectors by 4.

8.3 DETAILED RESULTS

8.3.1 Rotation to give more detectors

As discussed in §8.2.3.1, rotations about the beam axis can provide a greater number of effective detectors beyond the number of physical detectors. A simulation was performed with the same detector set up as described in figure 8.2, but with the sample rotated about the beam axis in intervals of 72° to give a total of 5 sets of 4 images. Reconstructions were then performed using different levels of signal to noise and different numbers of rotations (and hence effective detectors).

Figure 8.8 gives the root mean square error for different numbers of *effective detectors* – the product of the number of (true) detectors and the number of rotations – and different levels of SNR in the simulated images. It is noted that a similar improvement to the reconstruction is obtained both with an improvement of a factor of 2 in SNR or with an increase of the number of images by a factor 4. Since the noise in neutral helium microscopy is dominated by shot noise[14], both improvements require the same increase in acquisition time, however, multiple images with shorter dwell times may be more practical. There also seems to be a minimum level of error which is not improved by adding more information. That error is likely a result of failures of the method near vertical surfaces (such as around the central feature) or deep features that have a higher proportion of multiple scattering (such as the top left feature on the error map in figure 8.3).

Figure 8.9 breaks down the results from figure 8.8 by the number of true detectors. The same general trends can be seen as in the averaged plot however there are certain combinations that show poorer reconstructions

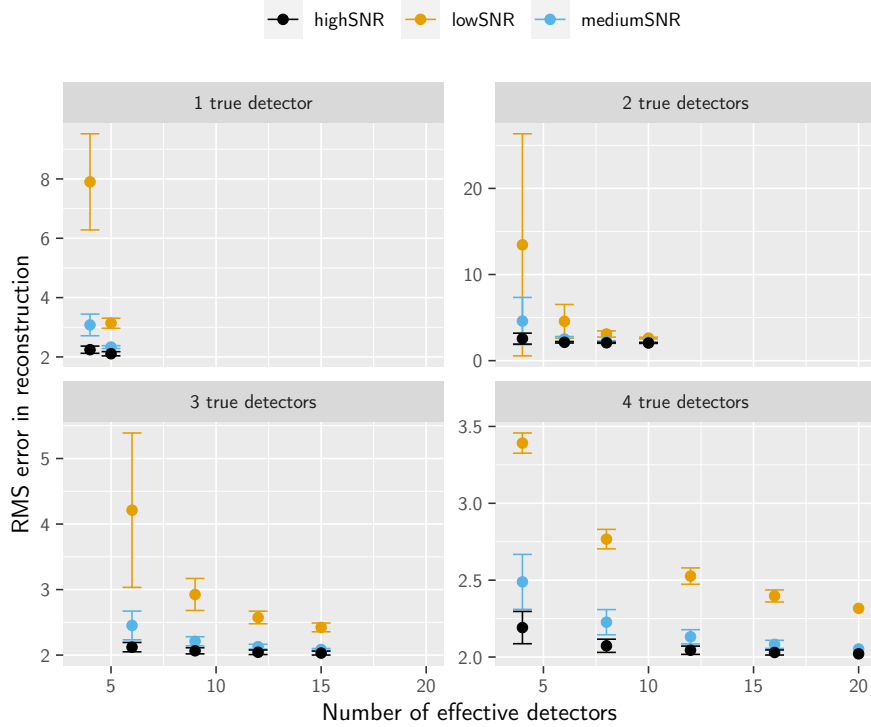


Figure 8.9: The root mean squared error (RMS) for the reconstructed surfaces as a function of the number of true detectors and the number of effective detectors for three different levels of signal to noise ratio (SNR) in the simulated images – note the y axis scales are not all the same. The error bars represent the standard deviation of the errors for the reconstructions: using different combinations of the available rotations. The RMS error tends towards a lower limit of $\sim 2\%$. The limit on the overall RMS error is due to elements of the sample that heliometric stereo cannot recover well with the cosine model, i.e. the sharp walls on the side of the central feature and the deepest trench on the top left feature (in the error map in figure 8.3).

than others, for example the lowest point for 1 true detector (5 effective detectors) performs noticeably better than the lowest point for 2 true detectors (4 effective detectors), with a very large spread depending on the exact combination of detectors used. Within the ‘4 effective detectors’ data point for ‘2 true detectors’ are various combinations of rotations and detectors, including some that place all the effective detectors close together and some that evenly spread them out. Those that place the effective detectors close together on the hemisphere produce significantly worse reconstructions and account for the poor average reconstruction and the large spread of error values. A similar phenomenon occurs for the ‘3 true detectors’, ‘6 effective detectors’ data point: the data points for higher numbers of effective detectors don’t present this behaviour because they do not cluster all the effective detectors in the same part of the hemisphere. These results highlight that for optimal reconstructions with the same quantity of data the detectors/effective detectors should be as evenly spread as is possible. For combinations that do

not have a large spread similar accuracies were observed for the same number of effective detectors with different numbers of true detectors, demonstrating the effectiveness of using rotations to simulate the presence of multiple detectors.

It was also found that reducing the number of detectors to 3 can result in good reconstructions, but can also cause the reconstruction to fail (if detectors 1, 2, & 3 are taken from figure 8.3 for example), demonstrating the importance of slightly overconstraining the problem to get reliable results.

8.3.2 *Using a single detector*

As discussed above heliometric stereo can be applied to a microscope with only a single detector, provided, rotations about the beam axis can be performed. It must be noted that all areas of a surface need to be covered by at least 3 and preferably 4 images and that due to the use of matrix-based techniques to reconstruct the surface from the gradient field rectangular images need to be used. This can be addressed either by i) padding the images, with the downside of some parts of the sample being unconstrained, or ii) using a special scanning pattern rotated counter to the sample rotation.

Single-detector heliometric stereo was successfully tested using the images obtained by rotating the sample but only using the first detector, effectively creating a reconstruction from 5 images with only a single detector, the images used for the reconstruction and the reconstructed surface are shown in figure 8.10. The method of rotating the scanning pattern along with the sample can be seen in the simulated helium images there. The possibility of implementing heliometric stereo using a single detector is important because the first generation of helium microscopes operate in a 1 detector configuration.

8.3.3 *Non-normal incidence*

The majority of the discussion thus far has orientated around a 'normal incidence' microscope where the beam axis is parallel to the average sample normal. However, alternative non-normal incidence angles are no impediment to performing heliometric stereo. In general, the incidence direction of the beam defines the z axis of the reconstruction method, and thus the scanning pattern used by the sample manipulation in the microscope should take this into account.

Once the surface is reconstructed it will appear tilted, as the helium images are taken 'from an angle'. The surface can then be rotated to match the original sample. To demonstrate the process, heliometric stereo has been applied to simulated images with an incidence angle of 30° and the results are shown in figure 8.11.

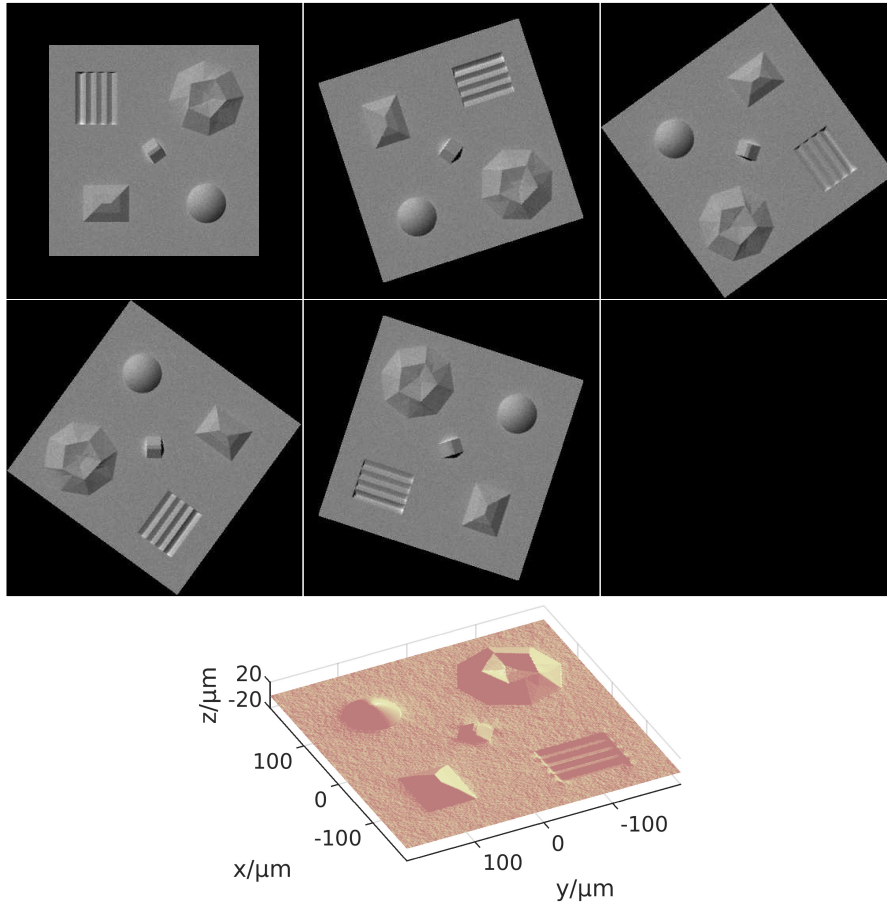


Figure 8.10: 5 images taken with a single detector while rotating the sample—note the masks face in the same direction across the images indicating the detector direction. The scanning pattern was rotated along with the images to minimise underconstrained parts of the sample (parts that have fewer than 3 data points), thus the same region of the sample is imaged in each case.

Non-normal incidence can be combined with sample rotation as described in §8.2.3.2: multiple reconstructions are combined rather than using the additional images to over-constrain a single reconstruction. Figure 8.12 compares the errors in the reconstructed surface for i) non-normal incidence and rotations with ii) a single non-normal incidence data-set and iii) a normal incidence data set. The reconstruction from a set of 4 images with a single sample orientation manages to capture a vertical surface in the central feature on the sample better than the normal incidence reconstructions (due to the surface not being parallel to the beam in the non-normal case).

However, as can be seen in the averaged image (rightmost in figure 8.12) simply averaging the 5 sets of data does not produce a better reconstruction than the normal incidence case (effectively adding more detectors), thus a more complex averaging mechanism is needed. A form of weighted averaging could be employed, however it will not be simple to identify which reconstructions to give a high/low weight when the original surface is unknown.

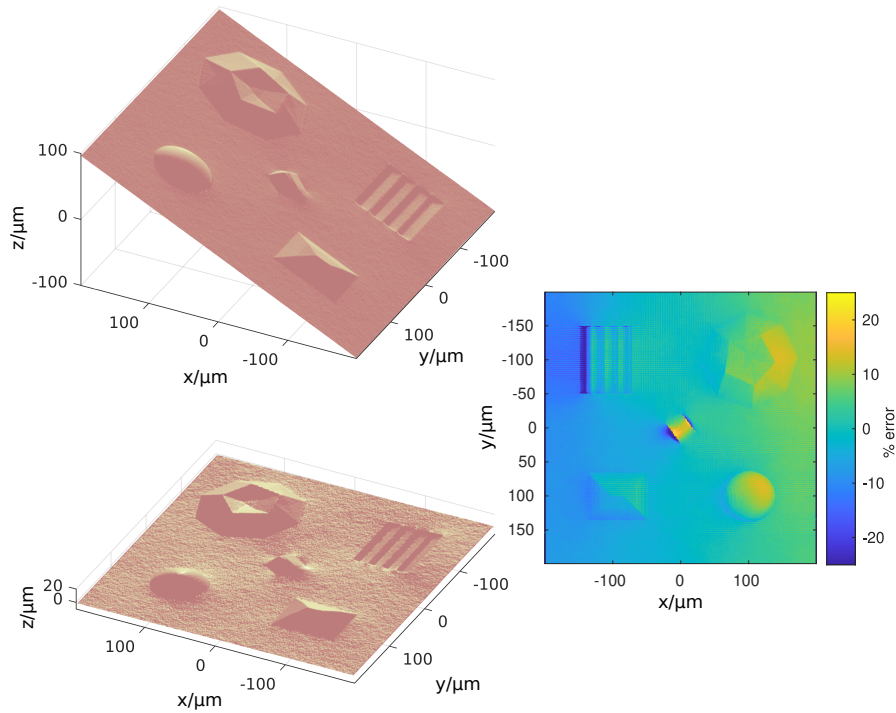


Figure 8.11: For non-normal incidence the initial reconstruction is tilted due to the sample being ‘viewed from an angle’ (top left) but may be rotated (bottom left) and then compared to the original surface. The root mean squared error (right) was 16.7%, the higher calculated error compared to the normal incidence case is due to a slight overall tilt, $\sim 0.4^\circ$ left on the sample after rotation which can be seen in the error image on the left. Correcting for the $\sim 0.4^\circ$ overall tilt by rotating the surface yields an overall RMS error of 3.4%, slightly greater but comparable to the error found in the normal incidence case.

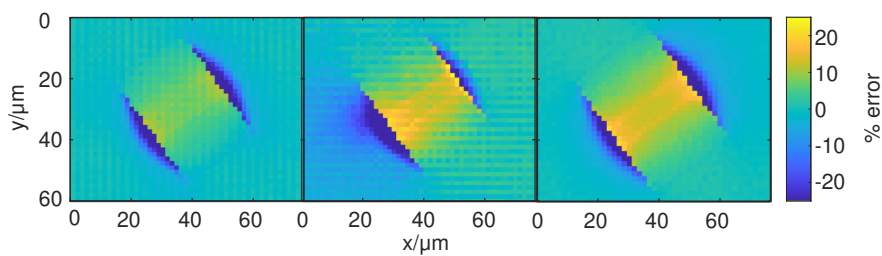


Figure 8.12: The errors in the reconstructed surface for: normal incidence and rotations (left), a non-normal incidence set of images without rotations (middle), and non-normal incidence with rotations (right). Note that the single orientation non-normal incidence reconstruction captures well one vertical surface and the other very poorly, the high error region being 1-2 pixel rather than 3 pixels wide—the beam intersected the right-hand side of the sample here. However, when all the different orientations are averaged in a simple manner the reconstruction loses the sharp verticals: non-normal incidence rotations do give us more accurate information, but simple averaging does not fully make use of them.

8.3.4 The impact of aspect ratio on reconstruction

The test sample considered in the previous section demonstrates the ability of the method to reconstruct surfaces with relatively low aspect ratios, where there is little masking or multiple scattering. In order to understand how the method works with higher aspect ratios and where masking and multiple scattering start to affect the reconstruction accuracy, a simple sample was designed with 4 rods whose height and slope were varied. Figure 8.13 shows an example with an aspect ratio of 0.6. The aspect ratio was quantified as the height over half the separation between the centres of two rods. For the simulated images used in this section the same virtual microscope set up was used as presented in figure 8.2.

To quantify the accuracy of the reconstruction two metrics are employed, first the height reproduction accuracy, measured as the difference between the height in the circular regions on the top and the four corners of the reconstruction, and second a measure of the shape reproduction accuracy. Figure 8.13 demonstrates that while under conditions where the height is not reconstructed to a high accuracy, it does appear that the shape of the surface is still reconstructed well. In order to quantify the accuracy of the shape reconstruction, allow the reconstructed surface heights to vary: $z_2 = \alpha z + \beta$ and perform a least squares minimisation to find α, β that fit the original surface best. The RMS error is then calculated for the scaled surface and normalised by the height of the cone structure.

Figure 8.14 shows how the accuracy of the reconstructed height of the rods, varies with the aspect ratio. To evaluate what proportion of the error was being introduced as a result of multiple scattering, reconstructions were also performed with only the single scattering contribution of the images as a comparison. Presented are the height accuracy both with and without multiple scattering and with and without applying thresholding as described in §8.2.2. It is notable that the error introduced by multiple scattering is present at all but the smallest aspect ratios, black points, but remains less

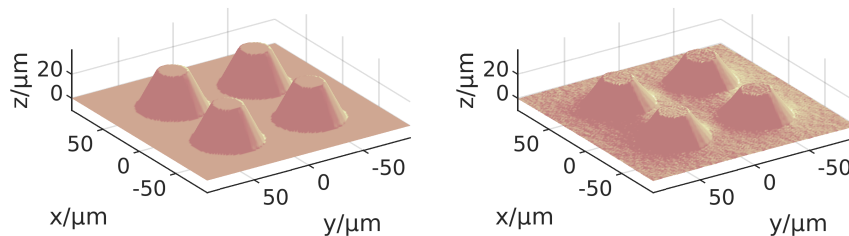


Figure 8.13: The original surface for the rod sample with an aspect ratio of 0.6 and the reconstruction with the microscope set-up shown in figure 8.2. It can be seen that there is a good qualitative reconstruction despite the height only being reconstructed as 75% of the original height. The other samples used in the aspect ratio investigation have same footprint and cone top but with varying slopes of the sides.

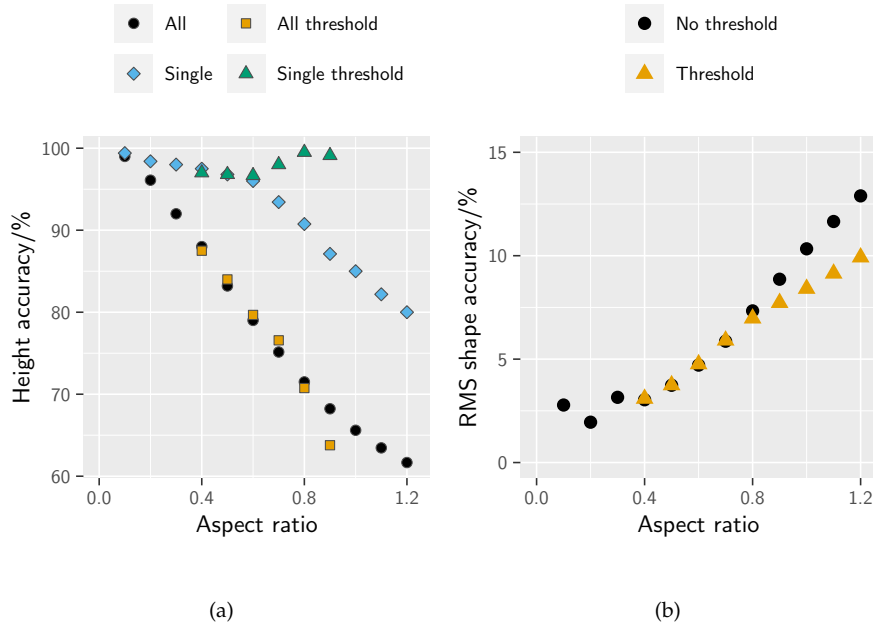


Figure 8.14: (a) Reconstructed height of the rod sample relative to the original surface, 100% represents the original height. Reconstructions were performed with and without multiple scattering, and with the thresholding method for removing masking introduced in §8.2.2. (b) The ‘shape error’ of the reconstructions. It can be seen that the errors remain below 10% for aspect ratios below 1 and below 5% for aspect ratio < 0.7. It can also be seen quantitatively that the application of thresholding to remove masked regions of the sample improves the accuracy of the shape reconstruction.

than 20% for aspect ratios less than 0.5. Using only single scattering, blue points, the reconstruction keeps a high accuracy until masking becomes a significant feature in the images. The application of thresholding does not appear to increase the accuracy of the reconstructed height, green points, though there is an effect on the shape as discussed in the next paragraph; however thresholding does improve the accuracy at high aspect ratios for the reconstruction where multiple scattering is excluded, purple points.

Figure 8.14 (b) gives the shape error as a function of aspect ratio, where it can be noted that the overall accuracy in the shape of the reconstruction remains better than 10% for all the samples below aspect ratio 1 and that for aspect ratios < 0.7 the RMS error is less than 5%. Overall there is good reproduction of the shape of the surface for low to modest aspect ratios in the sample. It is also shown that the application of the thresholding method discussed in section 8.2.2 improves the accuracy of the shape reconstruction where there is masking present. An example showing where the thresholding method improves the shape of the reconstructed surface is in figure 8.15 with an aspect ratio 0.8 sample. Here, without thresholding, masking distorts the footprint of the cone, but removing that masking from the reconstruction restores the footprint accurately.

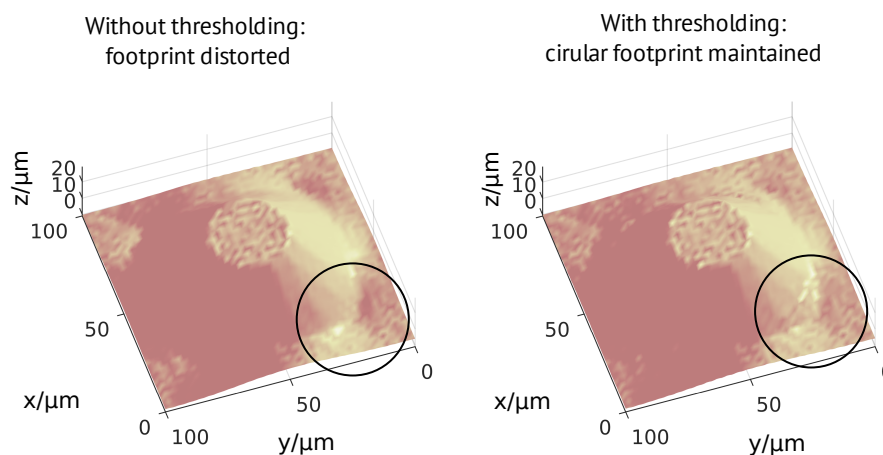


Figure 8.15: The reconstructed surfaces with and without thresholding applied for the aspect ratio 0.8 sample. It can be seen that the circular footprint of the cone is distorted where the thresholding is not applied and thus masked regions are included in the reconstruction. By removing the masked regions, the circular footprint is restored (see black circle).

8.4 DISCUSSION

8.4.1 Design recommendations

There are certain design principles that should be considered when designing a neutral helium microscope that is intended to perform heliometric stereo reconstruction. These considerations are given below and while some of them are necessary for the application of heliometric stereo to be possible, it should be noted that some may also be counter to other scientific or practical considerations.

First, in order to perform heliometric stereo without rotating the sample then at least 4 non co-planar detectors are needed. If 4 physical detectors are not possible then the ability to rotate the sample about the beam axis is required, which is likely to be easier with a normal incidence microscope, and in that case at least 2 detectors are recommended so that only one rotation is needed per reconstruction. More than 4 detectors may have benefits for difficult samples by allowing more aggressive thresholding and may allow the application of more advanced adaptations to heliometric stereo, but they are not necessary.

If at least 4 detectors are present then a non-normal incidence microscope would be more flexible as it allows the sample to be imaged from different directions giving more 3D information, it would also allow detection on the specular condition that may be desirable in other helium scattering experiments. The detectors should, as close as possible, occupy circular regions of solid angle to maintain the cosine assumption, and the solid angle of the detectors should be kept modest, as far as the signal level allows, in

order to reduce the possibility of ‘partial masking’ where only part of the detector is within line of sight of the sample. In order to keep the amount of masking modest that detectors should be placed not-too-far from the incidence direction to keep the amount of masking modest: no greater than $30 - 40^\circ$. All the above requirements are already met by the design of the B-SHeM.

An alternative, potentially ideal, design of a helium microscope for 3D reconstructions may involve detectors that can be rotated around the sample instead of fixed detector positions. Such a configuration would have a high degree of flexibility for both heliometric stereo and other experiments, however, such an instrument would be a major technical challenge that so far has not been demonstrated experimentally.

For a single detector microscope to perform reconstructions it is necessary to include the ability to rotate the sample about the beam axis to obtain a vector of intensities \vec{I} , which must be the key consideration if designing a microscope for heliometric stereo without multiple detectors. In practice enabling such rotations will likely mean designing a machine for normal incidence or one that can be adapted to operate at normal incidence.

8.4.2 Limitations

The main limitation of scanning helium microscopes is the difficulty of attaining an appropriate SNR, given the relatively low efficiency of neutral helium detectors. This low SNR together with the effect of multiple scattering can degrade the quality of the images and therefore of their 3D reconstruction. However, a high level of robustness to noise in images has been demonstrated in §8.3, with reconstructions being successful at SNR levels well below those observed in recently published SHeM images.

A further limitation of the presented method is its reliance on the diffuse scattering assumption. Although diffuse scattering seems to be the predominant scattering mode for neutral helium atoms scattering from technological samples, other scattering distributions are also to be expected. Deviation from diffuse scattering case can be separated in two sub-cases: that in which the scattering distribution is constant across the sample, and that in which it varies with position.

If the scattering distribution is expected to be constant but not diffuse, equations 8.2 & (8.3) and their dependencies must be re-written and it cannot be generally expressed as a matrix multiplication. Assuming a known distribution or distribution family, one can still numerically solve for \hat{n} and the distribution parameters using well-established methods [120–122]. If the distribution family (its parametric expression) is not known, a non-parametric solver can be used provided that there is enough experimental data [127]. Note that here the problem is to first find the function, f , so that $I = f(\hat{n}, \hat{d})$ where \hat{d} is known point-by-point and I is measured and then invert it.

If the parametric distribution varies across the sample, the problem is still solvable but significantly harder, as one must now establish the regions in which there has been a distribution shift. This problem has been addressed for light using the technique of orientation-consistency, that requires the measurement of sections with known orientation and similar scattering distribution [120]. Similar techniques could be potentially implemented for helium, especially in the case of technologically-inspired samples.

Masking and multiple scattering were highlighted as issues with heliometric stereo, however, it has been shown that where they are only present in small parts of a set of helium images, the overall reconstruction is still good. The thresholding method has been shown to improve the reconstruction results by removing masked regions of the sample from the reconstruction where there is sufficient constraint of the linear problem. Cases of large amounts of masking and significant regions of multiple scattering will occur where higher aspect ratios are present in the sample and so the reconstruction accuracy will be limited. Two potential solutions to the aspect ratio limitation present themselves. First given the ability of the ray tracing framework to model multiple scattering an iterative approach may be suggested as a route of further work, where scattering from the initial reconstruction is simulated with ray tracing and the multiple scattering signal then removed from the original images. Second additional 3D information could be used to inform the reconstruction, for example the height of specific features acquired using a method that is independent of both masking and multiple scattering via either triangulation-based photogrammetry or through the masks themselves that encode topographic information – as was done in §6.3 to measure the depths of a series of trenches.

8.5 METHODS OF IMPLEMENTATION

8.5.1 *A-SHeM*

The fundamental requirement for applying heliometric stereo is that multiple images, with the same optical projection, of the sample can be taken with different detection directions. As discussed in §8.2.3.1 rotations of the sample about the beam axis are equivalent to rotations of the detection direction, and so the required images can be taken without the need for multiple detectors. As rotations may be used in place of multiple detectors heliometric stereo may be applied to single detector microscopes such as the A-SHeM provided the appropriate rotations are possible.

One practical way of achieving the necessary rotations is to have a microscope operating in a normal incidence configuration, then rotations about the beam axis will correspond to rotations about the z axis of the sample manipulation. The correspondence between the sample manipulation coordinates and the beam axis makes the mounting of a rotation stage simpler – the same

rotator and mounting can be used as in §7.2.2 – as well as ensuring rotations do not cause interference between the sample and the pinhole plate.

Introduced in section §4.3 is a design of pinhole plate that rotates the sample mounting to modify the A-SHeM to operate in a normal incidence configuration. Figure 8.16 presents a renders of (a) the ‘standard’ 45° incidence pinhole plate, and (b) the normal incidence pinhole plate along with the positioning nano-stage assembly, highlighted are the beam axis and the rotator stage. From the renders it can be seen how the normal incidence plate rotates the stage assembly to allow rotations about the same axis as the beam. As all sample manipulation in the A-SHeM is mounted off an L-bracket attached to the pinhole plate, no modification is needed to the sample manipulation stages or the scanning software further than what was already implemented to allow the measurements presented in chapter 7, allowing for straightforward changes in operation between 45° incidence and normal incidence.

A proof of principle heliometric stereo reconstruction has been performed using the normal incidence pinhole plate and sample rotations – the installation of the normal incidence pinhole plate and the gathering of experimental data was performed by A Radić, while the author adapted the software for experimental data and performed the reconstruction that is presented. As a test sample an aluminium potassium sulphate crystal was grown on the surface of a sample stub and imaged at five different rotation angles. Figure 8.17 shows the set of SHeM images collected and a heliometric reconstruction of the crystal. Overall the reconstructed surface dimensions matched well with independent SEM measurements taken of the crystal. For more details on the experimental produce and a comparison of the reconstructed dimensions with those observed in SEM, A. Radić’s thesis should be referred to[72].

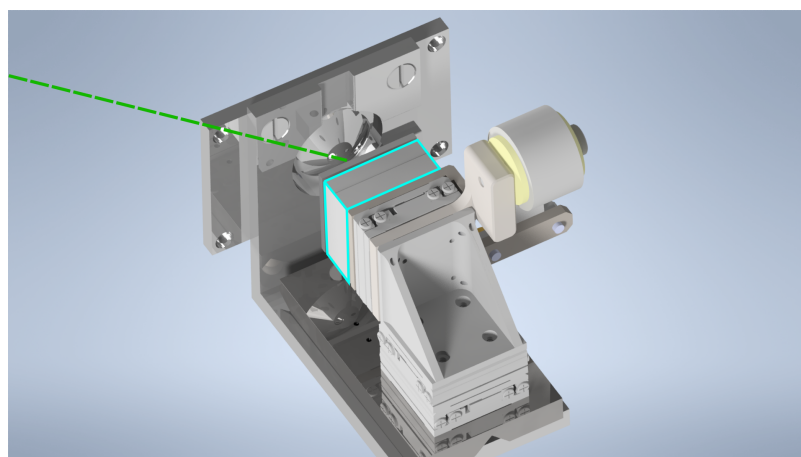
8.5.2 *B-SHeM*

8.5.2.1 *With 4 detectors*

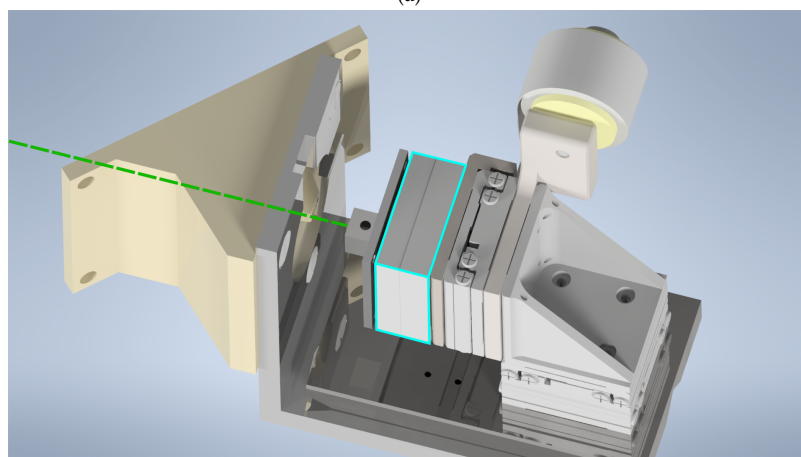
The B-SHeM design has the potential for four physical detectors allowing heliometric stereo to be applied directly to images produced by the instrument. In its default configuration the microscope will operate at 30° incidence so the appropriate perspective adjustments and re-orientation of the around the beam sample will need to be applied – see §8.3.3 for details. It would, however, be possible to use an alternative three dimensional scanning pattern that could provided pseudo-normal incidence, or any angle between 30° and 0°, and therefore overall surface tilt in the sample would not need to be considered.

8.5.2.2 *With fewer than 4 detectors*

In its initial configuration the B-SHeM will not have four detectors in place, so rotations around the beam axis will have to be employed to apply helio-



(a)



(b)

Figure 8.16: (a) Render of a 45° pinhole plate showing the beamline at an angle to the rotator stage. (b) Render of the normal incidence plate, showing how the stage assembly is moved so that the beamline is on the same axis as the rotator stage. The position of the mounting holes in the pinhole plate are fixed, as is the beamline shown as a green dashed line, the rotator stage block is highlighted in cyan.

metric stereo. As the sample manipulators are mounted from the chamber rather than the pinhole plate a different tactic is needed to that used with the A-SHeM: the rotator stage needs to be tilted to allow rotations about the beam axis. Then a modified scanning pattern can be used to ensure equivalence of image projection between between different orientations. With the reduced design angle of incidence of 30° , compared to the 45° used in the A-SHeM, rotations about the beam will be less likely to cause the sample to mechanically interfere with the pinhole plate assembly.

Figure 8.18 displays a render of the stage mounting and pinhole plate for the B-SHeM highlighting the direction of tilt that would be needed to perform rotation about the beam axis. In addition to a tilt of the rotator the scanning pattern would be changed: when scanning in the x direction the z – the definitions of the axes are in figure 8.18 – stage is used to move the sample in a plane perpendicular to the beam axis, thus the images produced

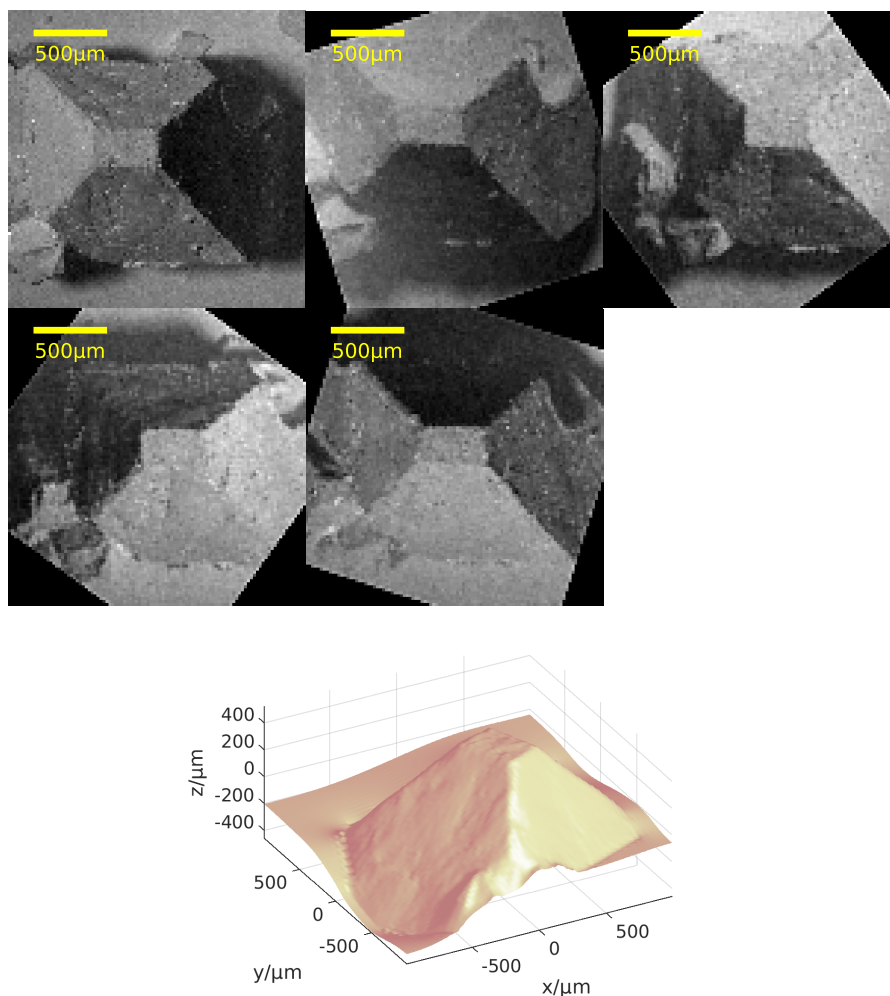


Figure 8.17: Top – five SHeM images taken with the normal incidence pinhole plate (data collected by A Radić) of a pyramidal aluminium potassium sulphate crystal, the images were taken by rotating the sample, here the images were taken without modification to the scanning pattern are re-rotated so that the sample appears in the same orientation in all of them. As with the simulated images in figure 8.10 the changing detection angle can be seen by the changing orientation of the lightest side of the pyramid. Bottom – heliometric reconstruction of the pyramidal crystal.

are effectively produced in a normal incidence configuration and changes in overall sample orientation between rotations can be avoided.

As described above, only very minor adaptations to the B-SHeM will be needed to adapt it for heliometric-stereo while it is in its initial configuration with 1-2 detectors. An additional advantage is gained once 2 detectors are installed as only a single rotation is needed to achieve the required number of images meaning full surface reconstructions will only require double the measurement time of standard imaging, which would be a significant advantage over the normal incidence configuration of the A-SHeM, which requires at least four times the usual measurement time.

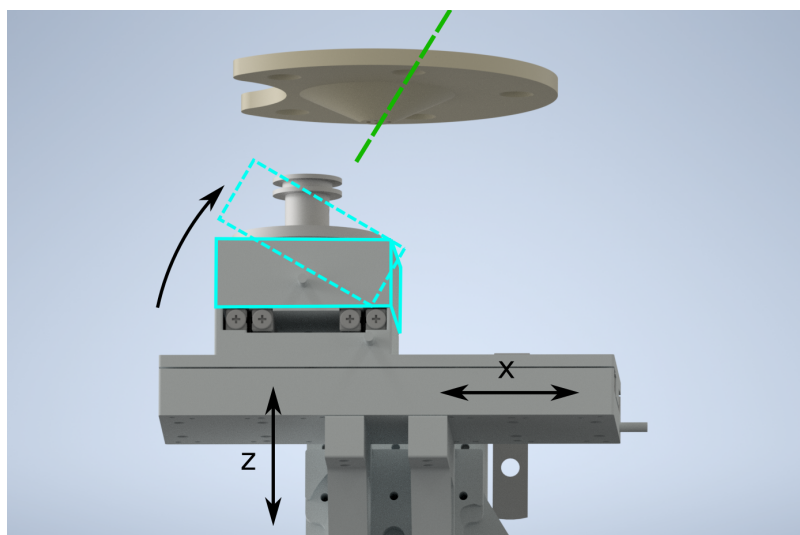


Figure 8.18: Stage mounting and pinhole plate for the SHeM-B. The dashed green line shows the beam line and highlighted in cyan is the rotator stage, the x and z axis of the stages are shown while the y axis is into the page. Tilting the top of the stage assembly in the direction shown into the dashed cyan position would allow rotations about the beam axis.

8.6 CONCLUSION

The existence of a simple and well supported model for helium scattering in SHeM that is dependent on the local surface orientation of the sample leads naturally to 3D reconstructions of the sample surface where there are multiple data points. An existing method, photometric stereo, employed successfully with photography, has been combined with the Knudsen cosine model to develop a technique given the term *heliometric stereo*. The method has been shown to be effective at reconstructing surfaces using simulated ray tracing data. With a realistic signal to noise ratio of 30 the reconstructed surface displayed a root mean squared error of roughly 2% of the characteristic length scale of the sample. Good shape reconstruction was found with samples with aspect ratio up to 0.6, with the shape being recovered with less than 5% error. Up to aspect ratio 1.2 the shape error is less than 10%. The success at recovering the shape of the sample, even at high aspect ratios, raises the possibility of accurate high resolution and high aspect ratio 3D reconstructions. As all the data points in acquired images can be used in a semi-automatic manner heliometric stereo compares favourably to alternative methods of 3D reconstructions such as triangulation-based photogrammetry, which requires manual point tracking to produce wire-frame models of the sample.

The primary condition for the implementation of heliometric stereo is that sufficient images of the sample are obtained to resolve the equations of the normals. For simple geometries this can be done with just three images – although four images are recommended for robustness. These can be obtained in a single experiment in a multi-detector helium microscope,

or by rotating the sample. Secondary considerations are the proportion of multiple scattering that is present in the images. While the results presented in this chapter demonstrate that the method is robust to small to moderate levels of multiple scattering, significant levels can lead to inaccuracies in the reconstruction, as can the proportion of the sample that is masked. The understanding developed here of how these factors impact the reconstruction allow judgements to be made on which samples are appropriate for the method, and whether auxiliary measurement could be made to compensate where multiple scattering or masking are identified as problems for a specific sample.

A proof of concept heliometric stereo measurement has demonstrated that the method can be successfully applied with current instrumentation and with only a single physical detector. In addition practical proposals have been made for adaptations to the newly built Cambridge B-SHeM, that will allow further exploration of the method on that instrument and the routine use of heliometric stereo within the broadening field of scanning helium microscopy.

SUMMARY AND OUTLOOK

Presented in this thesis has been a study of the formation of contrast in scanning helium microscopy. A general geometric framework has been developed to help understand the causes of contrast in helium micrographs, and extensions have been made to instrumentation to allow new measurements into diffraction, and 3D reconstructions, in addition to improving spatial resolution.

In chapter 2, a geometric model of contrast formation in SHeM was developed. A computational ray-tracing framework was built based upon a geometric model of contrast in SHeM that is capable of producing simulated helium micrographs provided parameters for a sample topography, a scattering distribution, a source beam, and a detection geometry. The approach has helped distinguish instrumental factors, such as working distance contrast, from more fundamental atom-surface interactions and useful information about the sample topography. In addition it has allowed the investigation of alternative imaging arrangements, including that of the Portland NAM. Extensions of the method have been made for diffraction, and the framework is designed so that future investigations can easily use it with other scattering models. One limitation of the approach, is that it is computationally expensive for complicated samples, or where multiple simulations are to be run. Given the highly parallel nature of the approach the code could benefit greatly from the emerging use of graphics processing units (GPU) to perform physical simulations. The use of GPU's could provide multiple orders of magnitude of speed-up which would allow much more complicated sample topographies, such as those measured by AFM, to be used. Simulation speed-up could also open the possibility of optimising the input sample topography or parametrised scattering distributions to match experimental data – something not possible when at most dozens of simulations can be performed even for simple samples.

Alternative models to predict contrast mechanism using analytic or numerical integrals have also proved useful. For example they have shown that there is great potential for signal increases with significantly larger detector apertures than used in the A-SHeM in the past, and that contrast due to deformation of the sample under the beam is not possible at present. While less flexible than the ray tracing framework, it is likely that for specific circumstances similar models will continue to be useful as parts of future investigations and in the designing of atom optical components of helium microscopes.

Results from both ray tracing simulation and the investigations using integral models have informed the design of a set of new pinhole-plates

for the Cambridge A-SHeM. A modular approach to SHeM, using multiple pinhole-plates, has been introduced, where the same overall instrument is used to perform different types of measurement by changing only the pinhole-plate. Modes of operation for normal incidence, high angular resolution, and high spatial resolution have all been demonstrated, with the latter producing the first beam widths below $1\ \mu\text{m}$ with large working distances. The general design improvements can be taken forward to improve the beamwidth even further, with values below $500\ \text{nm}$ possible. Overall the modular approach, especially in conjunction with the use of 3D printing, has the potential to enable tailored measuring conditions for each sample, and can be used with both the Cambridge A & B-SHeMs, as well as the Newcastle SHeM.

An important result, from chapter 5, is the observation, directly in SHeM, of the Knudsen cosine model of scattering from glass and sputtered gold surfaces. As diffuse contrast features are seen in a wide range of samples it is now reasonable for diffuse cosine-like scattering to be generally assumed for technological samples, although a claim to precise agreement with the cosine model cannot be made. The precise cause of diffuse scattering is still a major open question. Initial models using hard wall potentials, both by the author and others, have not yet reproduced the observations. The exact level of applicability of more exact cosine scattering to different surfaces remains somewhat unanswered, and as subtle changes in that scattering distribution are likely to cause contrast such as that observed by Barr et al.[38] future investigations would benefit greatly from more specialised instrumentation. For example, a moveable detector aperture coupled with a higher angular resolution would be able to pin down scattering distributions much more precisely than has been done here.

Multiple scattering in SHeM was thoroughly explored in chapter 6. In particular it was shown how multiple scattering can be the dominant contrast mechanism for features deeper than they are wide. The thorough understanding of multiple scattering in topographic contrast places the interpretation of helium micrographs, especially those of more complex porous structures, on firmer ground than it was previously.

In chapter 7 a process for measuring 2D atom diffraction patterns from a microscopic spot size in SHeM was presented. The method was demonstrated by measuring the lithium fluoride diffraction pattern. Atom diffraction is a highly promising area for future investigations as it makes direct use of the unique surface sensitivity of helium atoms. However the full potential of the approach is likely to require the development of some level of in situ sample cleaning to achieve sufficiently clean surfaces for atom diffraction, with the most simple method being that of 'flashing' the sample briefly to high temperatures. Using helium diffraction from microscopic regions of surface could also allow studies on specimens that are not especially suited to more traditional HAS measurements as the area of surface required is many orders of magnitude smaller, for example polycrystalline materials with small grain sizes.

Finally the observation of cosine-like scattering was used to develop the heliometric stereo technique, an adaptation of photometric stereo, where multiple detection angles are used to gather enough information to reconstruct the surface topography of the sample. Using simulated data heliometric stereo has been shown to be effective in certain cases, while certain limitations of the technique have also been found. Understanding the limitation of allows selective application of the technique to the most appropriate samples. Adaptations were made then made to the A-SHeM to allow the first proof of concept 3D reconstructions. The full potential of the method will be realised when multiple detector microscopes are used, such as the B-SHeM, as then reconstructions could form a routine part of imaging, with no extra experimental steps involved. In addition, the limitations of the technique on its own could be mitigated by combining it with stereo photogrammetry such as that used by Myles et al.[44] or by measuring aspects of topography from masks, as was demonstrated in chapter 6. Overall, quantitative 3D measurements form the natural evolution of topographic contrast and provide an attractive alternative to SEM and optical microscopy for delicate samples.

Overall scanning helium microscopy is an experimental technique that is starting to emerge out of initial demonstrations of its feasibility, into having applications to science and technology. Work investigating image formation and contrast mechanisms, both in this thesis and elsewhere, has now provided a robust foundation for the interpretation of topographic images. With resolutions being pushed beyond optical, future studies of biological specimens, similar to the taxonomic study of shark skin by Myles et al.[44] and the study of the skin scaffolding structures in §6.4, will likely form a major segment of SHeM use cases, and hopefully contribute significantly to the biological sciences. The specialisation of hardware, to allow more traditional atom scattering experiments, such as spatially resolved diffraction, to be performed in SHeM will have applications in surface science and potentially allow, thanks to the significantly smaller spot sizes needed, surface science approaches to be applied where they previously could not. A major transition for the technique will be moving from pinhole collimation to Fresnel zone plate focusing, which could, if coupled with improvements in detector technology, enable truly non-destructive nanoscale imaging.

THE CONDUCTANCE OF A CONE

Two models can be made for the back-pumping from the stagnation region into the sample chamber, either that of a simple orifice or of a circular cross section cone. One form applies at the entrance end of the detector cone the other at the far end in the stagnation region. The equation for the conductance through an orifice is[69]

$$C_O = 11.6FA \quad (\text{A.1})$$

where A is the area of the orifice and F is a correction factor depending on the gas used, 3.5 for helium. The case of a cone is more complex but considered by Mercier[70], who presents a semi-empirical formula:

$$C_A = \frac{4}{3}\pi V_m \frac{R_0^2 R_k^2 k}{(R_0 + R_k)L} \quad (\text{A.2})$$

$$\gamma = \frac{C_A}{C_R} = 1 + \frac{16}{3}k \tan \alpha \quad (\text{A.3})$$

where C_A is the ‘forwards’ conductance from the narrow to the wide end of the cone and C_R is the reverse conductance. In the current situation it is C_R that is of interest. The spatial variable are shown in figure A.1 and all variables are given in the table A.1 With the cone assumed to be circular take R_0 to be

Variable	Meaning
V_m	Average atom speed (m/s)
R_0	Radius of the smaller end of the cone
R_k	Radius of the larger end of the cone
L	Length of the cone
α	Cone half angle
k	Correction factor

Table A.1: Variables used in the equation for the pumping speed of a circular cone.

the average of the major and minor semi-axes. As the detection apertures are elliptical average the semi-minor and semi-major axis in quadrature in order to get R_0 . The correction factor is calculated by Monte-Carlo methods and can be read of the graph reproduced in figure A.2.

A.1 PINHOLE PLATES

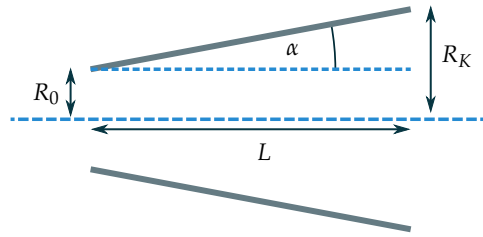


Figure A.1: Shape of the conical tube for conductance calculations. The derivation assumes a circular cone.

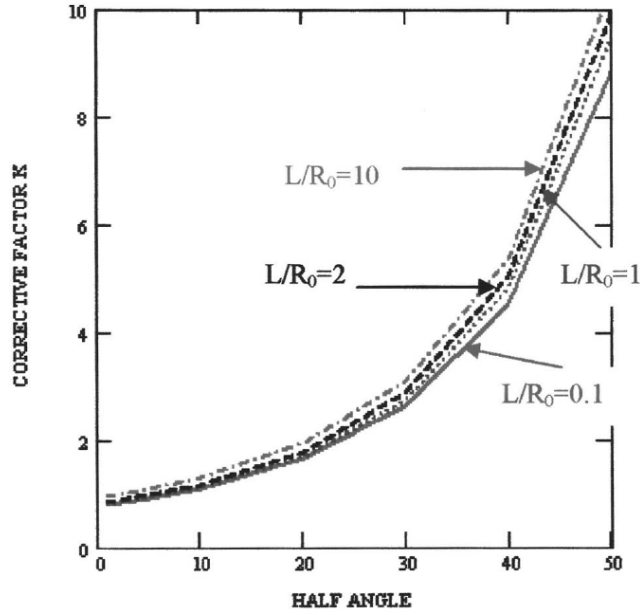


Figure A.2: Correction factor for cone conductance calculation. Reading off the graph for the 4 pinhole plate designs gives $k = 1.2, 1.6, 2.5, 2.0, 1.9$ for the old, normal incidence, angular resolution, 1mm z, and 0.6mm z pinhole plates respectively. Reprinted with permission from Mercier 2006[70]. Copyright 2006, American Vacuum Society.

Pinhole plate	Detection angle	Aperture diameter	α	L
1 mm WD	45°	1 mm	23°	15.6 mm
1 mm WD v2	45°	1.2 mm	23°	15.6 mm
0.6 mm WD	45°	1.2 mm	22°	16.1 mm
Normal incidence	38°	1.4 mm	17°	22.5 mm
Angular resolution	45°	0.5 mm	31°	12.0 mm
Previous	45°	1 mm	9.3°	14.1 mm

Table A.2: Relevant dimensions for calculating signal changes due to changing detection geometry in a series of implemented pinhole plates. The value for the aperture diameter of the ‘0.6mm z’ plate is an approximation as its aperture does not conform to the same shape as the others.

CONSTRAINED OPTIMISATION FOR NON-NORMAL INCIDENCE

The beam standard deviation for a pinhole microscope with an incidence angle of θ where the pinhole is mounted parallel to the scanning axes is

$$\phi^2 = \left(\frac{d}{2\sqrt{3}} \right)^2 + \left(\frac{1}{\cos \theta} \frac{\beta f}{\sqrt{3}} \right)^2 + \left(\frac{1}{\cos \theta} \frac{0.42\lambda f}{d \cos \theta} \right)^2, \quad (\text{B.1})$$

where the $1/\cos \theta$ factor accounts for the angle between the beam and the scanning directions while the change $d \rightarrow d \cos \theta$ in the diffraction term accounts for an effective reduction in the size of the pinhole. As scanning occurs parallel to the pinhole there is no effect on the term corresponding to the geometric pattern of the pinhole. Alternatively using σ_{source} as a measured source standard deviation (in units length):

$$\phi^2 = \left(\frac{d}{2\sqrt{3}} \right)^2 + \left(\frac{1}{\cos \theta} \frac{\sigma_{\text{source}}}{x_{\text{source}}} \right)^2 + \left(\frac{1}{\cos \theta} \frac{0.42\lambda f}{d \cos \theta} \right)^2, \quad (\text{B.2})$$

where x_{source} is the source-pinhole distance. Define $a = 0.42/\cos^2 \theta$, then the Lagrange multiplier is

$$\mathcal{L} = \gamma d^2 \beta^2 - \Lambda \left[\sqrt{\left(\frac{d}{2\sqrt{3}} \right)^2 + \left(\frac{\beta f}{\sqrt{3} \cos \theta} \right)^2 + \left(\frac{a}{d} \right)^2} - \sigma \right]. \quad (\text{B.3})$$

which must be minimised.

$$\frac{\partial \mathcal{L}}{\partial \beta} = 2\gamma d^2 \beta - \frac{\Lambda}{\sigma} \frac{2\beta f^2}{3} \quad (\text{B.4})$$

$$\implies \frac{\Lambda}{\sigma} = \frac{3\gamma d^2}{f^2} \quad (\text{B.5})$$

$$\frac{\partial \mathcal{L}}{\partial d} = 2\gamma \beta^2 d - \frac{\Lambda}{\sigma} \left(\frac{d}{12} - \frac{a^2}{d^3} \right) \quad (\text{B.6})$$

as for normal incidence.

$$\frac{3\gamma d_0^2}{f^2} = \frac{2\gamma \beta_0^2 d_0^4}{\frac{d_0^4}{12} - a^2} \quad (\text{B.7})$$

$$\implies \frac{2f^2 \beta_0^2}{3} = \frac{d_0^2}{12} - \frac{a^2}{d_0^2} \quad (\text{B.8})$$

Which gives the constrained optimisation values for pinhole size and virtual source size as

$$d_0 = \sqrt{6}\sigma \quad (\text{B.9})$$

$$\beta_0 = \frac{\sqrt{3}}{\sqrt{2}f} \left(\frac{\sigma^2}{2} - \frac{a^2}{6\sigma^2} \right)^{\frac{1}{2}} \quad (\text{B.10})$$

which is the same as for normal incidence with a re-definition of the constant a .

CONTRAST OF SUB-BEAM FEATURES

Consider a one dimensional feature on a flat sample that has a width $1/n$ of the beam width. Let the intrinsic Michelson contrast between the feature (Intensity I_f) and the surrounding (intensity I_s) region is, where the intensity of the feature is less than that of the surroundings,

$$C_i = \frac{I_s - I_f}{I_s + I_f}. \quad (\text{C.1})$$

For the case of $n \leq 1$ the contrast between the beam on the feature and the beam on the surroundings will be equal to C_i , with some transition where the beam is partially over the feature. For cases $n > 1$ the feature will never be fully under the beam and thus the observed contrast will be reduced. Consider the beam being a circle with uniform intensity and the beam width being the diameter of the circle. When the feature is under the centre of the beam the fraction of the beam spot with the feature under it will be, define the circle to have unit diameter,

$$F(n) = \frac{16}{\pi} \int_0^{1/2n} \sqrt{\frac{1}{4} - x^2} dx \quad (\text{C.2})$$

$$= \frac{2}{\pi} \left(\frac{1}{n} \sqrt{1 - \frac{1}{n^2}} + \arcsin \frac{1}{n} \right) \quad (\text{C.3})$$

with the fraction of the beam spot with the surroundings under it being $1 - F$. Thus the intensity detected with the spot over the feature (observed intensity I_o) will be

$$I_o = F(n) I_f + [1 - F(n)] I_s \quad (\text{C.4})$$

with the contrast being

$$C_o(n) = \frac{I_s - I_o}{I_s + I_o}. \quad (\text{C.5})$$

ALTERNATIVE SPHERE DERIVATION

Presented here is an alternative derivation for extracting the scattering distribution from SHeM images of spheres, that applies along the central line of the sphere only. The method is provided as validation of the results presented in the main text body as the two derivations are independent.

D.1 LINE SCAN

The geometry of the construction is given in figure D.1. The beam-sphere intersection point (x_0, y_0) in Cartesian coordinates needs to be converted to the raster scan position X and the detection angle from the surface normal θ , which will allow intensity data $I(X)$ to be converted to scattering distribution data $I(\theta)$.

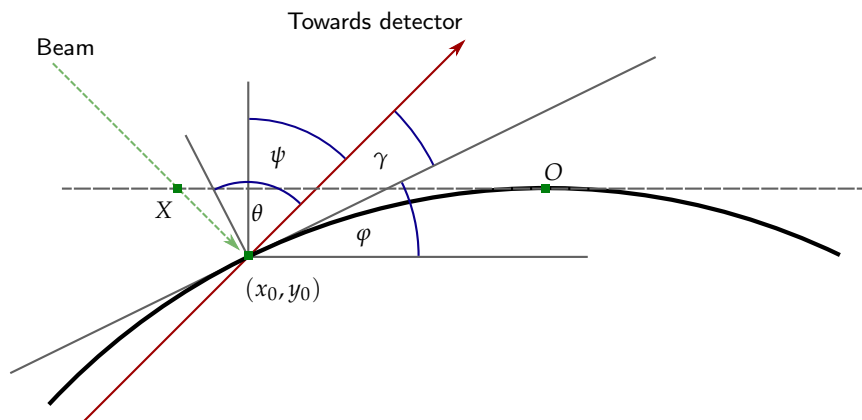


Figure D.1: Definition of variables and constants. ψ is defined by the z position. All others parameters vary with the scan position X .

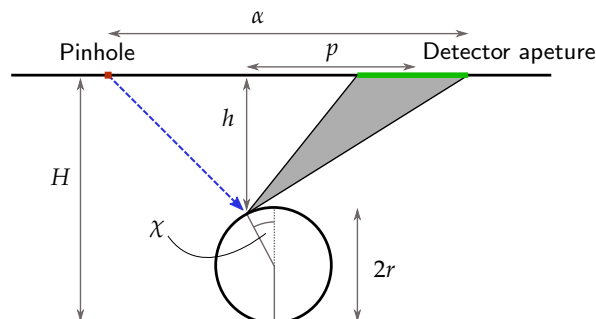


Figure D.2: The overall geometry of the data acquisition. The parameters here define the constant ψ . It can also be seen that as h varies across the sphere there is actually a neglected variable in the derivation.

D.1.1 First case

In the first case the beam intersects the sphere on the far side of the sphere to the detector.

The beam-sphere intersection point can be described by:

$$x_0^2 + (y_0 + r)^2 = r^2 \quad (\text{D.1})$$

$$x_0^2 + y_0^2 + 2y_0r = 0 \quad (\text{D.2})$$

$$y_0^2 + 2y_0r + x_0^2 = 0 \quad (\text{D.3})$$

$$y_0 = \underbrace{-r \pm \sqrt{r^2 - x_0^2}}_{\text{Take the positive root}} \quad (\text{D.4})$$

We can then relate that to the angles (noting that $\varphi = \chi$):

$$\gamma = \frac{\pi}{2} - \chi - \psi \quad \& \quad \theta = \frac{\pi}{2} - \gamma = \chi + \psi \quad (\text{D.5})$$

$$\tan \chi = \frac{-x_0}{r + y_0} \quad (\text{D.6})$$

$$= \frac{-x_0}{\sqrt{r^2 - x_0^2}} \quad (\text{D.7})$$

$$\therefore \theta = \arctan \frac{-x_0}{\sqrt{r^2 - x_0^2}} + \psi. \quad (\text{D.8})$$

The scan position X can be related to the coordinates of the intersection point:

$$X = x_0 + y_0 \quad (\text{D.9})$$

$$= x_0 - r + \sqrt{r^2 - x_0^2} \quad (\text{D.10})$$

Inverting:

$$r^2 - x_0^2 = (X - x_0 + r)^2 \quad (\text{D.11})$$

$$r^2 - x_0^2 = X^2 + 2X(r - x_0) + x_0^2 + r^2 - 2x_0r \quad (\text{D.12})$$

$$0 = 2x_0^2 - 2x_0(r + X) + X^2 + 2Xr \quad (\text{D.13})$$

$$x_0 = \frac{1}{2} \left[r + X \pm \sqrt{r^2 - X^2 - 2Xr} \right]. \quad (\text{D.14})$$

where we note we should take the negative root as $\lim_{X \rightarrow 0} x_0 = 0$.

Combining the above we can write the angle to the detector as a function of the scan position:

$$\theta = \arctan \frac{r + X - \sqrt{2rX - 3r^2 - X^2}}{2\sqrt{r^2 - \frac{1}{4}(r + X - \sqrt{2rX - 3r^2 - X^2})^2}} + \psi \quad (\text{D.15})$$

which is a serious mess... but hopefully correct.

Alternatively the following two equations can be employed to convert the scan data into scattering distribution data (simpler equations means lower likelihood of mistakes):

$$x_0 = \frac{1}{2} \left[r + X - \sqrt{r^2 - X^2 - 2Xr} \right] \quad (\text{D.16})$$

$$\theta = \arctan \frac{-x_0}{\sqrt{r^2 - x_0^2}} + \psi. \quad (\text{D.17})$$

As seen in figure D.1 the above derivation is specific for the beam incidence on the side of the sphere away from the detector.

D.1.2 Second case

Where the beam intersects the sphere on the side closer to the detector we need to slightly alter our equations. The geometry is described in figure D.3. The relation between x_0 and y_0 is the same, but now $x > 0$:

$$y_0 = -r + \sqrt{r^2 - x_0^2}, \quad (\text{D.18})$$

the relations between the angles are now

$$-\theta + \gamma' = \frac{\pi}{2} \quad \& \quad \psi + (\gamma' - \phi') = \frac{\pi}{2} \quad (\text{D.19})$$

$$\theta = \phi' - \psi \quad (\text{D.20})$$

$$= \arctan \frac{x_0}{r + y_0} - \psi \quad (\text{D.21})$$

$$= \arctan \frac{x_0}{\sqrt{r + y_0}} - \psi. \quad (\text{D.22})$$

We note that $X = x_0 + y_0$ still holds, although the sign of x_0 & X have now swapped, thus

$$x_0 = \frac{1}{2} \left[r + X - \sqrt{r^2 - X^2 - 2Xr} \right] \quad (\text{D.23})$$

and only the sign inside the arctan in the expression for θ has changed.

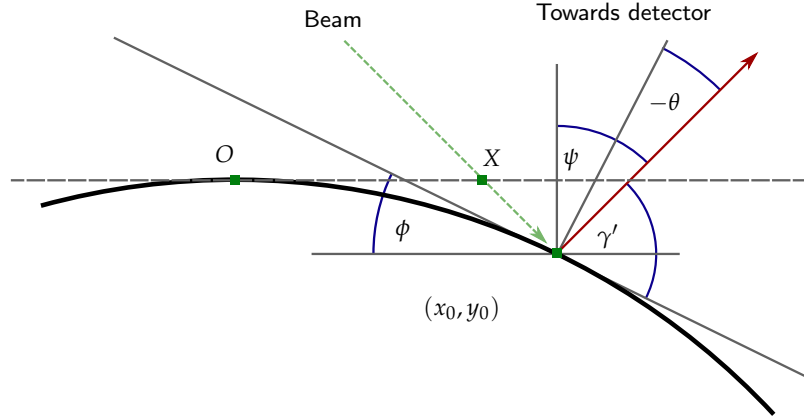


Figure D.3: Definition of variables and constants for the beam intersecting on the detector side of the sphere. ψ is defined by the z position. All other parameters vary with the scan position X .

D.2 EQUIVALENCE OF THE TWO DERIVATIONS

Let us take equation 5.9 and set $y = 0$ to force us onto the central line across the sphere that was considered in section 1:

$$\theta(x) = \arccos \left[\frac{x}{r} \cos \left(\frac{\pi}{4} - \psi \right) + \sqrt{1 - \frac{x^2}{r^2}} \sin \left(\frac{\pi}{4} - \psi \right) \right] \quad (\text{D.24})$$

the variable x can be convert to X through a simple scaling: $X = \sqrt{2}x - r$. A numerical comparison of the two expressions confirms that they agree for the relevant input parameters.

RANDOM SURFACE GENERATION

The derivation provided below was developed by Bentley Carr as part of his summer project[80].

A simple way of modelling a surface $f(x)$ with an autocorrelation function $g(x)$, and RMS height h_{RMS} is to take the convolution of points generated by a Gaussian distribution and convolute them with an exponential

$$f_n = \sum_m h Z_m e^{-|n-m|\Delta x/\lambda} \quad (\text{E.1})$$

where Z_m are the sampled Gaussian points and λ is associated with the correlation length. The important measures of surface roughness are: the height distribution function, the gradient distribution function, and the autocorrelation function.

Since the Z_m are sampled from independent Gaussians with standard deviation σ each single term $Z_m e^{-|n-m|\Delta x/\lambda}$ is sampled from independent Gaussians with standard deviation $\sigma^2 e^{-2|n-m|\Delta x/\lambda}$. Linearity of the variances of Gaussians tells us that f takes a Gaussian distribution

$$\text{Var}(f) = \sigma^2 h^2 \sum_{m=-\infty}^{\infty} e^{-2|n-m|\Delta x/\lambda} \quad (\text{E.2})$$

$$= \sigma^2 h^2 \left[\frac{2}{1 - e^{-2\Delta x/\lambda}} - 1 \right] \quad (\text{E.3})$$

$$= \sigma^2 h^2 \coth \frac{\Delta x}{\lambda} \approx \frac{\sigma^2 h^2 \lambda}{\Delta x}. \quad (\text{E.4})$$

To specify the RMS height value we require the above variance to equal h_{RMS}^2 and the height distribution function is

$$P(f_n = f) = \frac{1}{\sqrt{2\pi} h_{\text{RMS}}} e^{-f^2/2h_{\text{RMS}}^2}. \quad (\text{E.5})$$

Next the gradient function is desired. This is achieved by considering two adjacent vertices in the surface. It is found

$$P(s) = \frac{\lambda}{\sqrt{2\pi} h_{\text{RMS}}} e^{-\lambda^2 s^2/2h_{\text{RMS}}^2} \quad (\text{E.6})$$

and the variance of the normal distribution of gradients is

$$\text{Var}(s_n) = \frac{\sigma^2 h^2}{\Delta x^2} \left(1 - e^{-\Delta x/\lambda}\right)^2 \left(1 + \frac{2}{1 - e^{-\Delta x/\lambda}}\right) \quad (\text{E.7})$$

$$\approx \frac{\sigma^2 h^2}{\lambda \Delta x} \approx \frac{h_{\text{RMS}}^2}{\lambda^2} \quad (\text{E.8})$$

assuming that $\lambda \gg \Delta x$. It can be shown that the joint probability distribution $P(f, s)$ is equal to the product of the separate height and gradient distributions: $P(f)P(s)$ provided that $\lambda \gg \Delta x$.

Finally the autocorrelation function is needed, defined as

$$R(\tau) = R(n\Delta x) = R_n = \sum_m f_m f_{m+n} \quad (\text{E.9})$$

with the normalised autocorrelation function being

$$\rho(\tau) = \frac{R(\tau)}{R(0)} \quad (\text{E.10})$$

Again B. Carr shows that

$$R_k \approx h_{\text{RMS}}^2 e^{-|k|} \left[1 + \left(|k| + \frac{1}{2} \right) \frac{\Delta x}{\lambda} \right] \quad (\text{E.11})$$

$$\rho(\tau) \approx e^{-|\tau|/\lambda} \left(1 + \frac{|\tau|}{\lambda} \right) \quad (\text{E.12})$$

provided that $\lambda \gg \Delta x$. The variance of the correlation function is

$$\sigma^2 = \int_{-\infty}^{\infty} \tau^2 \rho(\tau) d\tau = 2 \int_0^{\infty} \tau^2 e^{-\tau/\lambda} (1 + \tau/\lambda) d\tau \quad (\text{E.13})$$

$$= \left[-e^{-\tau/\lambda} (8\lambda^3 + 8\lambda^2\tau + 4\lambda\tau^2 + \tau^3) \right]_0^{\infty} \quad (\text{E.14})$$

$$= 0 + 8\lambda^3 \quad (\text{E.15})$$

Thus if we wish to generate a surface of correlation length σ_C and RMS height r_{RMS} then the parameters need must satisfy

$$\lambda = \frac{1}{2} \sigma_C^2 \quad (\text{E.16})$$

$$h^2 \sigma^2 = h_{\text{RMS}}^2 \tanh \frac{\Delta x}{\lambda}.$$

The effect of h and σ on the generated distribution are the same and therefore it is safe to always set $\sigma = 1$.

Code was written to generate surfaces for simulations using equation E.1 and the parameter specification in equation E.16. For the ray tracing simulations an implementation was written in MATLAB, this is shown in E.1.

Listing E.1: Two functions used to generate random surfaces in Python for simulation.

One function takes input parameters referring to the statistic of the surface to be generated `random_surf_gen(...)` while the other is a helper function that performs the convolution in equation E.1. Surfaces are explicitly required to have an odd number of points to ensure a surface of symmetric length about the origin and parameters that break the assumption $\lambda \gg \Delta x$ are not allowed.

```
1 % N - surface points
2 % rL - length of surface
```

```

3 % h - rms height
4 % cl - correlation length
5 function [f, xs] = random_surf_gen(N, rL, h_RMS, cl)
6     Dx = rL/(N - 1);
7     lambd = 0.5*cl^(2/3);
8     h = h_RMS*sqrt(tanh(Dx/lambd));
9
10    [f, xs] = random_surf_gen_core(h, Dx, lambd, 1, N);
11 end
12
13
14 % Core routine to generate a random surface. Arguments should be
15 % chosen carefully. The number of points must be odd.
16 function [f, xs] = random_surf_gen_core(h, Dx, lambd, s, N)
17     if nargin == 4
18         N = 10001;
19     end
20     if mod(N, 2) == 0
21         error("Must be an odd number of points in the surface");
22     end
23     Z = normrnd(0.0, s, 1, N);
24     ms = linspace(-round(N/2), round(N/2), N);
25     e = exp(-abs(ms)*Dx/lambd);
26     f = h*conv(Z, e, 'same');
27     xs = ms*Dx;
28 end

```

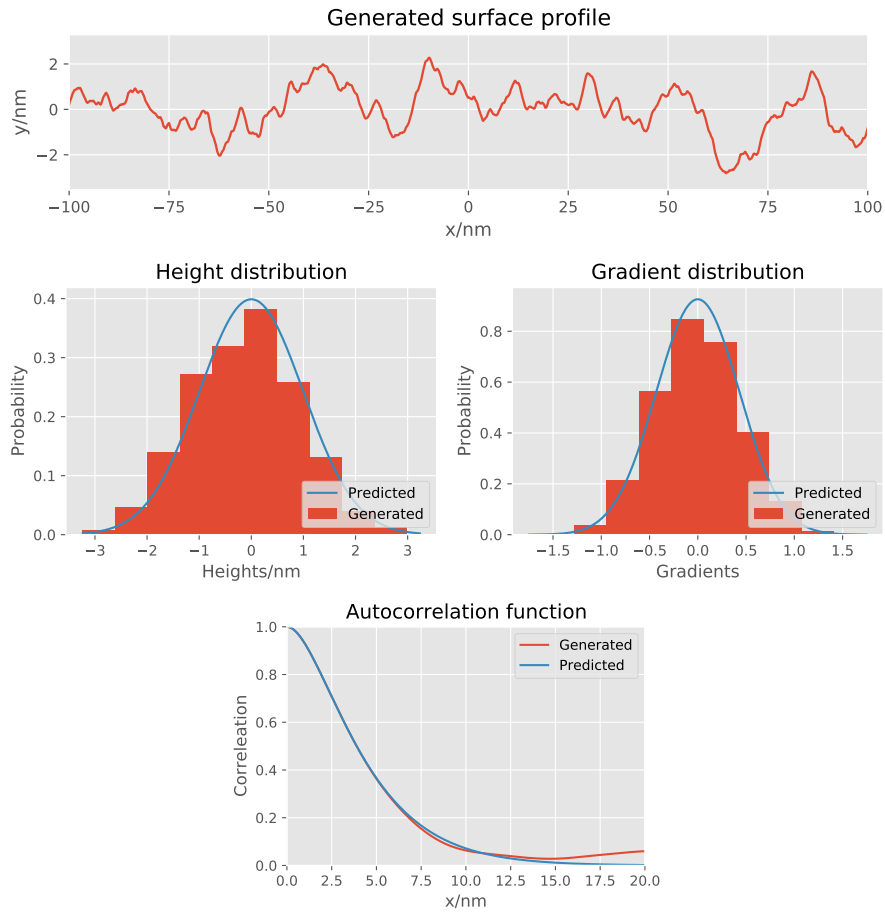


Figure E.1: An example randomly generated surface along with the statistics of that surface compared to the predictions given in equations E.5, E.6, and E.12. The generated surface had 10001 points, $D_x = 0.02$ nm an RMS height of 1 nm and a correlation length of 10 nm. It is notable that a surface is required to have $\sim 10^4$ points/line segments in order to reproduce the statistics well.

INTEGRAL FOR TRENCH LOCALISATION

M. Bergin developed the 3D integral that is presented below. It is included here for completeness.

F.1 THREE DIMENSIONAL CASE

The problem is to determine the amount of gas scattered directly out of a trench in three dimensions. Figure F.1 shows the coordinate system used with the bubble representing the scattering distribution. We shall model the scattering event as completely diffuse cosine scattering and assume that the trench is infinitely long in order to calculate the integral.

Let us use spherical polar coordinates, such that,

$$x = r \sin \theta \cos \phi, \quad (\text{F.1})$$

$$y = r \sin \theta \sin \phi, \quad (\text{F.2})$$

$$z = r \cos \theta. \quad (\text{F.3})$$

Thus we wish to calculate the integral,

$$I = 1 - \frac{1}{\pi} \iint_A \cos \theta \, d\Omega \quad (\text{F.4})$$

$$= 1 - \frac{1}{\pi} \iint_A \sin \theta \cos \theta \, d\theta \, d\phi, \quad (\text{F.5})$$

where A is the area across the top of the trench and π is a normalisation constant. Note that the total flux that leaves the trench is what is calculated and then used to find the localised flux. Finding the correct integral limits would be cumbersome in spherical polar coordinates, so instead let us change to Cartesian coordinates where the trench is easy to define.

Let the origin of both coordinate systems be at the scattering point. The top of the trench is at $x = d$, which sets,

$$r = \frac{d}{\sin \theta \cos \phi}. \quad (\text{F.6})$$

Substituting for r gives the other coordinates as,

$$\begin{aligned} y &= \frac{d \sin \theta \sin \phi}{\sin \theta \cos \phi}, \\ &= d \tan(\phi), \end{aligned} \quad (\text{F.7})$$

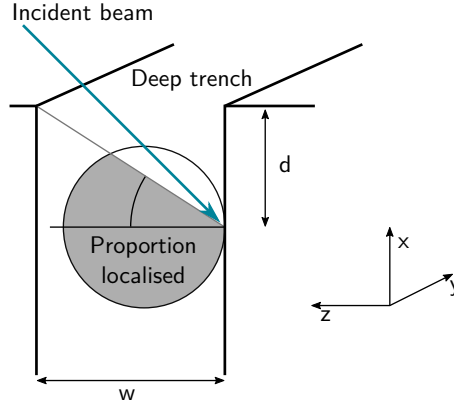


Figure F.1: Figure of the coordinate system for the localisation integral. The atom beam falls a distance d into the infinitely long trench of width w , the proportion of the scattered atoms that are localised is calculated by integrating the 3D cosine distribution, represented schematically as the bubble emerging from the point the beam impacts the side of the trench.

$$\begin{aligned} z &= \frac{d \cos \theta \sin \phi}{\sin \theta \cos \phi}, \\ &= \frac{d}{\tan \theta \cos \phi}, \end{aligned} \quad (\text{F.8})$$

To switch coordinates we need to calculate the Jacobian,

$$\begin{aligned} \left| \frac{\partial(y, z)}{\partial(\theta, \phi)} \right| &= \begin{vmatrix} \frac{dy}{d\theta} & \frac{dz}{d\theta} \\ \frac{dy}{d\phi} & \frac{dz}{d\phi} \end{vmatrix} \\ &= \begin{vmatrix} 0 & \frac{d}{\cos^2 \phi} \\ \frac{-d}{\sin^2 \theta \cos \phi} & \frac{d \sin \phi}{\tan \theta \cos^2 \phi} \end{vmatrix} \\ &= \frac{d^2}{\sin^2 \theta \cos^3 \phi}. \end{aligned} \quad (\text{F.9})$$

It can then be shown that[128],

$$dy dz = \left| \frac{\partial(y, z)}{\partial(\theta, \phi)} \right| d\theta d\phi, \quad (\text{F.10})$$

which gives the integral as,

$$1 - I = \frac{1}{\pi d^2} \iint_A \sin^3 \theta \cos \theta \cos^3 \phi dy dz. \quad (\text{F.11})$$

We can then use an inverse coordinate transform to complete the move to Cartesian coordinates (y, z) . Given that,

$$y = d \tan \phi, \quad (\text{F.12})$$

$$\cos \theta = \frac{z}{\sqrt{d^2 + y^2 + z^2}}, \quad (\text{F.13})$$

it can be shown that,

$$\cos \phi = \frac{d}{\sqrt{d^2 + y^2}}, \quad (\text{F.14})$$

$$\sin \theta = \frac{\sqrt{d^2 + y^2}}{\sqrt{d^2 + y^2 + z^2}}. \quad (\text{F.15})$$

Substituting equations F.14 and F.15 into equation F.11 gives,

$$1 - I = \frac{d}{\pi} \int_{z=0}^{z=w} \int_{y=-\infty}^{y=\infty} \frac{z}{(y^2 + d^2 + z^2)^2} dy dz. \quad (\text{F.16})$$

The double integral is now in a state where it can be analytically solved. Let $a^2 = d^2 + z^2$ and $y = a \tan(u)$, then since $dy/du = a/\cos^2 u$, the integral can be rewritten as,

$$1 - I = \frac{d}{\pi} \int_{z=0}^{z=w} \left[\int_{u=-\pi/2}^{u=\pi/2} \frac{z}{(a^2 \tan^2 u + a^2)^2} \frac{a}{\cos^2 u} du \right] dz. \quad (\text{F.17})$$

Using the identity $\tan^2 u + 1 = 1/\cos^2 u$, the integral can be simplified to,

$$1 - I = \frac{d}{\pi} \int_{z=0}^{z=w} \left[\int_{u=-\pi/2}^{u=\pi/2} \frac{z}{a^3} \cos^2 u du \right] dz. \quad (\text{F.18})$$

By recognising that for $L = n\pi$, where n is an integer,

$$\int_{L/2}^{L/2} \cos^2 u du = \frac{L}{2}, \quad (\text{F.19})$$

the inside integral can be solved to give,

$$1 - I_2 = \frac{d}{2} \int_0^w \frac{z}{(d^2 + z^2)^{3/2}} dz. \quad (\text{F.20})$$

Performing the final integration gives,

$$1 - I_2 = \frac{d}{2} \left[\frac{-1}{\sqrt{d^2 + z^2}} \right]_0^w. \quad (\text{F.21})$$

$$1 - I = \frac{1}{2} \left(1 - \frac{d}{\sqrt{d^2 + w^2}} \right). \quad (\text{F.22})$$

Finally giving that the total localised flux is,

$$I = \frac{1}{2} \left(1 + \frac{d}{\sqrt{d^2 + w^2}} \right). \quad (\text{F.23})$$

F.2 TWO DIMENSIONAL CASE

We can then show that this is equivalent to the two dimensional case. To see if there is an obvious equivalence between the two and three dimensional cases, we shall use an approach that is equivalent to before. The integral in two dimensions is given by,

$$1 - I_2 = \int_A \frac{1}{2} \cos \theta \, d\theta. \quad (\text{F.24})$$

The Cartesian coordinate transform is given by,

$$z = \frac{d}{\tan \theta}. \quad (\text{F.25})$$

Since the differential of the transform is given by,

$$\frac{dz}{d\theta} = \frac{-d}{\sin^2 \theta}, \quad (\text{F.26})$$

we can write the integral as,

$$1 - I_2 = \int_0^w \frac{1}{2d} \cos \theta \sin^2 \theta \, dz, \quad (\text{F.27})$$

$$1 - I_2 = \frac{d}{2} \int_0^w z (d^2 + z^2)^{-3/2} \, dz. \quad (\text{F.28})$$

We have obtained the same integral as proved in the three dimensional case showing the equivalence of the two cases. We can switch back to polar coordinates using,

$$\sin \theta = \frac{d}{\sqrt{d^2 + w^2}}, \quad (\text{F.29})$$

to obtain the integral,

$$I'_2 = \frac{1}{2} \sin \left(\arctan \frac{d}{w} \right) + \frac{1}{2}, \quad (\text{F.30})$$

which is the same expression stated in equation in the main text body.

HELIOMETRIC STEREO SAMPLE

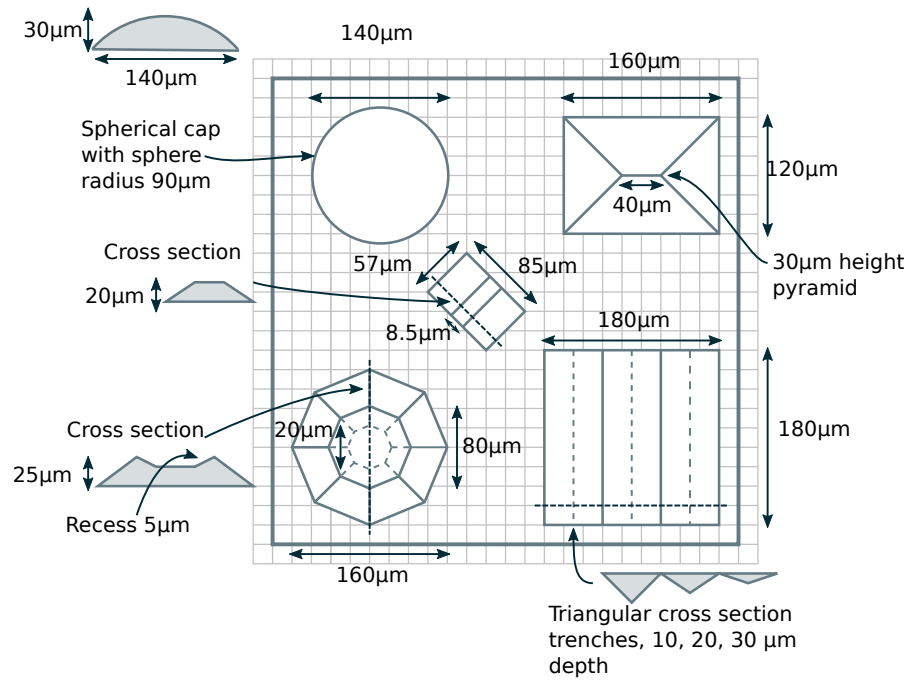


Figure G.1: Dimensions of heliometric stereo sample used for the tests in chapter 8

WORKING DISTANCE MEASUREMENT

Images taken of the sample and pinhole plate region from directly above can be used to measure the distance between the sample and the pinhole. A live video of the same view can also be used when positioning of the sample prior to imaging. The precise motions of the stages can be used to calculate a pixel calibration that gives a physical dimension to the pixels in the beam plane.

H.1 METHOD

The distance to be measured can be considered as the perpendicular distance between two lines, representing the sample plane and the front of the pinhole plate. Those lines are drawn by a user onto the image plotted as a MATLAB figure and the positions of the lines measured from that figure. What must then be calculated is the *average perpendicular distance* between those lines – it is necessary to average as the two lines will, most likely, not be exactly parallel.

H.1.1 Calculation of average distance

Figure H.1 displays the information acquired by the program after the human interaction. The four 2-element vectors labelled as the ‘bottom’ and ‘top’ positions for the two lines ‘1’ and ‘2’ can be used to calculate the average distance between the lines.

The average perpendicular direction between the lines is defined by the normal vector \hat{n} which is the normalised average of the normal vectors of the two lines, $\frac{1}{2}(\hat{n}_1 + \hat{n}_2)$. We define the normals to be pointing ‘right’ in figure H.1, such that a normal is calculated

$$\mathbf{n}_i = \begin{pmatrix} (\mathbf{b}_i - \mathbf{t}_i)[2] \\ -(\mathbf{b}_i - \mathbf{t}_i)[1] \end{pmatrix}, \quad (\text{H.1})$$

which must be normalised¹. With the average normal calculated the equation of the normal line is

$$\mathbf{q}(\alpha) = \alpha \hat{\mathbf{n}} + \mathbf{c} \quad (\text{H.2})$$

¹The $[i]$ notation is used here to unambiguously denote the i th element of a vector.

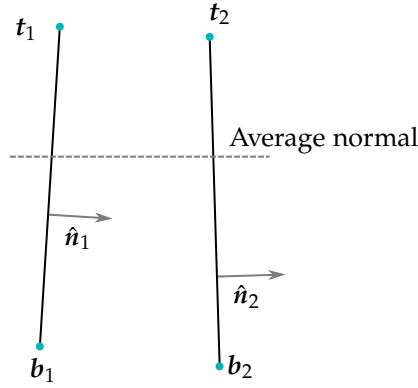


Figure H.1: The information acquired from the human interaction labelling. The aim is then to calculate the average perpendicular distance between two lines. That distance must be calculated from the 4 recorded locations denoted as the 'top' $\{t_i\}$ and the 'bottom' $\{b_i\}$ vectors. As the two lines will not be perfectly parallel we must calculate the average distance along the average normal between them.

where c defines a location that the line must pass through and α parametrises the line. Similarly we also parametrise the two lines we are measuring between using $\tau_i \in [0, 1]$:

$$p_i(\tau_i) = b_i + \tau_i(t_i - b_i). \quad (\text{H.3})$$

To calculate the distance parallel to the normal line for a set point we must find the intersects of the normal with the two measurement lines. Let $c = p_1(\tau_1)$, thus the intersection point with line 1 is when $\alpha = 0$, then the intersection with line 2 is

$$\alpha \hat{n} + b_1 + \tau_1(t_1 - b_1) = b_2 + \tau_2(t_2 - b_2) \quad (\text{H.4})$$

for some τ_1 . Solving equation H.4 for α gives the distance between the measurement lines along direction \hat{n} . Equation H.4 may be expressed as a linear equation

$$b_1 + \tau_1(t_1 - b_1) - b_2 = \begin{pmatrix} -\hat{n}, t_2 - b_2 \end{pmatrix} \cdot \begin{pmatrix} \alpha \\ \tau_2 \end{pmatrix} \quad (\text{H.5})$$

$$y = Mx. \quad (\text{H.6})$$

To calculate the average distance a range of τ_1 must be integrated over,

$$\bar{l} = \frac{1}{\tau_1^* - \tau_1'} \int_{\tau_1'}^{\tau_1^*} d\tau_1 \alpha(\tau_1), \quad (\text{H.7})$$

for the appropriate range.

H.1.2 Integration limits

Integration limits are chosen such that the maximum length is averaged over. If the normal line from the top of line 1 intersects line 2 then the upper limit of integration is $\tau_1^* = 1$ and if the normal line from the bottom of line 1 intersects line 2 then the lower limit of integration is $\tau_1' = 0$, however, if either/both of these are not the case then the limits need calculating.

By calculating the intersection of the normal line, starting at the top and bottom of line 1, with line it can be worked out if line 1 or line 2 determines the limits by testing if the parameter τ_2 falls outside its permitted range. The equations to be solved are: for the 'bottom' limit:

$$\mathbf{b}_1 + \alpha \hat{\mathbf{n}} = \mathbf{b}_2 + \tau_2(\mathbf{t}_2 - \mathbf{b}_2) \quad (\text{H.8})$$

and for the 'top' limit:

$$\mathbf{t}_1 + \alpha \hat{\mathbf{n}} = \mathbf{b}_2 + \tau_2(\mathbf{t}_2 - \mathbf{b}_2) \quad (\text{H.9})$$

These equations can be written as a linear system as in equation H.5, which ones constructed is solved numerically in MATLAB.

If the calculated values of τ_2 are outside the allowed range $[0, 1]$ then the limits of integration are defined by line 2, the appropriate limits are then calculated by considering the intersection of the normal line with the top and bottom points on line 2, e.g.

$$\mathbf{b}_2 + \alpha \hat{\mathbf{n}} = \mathbf{b}_1 + \tau_1(\mathbf{t}_1 - \mathbf{b}_1). \quad (\text{H.10})$$

The system of equations in equation H.5 may be rearranged for α thus

$$\alpha(\tau_1) = a + \tau_1 b \quad (\text{H.11})$$

$$a = \frac{\mathbf{b}_1[2] - \mathbf{b}_2[2] - \gamma(\mathbf{b}_1[1] - \mathbf{b}_2[1])}{\gamma \hat{\mathbf{n}}[1] - \hat{\mathbf{n}}[2]} \quad (\text{H.12})$$

$$b = \frac{\mathbf{t}_1[2] - \mathbf{b}_1[2] - \gamma(\mathbf{t}_1[1] - \mathbf{b}_1[1])}{\gamma \hat{\mathbf{n}}[1] - \hat{\mathbf{n}}[2]} \quad (\text{H.13})$$

$$\gamma = \frac{\mathbf{t}_2[2] - \mathbf{b}_2[2]}{\mathbf{t}_2[1] - \mathbf{b}_2[1]} \quad (\text{H.14})$$

hence

$$\bar{l} = \frac{1}{\tau_1^* - \tau_1'} \left[a\tau_1 + \frac{1}{2}b\tau_1^2 \right]_{\tau_1'}^{\tau_1^*} \quad (\text{H.15})$$

which may be evaluated once the limits τ_1', τ_1^* are known.

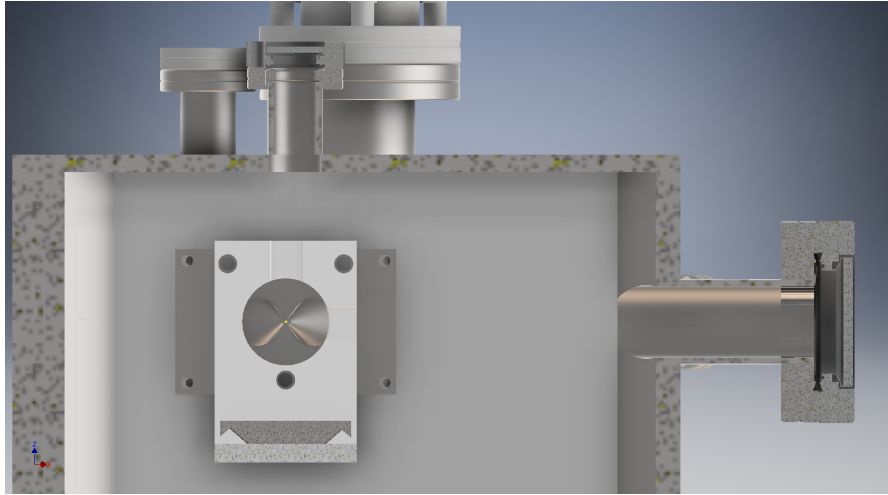


Figure H.2: A cross section of the new sample chamber showing the two viewports that look upon the sample point. The CF16 port on the top of the chamber is chosen to use for the USB microscope while the CF40 on the right on the render is for now kept as a human optical view.

Optical flatness	$\lambda/4$ at 632nm
Parallelism	$< 10''$
Surface finish	20-10 Scratch-dig
Inside diameter	16mm
BBAR coating	425 – 760nm

Table H.1: Specifications of the optical viewport imaged through to observe the sample and pinhole plate.

H.2.1 Chamber

The new sample chamber, designed by D.J. Ward, has two optical viewports placed to look directly at the sample-beam intersection point. Figure H.2 shows a cross section of the chamber in the sample plane, a CF40 flange can be seen on the right and a CF16 flange can be seen at the top.

Given the smaller distance from the CF16 port to the sample point and the relatively small field of view that is required the top CF16 is chosen for the optical microscope while the larger CF40 is used as a human view port – the location of that port on the side and the larger field of view through it make it more suited to the eye.

For undistorted viewing an optical grade fused silica viewport was purchased from Allectra. The viewport is BBAR coated on both sides and the specification for the viewport is given in table H.1.

Camera Sensor Format	1/4"
Magnification	10× – 100×
Sensor	Progressive Scan CMOS
Working Distance	10× at 112mm, 40× at 8.5mm
Resolution	5.0MP

Table H.2: Spec of the optical camera used to view the working distance in the SHeM.

H.2.2 Camera

A USB optical microscope was purchased from Edmund Optics². Table H.2 lists the spec of the microscope. The camera has a single combined focal length and focus adjustment ring, as such changing the focus changes the focal length and hence the magnification. The use of a compact USB camera is more convenient and less expensive than investing in a full digital camera system.

In order to mount the microscope on the sample chamber a 3D printed mount was designed that fits the camera and goes over the optical flange. The position of the mount on the flange and the position of the camera within the mount are adjustable using plastic screws, 4 to hold onto the flange, two sets of 4 at the top and bottom of the camera to adjust it's position. Once the microscope is in place the screws can all be adjusted until the view down the port is as desired. Figure H.3 shows a photograph taken with the USB camera after adjustment. It is probably desirable to have a more robust and accurate mount for the microscope made, however the limited space around the flange and the shape that the mound is desired makes it difficult to design for traditional manufacturing.

The installed camera may also be used as a live view of the sample mount and pinhole plate. A magnified live view is especially useful when setting the software lock on the minimum working distance.

H.3 IMPLEMENTATION

A MATLAB app has been constructed using the 'app builder' to provide a graphical user interface for the guided procedure of making a measurement with through the viewport. The app may be started by entering `measure_z` into the MATLAB command prompt or by selecting 'Measure z' from the drop-down list in the main SHeM control app.

Once the app is open the following procedure is undertaken, the interface is shown in figure H.4:

1. Press *Load scan* and select the `scan.mat` file that is wish to be opened. If an image not associated with a shemscan is to be loaded press *Load*

²<https://www.edmundoptics.com/p/10x-200x-usb-digital-microscope-with-polarizer-hr/30414/>



Figure H.3: Example photo taken with the USB microscope of the sample mounted on an SEM stub (slightly left of centre) and the pinhole plate (cone shape roughly in the centre). Multiple frames are taken and averaged because the chamber is relatively dark. When the 'z Measure' MATLAB app is used an image, such as that plotted here, will be plotted in a separate figure.

image If the measuring app is opened by another process then it may pre-load the image.

2. The image presented may be modified to aid the selection of the sample and pinhole planes. Use the *Brighten* slider to brighten or darken the image and use the *greyscale* button to convert the image to black and white.
3. Press *Add sample line* and add a line to represent the sample plane.
4. Press *Add pinhole line* and add a line to represent the pinhole plane.
5. Once the two lines are in place press *Measure pixel separation* to calculate the average distance between them in pixels.
6. The pixel to mm conversion factor may be modified in the *Pixel calibration* box.

The resulting measurement must be added to the shemscan data file manually or recorded in some other way. While designed for measuring the working distance in the SHeM sample chamber the app, with small amount of modification, can be used for measuring other distances from images.

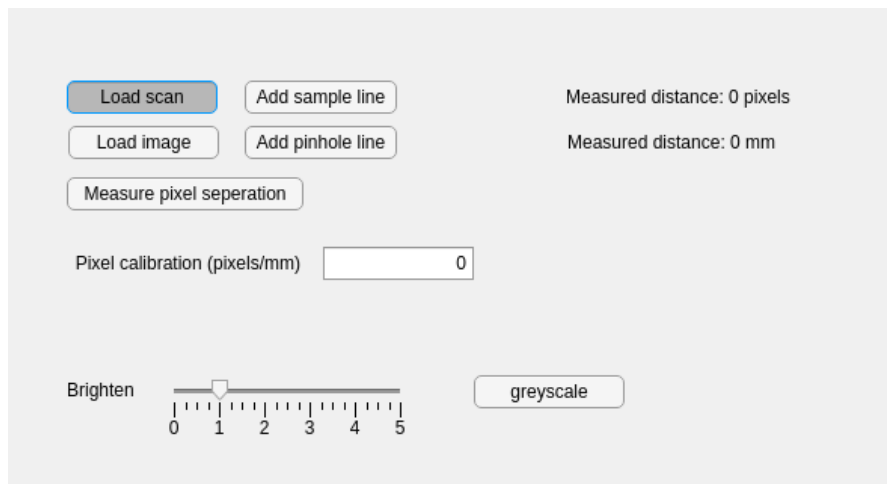


Figure H.4: The user interface of the measuring app. First an image is loaded, either from a shemscan data file or a pure image file, then two lines representing the sample and pinhole plate are drawn by the user, and finally the measure button is pressed to acquire a distance in pixel which may be converted to mm with an appropriate calibration. The image may be brightened/dimmed or converted to greyscale to aid the identification of the sample/pinhole plate.

H.4 CALIBRATION

The method outlined in section H.1 and the app presented in section H.3 give a measurement between the sample plane and the pinhole plate in *pixels*. A conversion from pixels to SI units is required. Calibration would need to be performed if the camera or it's mountings are touch or adjusted in any way, but without interference the conversion will remain the same.

The Attocube stages are used for calibration. With the sample in position (0,0) in xy the sample stage is moved in increments of ~ 0.2 mm – a script `ECC_calibrate` can be used to take the series of images – the app is then used to measure the pixel separation between the pinhole and the sample for each image. As the step sizes will be accurate to a degree much better than the optical system is capable of measuring the difference in distances measured is know and thus the distance per pixel is found. A number of measurement is taken and averaged to get the calibration for use.

By taking a series of pixel separation measurements the encoded position of $z = 0$ can be found by extrapolating a linear fit to the data. If the encoded position is plotted as a function of the pixel separation then the y intercept will give the encoded position for zero separation. Knowledge of the encoded position of $z = 0$ allows the z position of the sample to be known accurately through the encoded z on the Attocube drive. As there will be errors in identifying the sample and pinhole plate a full calibration should be performed if an accuracy better than ~ 50 μm is desired.

Size of pixels	$15 \pm 1 \mu\text{m}$
Encoded position of $z = 0$	$+90 \pm 20 \mu\text{m}$
Movement between pixels	$100 \mu\text{m}$
Average pixel separation	6.5 ± 0.4
Standard deviation of measurements	2 pixels or 31%

Table H.3: Results of the z position calibration for the transition metal on silicon sample.

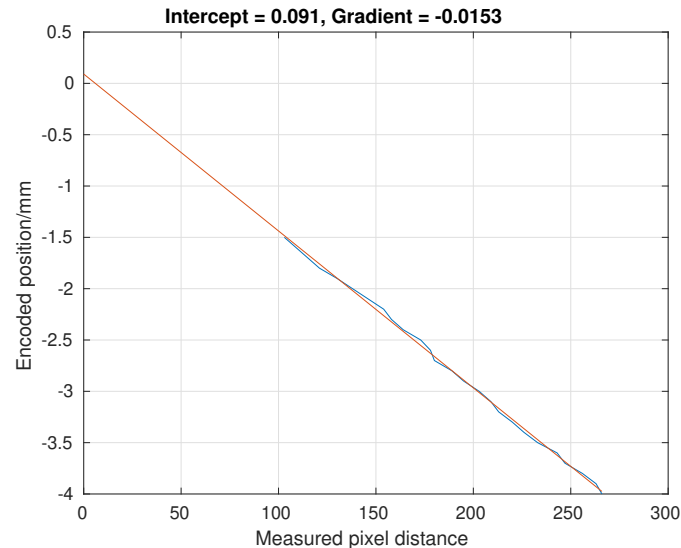


Figure H.5: A plot of the measured pixel distances as a function of the encoded z position. A linear fit is plotted in red showing the extrapolation to 0.

H.4.1 Calibration measurement for metal on silicon

The first calibration of the system was performed for a sample with e-beam evaporated transition metals on a silicon wafer. Step of $100 \mu\text{m}$ were used over a range of 2.5 mm for a total of 26 measurements.

The results of the calibration are given in table H.3. A plot of the encoded position against measured pixel distance is given in figure H.5, on the plot is a linear regression fit that extrapolates to the encoded position at zero pixel separation.

H.5 ACCURACY OF MEASUREMENT

H.5.1 Pixel size limit

The size of the pixels gives a limit on how accurate a measurement digitised by pixels. The pixel separation measured was $15 \pm 1 \mu\text{m}$. Thus the minimum error in a measurement based on counting the pixel separation is about $10 \mu\text{m}$ – an error of $7.5 \mu\text{m}$ on each position added in quadrature. In reality

the error is likely to be higher due to difficulty identifying features down to the nearest pixel.

H.5.2 *Identification error*

In order to measure the distance two lines are identified by the human user, user will not be able to perfectly identify either line down to the nearest pixel. How accurately the locations can be pinned down will vary between sample and user, for the calibration in the previous section the standard deviation on distances that are the same was 2 pixels, thus the identification error on an individual measurement is $\sim 30 \mu\text{m}$. As identification error is not the only source of error a conservative bound on the accuracy of measurement by pixel as $50 \mu\text{m}$.

H.5.3 *$z = 0$ position*

As a large number of individual measurements are used to estimate the encoded $z = 0$ position the identification error will be reduced. Without more sophisticated analysis the standard error on the intercept of the linear regression can be taken as the error on z positions measured via extrapolation to $z = 0$, for the calibration in the previous section the standard error on the gradient was $20 \mu\text{m}$, notably better than the $50 \mu\text{m}$ when just using the pixel calibration.

H.5.4 *Location of pinhole*

The pinhole membrane sits in a recess, therefore there is an unknown (order $\sim 0.1 \text{ mm}$) extra distance from the front of the pinhole plate to the pinhole. The extra distance does not introduce error if the distance to the detector aperture is desired—that is directly on the front of the pinhole plate—but it does if the distance to the pinhole itself is, e.g. in measurements of the source size.

H.5.5 *Selection of minimum working distance*

Within the `ECC_Move_z` function, which controls the motion of the z stage, there is a software lock that prevents the user driving the sample into the pinhole plate accidentally. When a new sample is loaded into the SHeM the software lock should be updated.

The USB camera view of the sample can be used in conjunction with the ‘human view port’ of the sample to set as close to the pinhole plate as the user is willing to take it. Once the minimum distance is found the lock position should be updated in the `ECC_Move_z.m` function file. When setting the stop

position care should be taken as the pinhole membrane is delicate and can easily be shattered.

BIBLIOGRAPHY

- [1] M. Koch et al. 'Imaging with neutral atoms—a new matter-wave microscope'. In: *Journal of Microscopy* 229.1 (Jan. 2008), pp. 1–5. DOI: [10.1111/j.1365-2818.2007.01874.x](https://doi.org/10.1111/j.1365-2818.2007.01874.x).
- [2] Philip Witham and Erik Sánchez. 'A simple approach to neutral atom microscopy'. In: *Review of Scientific Instruments* 82.10 (Oct. 2011), p. 103705. DOI: [10.1063/1.3650719](https://doi.org/10.1063/1.3650719).
- [3] M. Barr et al. 'A design for a pinhole scanning helium microscope'. In: *Nuclear Instruments and Methods in Physics Research Section B: Beam Interactions with Materials and Atoms* 340 (Dec. 2014), pp. 76–80. DOI: [10.1016/j.nimb.2014.06.028](https://doi.org/10.1016/j.nimb.2014.06.028).
- [4] Gianangelo Bracco and Bodil Holst. *Surface Science Techniques*. Springer Science & Business Media, Jan. 2013.
- [5] David C. Bell. 'Contrast Mechanisms and Image Formation in Helium Ion Microscopy'. In: *Microscopy and Microanalysis* 15.02 (Apr. 2009), pp. 147–153. DOI: [10.1017/S1431927609090138](https://doi.org/10.1017/S1431927609090138).
- [6] Daniel Farias and Karl-Heinz Rieder. 'Atomic beam diffraction from solid surfaces'. In: *Reports on Progress in Physics* 61.12 (1998), p. 1575. DOI: [10.1088/0034-4885/61/12/001](https://doi.org/10.1088/0034-4885/61/12/001).
- [7] I-Chen Chen et al. 'Fabrication of high-aspect-ratio carbon nanocone probes by electron beam induced deposition patterning'. In: *Nanotechnology* 17.17 (Aug. 2006), p. 4322. DOI: [10.1088/0957-4484/17/17/007](https://doi.org/10.1088/0957-4484/17/17/007).
- [8] I. Estermann and O. Stern. 'Beugung von Molekularstrahlen'. de. In: *Zeitschrift für Physik* 61.1 (Jan. 1930), pp. 95–125. DOI: [10.1007/BF01340293](https://doi.org/10.1007/BF01340293).
- [9] F. Knauer and O. Stern. 'über die Reflexion von Molekularstrahlen'. de. In: *Zeitschrift für Physik* 53.11 (Nov. 1929), pp. 779–791. DOI: [10.1007/BF01341278](https://doi.org/10.1007/BF01341278).
- [10] Giorgio Benedek and J. Peter Toennies. 'Helium atom scattering spectroscopy of surface phonons: genesis and achievements'. In: *Surface Science* 299-300 (Jan. 1994), pp. 587–611. DOI: [10.1016/0039-6028\(94\)90683-1](https://doi.org/10.1016/0039-6028(94)90683-1).
- [11] Andrew P. Jardine et al. 'Ultra-high-Resolution Spin-Echo Measurement of Surface Potential Energy Landscapes'. In: *Science* 304.5678 (June 2004), pp. 1790–1793. DOI: [10.1126/science.1098490](https://doi.org/10.1126/science.1098490).
- [12] A. Fahy, M. Barr, J. Martens and P. C. Dastoor. 'A highly contrasting scanning helium microscope'. In: *Review of Scientific Instruments* 86.2 (Feb. 2015), p. 023704. DOI: [10.1063/1.4907539](https://doi.org/10.1063/1.4907539).

- [13] M. Bergin et al. 'Low-energy electron ionization mass spectrometer for efficient detection of low mass species'. In: *Review of Scientific Instruments* 92.7 (July 2021), p. 073305. DOI: [10.1063/5.0050292](https://doi.org/10.1063/5.0050292).
- [14] Matthew Bergin. 'Instrumentation and contrast mechanisms in scanning helium microscopy'. English. PhD thesis. Fitzwilliam College, University of Cambridge, 2018. DOI: [10.17863/CAM.37853](https://doi.org/10.17863/CAM.37853).
- [15] Geetika Bhardwaj, Krishna Rani Sahoo, Rahul Sharma, Parswa Nath and Pranav R. Shirhatti. *Imaging atomically thin films using neutral atom microscopy*. 2021. arXiv: [2105.09777](https://arxiv.org/abs/2105.09777) [physics.chem-ph].
- [16] P. Witham and E. Sánchez. 'Exploring neutral atom microscopy'. In: *Crystal Research and Technology* 49.9 (Sept. 2014), pp. 690–698. DOI: [10.1002/crat.201300401](https://doi.org/10.1002/crat.201300401).
- [17] D. A. MacLaren, B. Holst, D. J. Riley and W. Allison. 'Focusing Elements and Design Considerations for a Scanning Helium Microscope (SHeM)'. In: *Surface Review and Letters* 10.02n03 (Apr. 2003), pp. 249–255. DOI: [10.1142/S0218625X03005062](https://doi.org/10.1142/S0218625X03005062).
- [18] D. A. MacLaren and W. Allison. 'Microscopy with atomic beams: contrast in a scanning helium microscope'. In: *Surface Review and Letters*. Vol. 179. <http://eprints.gla.ac.uk/36804/>. 2004, pp. 383–388.
- [19] A. P. Jardine, P. Fouquet, J. Ellis and W. Allison. 'Hexapole magnet system for thermal energy ^3He atom manipulation'. In: *Review of Scientific Instruments* 72.10 (Oct. 2001), pp. 3834–3841. DOI: [10.1063/1.1405794](https://doi.org/10.1063/1.1405794).
- [20] R.R. Chaustowski, V.Y.F. Leung and K.G.H. Baldwin. 'Magnetic hexapole lens focusing of a metastable helium atomic beam for UV-free lithography'. In: *Applied Physics B* 86.3 (Feb. 2007), pp. 491–496. DOI: [10.1007/s00340-006-2497-2](https://doi.org/10.1007/s00340-006-2497-2).
- [21] Bodil Holst and William Allison. 'An atom-focusing mirror'. In: *Nature* 390.6657 (Nov. 1997), p. 244. DOI: [10.1038/36769](https://doi.org/10.1038/36769).
- [22] D. Barredo et al. 'Si(111)–H(1×1): A mirror for atoms characterized by AFM, STM, He and H₂ diffraction'. In: *Surface Science* 601.1 (Jan. 2007), pp. 24–29. DOI: [10.1016/j.susc.2006.08.048](https://doi.org/10.1016/j.susc.2006.08.048).
- [23] K. Fladischer et al. 'An ellipsoidal mirror for focusing neutral atomic and molecular beams'. In: *New Journal of Physics* 12.3 (Mar. 2010), p. 033018. DOI: [10.1088/1367-2630/12/3/033018](https://doi.org/10.1088/1367-2630/12/3/033018).
- [24] Wikipedia. *Camera obscura* — *Wikipedia, The Free Encyclopedia*. https://en.wikipedia.org/w/index.php?title=Camera_obscura&oldid=1044500710. [Online; accessed 09-September-2021].
- [25] U. Dürig, D. W. Pohl and F. Rohner. 'Near-field optical-scanning microscopy'. In: *Journal of Applied Physics* 59.10 (May 1986). Publisher: American Institute of Physics, pp. 3318–3327. DOI: [10.1063/1.336848](https://doi.org/10.1063/1.336848).

- [26] S. D. Eder, T. Reisinger, M. M. Greve, G. Bracco and B. Holst. 'Focusing of a neutral helium beam below one micron'. In: *New Journal of Physics* 14.7 (2012), p. 073014. DOI: [10.1088/1367-2630/14/7/073014](https://doi.org/10.1088/1367-2630/14/7/073014).
- [27] M. Bergin, D. J. Ward, J. Ellis and A. P. Jardine. 'A method for constrained optimisation of the design of a scanning helium microscope'. In: *Ultramicroscopy* (Aug. 2019), p. 112833. DOI: [10.1016/j.ultramic.2019.112833](https://doi.org/10.1016/j.ultramic.2019.112833).
- [28] S. D. Eder et al. 'Zero-order filter for diffractive focusing of de Broglie matter waves'. In: *Physical Review A* 95.2 (Feb. 2017), p. 023618. DOI: [10.1103/PhysRevA.95.023618](https://doi.org/10.1103/PhysRevA.95.023618).
- [29] S. D. Eder et al. 'Focusing of a neutral helium beam with a photon-sieve structure'. In: *Physical Review A* 91.4 (Apr. 2015), p. 043608. DOI: [10.1103/PhysRevA.91.043608](https://doi.org/10.1103/PhysRevA.91.043608).
- [30] S. A. Boden, Z. Moktadir, D. M. Bagnall, H. Mizuta and H. N. Rutt. 'Focused helium ion beam milling and deposition'. In: *Microelectronic Engineering*. Proceedings of the 36th International Conference on Micro- and Nano-Engineering (MNE) 88.8 (Aug. 2011), pp. 2452–2455. DOI: [10.1016/j.mee.2010.11.041](https://doi.org/10.1016/j.mee.2010.11.041).
- [31] R. Flatabø et al. 'Fast resolution change in neutral helium atom microscopy'. In: *Review of Scientific Instruments* 89.5 (May 2018), p. 053702. DOI: [10.1063/1.5029385](https://doi.org/10.1063/1.5029385).
- [32] Rémi Carminati, Manuel Nieto-Vesperinas and Jean-Jacques Greffet. 'Reciprocity of evanescent electromagnetic waves'. In: *J. Opt. Soc. Am. A* 15.3 (Mar. 1998), pp. 706–712. DOI: [10.1364/JOSAA.15.000706](https://doi.org/10.1364/JOSAA.15.000706).
- [33] David J. Riley et al. 'Helium Detection via Field Ionization from Carbon Nanotubes'. In: *Nano Letters* 3.10 (Oct. 2003), pp. 1455–1458. DOI: [10.1021/nl034460c](https://doi.org/10.1021/nl034460c).
- [34] R. B. Doak et al. 'Field ionization detection of supersonic molecular beams'. In: *Review of Scientific Instruments* 75.2 (Jan. 2004), pp. 405–414. DOI: [10.1063/1.1642743](https://doi.org/10.1063/1.1642743).
- [35] A. Fahy et al. 'Image formation in the scanning helium microscope'. In: *Ultramicroscopy* 192 (Sept. 2018), pp. 7–13. DOI: [10.1016/j.ultramic.2018.05.004](https://doi.org/10.1016/j.ultramic.2018.05.004).
- [36] T. Myles, J. Martens, A. Fahy, M. Barr and P.C. Dastoor. 'Atom microscopy - Imaging with a deft touch'. In: *Australian Physics* 54.6 (Nov. 2017), pp. 206–213.
- [37] T.A. Myles. '3D Imaging with a Scanning Helium Microscope'. Honours thesis. University of Newcastle, 2016.
- [38] M. Barr et al. 'Unlocking new contrast in a scanning helium microscope'. In: *Nature Communications* 7 (Jan. 2016), p. 10189. DOI: [10.1038/ncomms10189](https://doi.org/10.1038/ncomms10189).

- [39] Adam Joseph Fahy. 'A practical consideration of scanning helium microscopy'. PhD thesis. University of Newcastle, 2019.
- [40] M. Bergin et al. 'Observation of diffraction contrast in scanning helium microscopy'. In: *Scientific Reports* 10.1 (Feb. 2020), pp. 1–8. DOI: [10.1038/s41598-020-58704-1](https://doi.org/10.1038/s41598-020-58704-1).
- [41] J. R. Manson. 'Theoretical Aspects of Atom-Surface Scattering'. In: *Helium Atom Scattering from Surfaces*. Ed. by E. Hulpke. Springer Series in Surface Sciences. Berlin, Heidelberg: Springer, 1992, pp. 173–205. DOI: [10.1007/978-3-662-02774-5_8](https://doi.org/10.1007/978-3-662-02774-5_8).
- [42] M. Barr, K. M. O'Donnell, A. Fahy, W. Allison and P. C. Dastoor. 'A desktop supersonic free-jet beam source for a scanning helium microscope (SHeM)'. In: *Measurement Science and Technology* 23.10 (2012), p. 105901. DOI: [10.1088/0957-0233/23/10/105901](https://doi.org/10.1088/0957-0233/23/10/105901).
- [43] G. Scoles. *Atomic and molecular beam methods / edited by Giacinto Scoles*. eng. Oxford: Oxford University Press, 1988.
- [44] Thomas A. Myles et al. 'Taxonomy through the lens of neutral helium microscopy'. In: *Scientific Reports* 9.1 (Feb. 2019), p. 2148. DOI: [10.1038/s41598-018-36373-5](https://doi.org/10.1038/s41598-018-36373-5).
- [45] S. M. Lambrick, M. Bergin, A. P. Jardine and D. J. Ward. 'A ray tracing method for predicting contrast in neutral atom beam imaging'. In: *Micron* 113 (Oct. 2018), pp. 61–68. DOI: [10.1016/j.micron.2018.06.014](https://doi.org/10.1016/j.micron.2018.06.014).
- [46] Sam Lambrick. 'Use of optical tools to reconstruct contrast in Helium Atom Microscope images'. M.Sci. Part III report. Cambridge University, 2017.
- [47] Fred E. Nicodemus. 'Directional Reflectance and Emissivity of an Opaque Surface'. In: *Applied Optics* 4.7 (July 1965), pp. 767–775. DOI: [10.1364/AO.4.000767](https://doi.org/10.1364/AO.4.000767).
- [48] Sam Lambrick. *slambrick/SHeM-Ray-Tracing-Simulation: SHeM Ray Tracing Simulation*. Apr. 2018. DOI: [10.5281/zenodo.1228079](https://doi.org/10.5281/zenodo.1228079).
- [49] M. Born and E. Wolf. *Principles of optics*. 4th. Oxford University Press, 1968.
- [50] F. A. Dahlen and Jeroen Tromp. *Theoretical global seismology*. Princeton University Press, 1998.
- [51] G. H. Spencer and M. V. R. K. Murty. 'General Ray-Tracing Procedure'. In: *Journal of the Optical Society of America* 52.6 (June 1962), p. 672. DOI: [10.1364/JOSA.52.000672](https://doi.org/10.1364/JOSA.52.000672).
- [52] S. Marschner and P. Shirley. *Fundamentals of Computer Graphics*. 4th. Taylor & Francis, 2016.
- [53] *Photometria sive de mensura et gradibus luminis, colorum et umbrae*. lat. Augsburg: Augustae Vindelicorum, 1760. DOI: [10.3931/e-rara-9488](https://doi.org/10.3931/e-rara-9488).

- [54] M Knudsen. *The kinetic theory of gases: some modern aspects*. 3rd ed. London, 1950.
- [55] John Greenwood. 'The correct and incorrect generation of a cosine distribution of scattered particles for Monte-Carlo modelling of vacuum systems'. In: *Vacuum* 67.2 (Sept. 2002), pp. 217–222. DOI: [10.1016/S0042-207X\(02\)00173-2](https://doi.org/10.1016/S0042-207X(02)00173-2).
- [56] R. Kersevan and M. Ady. *Molflow+ is a Monte Carlo code developed at CERN*. <https://molflow.web.cern.ch>.
- [57] R. Kersevan and J.-L. Pons. 'Introduction to MOLFLOW+: New graphical processing unit-based Monte Carlo code for simulating molecular flows and for calculating angular coefficients in the compute unified device architecture environment'. In: *Journal of Vacuum Science & Technology A* 27.4 (July 2009). Publisher: American Vacuum Society, pp. 1017–1023. DOI: [10.1116/1.3153280](https://doi.org/10.1116/1.3153280).
- [58] Adrià Salvador Palau, Gianangelo Bracco and Bodil Holst. 'Theoretical model of the helium pinhole microscope'. In: *Physical Review A* 94.6 (Dec. 2016). DOI: [10.1103/PhysRevA.94.063624](https://doi.org/10.1103/PhysRevA.94.063624).
- [59] Dan Serement. 'Chemical Contrast from Diffraction and Debye-Waller Scattering in SHeM'. M.Sci. Part III report. University of Cambridge, 2020.
- [60] P. J. Witham and E. J. Sánchez. 'Increased resolution in neutral atom microscopy'. In: *Journal of Microscopy* 248.3 (Dec. 2012), pp. 223–227. DOI: [10.1111/j.1365-2818.2012.03665.x](https://doi.org/10.1111/j.1365-2818.2012.03665.x).
- [61] Mahmoud I. Abbas, Sami Hammoud, Tarek Ibrahim and Mohamed Sakr. 'Analytical formulae to calculate the solid angle subtended at an arbitrarily positioned point source by an elliptical radiation detector'. In: *Nuclear Instruments and Methods in Physics Research Section A: Accelerators, Spectrometers, Detectors and Associated Equipment* 771 (Jan. 2015), pp. 121–125. DOI: [10.1016/j.nima.2014.10.061](https://doi.org/10.1016/j.nima.2014.10.061).
- [62] John T. Conway. 'Analytical solution for the solid angle subtended at any point by an ellipse via a point source radiation vector potential'. In: *Nuclear Instruments and Methods in Physics Research Section A: Accelerators, Spectrometers, Detectors and Associated Equipment* 614.1 (Feb. 2010), pp. 17–27. DOI: [10.1016/j.nima.2009.11.075](https://doi.org/10.1016/j.nima.2009.11.075).
- [63] Michelson A A. *Studies In Optics*. Chicago: The University of Chicago Press, 1927.
- [64] Eli Peli. 'Contrast in complex images'. In: *J. Opt. Soc. Am. A* 7.10 (Oct. 1990), pp. 2032–2040. DOI: [10.1364/JOSAA.7.002032](https://doi.org/10.1364/JOSAA.7.002032).
- [65] Kenneth Langstreth Johnson. *Contact Mechanics*. Cambridge University Press, Aug. 1987.

- [66] D. P. DePonte, S. D. Kevan and F. S. Patton. 'Brightness of micronozzle helium source'. In: *Review of Scientific Instruments* 77.5 (May 2006), p. 055107. DOI: [10.1063/1.2198813](https://doi.org/10.1063/1.2198813).
- [67] Engineering ToolBox. *Young's Modulus - Tensile and Yield Strength for some common Materials*. www.engineeringtoolbox.com/young-modulus-d_417.html. 2003.
- [68] Adrià Salvador Palau, Gianangelo Bracco and Bodil Holst. 'Theoretical model of the helium zone plate microscope'. In: *Physical Review A* 95.1 (Jan. 2017). DOI: [10.1103/PhysRevA.95.013611](https://doi.org/10.1103/PhysRevA.95.013611).
- [69] Pfeiffer Vacuum. *Introduction to Vacuum Technology*. <https://www.pfeiffer-vacuum.com/en/know-how/introduction-to-vacuum-technology/>. [Online; accessed 09-September-2021].
- [70] B. Mercier. 'Conductance measurement of a conical tube and calculation of the pressure distribution'. In: *Journal of Vacuum Science & Technology A* 24.3 (Apr. 2006), pp. 529–536. DOI: [10.1116/1.2187996](https://doi.org/10.1116/1.2187996).
- [71] M. Bergin et al. 'Complex optical elements for scanning helium microscopy through 3D printing'. In: *Measurement Science and Technology* (2021). In Review.
- [72] Aleksandar Radić. 'Implementing photometric stereo for SHeM to reconstruct true-to-size 3D surfaces'. M.Phil Thesis. University of Cambridge, Sept. 2021.
- [73] Lord Rayleigh F.R.S. 'XXXI. Investigations in optics, with special reference to the spectroscope'. In: *The London, Edinburgh, and Dublin Philosophical Magazine and Journal of Science* (May 2009). DOI: [10.1080/14786447908639684](https://doi.org/10.1080/14786447908639684).
- [74] Nick A von Jeinsen. 'Leveraging Spatial and Angular Resolution in Scanning Helium Microscopy to Study Technological Samples'. M.Phil Thesis. University of Cambridge, Aug. 2021.
- [75] Salvador Miret-Artés and Eli Pollak. 'Classical theory of atom-surface scattering: The rainbow effect'. In: *Surface Science Reports* 67.7-8 (July 2012), pp. 161–200. DOI: [10.1016/j.surfrep.2012.03.001](https://doi.org/10.1016/j.surfrep.2012.03.001).
- [76] J. Boheim and W. Brenig. 'Theory of inelastic atom-surface scattering: Examples of energy distributions'. In: *Zeitschrift für Physik B Condensed Matter* 41.3 (Sept. 1981), pp. 243–250. DOI: [10.1007/BF01294430](https://doi.org/10.1007/BF01294430).
- [77] D. R. O'Keefe and R. L. Palmer. 'Atomic and molecular beam scattering from macroscopically rough surfaces'. In: *Journal of Vacuum Science and Technology* 8.1 (Jan. 1971), pp. 27–30. DOI: [10.1116/1.1492975](https://doi.org/10.1116/1.1492975).
- [78] S. M. Lambrick et al. 'Multiple scattering in scanning helium microscopy'. In: *Applied Physics Letters* 116.6 (Feb. 2020), p. 061601. DOI: [10.1063/1.5143950](https://doi.org/10.1063/1.5143950).

- [79] D. Bergström, J. Powell and A. F.h. Kaplan. 'The absorption of light by rough metal surfaces—A three-dimensional ray-tracing analysis'. In: *Journal of Applied Physics* 103.10 (May 2008), p. 103515. DOI: [10.1063/1.2930808](https://doi.org/10.1063/1.2930808).
- [80] Bentley Carr. *Scattering from Rough Surfaces*. University of Cambridge. Summer project report. Sept. 2020.
- [81] Kakuen Tang and Richard O. Buckius. 'A statistical model of wave scattering from random rough surfaces'. In: *International Journal of Heat and Mass Transfer* 44.21 (Nov. 2001), pp. 4059–4073. DOI: [10.1016/S0017-9310\(01\)00050-3](https://doi.org/10.1016/S0017-9310(01)00050-3).
- [82] Torstein Storflor Hegge, Torstein Nesse, Alexei A. Maradudin and Ingve Simonsen. 'The scattering of a scalar beam from isotropic and anisotropic two-dimensional randomly rough Dirichlet or Neumann surfaces: The full angular intensity distributions'. In: *Wave Motion* 82 (Nov. 2018), pp. 30–50. DOI: [10.1016/j.wavemoti.2018.07.001](https://doi.org/10.1016/j.wavemoti.2018.07.001).
- [83] David E. Manolopoulos, Robert E. Wyatt and David C. Clary. 'Iterative solution in quantum scattering theory. The log derivative Kohn approach'. In: *Journal of the Chemical Society, Faraday Transactions* 86.10 (Jan. 1990), pp. 1641–1648. DOI: [10.1039/FT9908601641](https://doi.org/10.1039/FT9908601641).
- [84] F. Borondo, Charles Jaffé and S. Miret-Artés. 'Classical chaotic elastic atom-surface scattering'. In: *Surface Science* 317.1 (Sept. 1994), pp. 211–220. DOI: [10.1016/0039-6028\(94\)90268-2](https://doi.org/10.1016/0039-6028(94)90268-2).
- [85] R. Guantes, F. Borondo, J. Margalef-Roig, S. Miret-Artés and J. R. Manson. 'Threshold resonances in classical chaotic atom—surface scattering'. In: *Surface Science* 375.2 (Apr. 1997), pp. L379–L384. DOI: [10.1016/S0039-6028\(97\)80008-8](https://doi.org/10.1016/S0039-6028(97)80008-8).
- [86] Erwin Fehlberg. *Low-order Classical Runge-Kutta Formulas with Step-size Control and Their Application to Some Heat Transfer Problems*. en. Google-Books-ID: IMAJw5g4hGkC. National Aeronautics and Space Administration, 1969.
- [87] M. C. W. van Rossum and Th. M. Nieuwenhuizen. 'Multiple scattering of classical waves: microscopy, mesoscopy, and diffusion'. In: *Reviews of Modern Physics* 71.1 (Jan. 1999), pp. 313–371. DOI: [10.1103/RevModPhys.71.313](https://doi.org/10.1103/RevModPhys.71.313).
- [88] B. J. Inkson. '2 - Scanning electron microscopy (SEM) and transmission electron microscopy (TEM) for materials characterization'. en. In: *Materials Characterization Using Nondestructive Evaluation (NDE) Methods*. Ed. by Gerhard Hübschen, Iris Altpeter, Ralf Tschuncky and Hans-Georg Herrmann. Woodhead Publishing, Jan. 2016, pp. 17–43. DOI: [10.1016/B978-0-08-100040-3.00002-X](https://doi.org/10.1016/B978-0-08-100040-3.00002-X).

- [89] Amaury Badon, A. Claude Boccara, Geoffroy Lerosey, Mathias Fink and Alexandre Aubry. 'Multiple scattering limit in optical microscopy'. In: *Optics Express* 25.23 (Nov. 2017), pp. 28914–28934. DOI: [10.1364/OE.25.028914](https://doi.org/10.1364/OE.25.028914).
- [90] W. Steckelmacher. 'Knudsen flow 75 years on: the current state of the art for flow of rarefied gases in tubes and systems'. In: *Reports on Progress in Physics* 49.10 (Oct. 1986), pp. 1083–1107. DOI: [10.1088/0034-4885/49/10/001](https://doi.org/10.1088/0034-4885/49/10/001).
- [91] M. Vielreicher et al. 'Taking a deep look: modern microscopy technologies to optimize the design and functionality of biocompatible scaffolds for tissue engineering in regenerative medicine'. In: *Journal of The Royal Society Interface* 10.86 (Sept. 2013), p. 20130263. DOI: [10.1098/rsif.2013.0263](https://doi.org/10.1098/rsif.2013.0263).
- [92] David S. Hill et al. 'A Novel Fully Humanized 3D Skin Equivalent to Model Early Melanoma Invasion'. In: *Molecular Cancer Therapeutics* 14.11 (Nov. 2015), pp. 2665–2673. DOI: [10.1158/1535-7163.MCT-15-0394](https://doi.org/10.1158/1535-7163.MCT-15-0394).
- [93] Mathilde Roger et al. 'Bioengineering the microanatomy of human skin'. In: *Journal of Anatomy* 234.4 (2019), pp. 438–455. DOI: [10.1111/joa.12942](https://doi.org/10.1111/joa.12942).
- [94] K.H. Rieder and T. Engel. 'Atomic beam diffraction from solid surfaces'. In: *Nuclear Instruments and Methods* 170.1-3 (Mar. 1980), pp. 483–487. DOI: [10.1016/0029-554X\(80\)91061-7](https://doi.org/10.1016/0029-554X(80)91061-7).
- [95] N. Avidor and W. Allison. 'Helium Diffraction as a Probe of Structure and Proton Order on Model Ice Surfaces'. In: *The Journal of Physical Chemistry Letters* 7.22 (Nov. 2016), pp. 4520–4523. DOI: [10.1021/acs.jpcllett.6b02221](https://doi.org/10.1021/acs.jpcllett.6b02221).
- [96] Claus Jönsson. 'Elektroneninterferenzen an mehreren künstlich hergestellten Feinspalten'. In: *Zeitschrift für Physik* 161.4 (Aug. 1961), pp. 454–474. DOI: [10.1007/BF01342460](https://doi.org/10.1007/BF01342460).
- [97] O. Carnal and J. Mlynek. 'Young's double-slit experiment with atoms: A simple atom interferometer'. In: *Physical Review Letters* 66.21 (May 1991), pp. 2689–2692. DOI: [10.1103/PhysRevLett.66.2689](https://doi.org/10.1103/PhysRevLett.66.2689).
- [98] Markus Arndt et al. 'Wave-particle duality of C₆₀ molecules'. In: *Nature* 401.6754 (Oct. 1999), pp. 680–682. DOI: [10.1038/44348](https://doi.org/10.1038/44348).
- [99] James R. Bledsoe and Sam S. Fisher. 'Scattering of helium nozzle beams from LiF(001) and NaCl(001) crystal surfaces: I. Elastic and inelastic transitions'. In: *Surface Science* 46.1 (Nov. 1974), pp. 129–156. DOI: [10.1016/0039-6028\(74\)90245-3](https://doi.org/10.1016/0039-6028(74)90245-3).
- [100] Pablo Nieto, Daniel Barredo, Daniel Farías and Rodolfo Miranda. 'In-Plane and Out-of-Plane Diffraction of H₂ from Ru(001)'. In: *The Journal of Physical Chemistry A* 115.25 (June 2011), pp. 7283–7290. DOI: [10.1021/jp200502v](https://doi.org/10.1021/jp200502v).

- [101] Barbara A. J. Lechner. 'Studying complex surface dynamical systems using helium-3 spin-echo spectroscopy'. Thesis. University of Cambridge, Oct. 2012. DOI: [10.17863/CAM.16686](https://doi.org/10.17863/CAM.16686).
- [102] Gefen Corem et al. 'Ordered H₂O Structures on a Weakly Interacting Surface: A Helium Diffraction Study of H₂O/Au(111)'. In: *The Journal of Physical Chemistry C* 117.45 (Nov. 2013), pp. 23657–23663. DOI: [10.1021/jp405101q](https://doi.org/10.1021/jp405101q).
- [103] T. Engel. 'A molecular beam investigation of He, CO, and O₂ scattering from Pd(111)'. In: *The Journal of Chemical Physics* 69.1 (July 1978), pp. 373–385. DOI: [10.1063/1.436363](https://doi.org/10.1063/1.436363).
- [104] G. Vidali, M. W. Cole, W. H. Weinberg and W. A. Steele. 'Helium as a Probe of the (111) Surface of Diamond'. In: *Physical Review Letters* 51.2 (July 1983), pp. 118–121. DOI: [10.1103/PhysRevLett.51.118](https://doi.org/10.1103/PhysRevLett.51.118).
- [105] Franziska Traeger. 'Helium Atom Scattering from Oxide Surfaces'. In: *ChemPhysChem* 7.5 (May 2006), pp. 1006–1013. DOI: [10.1002/cphc.200500599](https://doi.org/10.1002/cphc.200500599).
- [106] D. J. Riley et al. 'A refined He–LiF(001) potential from selective adsorption resonances measured with high-resolution helium spin-echo spectroscopy'. In: *The Journal of Chemical Physics* 126.10 (Mar. 2007), p. 104702. DOI: [10.1063/1.2464087](https://doi.org/10.1063/1.2464087).
- [107] Vittorio Celli, Dieter Eichenauer, Achim Kaufhold and J. Peter Toennies. 'Pairwise additive semi ab initio potential for the elastic scattering of He atoms from the LiF(001) crystal surface'. In: *The Journal of Chemical Physics* 83.5 (Sept. 1985), pp. 2504–2521. DOI: [10.1063/1.449297](https://doi.org/10.1063/1.449297).
- [108] G. Boato, P. Cantini and L. Mattera. 'A study of the (001)LiF surface at 80 K by means of diffractive scattering of He and Ne atoms at thermal energies'. In: *Surface Science* 55.1 (Apr. 1976), pp. 141–178. DOI: [10.1016/0039-6028\(76\)90381-2](https://doi.org/10.1016/0039-6028(76)90381-2).
- [109] M. Minniti et al. 'Helium, neon and argon diffraction from Ru(0001)'. In: *Journal of Physics: Condensed Matter* 24.35 (Aug. 2012), p. 354002. DOI: [10.1088/0953-8984/24/35/354002](https://doi.org/10.1088/0953-8984/24/35/354002).
- [110] D. R. O'Keefe, Joe N. Smith, R. L. Palmer and Howard Saltsburg. 'Comparisons of the Reflection and Diffraction of ³He, ⁴He, H₂, and D₂ from the (001) Surface of LiF'. In: *The Journal of Chemical Physics* 52.9 (May 1970), pp. 4447–4458. DOI: [10.1063/1.1673671](https://doi.org/10.1063/1.1673671).
- [111] David R Lide. *CRC Handbook of Chemistry and Physics*. 72nd ed. CRC Press, 1992.
- [112] Sam M. Lambrick et al. 'True-to-size surface mapping with neutral helium atoms'. In: *Physical Review A* 103.5 (May 2021), p. 053315. DOI: [10.1103/PhysRevA.103.053315](https://doi.org/10.1103/PhysRevA.103.053315).

- [113] Robert J. Woodham. 'Photometric Method For Determining Surface Orientation From Multiple Images'. In: *Optical Engineering* 19.1 (Feb. 1980), p. 191139. DOI: [10.1117/12.7972479](https://doi.org/10.1117/12.7972479).
- [114] Berthold K. P. Horn, Robert J. Woodham and William M. Silver. 'Determining shape and reflectance using multiple images'. In: 1978.
- [115] John C. Stover. *Optical scattering : measurement and analysis*. International Society for Optics and Photonics (SPIE), July 2012.
- [116] Matthew Harker and Paul O'Leary. *Surface Reconstruction from Gradient Fields: grad2Surf Version 1.0*. <https://uk.mathworks.com/matlabcentral/fileexchange/43149-surface-reconstruction-from-gradient-fields-grad2surf-version-1-0>. MATLAB Central File Exchange, Sept. 2021.
- [117] M. Harker and P. O'Leary. 'Least squares surface reconstruction from measured gradient fields'. In: *2008 IEEE Conference on Computer Vision and Pattern Recognition*. June 2008, pp. 1–7. DOI: [10.1109/CVPR.2008.4587414](https://doi.org/10.1109/CVPR.2008.4587414).
- [118] Matthew Harker and Paul O'Leary. 'Regularized Reconstruction of a Surface from its Measured Gradient Field'. In: *Journal of Mathematical Imaging and Vision* 51.1 (Jan. 2015), pp. 46–70. DOI: [10.1007/s10851-014-0505-4](https://doi.org/10.1007/s10851-014-0505-4).
- [119] Thomas Reisinger et al. 'Direct Images of the Virtual Source in a Supersonic Expansion'. In: *The Journal of Physical Chemistry A* 111.49 (Dec. 2007), pp. 12620–12628. DOI: [10.1021/jp076102u](https://doi.org/10.1021/jp076102u).
- [120] A. Hertzmann and S. M. Seitz. 'Example-based photometric stereo: shape reconstruction with general, varying BRDFs'. In: *IEEE Transactions on Pattern Analysis and Machine Intelligence* 27.8 (Aug. 2005), pp. 1254–1264. DOI: [10.1109/TPAMI.2005.158](https://doi.org/10.1109/TPAMI.2005.158).
- [121] S. Ikehata, D. Wipf, Y. Matsushita and K. Aizawa. 'Robust photometric stereo using sparse regression'. In: *2012 IEEE Conference on Computer Vision and Pattern Recognition*. ISSN: 1063-6919. June 2012, pp. 318–325. DOI: [10.1109/CVPR.2012.6247691](https://doi.org/10.1109/CVPR.2012.6247691).
- [122] D. B. Goldman, B. Curless, A. Hertzmann and S. M. Seitz. 'Shape and Spatially-Varying BRDFs from Photometric Stereo'. In: *IEEE Transactions on Pattern Analysis and Machine Intelligence* 32.6 (June 2010), pp. 1060–1071. DOI: [10.1109/TPAMI.2009.102](https://doi.org/10.1109/TPAMI.2009.102).
- [123] T. Higo, Y. Matsushita and K. Ikeuchi. 'Consensus photometric stereo'. In: *2010 IEEE Computer Society Conference on Computer Vision and Pattern Recognition*. June 2010, pp. 1157–1164. DOI: [10.1109/CVPR.2010.5540084](https://doi.org/10.1109/CVPR.2010.5540084).
- [124] Hiroaki Santo, Masaki Samejima, Yusuke Sugano, Boxin Shi and Yasuyuki Matsushita. 'Deep Photometric Stereo Network'. In: *Proceedings of the IEEE International Conference on Computer Vision Workshops*. Oct. 2017, pp. 501–509. DOI: [10.1109/ICCVW.2017.66](https://doi.org/10.1109/ICCVW.2017.66).

- [125] Tilo Strutz. *Data Fitting and Uncertainty (A practical introduction to weighted least squares and beyond)*. Springer Vieweg, Oct. 2010.
- [126] J. Garnaes et al. 'Profiles of a high-aspect-ratio grating determined by spectroscopic scatterometry and atomic-force microscopy'. In: *Applied Optics* 45.14 (May 2006), pp. 3201–3212. DOI: [10.1364/ao.45.003201](https://doi.org/10.1364/ao.45.003201).
- [127] Satoshi Ikehata and Kiyoharu Aizawa. 'Photometric Stereo using Constrained Bivariate Regression for General Isotropic Surfaces'. In: *Proceedings of the IEEE Conference on Computer Vision and Pattern Recognition (CVPR)*. June 2014, pp. 2179–2186. DOI: [10.1109/CVPR.2014.280](https://doi.org/10.1109/CVPR.2014.280).
- [128] K.F. Riley, M.P. Hobson and S.J. Bence. *Mathematical Methods for Physics and Engineering*. 3rd ed. Cambridge: Cambridge University Press, 2006.

COLOPHON

This document was typeset using the typographical look-and-feel `classicthesis` developed by André Miede and Ivo Pletikosić. The style was inspired by Robert Bringhurst's seminal book on typography "*The Elements of Typographic Style*". `classicthesis` is available for both \LaTeX and \LyX :

<https://bitbucket.org/amiede/classicthesis/>

Final Version as of 8th April 2022 (`classicthesis v4.6`).